NOVEL *IN OPERANDO* CHARACTERIZATION METHODS FOR ADVANCED LITHIUM-ION BATTERIES

A Dissertation
Presented to
The Academic Faculty

by

Cole Fredrick Petersburg

In Partial Fulfillment
of the Requirements for the Degree
Doctor of Philosophy in the
School of Materials Science and Engineering

Georgia Institute of Technology
May 2013

NOVEL *IN OPERANDO* CHARACTERIZATION METHODS FOR ADVANCED LITHIUM-ION BATTERIES

Approved by:

Professor Faisal Alamgir, Advisor
School of Materials Science and Engineering
Georgia Institute of Technology

Professor Brent Carter
School of Materials Science and Engineering
Georgia Institute of Technology

Professor Thomas Fuller
School of Chemical Engineering
Georgia Institute of Technology

Professor Rosario Gerhardt
School of Materials Science and Engineering
Georgia Institute of Technology

Professor Meilin Liu
School of Materials Science and Engineering
Georgia Institute of Technology

Date Approved: 9 Jan 2013

ACKNOWLEDGEMENTS

I thank Prof. Alamgir for guiding me on a fascinating path of research. His vision of combining electrochemistry with spectroscopy is both useful and beautiful, and I hope that this dissertation demonstrates that. If that is the case, my committee deserves much of the credit, as their keen insights helped me reshape this document to make it presentable to a wider audience.

I thank Dr. Daniel Fischer at the National Synchrotron Light Source for similarly keeping the faith by frequently bestowing collaborator beamtime, in addition to awarded beamtime, at NIST beamline U7A. This generosity is evident in the amount of data presented in Chapter V. Dr. Fischer's development of new and unique technologies at the NSLS is an inspiration.

I thank Jordan Greenlee for adding a third dimension to the work, that of adding electronic property considerations to the electrochemistry and spectroscopy. Our collaboration was unique, fruitful, and enjoyable. I also thank my undergraduate assistants, in particular Reece Daniel and Kevin Bogaert. Working with Reece was like working with a second graduate student assigned to the same project. Kevin was a hard worker from day one, but his development towards the skills of a graduate-level researcher has been breathtaking.

My MSE professors at Iowa State University deserve much credit for helping me to get this far. In addition to their excellent teaching, their attitude made it clear that they truly enjoyed academia. In particular, Prof. Vikram Dalal gave me my first opportunities in graduate-level research and inspired me to continue.

The support of my parents, Fred and Paula, has been constant and overwhelming, even in the toughest times. The brunt of the burden, however, has fallen on my wife Kristin. Time and again, my work has continued past deadlines, taking away from our time together. Through it all, Kristin has stood by me, and I cannot thank her enough.

TABLE OF CONTENTS

LIST OF TABLES

LIST OF FIGURES

LIST OF SYMBOLS OR ABBREVIATIONS

E_0	Reference energy for the EXAFS photoelectron.
EIS	Electrochemical Impedance Spectroscopy.
EXAFS	Extended X-ray Absorption Spectroscopy.
FY	Fluorescence Yield, a detection mode for soft X-ray spectroscopy.
L-edge	X-ray absorption feature; here, a 2p $\rightarrow$ 3d electron transition.
LMCT	Ligand-to-metal charge transfer.
mAh	milliamp-hours, a unit of charge equal to a current of one milliamp held for one hour.
NEXAFS	Near-Edge X-ray Absorption Fine Structure in the soft X-ray context.
NSLS	National Synchrotron Light Source at Brookhaven National Laboratory.
PEY	Partial Electron Yield, a detection mode for soft X-ray spectroscopy.
TEY	Total Electron Yield, a detection mode for soft X-ray spectroscopy.
U7A	National Institute of Standards and Technology soft X-ray beamline.
VUV	Vacuum Ultraviolet rays, synonym for soft X-rays.
X11A	Naval Research Laboratories hard X-ray beamline.
XANES	X-ray Absorption Near-Edge Structure in the hard X-ray context.
XAS	X-ray Absorption Spectroscopy.
XDAC	Data acquisition program by Johnny Kirkland, for soft and hard X-ray beamlines.
XPS	X-ray Photoelectron Spectroscopy.

SUMMARY

Lithium-ion batteries provide high-density energy storage, in terms of both mass and volume, for electronics and even for automobiles. However, the cost of lithium-ion cathode materials is high, and new cathode chemistries are desired which provide a higher density of energy storage relative to their cost. Such chemistries could include oxide materials incorporating cheaper and lighter combinations of transition metal ions, or ultimately lithium-oxygen batteries which utilize oxygen in the atmosphere to provide charge capacity. In each case, lithium is effectively "burned" or oxidized in a reversible way rather than in an irreversible way as is the case with fossil fuels. In the latter case, oxygen gas is the oxidizer. In the former case, a mixture of transition metal ions is used as the oxidizer in the reaction. However, contrary to expectations, there is evidence that when the reaction is reversed and the battery is charged, both the transition metal ions and the oxygen in the crystal lattice of the oxide material are oxidized. This complex mechanism of charge compensation must be well known if new cathodes are to be developed.

Currently, cathode characterization methods, based on the absorption of hard X-rays, are limited in their ability to detect the oxidation of mixtures of transition metal ions in an element-specific and precise manner. Furthermore, the oxidation of oxygen has only been detected in cathode material from dismantled batteries which has already reacted with liquid electrolytes and possibly with atmospheric moisture. More precise oxidation states can be determined using the absorption of soft X-rays, including both the individual transition metals as well as oxygen.

In this study a new and long-sought technique is developed which enables soft X-ray absorption studies *in operando*, i.e., on working batteries. These batteries are free-standing ceramic batteries in which the intercalation cathode material under study is directly exposed to vacuum while remaining electrically connected to the cell during charge and discharge operations. This design simultaneously allows the incident soft X-ray beam to reach the intercalation cathode material while allowing Auger electrons and photoelectrons to leave the sample, making the technique highly surface-sensitive.

The scientific goal which has been achieved via this technique is the detection of oxygen hole formation (or oxygen oxidation) during the charging of a lithium battery. By the process of elimination, the oxidation of oxygen has long been inferred to occur at high states of charge after the transition metal ions cease to oxidize. However, in this study the oxidation of oxygen is seen in the early stages of delithiation in tandem with the oxidation of nickel ions. Using this technique, new mixed transition metal oxide materials can be screened and characterized in terms of their ability to allow reversible oxygen oxidation. Furthermore, this technique is ideal for research on lithium-oxygen batteries. The free-standing ceramic battery technique is also extended to high-temperature experimentation which will enable accelerated studies of battery cathodes at high temperatures without the associated electrolyte decomposition problems inherent in liquid electrolyte batteries.

In concert with soft X-ray absorption spectroscopy, innovative hard X-ray absorption data analysis methods have been used to obtain detailed local structure information, especially metal-oxygen bond distances which can also indicate subtle, element-specific oxidation and reduction trends.

In a closely related series of studies in collaboration with Prof. Alan Doolittle and Jordan Greenlee, *in operando* soft X-ray methods were developed in order to measure charge compensation trends in thin film memristor devices which are being developed for novel computing applications. Because lithium-based memristor materials are similar or identical to transition metal oxide cathode materials, the charge compensation trends seen in memristors can be compared with trends seen in batteries to gain new insights.

CHAPTER I

INTRODUCTION

Technological progress often seems limitless given the constant improvements seen in technological devices such as automobiles, computers, and in communication devices. For over a century, the internal combustion engine has gained efficiency, power, and cleanliness.[1] Computers have gained computing power exponentially for many decades according to Moore's Law, in spite of many apparent limits which have appeared before being conquered.[2] Communications devices are evolving so rapidly that the term "smartphone" may quickly become an anachronism due to the vast array of communications and navigation antennas, magnetic, temperature, and pressure sensors, and audiovisual capabilities combined in a single unit. The battery life of such devices is outstripped by the power consumption of the electronics.[3] Lithium-ion battery capacity has grown only slowly in spite of consumer demand.[4,5] It appears that there is an asymptotic limit to the energy which can be stored in a lithium-ion battery of a given mass.[6] Furthermore, this energy storage limit is much too low to be used in all-electric automobiles of the same range as conventional automobiles.[4]

This energy storage limit is firmly grounded in terms of chemistry and crystal structures. In a lithium-ion battery, positive ions of the lightest metallic element, lithium, travel between a negative electrode (termed an anode) where its potential energy is high, and a positive electrode (termed a cathode) in which its chemical potential is extremely low. Each of these electrodes acts like a set of deep shelves, allowing lithium ions to be stored deep within a crystalline anode or cathode rather than only on the surface of the electrodes. To the extent that these shelves are rigid, they can accept and deliver lithium ions hundreds of times reversibly, without failing. The energy stored within the battery is proportional to the product of cell voltage, or the difference in the chemical potential of lithium between the anode and cathode, and the number of lithium ions which can be shuttled between the anode and cathode. The gravimetric energy density is the ratio of the energy stored and the mass of the cell. Although very lightweight anode materials such as carbon and silicon[7] can store large quantities of lithium ions in a small volume, the capacity of a cell is currently limited

by heavy cathode materials which can only store small quantities of lithium ions. Therefore, for a given mass of a lithium battery, the gravimetric energy density can only be improved by increasing the capacity and decreasing the mass of cathode materials.[8]

The maximum energy storage limit appears to be imminent due to the limitations of lithiated transition metal oxide cathodes (see section 1.2). Researchers have repeatedly replaced heavy transition metal elements with slightly less heavy transition metal elements while discovering ratios of these metals which lead to incrementally higher reversible charge capacities.[6] This is analogous to computation technologies: Moore's Law of exponential growth appears to face fundamental limits as well. However, radically new technologies are being developed to allow computing power to continue to increase.[9] The traditional lithium-ion battery may be replaced by the lithium-air battery, which dispenses with the transition metal oxide cathode entirely. Instead, air from the atmosphere reacts with a catalyst at the positive electrode, forming lightweight lithium peroxide in a reversible way.[10] Such a battery would be limited in capacity not by the heavy cathode, but by the compact, lightweight anode materials which already exist.[11] Nevertheless, the development of lithium-air batteries has been slow, and their energy storage capacity is currently hindered by the slow cathode reaction, which is poorly understood at present.[12]

The common link between the limitations of transition metal oxide cathodes and lithium-air cathodes is the role of oxygen. In lithium-air batteries oxygen gas from the air must be reduced to form a peroxide and then oxidized again to oxygen gas during recharging. Surprisingly, in transition metal oxides the oxygen ions undergo the same reduction and oxidation, although to a lesser extent.[6,13] Although the release of oxygen gas is a severe safety hazard, it is *inferred* that oxygen can be reduced and oxidized reversibly because beyond the charge capacity expected based on transition metal chemistry, additional anomalous reversible capacity appears in some cathode materials.[14,15] Although these same materials do release oxygen gas during the first charge cycle,[16] the anomalous capacity continues to appear in subsequent cycles.[17] The oxidation of oxygen *without* the release of oxygen gas necessitates a new and unfamiliar term: oxygen hole. An oxygen hole is not an oxygen vacancy but a missing electron where one is expected at the oxygen site; this is explained in more detail in section 2.1.1.3. The electron which has gone missing has, in fact, contributed to the electronic current through the external load which can be an electric vehicle or a communications

device. Although oxygen holes may be tolerated in low concentrations, in large concentrations they can potentially contribute to the release of oxygen gas which is a severe hazard as described in section 1.1.2.

In this study, existing methods of monitoring transition metal chemistry in a working battery, and thereby *inferring* the presence of oxygen holes, are extended to reach new levels of precision, detail, and reliability. In addition, a new experimental method of *detecting* the presence of oxygen holes in a working battery, which was not previously possible, is developed in this work. Although different types of batteries were used for each method, the exact same cathode material was used in each. For the first time it is possible to obtain direct data on the chemical state of oxygen, as well as transition metals, in a working battery in order to explain the source of the measured charge capacity. This knowledge is crucial in improving transition metal ion batteries. Furthermore, the newly developed methods in this work will be indispensable in developing lithium-air batteries due to the central role of oxygen in such cells.

1.1 Importance of Lithium-ion Batteries and Research

Conventional vehicles propelled by the combustion of (increasingly costly) fossil fuels are a well-known source of pollution. In contrast, all-electric vehicles generate no direct emissions, can utilize non-mobile renewable energy sources,[18] and have excellent performance characteristics.[19] Because lithium-ion batteries can be as much as 95 percent energy efficient,[20] and propulsion can be 90% energy efficient,[10] all-electric cars represent a 21st century energy technology with clear environmental benefits. However, at present the economics are less favorable, although that could change in the future.

The global production of fossil fuels is not expected to increase significantly above current levels even though per capita consumption of these fuels is increasing, especially in developing nations such as India and China. Therefore, the relative cost of operating a conventional vehicle is increasing over time.[21] However, at present the costs of purchasing and operating an all-electric automobile based on lithium-ion batteries are so much higher than that of operating a conventional vehicle that for economic reasons, electric vehicles are only expected to comprise 5% of the automobile market in the United States by 2017.[22] While economics cannot currently justify the use of lithium-ion

battery vehicles, environmental concerns are more compelling. There is wide agreement that the combustion of fossil fuels has produced so much carbon dioxide that global warming has already begun, and will continue.[23] The concentration of carbon dioxide in the atmosphere has risen so much that the acidity of the ocean is increasing and is corroding coral reefs.[24] It is possible that governmental mandates for average fuel efficiency may necessitate the use of lithium-ion batteries in spite of the cost.[25]

1.1.1 Energy Density of Lithium-Ion Batteries

The average worker in the United States commutes more than 30 miles to and from work,[26] while in Atlanta, Georgia the average distance comes to 35 miles round trip on average.[27] Assuming these workers fuel their vehicles once per week, and disregarding non-work trips, their vehicles should have a range of at least 175 miles. Given current lithium-ion battery technology and economic constraints, the all-electric Nissan Leaf has a range of under 100 miles per charge, making it less practical than a conventional automobile.[28] This limited range is a roadblock to the further adoption of lithium ion batteries in automotive applications and therefore represents an important object for research.

Conventional automobiles derive energy from the combustion (or oxidation) of fossil fuels, a process which is inherently irreversible. In principle, a lithium-air battery is very similar in that lithium is oxidized with air to provide energy, although lithium-air batteries are intended to be rechargeable. Both processes are relatively high in gravimetric energy density in terms of watt-hours per kilogram: unburnt gasoline represents 13,000 Wh/kg, although the efficiency of a conventional vehicle is only around 12.6%. Unburnt lithium metal represents 11,680 Wh/kg; given that all-electric propulsion is about 90% energy efficient, it is *conceivable* that automobiles based on lithium-air could one day attain the same range possible with conventional automobiles. Until then, lithium-ion batteries appear to be limited to only about 200 Wh/kg.[10] This low value is due to the great weight of the transition metal oxide cathode described in section 1.2. In effect, a lithium-ion battery achieves the combustion of metallic lithium (or lithium alloys) using the transition metal oxide as an oxidizer in place of oxygen gas. However, lithium-ion batteries are rechargeable and

highly energy efficient while making use of electricity from fixed power sources such as solar thermal power plants.[4] In the near term, however, all-electric automobiles will not achieve the range of conventional automobiles. On the other hand, gasoline-electric, diesel-electric, battery powered and fuel cell cars all require energy storage, either as a mobile power source or to store energy from regenerative braking. Nickel Metal Hydride (NiMH) batteries are quite mature, having already provided some motorists with one hundred thousand miles of service.[29] However, lithium-ion batteries will eventually replace NiMH technology. Where NiMH allows for 80 Wh/kg of capacity, lithium-ion batteries can store 130 watt-hours per kilogram while delivering 50 percent more power per kilogram.[30,31]

1.1.2 Safety Issues for Automotive Applications

In a conventional automobile, a lead-acid battery is used to start an internal combustion engine. The energy density is low because metallic lead is very dense, but the safety is relatively high because the electrolyte is aqueous sulfuric acid. Although during overcharge the battery releases flammable hydrogen gas as well as oxygen gas through electrolysis of water, these two gases can recombine over time (if they are not vented) without causing an explosion.[32]

Another aspect of the lead-acid battery is that it is a true *battery* according to the traditional definition of a combination of electrochemical cells. This term was coined by Ben Franklin in analogy with a battery of military guns.[33] In a lead-acid battery, six cells of approximately 2 V each are arranged in series to generate 12 V. If the state of charge of one or more cells is lower than that of the others, it suffices to overcharge most of the cells while releasing hydrogen and oxygen gas. By this method, the state of charge of a series of cells may be equalized.[34] Such a simple approach is not possible for lithium ion batteries because there is no safe overcharge mechanism.[35] This may be one reason that in the literature, the term “battery” is used interchangeably with “cell” to refer to a single electrochemical cell, and the term “battery pack” is used to refer to multiple cells.

A lithium-ion cell, which is described in greater detail in section 2.1.1, consists of an anode such as graphite which can be alloyed with lithium, a nonaqueous (and usually flammable) electrolyte, and a lithiated cathode material which is typically a transition metal oxide. The flammable nonaqueous electrolyte is substituted for an aqueous electrolyte because on contact with lithium metal

or lithium alloys, water will hydrolyze into hydrogen gas and oxygen gas. Instead, an ionically conductive polymer forms between the nonaqueous electrolyte and the lithium alloy.[36] Therefore, there is no release of hydrogen. Oxygen, however, can be released from the cathode material, rather than from the electrolyte, and subsequently react with the nonaqueous electrolyte. Because the cells are sealed to prevent moisture from reacting with the lithium anode, overcharged cells will swell, or even explode, when overcharged. The risk of swelling or explosions is exacerbated by high temperatures which can be generated by a combination of high ambient temperature and ohmic heating at high current levels.[37] This combination of a sealed cell filled with a flammable electrolyte and an internal supply of oxygen gas is not unlike a grenade. If the internal resistance of a single cell is higher than that of the others in a battery pack, one exploding cell can ignite the remaining cells.[38]

To deal with these safety issues, every single lithium-ion cell needs a combination of protective devices, as well as cooling, in spite of the cost and complexity it adds to the system. Tesla Motors manufactures the Tesla Roadster, which has a battery pack consisting of 6,831 cylindrical lithium-ion batteries. Each individual cell is a small steel cylinder 6.52 cm in length by 1.86 cm.[39] To prevent thermal runaway reactions, each cell has a semiconductor device designed with a positive temperature coefficient which automatically limits cell current as the temperature increases. Inside each cell, a current interrupt device disconnects the cell when the internal pressure rises to a dangerous level. Several microprocessors are included to monitor and control the pack. Aluminum packaging is substituted for plastic packaging for heat dissipation. Finally, the entire pack is water-cooled to prevent overheating.[40] Such a system is drastically more complicated, and certainly more expensive, than a simple lead-acid battery.

All of these thermal issues depend on chemical reactions which occur at the cathode-electrolyte interface. Fundamentally, these reactions depend on the oxidation of the electrolyte due to electron transfer from the electrolyte into the cathode material. This depends on the interplay between the electronic structure of the cathode material and the electronic structure of the liquid electrolyte, both of which depend on temperature. For each combination of cathode material, electrolyte, and temperature, there exists some level of delithiation (or state of charge) which cannot be safely exceeded.[6,41] Although this limit can be found through trial and error, a theoretical understanding of this limit would allow new intercalation cathode materials to be designed intelligently. In this study,

the electronic structure of the bulk of the cathode material is studied using hard X-ray methods while the electronic structure of the surface of the cathode material is studied using soft X-ray methods in the absence of the liquid electrolyte.

1.2 Lithium-ion Intercalation Cathodes

In contrast to a lithium-air battery in which lithium is oxidized using O_2 gas to form Li_2O_2, lithium-ion batteries use transition metal oxides as an oxidizer for lithium. In this work, the focus is on layered transition metal oxides of the formula $LiMO_2$ where M is a mixture of transition metals and, in some cases, additional lithium ions. The choice of the transition metal ion M in the $LiMO_2$ formula is the central factor determining the energy density, cost, and safety criteria discussed in section 1.1. A widely used (and simple) compound $LiCoO_2$ is, unfortunately, costly due its cobalt content.[5] As discussed in section 2.1.1.2, $LiNiO_2$ is so prone to oxygen evolution and thermal runaway that it is no longer used. $LiMnO_2$ is ideal due to its relatively low cost and slightly lower mass, but its crystal structure changes due to delithiation, forming a lower-capacity compound which provides inferior cell potential. Therefore, research has turned to compounds in which M becomes a mixture of these three transition metal ions along with other transition metal ions as dopants. The ideal mixture of these elements should have lower aggregate cost than cobalt alone, more thermal stability than nickel alone, and a more stable crystalline structure than manganese alone. Unfortunately, the analysis of such compounds, including the effects of several dopants, quickly becomes complex.

In this layered $LiMO_2$ structure, depicted in section 2.1.1.2, layers of oxygen separate a layer of lithium ions from the transition metal layer in the sequence M, O, Li, O, M. These are the layers which make up the rigid shelving from which lithium ions can be extracted repeatedly. (Note that these materials are synthesized with the lithium included and that because the potential energy of the ions is low in the cathode, a newly constructed battery will be in the discharged state.) To be certain, not all the lithium ions can be removed from the structure lest it collapse, although in many cases more than half the lithium ions may be removed reversibly. Intuitively, however, the gravimetric capacity of the battery is proportional to the percentage of lithium ions which can be removed without damaging the crystal structure.

When lithium ions are removed from the structure however, the process is not purely structural. Electroneutrality requires a balance between positive and negative charges in the cathode, so when a positive lithium ion moved from the cathode to the anode, a negative electron must also be removed from the structure; because the lithium ion cannot lose any further electrons, the electron must come from another species. This process is called charge compensation. For this process, transition metals are ideally suited because they can sustain multiple formal oxidation states in addition to the elemental state. In other words, they can undergo reduction and oxidation without breaking bonds with their ligands. As discussed in section 2.1.2.2, however, there are limits on the range of oxidation states which are stable for each element. The gravimetric capacity of the battery should be limited to the range of stable oxidation states; however, it is frequently found that the *reversible* capacity of the cell extends beyond what can be expected for the range of oxidation states possible for the given compound. This excess reversible capacity cannot be attributed to oxygen loss, which is irreversible in these materials. Instead, the excess capacity is assigned to the reversible oxidation of oxygen ions in the lattice.

1.3 Advantages and Limitations of X-ray Absorption Spectroscopy

To assess the reversibility (or failure modes) of intercalation in transition metal oxides, a fine grained picture of both the crystal structure *and* the electronic structure as a function of delithiation is desired. Ideally, the location of every lithium ion, oxygen ion, and transition metal ion *relative to* the crystal structure should be measured, along with the concentration of vacancies at each of these sites, together with some knowledge of the clustering of metal ions which share the same crystal plane. The electron orbitals around each species, including both filled and unfilled orbitals, should also be measured to assess the likelihood that each species could leave the crystal, either as a gas or as a second phase. Furthermore, it would be desirable to assess the differences in these parameters between the surface and the bulk. If this knowledge is sufficiently fine-grained, the reversible limit of a cathode material could be determined in a single experiment, rather than as a result of dozens of trial-and-error experiments. The discovery of new and viable cathode materials could be greatly accelerated, and safer batteries could be developed quickly.

Unfortunately, no single experimental technique can measure the crystal structure, electronic

structure, level of defects, and degree of clustering in an element-specific way. Although X-ray diffraction is frequently used to measure changes in crystal symmetry and in the spacing of crystal planes, this technique has little sensitivity to low-atomic-number elements such as lithium. (A positive lithium ion has only two electrons to scatter X-rays.) In fact, recently the crystal structure of lithium peroxide, Li_2O_2, was redetermined with the help of electronic structure calculations.[42] Neutron scattering, which is sensitive to the nucleus of the atom and is therefore relatively more sensitive to the position of lithium ions has been used to refine structural parameters for battery materials.[43] However, both of these methods determine long-range structure and are incapable of detecting either defects or the clustering of atoms because they are insensitive to the local structure of nearest-neighbor elements. To determine local structural information, and to probe the lithium nucleus, nuclear magnetic resonance (NMR) has been used to assess the clustering of transition metal ions.[44] However, NMR is only sensitive to specific isotopes of a subset of elements in the periodic table, meaning that samples must be specially synthesized using those isotopes.[45]

X-ray absorption techniques, which are detailed in section 2.1.3, can come close to the ideal of providing element-specific structural and electronic information. Although X-ray absorption is virtually insensitive to lithium, it is extremely element-specific because, especially in the hard X-ray regime (photon energy above 4000 eV), the spectral features are separated widely in terms of X-ray photon energy according to the binding energy of the core electrons of each element. The binding energies are a monotonic function of atomic number, eliminating any elemental ambiguity.[46] This is crucial in mixed metal oxides which frequently contain more than two transition metal elements (e.g. Ni, Mn, Co, Al, Ti), as described in section 2.1.2.2.

In essence, X-ray Absorption Spectroscopy (XAS) is a measurement of the partially and completely empty electron orbitals, which are, by definition, above the Fermi level. This sets it apart from X-ray Photoelectron Spectroscopy (XPS) which is sensitive only to partially filled and fully filled orbitals; a detailed comparison is given in section 2.1.3. Changes in these features can indicate a movement of the Fermi level in the material as well as the filling or emptying of different orbitals. Furthermore, X-ray absorption is sensitive to the s-, p-, d-, or f-symmetry of unfilled orbitals, thereby revealing a different view of the same Fermi level. Although the hybridization of the bonding orbitals causes some overlap of metal and ligand features in the soft X-ray regime

(photon energy below 1000 eV), by comparing the two, deductions can be made as to the filling of p-symmetry (ligand) and d-symmetry (transition metal) orbitals which are extremely close in energy. This allows insight into the critical difference between transition metal oxidation and oxygen oxidation in a way that is not provided by any other characterization method.

In addition to this electronic structural information, X-ray absorption provides "bonus" information on the distances to, and coordination number of, neighboring atoms. As described in section 2.1.3, Extended X-ray Absorption Fine Structure (EXAFS) is a modulation of the X-ray absorption spectrum which is found just above each element's X-ray absorption edge. This non-obvious effect is a result of a resonance between neighboring atoms over a series of photoelectron kinetic energies. By extracting the extended fine structure resulting from this resonance from the X-ray absorption data and Fourier transforming the function to real space, the distances to the first 2–4 nearest neighbor shells can be measured in a completely element-specific way, although the distances obtained are not absolute. Because the photoelectron backscattering amplitude depends on the size of the electron shells of the neighboring atoms, the types of neighbors in each shell can be roughly determined, although elements of similar atomic number cannot easily be differentiated. However, the difference between a transition metal ion and a lithium ion is substantial, making it possible to infer the degree of clustering of metal ions. Together with X-ray diffraction measurements, EXAFS can yield very direct insights into the movements of neighboring atoms as a function of delithiation.

As discussed in detail in section 3.1, XAS is constrained by the ability of different X-ray energies to pass through matter. Hard X-rays are highly penetrating, making it possible to make bulk-sensitive measurements of electronic and local structure while making surface-sensitive measurements difficult. Conversely, soft X-rays are strongly absorbed by almost all forms of matter, making bulk-sensitive measurements impossible. Also, in the soft X-ray regime the element-specific absorption edges are closely spaced,[46] so that EXAFS modulations are almost always interrupted and the structural information is lost.

In this work, an existing technology is used for *in operando* hard X-ray measurements (see section 3.4) in order to obtain element-specific EXAFS measurements for transition metal elements. A new technology, however, is developed for surface-sensitive *in operando* soft X-ray measurements

for oxygen while providing additional information on the transition metal elements. A single cathode material, using the same synthesis method in each case, is studied using hard and soft X-ray *in operando* methods so that the charge compensation mechanism can be determined.

1.4 Scientific Goals

In broad terms, it is hoped that the results of this study will advance the science of lithium-ion batteries while also advancing the engineering of *in operando* batteries. For a new battery design to be useful to the broadest possible segment of battery researchers, it should incorporate powders generated by, for instance, sol-gel synthesis which produces powders with finely-tuned stoichiometries (including Mn, Ni, and Co in the correct ratios) and large surface areas using solution processing.[47] Thin film batteries are used mainly for specialized applications at present,[48] although in the future they may be incorporated into consumer microelectronics; therefore, new characterization methods should use powdered materials instead. Furthermore, the complex stoichiometries used in battery materials are difficult to reproduce using thin film methods.[49,50] In this study, an overlithiated nickel manganese oxide, $Li_{1.17}Ni_{0.25}Mn_{0.58}O_2$, is synthesized using sol-gel methods[17] and is incorporated into both hard X-ray *in operando* batteries and into soft X-ray *in operando* batteries so that direct comparisons can be made between the two experiments.

Although soft X-ray spectroscopy at the O K-edge is inherently limited to near-surface layers of a solid material rather than the bulk, it is also true that reactions between the oxide cathode and the electrolyte occur at the cathode-electrolyte interface. As discussed below, the soft X-ray *in operando* battery (like the thin film *in operando* cell of Lu et al.[51]) presents a cathode-vacuum interface while maintaining a connection with electrolyte particles. This allows the near-surface electronic structure of the cathode material to be studied in the *absence* of the electrolyte, which would otherwise react with the cathode material and change its near-surface electronic structure. (Comparisons with thin film memristor devices, described below, help to interpret the soft X-ray results.) Although a liquid electrolyte is used for the hard X-ray *in operando* battery, the measurements in that case are inherently bulk-sensitive. In each case, the electronic structure of the material is studied without the interference of the electrolyte which taints the results of most *ex situ* studies of battery materials.

1.4.1 Charge Compensation in Complex Transition Metal Oxides

Although most elements of the periodic table are restricted to a single oxidation state in order to satisfy the octet rule, the transition metals are able to take on a variety of states in order to balance the charge of a compound by exchanging electrons with negatively-charged ligands such as oxygen. The oxidation states of transition metals tend to be at least 2+, while the maximum oxidation states are obtained with oxygen and ligands and decrease from left to right across the transition metal series.[45]

Naively, it could be expected that in $LiNi_{1/3}Mn_{1/3}Co_{1/3}O_2$, which is studied in Chapter 4, would contain Ni^{3+}, Mn^{3+}, and Co^{3+} in order to balance charge evenly. The removal of lithium, then, would result in the oxidation of all three to the 4+ state. However, element-specific X-ray absorption experiments, discussed in the Literature Review (section 2.2) show that this description is inaccurate. Instead, Ni^{2+}, Mn^{4+}, and Co^{3+} are more typically found. Given this information, the removal of lithium can again (naively) be expected to result in the oxidation of nickel and cobalt. Again, the surprising finding is that only nickel participates in charge compensation. In each case, however, there is a point at which none of the transition metals appear to oxidize even though delithiation continues. To explain the nature of the capacity of different lithium-ion battery chemistries, it is crucial to use only element-specific methods to directly measure oxidation states, rather than attempting to estimate the oxidation states which are unknown. Element-specific methods must include oxygen in addition to the transition metal ions.

By using X-ray Absorption Spectroscopy, the oxidation states of transition metal oxides can be extracted in two ways. First, the electron occupancy of the bonding orbitals can be probed directly as discussed in section 1.3, although there are some theoretical limitations to this method as discussed in section 2.1.3 and practical difficulties as discussed in section 3.1. Second, the EXAFS information introduced in section 1.3 can be used to measure trends in the metal-oxygen bond distance relative to each transition metal element. The metal-oxygen bond distance will depend on the number of electrons between a metal and an oxygen ion, although this technique does not identify whether the metal or the oxygen ion loses electrons. In the case of nickel, however, the presence of multiple Ni–O bond distances can uniquely identify an oxidation state, as discussed in

section 2.1.3. Each technique is discussed in the Literature Review (section 2.2).

In this study, trends in metal-oxygen bond distances and electron configurations will be measured in order to determine detailed element-specific trends in charge compensation. However, due to the limitations of XAS, metal-oxygen bond distances are estimated by comparisons with X-ray diffraction data rather than being obtained directly, and the arrangement of atoms around an oxygen center are not available. Neither the oxidation state of the transition metals, nor of oxygen, can be determined beyond one significant figure, although subtle shifts are seen. As discussed in section 1.4.3, the majority of the experiments described herein are performed *in operando* in order to generate a highly detailed data set while ensuring that each spectrum differs from the previous only in terms of the concentration of lithium. By this method, the element responsible for charge compensation over a given range of lithium concentration is identified.

1.4.2 Oxygen-specific Electronic Structure Changes in Memristors

In the course of this work, a fruitful collaboration was formed with the research group of Alan Doolittle,[52] in the School of Electrical and Computer Engineering at Georgia Institute of Technology. Although that group's work centers around electronics instead of electrochemistry, much of their work is based on the same prototype material, $LiCoO_2$. From both perspectives, the ability of lithium ions to diffuse through a crystal without destroying it, or generating second phases, is crucial. The electrical stimulus differs, however: in their work, an electric field across the crystal causes lithium ions to become more concentrated near one (blocking) contact and less concentrated near another (blocking) contact. In lithium batteries, an electric field drives lithium ions away from the (blocking) current collector and into the electrolyte, which is blocking for electrons but non-blocking for lithium ions.

The electronic device constructed from two electrical contacts applied to the same lithiated crystal is known as a memristor. The name memristor signifies its theoretical importance as a fundamental circuit element along with resistors, capacitors, and inductors; it is essentially a resistor with a memory. When an electric field is applied to the memristor, lithium ions drift to one side of the device, altering the electronic band structure in a way that is similar to the effect of delithiation on the material. In either case, delithiation will tend to induce holes in the material, increasing

conductivity. Simultaneously, though, a pile-up of lithium ions at the opposing contact may cause a reduction in conductivity. Between the two contacts, then, the total resistance will increase and will not decrease until the electric field is removed and the ions have time to diffuse back to their original distribution. Potential applications of memristors include computer memory as well as computing architectures which simulate the activity of animal neurons.[53]

The memristor concept makes it possible to study charge compensation in thin film cathode materials in the absence of electrolyte. In particular, the O K-edge is easy to study by this method. This not only makes cell design far simpler, but it also drastically reduces the amount of time needed for a spectroscopic experiment. Still, a memristor is not a replacement for battery studies because only a limited and difficult-to-quantify percentage of lithium ions can be removed from the vicinity of one electrical contact. Because there is no electrolyte, larger percentages of lithium ions cannot be removed, and therefore an excess of lithium ions appears at the opposing contact.

1.4.3 Cell Design for *In Operando* Characterization Methods

Hard X-ray spectroscopy on working lithium-ion batteries is an established technique which can utilize packaged thin film cells[54] or liquid-electrolyte pouch cells.[55] In this work, pouch-cell methods 3.4 are used for hard X-ray spectroscopy with little modification as compared to previous work. However, the data reduction procedures discussed in section 1.4.4 and detailed in section 3.3 allow for more precise and reliable conclusions to be drawn from the data.

The scientific goal of determining the charge compensation process using soft X-ray methods, however, cannot be achieved without achieving an engineering goal: the development of a soft X-ray-compatible battery. This has never before been achieved; in the literature, any reference to "*In situ* X-ray absorption," even where soft X-ray spectroscopy is discussed,[13] always refers to hard X-ray spectroscopy. To circumvent the limitations of soft X-ray characterization methods (discussed in section 3.1), a specialized spectroelectrochemical cell was developed. The challenge of developing such a cell is highlighted by multiple failed attempts which have been published in the literature. Thiß en et al.,[50] a variety of ingenious methods were developed to attempt to lithiate thin film oxides while performing surface-sensitive spectroscopy, although ultimately these methods were not successful. Their approach of evaporating lithium onto vanadium oxide is creative, but it is not

applicable to cathode materials which are synthesized with lithium included. In a paper by Oswald et al.,[56] a method of transferring *ex situ* lithium-ion battery parts from a glovebox to an X-ray Photoelectron Spectroscopy (XPS) characterization chamber without exposure to air is described as a "Quasi *in situ* XPS" investigation. Despite the differences in methodology, both studies share many goals in common with this study.

To achieve the scientific goals of section 1.4.1, the engineering goals and constraints must be sorted out. Firstly, the surface sensitivity of soft X-ray spectroscopy, which is discussed in detail in section 3.1, is a double-edged sword. Although in many battery studies the condition of the surface layers is important, the behavior of oxygen ions throughout the bulk is important in spite of the practical limitation that the X-rays sensitive to oxygen do not penetrate matter easily. The goal of bulk-sensitive oxygen spectroscopy is being pursued by developing new X-ray spectroscopic techniques which were not used in this work, but which at present suffer from limitations of energy resolution.[57] Furthermore, any oxygen-sensitive spectroscopic method must cope with the oxygen found throughout a lithium-ion battery, including in the electrolyte.

As discussed in section 2.1.1.1, typical lithium-ion battery electrolytes are solvents which contain oxygen in their molecular structure. These solvents can react with the surface of cathode particles to either generate a thin surface film, or possibly to cause an explosion. In performing surface-sensitive spectroscopy, either the solvent itself or products of reactions can act as a barrier to accessing the electronic structure of the solid cathode particles. In this study, a solid electrolyte was substituted for the liquid electrolyte – although this reduces the realism of the experiment, it allows the cathode particle itself to be studied. The present study focuses on the charge compensation mechanism of cathode materials, and not on the interaction of the electrolyte with the cathode particle. Although the rate of charge and discharge depends strongly on the nature of the cathode-electrolyte interface, the charge compensation mechanism should not be directly rate-sensitive.

These coupled constraints of surface-sensitivity and the need to eliminate the cathode-electrolyte interface make it necessary to create a new interface not present in typical lithium-ion batteries: the cathode-vacuum interface. For a soft X-ray *in operando* battery to be charged during the spectroscopic experiment, the cathode particles must have a cathode-solid-electrolyte interface to transfer ions, a cathode-conductive-additive interface to transfer electrons, and a cathode-vacuum interface

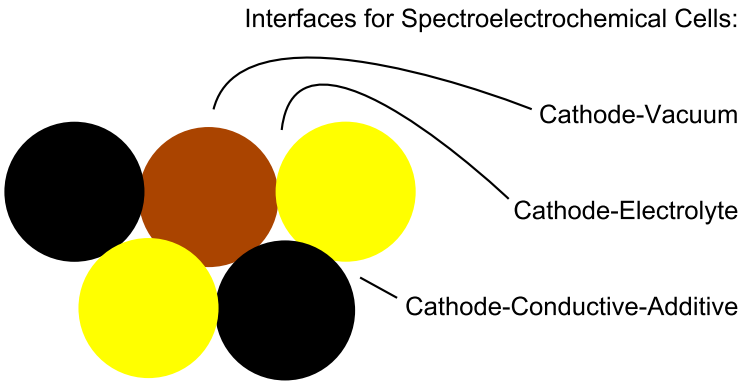

Figure 1: Schematic of the cathode of a spectroelectrochemical cell for surface-sensitive spectroscopy with the cathode particle, center, in brown, electrolyte particles in yellow, and conductive additive in black

to allow for surface-sensitive spectroscopy. Figure 1 illustrates these necessary interfaces in addition to an unwanted interface: the interface with internal porosity which limits the transfer of ions from the cathode particle to the electrolyte particle. There is also one interface which has been omitted: the cathode-cathode interface. This interface not necessary to the operation of the battery and in fact can hinder the transfer of ions to the electrolyte as well as the transfer of electrons to the conductive additive. While it should be possible to develop a thin-film battery to meet these constraints, there are disadvantages and difficulties which are not found in a powder-compact solid-state battery, which has been developed in this work.

Thin film cells The primary drawback of a thin film battery is their limited use by industry as opposed to powdered material, although specialized applications in spacecraft are possible.[48] Studies of thin film materials, which are typically oriented crystallographically, may not correspond exactly to studies of the powdered form of the same material. Furthermore, thin film methods are limited by thin-film deposition methods to relatively simple materials such as $LiCoO_2$[54] whereas by synthesizing powders with sol-gel methods,[17] new stoichiometries such as $Li_{1.17}Ni_{0.25}Mn_{0.58}O_2$ can be developed rapidly.

A practical difficulty in creating thin film batteries for surface-sensitive spectroscopy is the problem of exposing the cathode material to vacuum. The ideal deposition sequence involves adding lithium metal to a substrate, followed by the addition of a thin film solid electrolyte, followed by the

cathode material. A low-oxygen carbonaceous mesh on the surface may be required to enhance current collection. However, the deposition of $LiCoO_2$ onto the amorphous thin film solid electrolyte, lithium phosphorous oxynitride (LiPON), has not been successful – because the substrate is amorphous, crystalline $LiCoO_2$ does not form and an amorphous mixture of Co_3O_4 and Li_2O results.[50] In place of $LiCoO_2$, amorphous V_2O_5 has recently been used with some success for *in operando* XPS.[5051,58] Although valuable insights are gained through this experimental technique, the range of materials which can be studied is limited.

Instead of depositing the cathode last, thin film batteries typically[59,60] comprise a cathode deposited onto a metal-coated substrate, followed by LiPON and Li metal. Such a battery was used by Alamgir et al.[54] to perform hard X-ray absorption experiments in transmission mode[54] to investigate the oxidation state of cobalt as a function of delithiation; the soft X-rays sensitive to oxygen could not have penetrated the substrate or the overlayers. It is speculated that the cathode in such a battery could be exposed by sputtering or etching. However, the inherent drawbacks of thin film batteries remain.

Powder cells By substituting a powdered solid electrolyte for the thin film solid electrolyte, a powder composite cell can be constructed according to the schematic in Figure 1. The pellet batteries developed by Hayashi et al.[61] have been modified in this work (see section 3.6.3) to create a cell which exposes the cathode particles to vacuum while maintaining the cathode-electrolyte interface. This allows a battery to be charged while surface-sensitive spectroscopy is performed. As discussed in section 3.1, the soft X-ray probe only penetrates the top surface of the battery, meaning that the cathode-electrolyte interface is not probed. Instead, the cathode-vacuum interface is probed while lithium ions are extracted through the cathode-electrolyte interface. Also, although the soft X-ray beam illuminates many particles, including the solid electrolyte, in this work an oxygen-free sulfide electrolyte material is used so that the total signal, at the wavelengths sensitive to oxygen, will contain only information from the transition metal oxide intercalation material. Because the method uses mixtures of powders, the range of intercalation cathode materials which can be used is virtually unlimited. Because the cathode particles are exposed and because the solid electrolyte has a very low vapor pressure, oxygen evolution experiments can, in theory, be performed. Finally,

the thermal stability of the electrolyte allows high temperature experiments to be performed, as discussed in section A.3.

1.4.4 Improved Hard and Soft X-ray Data Reduction Procedures

The interpretation of X-ray Absorption spectra, discussed in section 3.3, can vary widely from one type of material to the next, ranging from single crystal materials to glasses to chemicals in solution. Researchers must make a large number of assumptions, many of which are based on previously made assumptions, regarding background subtraction as well as the data extraction which follows. Not only are these assumptions barely discussed in the literature, but the order in which these assumptions are made is almost never discussed. Frequently, background subtraction parameters must be altered in an iterative manner to improve the choice of parameters, although there is no guarantee that a unique solution to background subtraction can be found.[62] The uncertainty in background subtraction and data extraction is usually not a serious problem, however, because in most cases distinctly different materials are compared to one another. The spectroscopic differences between CoO and $LiCoO_2$, for instance, will tend to include different spectroscopic features. Likewise, the spectroscopic differences between $LiCoO_2$ and $Li_{0.5}CoO_2$ will be large, even if the features involved are not well understood.

For *in operando* experiments, however, a single sample is delithiated smoothly while taking as many spectra as possible in an attempt to discover the finest possible changes in the spectrum. As seen in Chapter 4, while hard X-ray spectra for redox active species such as nickel can show fairly clear trends with delithiation, the spectra for a redox-inactive species such as manganese can be exceedingly subtle. The changes in the spectrum due to delithiation can be drowned out by changes in data reduction parameters from one spectrum to the next. Although ideally the data reduction parameters should not change, the overlapping of features in hard X-ray spectra make it impossible to completely eliminate the adjustment of data reduction parameters. For soft X-rays the problem is more severe for three reasons. First, the signal-to-noise ratio is lower than that for hard X-ray experiments. Second, multi-element interference in the spectra can complicate normalization. Third, the spectral changes in the soft X-ray spectra can be even smaller than those in the hard X-ray spectra.

Table 1: Intercalation Cathode Materials Studied and Mode of XAS Characterization

	Short Name	Hard X-ray *Ex Situ*	Hard X-ray *In Operando*	Soft X-ray *In Operando*
$LiCoO_2$				Ch. 5
$LiNbO_2$				Ch. 5
$LiNi_{1/3}Mn_{1/3}Co_{1/3}O_2$	333 Compound	Ch. 4		
$Li_{1.17}Ni_{0.25}Mn_{0.58}O_2$	Overlithiated		Ch. 4	Ch. 5

In section 3.3 straightforward methods of data reduction for hard X-ray and soft X-ray data are given. Although these methods are not applicable to all material systems, and although no new mathematical or physical principles are developed, these procedures can produce more certain conclusions in less time as compared to previous methods. These procedures eliminate biases in order to reveal subtle differences from one scan to the next. This is done by curtailing the amount of iterative parameter adjustments employed and by adjusting only those background subtraction parameters which do not affect the final conclusions. The established procedure of fitting the data in order to refine the data reduction parameters, and then repeating the data reduction with refined parameters before performing the final fitting is incorporated into the improved system.

Compared to data found in the literature, the processed spectra given in Chapters 4 and 5 are extremely uniform except for changes in the features due to delithiation. This high data processing quality allows conclusions to be drawn based on relatively small spectral changes detected during *in operando* experiments.

1.5 Dissertation Structure

In this Dissertation, *ex situ* and *in operando* X-ray Absorption Spectroscopy data using both hard and soft X-rays are presented in order to reveal the role played by oxygen in charge compensation in lithium-ion battery cathode materials. There is a strong focus on the experimental methods employed in the work, which include innovative data analysis procedures as well as a completely new system for *in operando* soft X-ray spectroscopy. The materials discussed in this work, which all share the $R\bar{3}m$ crystal structure (see section 2.1.1.2), are detailed in Table 1. These materials include $LiCoO_2$, which is not only a widely used cathode material, but also the template for improved cathode materials. Although $LiNbO_2$ is not likely to be used as a cathode material due to its greater molar mass, its superior electronic properties make it useful for new types of electronic devices.[52]

$LiNi_{1/3}Mn_{1/3}Co_{1/3}O_2$ is recently commercialized cathode material meant to replace $LiCoO_2$; although its gravimetric capacity is higher due to its lower mass, its charge compensation mechanism is suspected to involve oxygen oxidation due to its low nickel content. Finally, $Li_{1.17}Ni_{0.25}Mn_{0.58}O_2$ which is even more likely to use oxygen oxidation in charge compensation, was studied using both hard X-ray and soft X-ray *in operando* batteries in order to determine its charge compensation mechanism in the greatest detail possible.

In Chapter 2, the literature on lithium-ion batteries is reviewed with a focus on transition metal oxide cathode materials and the unexpected behavior of oxygen in those materials. The crystal structure and electronic structure of layered transition metal oxide intercalation materials is discussed for both the as-synthesized material and for the delithiated material. Relevant X-ray Absorption methods are discussed, followed by a Literature Review which reviews *ex situ* and *in operando* X-ray Absorption and oxygen evolution experiments. In Chapter 3, experimental methods are reviewed with an emphasis on the development of the first *in operando* soft X-ray battery.

Hard X-ray and soft X-ray Absorption data are discussed in Chapters 4 and 5, respectively. Although hard X-ray absorption and soft X-ray absorption techniques are philosophically similar, the practical details and the data analysis methods differ significantly enough to discuss them in separate chapters. In Chapter 6, conclusions are drawn regarding the charge compensation mechanism in $Li_{1.17}Ni_{0.25}Mn_{0.58}O_2$ using *in operando* data from both hard X-ray and soft X-ray experiments.

Finally, several Appendices provide information not directly related to charge compensation. Appendix A details an *in operando* study of the resistivity of thin film $LiCoO_2$, results of Raman experiments on the sulfide-based solid electrolyte used for soft X-ray *in operando* studies, and high temperature experiments on solid state batteries. Appendix B gives detailed experimental procedures used for this work, while Appendix C discusses the design process behind the sample fixtures described in section 3.6. Appendix D gives step-by-step instructions for the data reduction strategy described in section 3.3.

CHAPTER II

BACKGROUND AND LITERATURE REVIEW

In this Chapter, background information on lithium ion batteries is given with a focus on transition metal oxide intercalation cathode materials. The electronic structure of these materials is dicussed, followed by a discussion of X-ray Absorption Spectroscopy (XAS). The central insight into these materials is that they are unusually complex semiconductors which can be "doped" to a very high extent via delithiation. At high doping levels, chemical instability results. The extent of this chemical instability can be probed using XAS.

In the Literature Review in Section 2.2, important experiments are discussed which have measured the chemical instability of the oxygen ions either directly, by detecting oxygen evolution, or in a more comprehensive way by using XAS to detect the oxidation of oxygen prior to the release of oxygen gas. The methods of analysis discussed in the Literature Review are later applied in Chapters 4 and 5.

2.1 Background

2.1.1 Lithium Ion Batteries

A battery usually consists of a solid anode, a solid cathode, and a liquid electrolyte. However, the electrolyte can also be gelled, polymeric, glassy, or crystalline. Each electrode must be a good conductor of both lithium ions and electrons, while the electrolyte must be a very poor conductor of electrons.[63] Any conduction of electrons by the electrolyte will tend to discharge the battery.

When the anode of a lithium battery is not lithium metal, it is termed a lithium ion battery because lithium never leaves the ionic state, as shown by Figure 2. The cathode, electrolyte, and anode each plays host to lithium ions which are never fully reduced to the metallic state.

Galvanostatic charge and discharge steps are designed to continue for a specified time according to the C-rate convention. If the capacity C of a battery is to be reached in 20 hours, the C-rate is C/20. If the units of capacity are milliamp-hours (mAh), the charging current can be calculated by dividing the capacity by 20. The measured capacity will be greater at a slower rate because diffusion

through the electrodes is slow.[63]

Unlike a lead-acid battery in which chemical species react only on the surface, in a lithium battery lithium ions diffuse into the cathode and anode structures gradually. The composition (and crystal structure) of each electrode varies over a wide range while (typically) maintaining a single-phase structure. This is shown schematically in Figure 2.

As a consequence, the electrode voltages (and, hence, the cell voltage) do not remain constant during charge and discharge reactions. Instead, as seen in Figure 3, various electrodes can have a wider or narrower range of electrode potentials as a function of lithium concentration. (Necessarily, lithium metal has only one chemical potential for lithium atoms.) Because lithium ions intercalate into either electrode, any intercalation material can, in theory, take on the role of cathode relative to an electrode material of lower potential, or vice versa. For instance, the titanium-based materials can be cathode materials relative to lithium metal, or anode materials relative to oxide materials. In general, however, energy density is maximized by choosing an oxide cathode and a lithium metal anode.

2.1.1.1 Electrolytes

The electrolyte should not react with the anode, cathode, or either current collector over the full range of temperatures and states of charge. The potential difference between the cathode and anode is large enough to electrolyze water, so nonaqueous solutions have become necessary. Nevertheless, deleterious reactions at the anode lead to the growth of a solid-electrolyte-interphase (SEI), a soft mixture of lithium ion conducting substances. This growth is self-limiting, although changes in volume during cycling cause this layer to repeatedly break and re-heal.[64,65] The cell must be well-sealed against water to prevent reactions with the lithium salts in the electrolyte, which cause gas evolution.[64]

A liquid electrolyte should have a sufficiently large liquid range to prevent solidification or boiling while in service. Any conduction of electrons will serve to discharge the battery. Also, electrolytes with chemical self-discharge mechanisms should be avoided. An example would be sealed nickel-metal hydride batteries which slowly electrolyze their aqueous electrolytes into dioxygen and hydrogen gases, which spontaneously recombine over time.

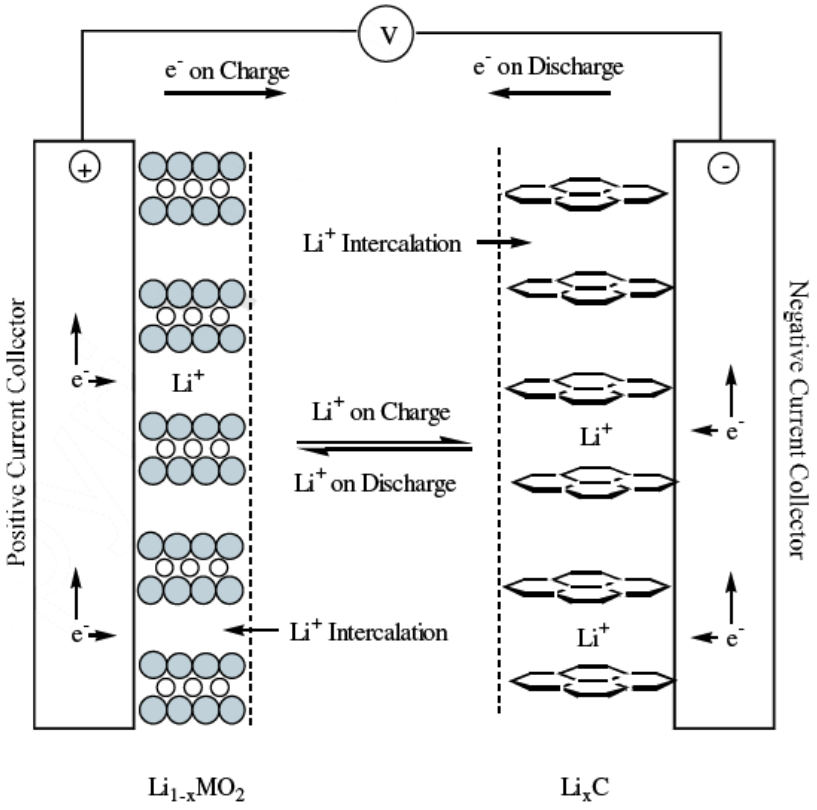

Figure 2: Schematic of a lithium-ion cell including layered anode and layered cathode from Linden[63]

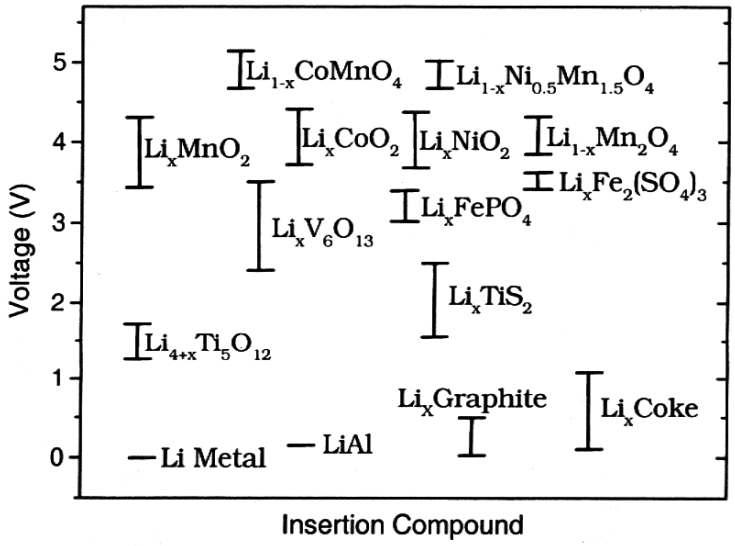

Figure 3: Potential ranges for intercalation electrodes and absolute potentials for non-intercalation materials from Linden[63]

Solid-state batteries can take the form of a thin film or a powder compact, and require no liquid. In 1992, researchers at Oak Ridge National Laboratory[66,67] invented lithium phosphorous oxynitride, or LiPON, a solid conductor of lithium ions which is formed by sputtering lithium phosphate in a the presence of nitrogen gas. Electrodes can then be formed by thin film processes to create a battery, a process which they patented.[68] Powder pellet batteries are based on solid ionic conductors, including glasses and some crystalline materials. Conductive glasses, like conventional glasses, consist of network formers such as B_2S_3, GeS_2, P_2S_5 and network modifiers such as Li_2S, and ionic dopants such as LiI and Li_4SiO_4.[61]

In this study, a conventional electrolyte, described in section 3.4, is used for hard X-ray *in operando* spectroscopy. This is possible hard X-rays easily penetrate liquid volumes of millimeter path lengths and because only low-atomic-number elements are present in the electrolyte. For soft X-ray *in operando* spectroscopy, however, a combination of severe constraints are described in section 3.6.3. For soft X-ray spectroscopy, pellet batteries were designed using an amorphous glass of the formula $70Li_2S \cdot 30\ P_2S_5$ which is further detailed in section 3.5.2. This solid electrolyte satisfies the requirements of chemical stability in contact with the electrode materials, extremely high thermal stability, and low self-discharge.[61]

2.1.1.2 Layered Crystal Structure of Intercalation Cathodes

Although intercalation cathodes include sulfides and phosphates as well as oxides, and cubic as well as hexagonal compounds, the largest range of possibilities is found in oxides with the $R\bar{3}m$ structure, pictured in Figure 4. This structure can be visualized as 2D layers of oxygen ions alternating with metal ions. The metal layers alternate between lithium and transition metal layers. When lithium ions are removed (within certain limits), vacancies form in the lithium layer and the remaining lithium ions can diffuse rapidly through the lithium plane.

Within the metal layer, the transition metal or lithium ions are arranged hexagonally. Each metal center is surrounded by an octahedral cage of six oxygens. This coordination environment is shown in Figure 5, which is centered about a cobalt ion. The first nearest neighbors are the six oxygens above and below the central atom, and the second nearest neighbors are six cobalt atoms within the basal plane. Slightly farther away are the lithium ions above and below the oxygen ions. In section

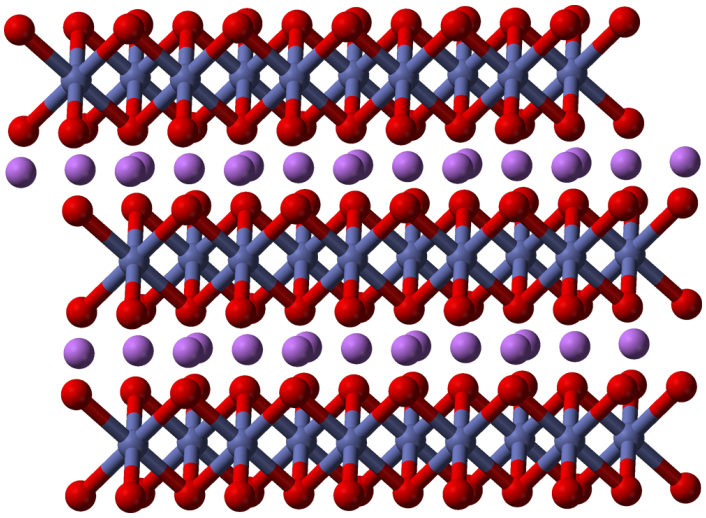

Figure 4: Diagram of the $R\bar{3}m$ crystal structure from[69] with oxygen in red, transition metals in blue, and lithium in purple

2.1.3, this arrangement of nearest neighbors is crucial in interpreting EXAFS data. Fourth nearest neighbors will not be considered.

This neat arrangement is exemplified by lithium cobalt oxide ($LiCoO_2$) in which 47% of the lithium can be reversibly removed without permanent destruction of the crystal structure.[8,70] Beyond this point, a series of violent changes including the collapse and rotation of planes renders the crystal unable to accept lithium ions again.[71]

The outcome is less catastrophic for $LiMnO_2$ which converts, after 50% of the lithium is removed, to its preferred (cubic) spinel form, $LiMn_2O_4$.[72] This compound, which can be synthesized directly, is a viable intercalation cathode.[8] Here, a convention must be noted in which the formula for layered compounds are given in terms of one lithium and two oxygens. The formulas of spinel compounds are given in terms of one lithium and four oxygens. Such compounds, naturally, have half the gravimetric capacity of the corresponding layered compound.

The delithiation of $LiNiO_2$ leads to a less graceful failure, however, and that compound is no longer used.[4] At 50% delithiation, and upon heating to 380°C, oxygen is released. At 70% delithiation, oxygen is released at only 200°C. In comparison, the temperature at which oxygen is released is higher for $LiCoO_2$, and for $LiMn_2O_4$, is over 400°C.[73] Although ambient temperatures are typically much lower, cell resistance issues can lead to thermal runaway, in which the combustion of

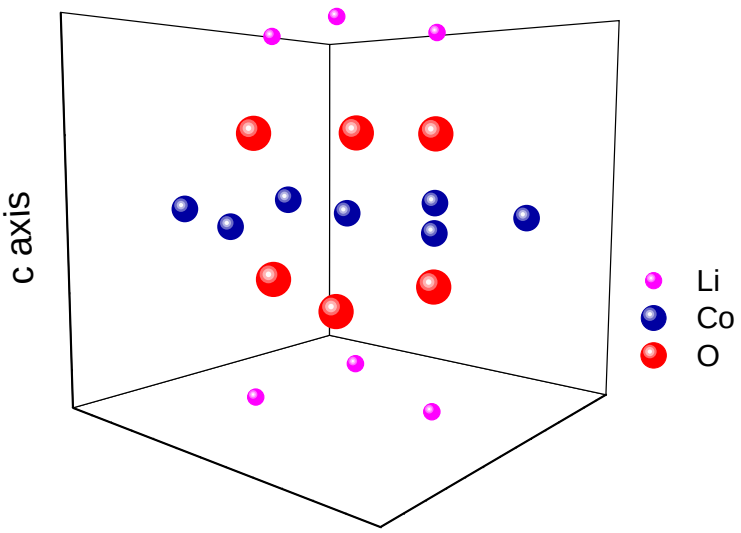

Figure 5: Diagram of the local atomic structure $R\bar{3}m$ around a central cobalt ion including first-, second-, and third-nearest neighbors

electrolyte becomes self-sustaining.

The safety and performance limitations of these three materials have led to the study of solid solutions such as $LiNi_{1/3}Mn_{1/3}Co_{1/3}O_2$[74] as well as "overlithiated"[75,76] compounds in which additional lithium is added to the transition metal layer. The study of these compounds requires sophisticated characterization techniques which are advanced in the present work. However, predicting and understanding the safety and performance characteristics of these complex materials requires an accurate understanding of the electronic structure of the material as a function of lithium content.

2.1.1.3 Electronic Structure of Intercalation Cathodes

Transition metal oxides are frequently referred to as lithium ion "hosts" which reversibly accept and deliver lithium ions. This is only half of the mechanism of intercalation, however, because lithium ions are positively charged. Removal of positive charge requires the removal of a negative electron, and that electron must have resided somewhere within the electronic structure of the starting compound. The process of charge compensation is frequently simplified in terms of purely ionic bonding, in which transition metal ions deliver electrons to the circuit while oxygen ions remain in the form of O^{2-}, satisfying the octet rule. Under this assumption, the chemistry-based Equation 1 can be explained entirely by Equation 2 in which cobalt satisfies the requirements of charge

compensation completely independently of oxygen.

$$\mathrm{LiCoO_2} \rightarrow 0.5\mathrm{e^-} + \mathrm{Li_{0.5}CoO_2} + 0.5\mathrm{Li^+} \tag{1}$$

$$\mathrm{Co^{3+}} \rightarrow 0.5\mathrm{e^-} + \mathrm{Co^{3.5+}} \tag{2}$$

However, the evolution of oxygen from cathode materials[73] at high levels of delithiation constitutes oxidation of oxygen, or the removal of electrons from oxygen. Furthermore, the thermal activation of the process suggests that at low temperatures, the oxygen ions are only metastable and that thermal excitation can transfer electrons from oxygen to the metal ions.

$$4\mathrm{O^{2-}} \rightarrow 4e^- + 2\mathrm{O^{2-}} + \mathrm{O_2} \uparrow \tag{3}$$

To fully understand these results, as well as the spectroscopic results discussed in section 2.2, the electronic band structure of transition metal oxides must be explored. Compounds such as $LiCoO_2$ have more in common with silicon than with sodium chloride: their temperature-dependent electronic conductivities, which change with the degree of delithiation, demonstrate that they are semiconductors which can be doped with lithium vacancies over a wide range. In these oxides, a continuous conduction band is formed from oxygen 2p orbitals which are hybridized with metal 4sp orbitals. The valence band consists of oxygen 2p orbitals hybridized with metal 3s and 3d orbitals.[77] The Fermi level lies just above the valence band, making these materials p-type, or hole-conducting, semiconductors.[78] The band diagram is given in Figure 6. It should be noted that Li^+, with its electron configuration of $1s^2 2s^0$, will have an empty 2s band far above the Fermi level and a filled 1s band far below the Fermi level; its formal charge is never in question.

A complication arises, however, due to the small spatial extent of the 3d orbitals. While these orbitals do overlap with O 2p orbitals, they do not overlap with each other. Therefore, when multiple transition metals are present in the same oxide, they need not adopt the same formal charge because electrons can "hop" from the 3d orbitals of one transition metal into the 3d orbitals of a transition metal with lower-lying 3d orbitals. This complicates the determination of the oxidation state of each transition metal because, within certain limits, they are independent. In early transition metals

such as titanium, the 3d orbitals are higher in energy while in late transition metals, the 3d orbitals overlap greatly with the continuous valence band. This is shown in Figure 6 in which the manganese orbitals are higher-lying relative to the nickel orbitals. The 3d orbitals which lie within the valence band tend to be filled while those above the valence band are unfilled. Therefore, in a mixed nickel-manganese oxide, electrons will tend to move from manganese to nickel, leading to oxidation states of Mn^{4+} an Ni^{2+}. When the compound is "doped" with lithium vacancies, electrons are taken from the highest-lying partially filled 3d orbitals; the identity of the metal which releases electrons to compensate charge is not obvious. The exact arrangement of different 3d orbitals, along with the position of the Fermi level, determines which element compensates charge. To identify which metal is compensating charge, therefore, a valence-band-sensitive, element-specific characterization method is necessary.

A final complication is the observed fact that as the material is "doped" by large amounts of lithium vacancies, the Fermi level moves downward to large extent, even crossing into the valence band. The result is an insulator-to-metal transition in which the temperature dependence of the conductivity decreases greatly.[78] In semiconductor terminology, the material has become a degenerate semiconductor because the doping level has pushed the Fermi level out of the band gap. An example of an extremely conductive oxide is ReO_3 in which the Fermi level cuts through a hybridized O 2p - Re 3d orbital, leading to temperature-independent conductivity and magnetic susceptibility.[79,80]

The exact nature of the band gap has been the subject of debate and many unsuccessful attempts at an accurate calculation of the spectroscopic results. It has been widely found, however, that transition metal oxides such as NiO can be described as "charge-transfer insulators"[81] in which electrons from the oxygen site are thermally activated into the 3d orbitals, which are very near in energy. The same thermal phenomenon is termed ligand-to-metal charge transfer (LMCT) in the context of transition metal complexes.[45] For crystalline solids, Zaanen, Sawatzky, and Allen[82] categorized transition metal oxides into two categories: Mott-Hubbard insulators in which thermal fluctuations cause excitations from one d-orbital to a higher d-orbital, and charge-transfer insulators in which electrons are excited from the anion p-band into a d-orbital. (It must be stressed that although such transitions can be enhanced during infrared spectroscopy,,[45] in this study the spectroscopy involves transitions of much higher energies.) The former category applies to early 3d transition

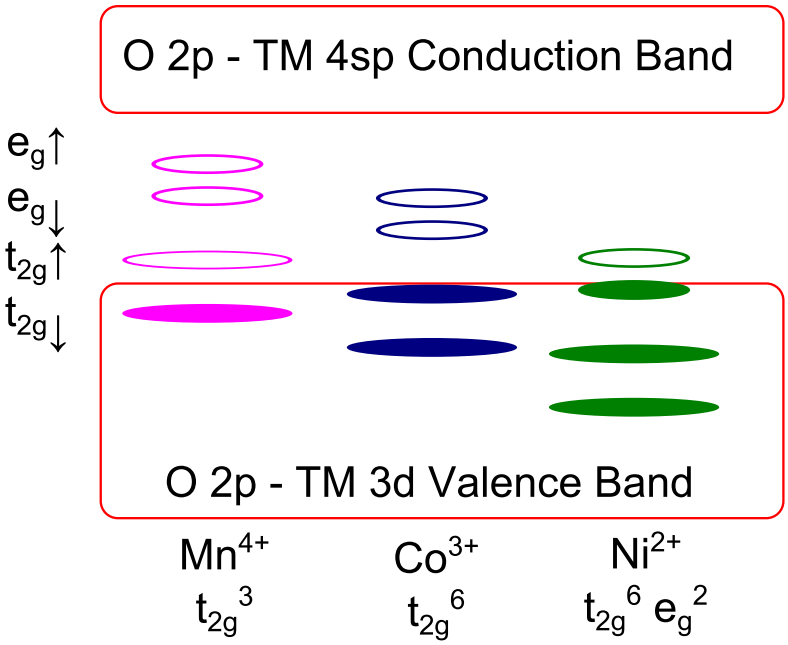

Figure 6: Schematic electronic band structure of mixed transition metal oxides including continuous conduction and valence bands and localized 3d orbitals which are split in energy according to opposite spins (see de Groot,[83] Goodenough[6])

metals, while the latter category applies to late transition metals. Early transition metal oxides can be understood in terms of ionic bonding, but as the atomic number increases, the bonding becomes increasingly covalent and complex.

Magnetic Moments These unusual properties allows for the 3d electron spins to align, generating a magnetic moment, instead of becoming anti-aligned to reduce their total energy.[77] As the occupation of these 3d orbitals changes during the delithiation of a transition metal oxide, the magnetic moment will change according to the number of aligned spins. The pairing of electrons will depend both on the oxidation state of the transition metal ions and on temperature. In fact, several *ex situ* studies on lithium battery cathodes have been performed which include measurements at cryogenic temperatures.[47] Because all batteries, regardless of the type of electrolyte, rely on diffusion, the temperature cannot be much lower than room temperature, although high temperature experiments are possible.

Table 2 gives the number of unpaired electrons for different 3d electron configurations. Depending on the geometry and on the ligand,[45] high-spin configurations, in which electrons occupy

Table 2: Number of Unpaired Spins for High- and Low-Spin Configurations for 3d Transition Metal Ions

	d^3	d^4	d^5	d^6	d^7	d^8
High Spin	3 (Mn^{4+})	4 (Mn^{3+})	5 (Co^{4+})	4 (Ni^{4+}, Co^{3+})	3 (Ni^{3+})	2 (Ni^{2+})
Low Spin		2 (Mn^{III})	1 (Co^{IV})	0 (Ni^{IV}, Co^{III})	1 (Ni^{III})	

higher-energy orbitals to minimize electrostatic repulsion, and low-spin configurations, in which electrons pair according to opposite spins, are possible. (For some configurations, only one spin state is possible.) The magnetic susceptibility of the compound will depend in part on the number of unpaired spins. However, as can be seen in the table, the number of unpaired spins is not correlated with either the formal oxidation state or the identity of the transition metal ion. When multiple transition metals are present, the average number of unpaired spins can be attributed to multiple possible combinations of oxidation states. However, given some degree of spectroscopic information, trends in magnetic moments can potentially be the "key" that helps determine element-specific oxidation states. However, as discussed in section 4.1, trends in the total number of unpaired spins with delithiation can deviate from a number explainable in terms of transition metals alone; unpaired spins on the oxygen site are also possible.[76,84]

To summarize, the lack of overlap of the d-orbitals makes discrete oxidation states possible for transition metals, yet the overlap of these orbitals with oxygen 2p orbitals makes fractional oxidation states possible for oxygen ions. To the extent that the remaining electrons are unpaired, unpaired spins can reside on discrete transition metal ions as well as in hybridized states involving oxygen. The exact nature of these fractional oxidation states is not well-known. It stands to reason that if the fractional occupation of O 2p orbitals becomes too low, oxygen gas (with an integer oxidation state) may form irreversibly. To determine the origin of charge compensation, and to predict chemical stability, it becomes necessary to differentiate between unfilled d-orbitals and unfilled p-orbitals. This can be done using soft X-ray absorption spectroscopy[83] which is detailed in section 2.1.3.

2.1.2 Cathode Delithiation Process

The synthesis of transition metal oxides is typically performed in air at temperatures high enough to permit the diffusion of transition metal ions into equilibrium positions in the crystal lattice. Temperatures above 400°C are typically required to achieve a favorable crystal structure[85] such as $R\bar{3}m$

while temperatures above 800°C[47] can lead to the preferential evaporation of lithium. Neither oxygen holes nor oxygen vacancies are found in large concentrations, and the transition metal ions will adopt oxidation states which balance the charge on oxygen.

However, when a battery is charged, very large concentrations of lithium vacancies (along with electronic holes) are created in alternating planes of the cathode crystal structure at room temperature; the diffusion of transition metal ions does not *necessarily* fill in the vacancies to "prop up" the structure. Instead, the crystal can contract along the c-axis and a-axis due to lithium vacancies as well as due to electronic holes in the bonding orbitals. The two types of effects, electronic and structural, influence each other and cannot be separated, and should be measured simultaneously. The methods described in the next Subsection are ideally suited in detecting the changes described in this Subsection.

2.1.2.1 Charge Compensation

At all states of delithiation, and regardless of the details of the electronic structure, local electroneutrality must always prevail. The net charge will be zero, making it possible to deduce the formal charge on one element based on a well-known formal charge on the other elements. As a compound is delithiated, the same assumption can be applied at all stages. However, the starting compound is a special case because it is synthesized at very high temperatures; any unstable species can rapidly phase separate at these temperatures. For example, oxygen species other than O^{2-} can form dioxygen gas and leave the crystal. As is shown in detail in section 2.2.4.1, oxygen holes and oxygen vacancies are not found in the same material due to charge balance issues. Therefore, in $LiCoO_2$, the starting compound must contain O^{2-} ions.

The second assumption which can be made is that lithium exists as Li^+ at all times, with no possibility of deviation. This assumption was checked by Hightower et al.[86] who studied lithiated graphite using Electron Energy Loss Spectroscopy (EELS) which is similar, in principle, to the techniques discussed in section 2.1.3. It was found that in LiC_6, the electron configuration of lithium had deviated only minutely from that of lithium metal ($1s^2 2s^1$). The minute shifts agreed with the small electrochemical voltage between lithium and LiC_6. In cathode material with a large potential difference versus lithium metal, lithium can only be in the +1 oxidation state.

2.1.2.2 Theoretical Charge Capacity

If the $R\overline{3}m$ crystal structure is viewed as a rigid structure with completely ionic bonding, the theoretical capacity is easy to calculate from the stoichiometry. However, as will be seen in the Literature Review (section 2.2), the crystal structure is neither rigid nor even reproducible from the first cycle to the next, and as already discussed in 2.1.1.3, the bonding is far from ionic. In addition, the charge capacity of many intercalation cathode materials decreases (or even increase) after the first cycle. More importantly, even over several cycles, the measured *reversible* charge capacity can significantly exceed the capacity that can is expected to be charge-compensated.

The theoretical capacity of a cathode material is frequently expressed as a gravimetric capacity. It can be calculated by dividing the expected amount of charge per formula unit in milliamp-hours (mAh) by the calculated mass of the *pristine* compound per formula unit in grams. (For cathodes, the mass decreases somewhat during charge, while for anodes the mass can increase greatly during charge; the pristine compound must be used when making a calculation for anodes.) The expected charge is the number of moles multiplied by Faraday's constant, which is 96,485 C/mol[87] or 26,801 mAh/mol. For $LiCoO_2$,[88] 26,801 mAh (one mole of lithium per formula unit) of charge capacity can theoretically be extracted from every 98 grams (mass of one formula unit) of pristine material, yielding 273 mAh/g.

It must be emphasized that the lithium content of a cathode material can never be entirely removed because, at the very least, it would leave a plane of vacancies within the crystal. The crystal could be expected to cleave along such a plane before all the lithium ions were removed. Before even that occurred, however, atoms can be expected to rearrange over short distances, leading to transformations of the crystal structure. In addition to these structural effects, however, a charge balance must be established at all stages of delithiation. An example is lithium cobalt oxide ($LiCoO_2$). Due to crystallographic changes with delithiation,[89] only approximately half the lithium can be reversibly removed from the structure. The charge balance for the limits of delithiation are given in Table 3. The removal of 50% of the lithium ions should result in the formation of $Co^{3.5+}$. As will be seen in the Literature Review (section 2.2), this cannot be described by either a mixture of Co^{2+} ($t_{2g}{}^6\ e_g{}^1$) and Co^{4+} ($t_{2g}{}^5$) or even by an average configuration of $Co^{3.5+}$.[13] However, the reversible

capacity (140 mAh/g)[88] is not unexpected. While the charge compensation mechanism has not been fully determined, the reversible capacity is not mysterious. Further research has investigated increasing the reversible limits of delithiation and substituting cheaper and lighter metal ions for cobalt.

A very reasonably-designed cathode material is $LiNi_{0.5}Mn_{0.5}O_2$, detailed in Table 4. The average charge state of the transition metals is expected to be 3+, although spectroscopy shows that Ni^{2+} and Mn^{4+} are found in the starting compound due to the relative binding energies of the Ni and Mn orbitals.[90] The removal of one mole of lithium ions should be compensated by the oxidation of the transition metals to an average state of 4+. This oxidation state is reasonable for both nickel and manganese, and spectroscopy shows[90] that nickel, indeed, provides the charge compensation by oxidizing to Ni^{4+}.

Some compounds, however, were designed with even less nickel in the pristine compound. In $LiNi_{1/3}Mn_{1/3}Co_{1/3}O_2$, assuming Ni^{2+} oxidizes to Ni^{4+}, only $2/3$ of the lithium ions can be removed while maintaining charge compensation. Nevertheless, Li et al.[76] found a reversible capacity in excess of the expected amount, suggesting that more than $2/3$ of the lithium can be removed while maintaining charge balance over many cycles. The charge compensation mechanism is investigated in section 4.1; further investigation found evidence that oxygen, rather than cobalt or manganese, was taking part in charge compensation.

An even more "extreme" compound is $Li_{1.17}Ni_{0.25}Mn_{0.58}O_2$, which contains a high amount of inactive manganese, no cobalt, and a low amount of nickel ions, and enough lithium ions to "spill over" into the transition metal ion layer. Only 0.5 Li can be expected to be removed if charge compensation is assumed to be achieved by nickel alone, leaving 0.67 Li in the structure. (Although ideally 0.17 Li would remain in the transition metal layer, the literature in section 2.2 shows that the opposite is the case.) Intriguingly, the results of West et al. show that much more lithium can be removed reversibly.[17]

2.1.2.3 Structural changes with delithiation

As lithium ions are removed from a transition metal oxide, the $R\bar{3}m$ structure tends to shrink, including a contraction of the basal plane as well as a contraction within the basal plane. Overall,

Table 3: Theoretical Charge Balance, Lithium Cobalt Oxide at 0% and 50% Delithiation

	Stoich.	Ox. State	Charge		Stoich.	Ox. State	Charge
Li	1	1	1		0.5	1	0.5
Co	1	3	3		1	3.5	3.5
O	2	-2	-4.00		2	-2	-4.00
Sum			0.0				0.0

Table 4: Theoretical Charge Balance, Lithium Nickel Manganese Oxide at 0% and 50% Delithiation

	Stoich.	Ox. State	Charge		Stoich.	Ox. State	Charge
Li	1	1	1		0	1	0
Ni	0.5	2	1		0.5	4	2
Mn	0.5	4	2		0.5	4	2
O	2	-2	-4.00		2	-2	-4.00
Sum			0.0				0.0

Table 5: Theoretical Charge Balance for the "333 compound" at 0% and 100% Delithiation

	Stoich.	Ox. State	Charge		Stoich.	Ox. State	Charge
Li	1	1	1		$1/3$	1	$1/3$
Ni	$1/3$	2	$2/3$		$1/3$	4	$4/3$
Mn	$1/3$	4	$4/3$		$1/3$	4	$4/3$
Co	$1/3$	3	1		$1/3$	3	1
O	2	-2	-4.00		2	-2	-4.00
Sum			0.0				0.0

Table 6: Theoretical Charge Balance for overlithiated $Li_{1.17}Ni_{0.25}Mn_{0.58}O_2$ at 0% and 100% Delithiation

	Stoich.	Ox. State	Charge		Stoich.	Ox. State	Charge
Li	1.17	1	1.17		0.67	1	0.67
Ni	0.25	2	0.5		0.25	4	1
Mn	0.5825	4	2.33		0.5825	4	2.33
O	2	-2	-4.00		2	-2	-4.00
Sum			0.0				0.0

the volume of the unit cell tends to decrease.[76] From the point of view of the local coordination about the transition metal center, as shown in Figure 5, the other transition metal ions will move closer while the oxygen atoms also move inwards.

The source of this contraction is reduction in the repulsion of electron clouds about each atom. The loss of lithium ions removes the Li $1s^2$ electrons from the structure, but the oxidation of transition metal ions, and of oxygen, also leads to contraction of metal-oxygen bond distances.[54] For reasons discussed in section 2.1.3, the two effects can be difficult to separate without measuring the element-specific electronic structure.

Although metal-oxygen bond distances can decrease smoothly, the well-known Jahn-Teller Effect can distort the oxygen coordination shell. The Jahn-Teller Effect arises when transition metal d-orbitals of nominally equal energy are not evenly filled. For instance, in Ni^{3+} the electron configuration is $3d^7$; in octahedral coordination the d-orbital split into a triply-degenerate (full) level denoted $t_{2g}{}^6$ and a doubly-degenerate level denoted $e_g{}^1$ which contains only one electron out of a possible four. These e_g states can be specified as d_{z^2} and $d_{x^2-y^2}$, which, despite being equal in energy, are not geometrically equivalent. This degeneracy is resolved when the electron hops to whichever orbital is favored by the crystal structure. Most frequently, the electron will reside on the d_{z^2} orbital which will have the effect of repelling two out of the six oxygen ions along the z-axis.[45] If such a distortion can be detected by measuring two distinct nickel-oxygen distances, the existence of Ni^{3+} can be assured.

2.1.2.4 Electronic changes with delithiation

In the preceding discussion of charge compensation in the pristine material in section 2.1.2.1, the oxidation state of oxygen was assumed to be -2 due to the high synthesis temperatures involved. The oxidation state of lithium was assumed to be +1, and the oxidation state of the transition metal ion was deduced. Batteries are charged, however, at room temperature in well-sealed cells, preventing any ingress of dioxygen gas. This makes it possible for oxygen to become oxidized as a result of charge compensation during delithiation. Also, as discussed in section 2.1.3, the oxidation states of the transition metal ions are far easier to measure than that of oxygen. And, as shown in the Literature Review, it is extremely well known that transition metal ions of cobalt and manganese

tend not to oxidize or reduce at all during battery charging. Therefore, the problem changes from deducing the oxidation state of the transition metal ions to that of deducing the oxidation state of oxygen after measuring the oxidation states of the transition metal oxides.

Due to the band structure of the transition metal oxide, it is possible for oxygen to lose electrons without forming dioxygen gas.[82] However, excessive quantities of oxygen holes should, in theory, lead to the formation of species such as dioxygen (O_2) with a formal oxidation state of 0, or intermediate species such as peroxide (O_2^{2-}) with a formal charge of -1, or superoxide (O_2^-) with a formal charge of $-1/2$. These three species are problematic because they all require a covalent bond between two oxygen ions. For superoxide, the O–O bond length[91] is 1.33Å, which is much shorter than the O–O distances found in cathode materials which tend to be approximately[92] 1.9Å. The formation of these species can only take place at the surface of the crystal, or inside pores in the cathode material. Any formation of oxygen holes in the *bulk* of the material signifies the formation of oxygen holes rather than the formation of molecular species.

If oxygen holes are stable within the crystal lattice, then oxygen may take part in reversible charge compensation. However, there must be a limit to the amount of oxygen holes per oxygen ion, beyond which dioxygen gas, or other species, are lost. This limit likely depends on the symmetry and lattice spacing of the crystal structure and the types of transition metal ions bonded to oxygen. More importantly, this limit will depend on temperature: at higher temperatures, ligand to metal charge transfer (LMCT) can be expected to increase. Unfortunately, as discussed in section 2.2.4.1, the quantification of oxygen holes is very difficult due to overlapping nature of the electronic structure of the valence band.

2.1.3 X-ray Absorption Spectroscopy

List of Symbols used in hard X-ray absorption[93]

$h\nu$ Photon energy in units of electron-volts

I_0 Beam intensity incident on the sample

I_T Beam intensity transmitted through the sample

I_{REF} Beam intensity transmitted through the sample and a reference foil

μx Absorption through the pathlength x; unitless

$\mu(E)$ Absorption coefficient, in units of inverse length, as a function of photon energy

E_0 Reference energy for the photoelectron

k Photoelectron wavevector in units of inverse length

$\mu(k)$ Absorption as a function of k

$\mu_0(k)$ Background absorption function in the absence of neighboring atoms as a function of k

$\Delta\mu(k)$ Deviation of absorption relative to $\mu_0(k)$ as a function of k due to neighboring atoms

$\chi(k)$ Extended fine structure as a function of k

N_j Number of neighboring atoms per coordination shell j

R_j Radial distance to each coordination shell j

σ_j^2 XAFS Debye-Waller factor for each coordination shell j

F_j Scattering factor for each coordination shell j

$\delta_j(k)$ Photoelectron phase shift for each coordination shell j

2.1.3.1 XAS Detectors

Fundamentally, when photons are incident on matter, the entire incident photon flux (I_0) must be transmitted (I_T), absorbed (A), or reflected (R) according to Equation 4. In X-ray absorption, reflections or scattering are not considered directly even though some fraction of the beam is always diffracted by crystalline or noncrystalline samples. Instead, the modulation of the transmitted beam is used to assess the absorption due to the sample, provided that the transmitted beam is sufficiently intense. If this is not the case, either due to low sample thickness at hard X-ray beamlines, or due to extremely short X-ray absorption lengths at soft X-ray beamlines, the X-ray fluorescence yield is measured to assess the absorption due to the sample. Finally, because soft X-ray beamlines rely on high or ultrahigh vacuum to prevent gaseous absorption of the beam, photoelectrons and Auger electrons can also be detected to assess the absorbance at each wavelength.

$$I_0 = I_T + A + R \tag{4}$$

X-ray absorption is measured by correlating the response of a detector (X-ray flux or Auger electron flux) with the position of a monochromator (X-ray wavelength); i.e., the detector need not be energy dispersive, although advanced photon-in photon-out techniques utilize the correlation of emitted photon energy to incident photon energy. In transmission experiments, the X-ray beam passes through a series of three detectors consisting of metal boxes filled with various gases. A high voltage applied from the top to the bottom of each box captures ions in proportion to the intensity of the beam before it reaches the sample, after it reaches the sample, and then again after the beam passes through a reference sample. Standard metal foils allow for frequent calibration of the monochromator. Software at each synchrotron beamline allows for the use of two or more absorption edges in ensuring that the beam energy is linear with respect to the monochromator angle over the region of interest.

At soft X-ray beamlines, the most intense signal is from Auger electrons leaving the sample. These can be detected simply by isolating the sample electrically apart from a wire connected to a picoammeter. As electrons leave the sample due to the excitation of the soft X-ray beam, regardless of their direction or energy, they must be replaced by electrons returning through the grounded vacuum chamber. The picoammeter measures Total Electron Yield (TEY). A modification of this technique is Partial Electron Yield (PEY) in which a metal screen between the sample and the detector is charged negatively to repel low-energy electrons which add noise to the signal. For the oxygen K-edge at ~546 eV, a grid bias of -150 V is typically sufficient, although a bias of -250 V can enhance the surface sensitivity by repelling electrons coming from deeper in the sample. (A grid bias of -350 V was found to be detrimental to the spectrum, however.) Because the detector has only a limited solid angle of collection compared to TEY, the PEY signal is amplified by a channeltron multiplier charged positively to thousands of volts. In either electron yield technique, sample grounding is essential.

X-ray fluorescence yield (FY) measurements offer greater bulk sensitivity at the cost of signal intensity. The detector in this case is a solid-state photodetector[94] which must be protected from ambient light. At hard X-ray beamlines, thin aluminum foils are satisfactory but at soft X-ray

beamlines, a more transmissive window must be used. At NIST beamline U7A, a cesium iodide (CsI) coating is used.

In the simplest case, X-ray absorption spectroscopy utilizes hard X-rays in transmission mode. The incident X-rays from the beamline are measured using an ionization chamber which is (exponentially) sensitive to the intensity of the beam. Although the gas mixture is adjusted for sensitivity to different wavelength ranges, the ionization chamber does not detect the photon energy. This first chamber is labeled I_0 and is followed by the sample and then a second ionization chamber labeled I_T. A reference foil of the element of interest (often a metal) is included between I_T and I_{ref}.

2.1.3.2 Theory of X-ray Absorption Spectroscopy

X-ray absorption occurs when an incident photon of the correct energy excites electrons (as opposed to nuclei) in matter. The excited electron may gain enough energy to leave solid matter, or only enough to reach a neighboring atom, or just enough to reach a higher energy state with a lower binding energy. If the photon energy is too low, the electron may not be excited at all.[95]

The promoted core electron (frequently a 1s, 2s, or 2p electron) to a higher bound state, at which point that electron is termed a photoelectron. (This terminology[93] is unfortunate because in hard X-ray absorption, the term “photoelectron” refers to an electron which remains within the sample, while in soft X-ray absorption, the traditional definition is used in which the photoelectron leaves the sample.) In XAS, the final state is an unoccupied, but bound, state above the Fermi energy level. In atomic terms, the unfilled states in and above the 3d band in transition metals are above the Fermi level. Inevitably, an electron, usually not the one which was promoted to the final state, will fill the “core hole" left behind by the original, promoted electron. This leads to re-emission, known as fluorescence, of an X-ray of lesser energy compared to the incoming beam. Alternatively, this same energy is given to an electron already bound in the final state, and this electron is ejected from the material; this electron is termed an Auger electron.[95]

Absorption of X-rays is governed by Fermi’s Golden Rule which states electron transitions will happen most frequently when the photon energy promotes the electron to an energy band with a high density of unoccupied states. Intuitively, when the photon energy is insufficient to promote an electron from an occupied core level to the lowest-energy unoccupied state, the transition does not

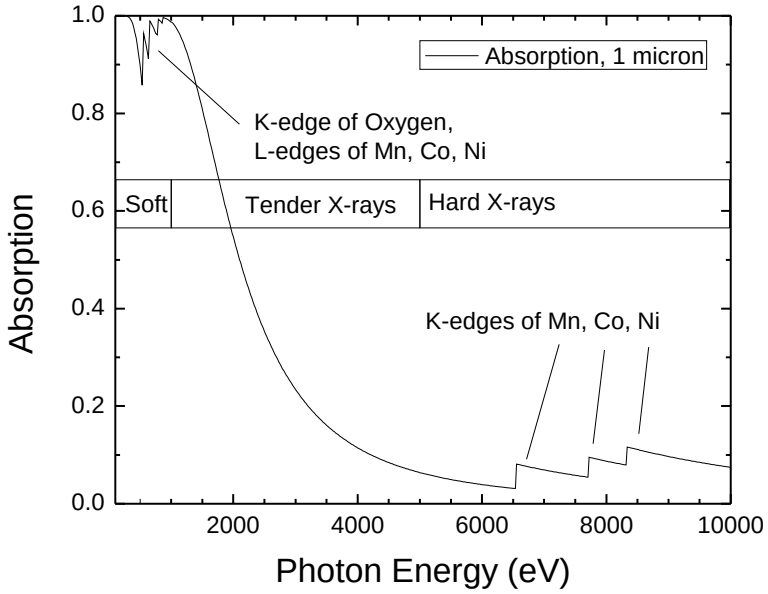

Figure 7: Calculated[96] X-ray absorption of 1 micron of $LiCoO_2$ at soft, tender, and hard X-ray energies

occur. Less intuitively, when the photon energy is more than the necessary value, the probability of X-ray absorption decreases. This results in the "sawtooth" shape of an X-ray absorption edge seen in Figure 7.[93,95]

A simplification of Fermi's Golden Rule is the Dipole Selection Rule, which states that the angular momentum of the final state should differ from that of the initial state by one unit of angular momentum. Because all photons have a spin of unity, an electron in a 1s orbital (which is spherical and has no angular momentum) can only be promoted to an orbital of angular moment one, such as a 2p, 3p, or 4p orbital due to the absorption of a photon. Likewise, an electron in a 2p orbital can only be promoted to a 3d or 4d orbital which has an angular moment value of two. There are exceptions to this rule: given sufficient X-ray intensity, the small quadrupole moment of a photon can promote electron from 1s to 3d orbitals. More commonly, hybridization between transition metal 3d orbitals and the oxygen 2p orbitals to which they are bonded can allow electrons from transition metal 1s orbitals to land in 3d orbitals, creating a small pre-peak in a hard X-ray spectrum which is dominated by the 1s $\rightarrow$ 4sp transition. This hybridization can be very large in the case of tetrahedrally-coordinated transition metal oxides, and the effect can be amplified by altering the orientation of the crystal planes of the sample relative to the polarized synchrotron beam.[97]

This Dipole Selection Rule is key in explaining the strategy of this study, in which soft X-rays and hard X-rays are used to probe different elements at different absorption edges. For oxygen, the only relevant transition is from 1s $\rightarrow$ 2p (the K-edge) with a binding energy of approximately 540 eV. Hybridization of the 2p orbitals with transition metal 3d orbitals (which overlap physically) gives rise to absorption features just below this binding energy. For transition metals, however, two transitions are possible for each: although the 1s $\rightarrow$ 2p transition is impossible because the 2p orbitals are filled, the 1s $\rightarrow$ 4sp transition is possible because the 4sp band is high above the Fermi level; the photon energy needed for this transition is several thousand eVs. Crucially, the hard X-rays required for this transition can easily penetrate low-atomic-number materials such as aluminum foil, liquid solvents, and polymer packaging. Additionally, the 2p $\rightarrow$ 3d transition is available because the 3d orbitals are only partially filled. The filling of these orbitals determines the oxidation state of a transition metal, making this measurement especially important in battery research. Conveniently, the binding energy for these transitions is generally higher than that for the O K-edge, although the binding energies for the vanadium and chromium L-edges do interfere with the O K-edge. The L-edges for manganese, iron, cobalt, and nickel are all above the O K-edge in energy and, furthermore, they do not interfere with each other in energy. This allows the oxidation states of each transition metal to be determined separately.

In practice, XAS is nearly always performed at a synchrotron with the assistance of a monochromator. This allows for a wide spectrum of high-energy-resolution, high intensity X-rays. During an experiment, the monochromator is rotated to select each wavelength in ~0.5 eV steps. XPS typically employs a single incident wavelength for an entire scan, and therefore can take advantage of conventional rotating-anode X-ray sources. However, the high brightness and energy resolution of a synchrotron can also benefit XPS experiments, while the energy selection capability allows the experimenter to achieve higher resolution in a desired band.[94]

In a transmission experiment, Beer's Law is used to calculate the absorption from the incident and transmitted beam intensities. (See Equation 5) The ratio of the base ten logarithms is taken as the negative of the absorbance, μx. The sample is typically designed for an absorbance of ~2.5 above the absorption edge.[93]

$$I_t = I_0 \exp(-\mu x) \tag{5}$$

For thick samples, fluorescence can be used with the help of Equation 6. The fluorescent intensity is proportional to the incident beam intensity and to the absorption of X-rays in the sample. (Although Beer's Law still applies, both the incident beam and the fluorescence are absorbed, complicating the analysis.) The fluorescent wavelength may be longer than the incident beam wavelength; because only the absorption at the incident beam energy is of interest, all fluorescent intensity is summed and plotted against the incident beam energy.[93]

$$I_f \propto I_0 \mu x \tag{6}$$

The X-ray absorption of $LiCoO_2$ is approximated in Figure 7 which is calculated using an online program by Eric Gullickson[96] at Lawrence Berkeley Laboratory. The range of energies is 100 eV (very soft X-rays) to 10,000 eV (hard X-rays); this range of energies is never available at a single beamline. In fact, this range of energies could not be reproduced by fewer than four or five beamlines because a variety of magnets and very different optics and detectors are required. At the same time, the range of transmission ratios spans the range from total absorption to almost total transmission. Below 540 eV, oxygen's 2p orbitals absorb almost all of the radiation, although above this energy the radiation is no longer resonant with the atomic orbitals and transmission increases. Between 540 eV and 780 eV, radiation is strongly absorbed by cobalt's 3d orbitals. Transmission increases up to 7770 eV, where cobalt's 4sp orbitals begin to absorb radiation. This general picture of the absorption of X-rays does not include the finer details of individual orbitals which show up just below each edge (NEXAFS/XANES), nor does it show the modulations of Extended X-ray Absorption Fine Structure (EXAFS) above each edge.

It must be further pointed out that the calculation was performed for a 1 micron thick particle. This is at least five times thinner than a typical cathode particle, which is embedded in a composite layer with other cathode particles and packaged into a battery. In the *ex situ* case of a composite cathode layer on aluminum foil, or in the *in situ* case of a solid state or pouch cell battery, the transmission of soft X-rays is practically zero, the absorption is unity, and the soft X-ray fluorescence and Auger electron emission (from the near-surface) must be detected to measure the fine details of

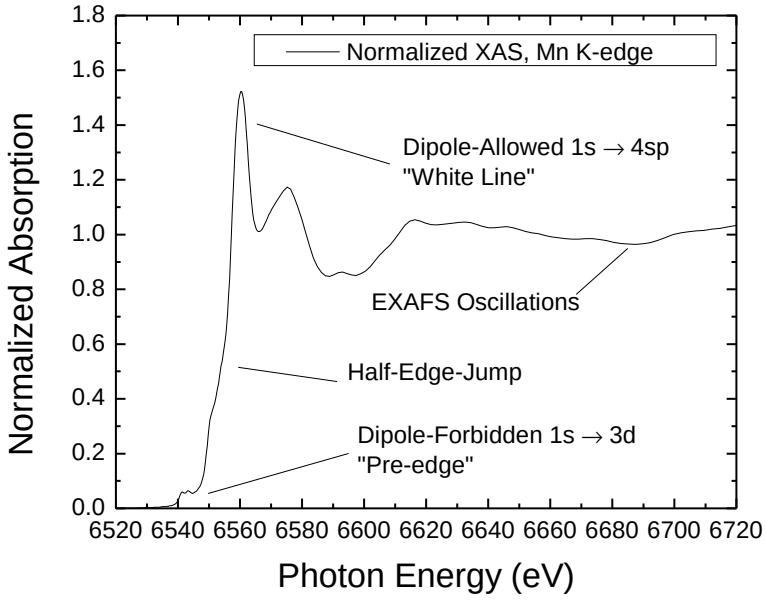

Figure 8: X-ray absorption spectrum, normalized to unity absorption for the Mn K-edge in the 333 compound

the absorption. The transmission mode can still be used at hard X-ray energies with the trade-off that the entire bulk of the material is probed, and surface-sensitivity is lost.

2.1.3.3 Extended X-ray Absorption Fine Structure (EXAFS)

Detailed analysis of XAFS requires that the incident X-rays be seen as a particle (a photon), and that the electron be seen as a wave.[94] The photoelectron resonates between the initial and final states and interferes with itself after backscattering. Because the final states are molecular orbitals overlapping with those of neighboring atoms, the fine structure gives information on the nearest neighbors. The theory of this process was developed in the 1970s.[94]

X-ray absorption fine structure (XAFS) is divided into two regimes which can be seen in Figure 8. Just above the absorption edge is the near-edge region; hard X-ray scientists term this the X-ray Absorption Near Edge Structure (XANES) while scientists using soft X-rays prefer Near-Edge X-ray Absorption Fine Structure (NEXAFS).[93,94] In either case, the onset of X-ray absorption is the Fermi level where the metal 3d and O 2p orbitals are partially empty. However, as seen in Figure 8, the absorption near 6539 eV (the pre-edge) is very weak compared to the absorption at 6560 eV (the "white line;" see section 3.3 for the etymology) due to the Dipole Selection rule. Between them is the half edge-jump where $\mu x = 0.5$.

Beyond approximately 20 eV above the half edge-jump is the Extended X-ray Absorption Fine Structure (EXAFS) region. This demarcation exists because the internal photoelectron behaves differently above and below it. Above the absorption edge it can be assumed that each photoelectron interacts with one other atom (a “scatterer") and returns to the central atom. These scatterers may be nearest neighbors or second or third nearest neighbors. This process can be modeled mathematically. However, within the edge the photoelectron interacts with several of the nearest neighbors simultaneously. Physicists have not been able to model the XANES region because a many-body problem must be solved.[93,94] The scattering process just above the absorption edge is termed “multiple scattering" not because the photon is scattered multiple times, but because the photoelectron is scattered multiple times. In EXAFS, a single-scattering model can account for experimental observations.[94]

EXAFS data analysis begins with the removal of the background function, or in other words, the separation of the fine structure from the original absorption edge. The background removal method was refined in the 1990s.[98] The fine structure, $\chi(k)$, is simple to express as $\Delta\mu/\mu_0$, although it is difficult to determine accurately. The photoelectron wavevector k is defined by Equation 7, where E_0 is the absorption edge energy.[94] This equation shows how the wavevector (and therefore the wavelength) of the photoelectron wave changes with beam energy. The interference must change as a function of photoelectron wavelength, and therefore XAFS oscillations arise.

$$k = 2\pi h^{-1}\sqrt{2m(h\nu - E_0)} \tag{7}$$

The $\chi(k)$ data is Fourier transformed into real space, giving a partial distribution function of the nearest neighbors versus radial distance in angstroms. The nearest, second nearest, and third nearest neighbors can be seen.[93]

The mathematical model for EXAFS oscillations (but not XANES features) is given by Equation 8.[93,94] It is used to predict the fine structure in the EXAFS region, but not the total absorption. By comparison between the model and the data, the identity, number, and distance of neighboring atoms can be found. Modeling in ARTEMIS[99] is discussed in section 3.3.

The index j refers to each coordination shell of neighboring atoms, and R refers to the distance to that scatterer. N refers to the number of nearest neighbors, σ^2 is the XAFS Debye-Waller factor

describing disorder (both thermal and static), F_j is the amplitude of the backscattered wave, and $\delta_j(k)$ is a phase shift correction.[93,94] Two sets of variables are potentially difficult to separate when applying the equation to experimental data. Clearly, an increase in N is indistinguishable from a decrease in F_j. Through the exponential function, each is confounded with σ^2. Less obviously, via Equation 7, the nearest neighbor distance R depends on the choice of E_0. Strategies for determining accurate values for these variables are discussed in section 3.3.

$$\chi(k) = \sum_j \frac{N_j F_j \exp(-2k^2\sigma_j^2)}{kR_j^2} \sin(2kR_j + \delta_j(k)) \tag{8}$$

2.1.3.4 Soft X-ray Absorption Spectroscopy

The soft X-ray technique corresponding to hard X-ray absorption spectroscopy is Near-Edge X-ray Absorption Spectroscopy or NEXAFS. Although in principle the process is the same as hard X-ray XANES, in practice the NEXAFS technique is more closely related to X-ray Photoelectron Spectroscopy (XPS). In both techniques, a soft X-ray beam is incident on a sample and electrons are released. Therefore, both techniques require vacuum, and only the surface of the sample can be probed. The two techniques differ fundamentally in that XPS is sensitive to occupied electron states, NEXAFS is sensitive to unoccupied electron states. Furthermore, while XPS is sensitive to core electrons far below the Fermi level and continuing up to the valence band, NEXAFS is sensitive to unoccupied states just above the Fermi level and into the conduction band.

Figure 9 which gives the XPS photoelectron spectrum for $LiCoO_2$. In the XPS experiment, a fixed-energy X-ray source illuminates the sample, giving core electrons enough kinetic energy to overcome their binding energy within the atom. Given an X-ray energy greater than its binding energy, an electron will leave the sample and travel to a detector within the vacuum chamber. Because the detector is sensitive to the electron's kinetic energy, its binding energy can be calculated according to a simple formula.[100] The resulting plot shown in Figure 9 gives the electron counts at each kinetic energy. The most intense peaks are core level states include O 1s, C 1s, Co 2p, and the very small Li 1s. In addition, broader Auger electron peaks are seen which result from a more complex mechanism. In these transitions, a core electron does not leave the atom but is promoted to a partially occupied state near the valence band, and when the core electron returns its core level, an

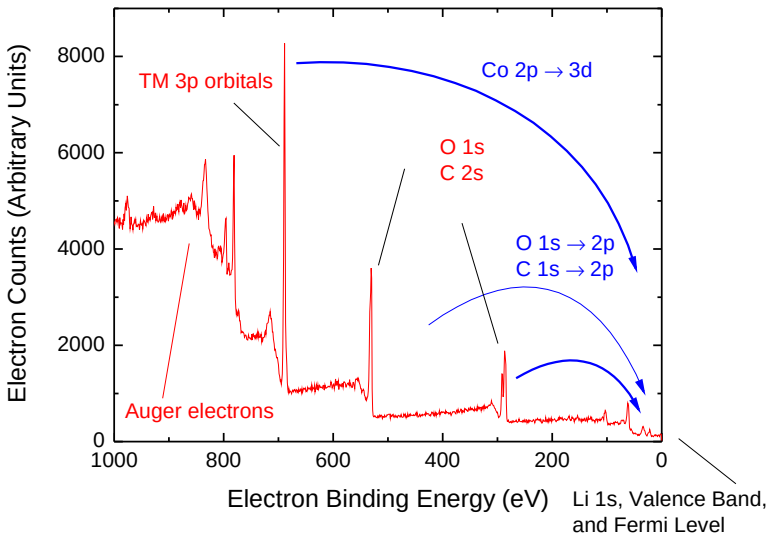

Figure 9: X-ray photoelectron spectrum for lithium cobalt oxide (unpublished)

electron from the valence band receives the energy and is ejected from the sample and detected.[100]

The photoelectron peaks, more so than the Auger peaks, are useful in identifying elements in the sample. Due to the large differences in energy between the binding energies of different elements, neighboring elements such as manganese, iron, cobalt, and nickel can easily be distinguished. Additionally, chemical shifts in the core level peaks have been found which indicate slight changes in the binding energies of the core electrons due to changes in occupation of the valence band. Unfortunately, these shifts are small and therefore difficult to accurately differentiate, and they are not linear from one oxidation state to the next. Also, from one element to the next, the correlation between chemical shift and the oxidation state is not the same. The chemical state of an atom is generally determined by comparison of the spectrum with the Handbook of X-ray Photoelectron Spectroscopy[100] which gives chemical shifts for well-known compounds whose oxidation states have been agreed upon. XPS, therefore, does not provide *a priori* oxidation states, but a fingerprint which can be compared to known compounds.

The existence of the Auger electron peaks suggests a more sophisticated experiment in which the core level to valence band transitions are used as a probe of the density of states in the valence band. In Figure 9, the blue arrows indicate electron transitions from core levels into the valence band. The promoted core electron tends to stay within the original atom, rendering the technique element-specific. Therefore, the density of states in the manganese orbitals can be probed separately

from the density of states in the nickel orbitals, even though the binding energies of the 3d states overlap each other. The different elements are selected by adjusting the X-ray photon energy in fine steps across the core level binding energy. As a practical matter, this is possible only with synchrotron radiation which contains a broad spectrum of X-ray energies.[94]

These transitions are also governed by the Dipole Selection Rule[93] which states that when an electron is promoted into a bound state, the angular momentum of the electron must increase by unity. Therefore, s $\rightarrow$ p, p $\rightarrow$ d, and d $\rightarrow$ f transitions are allowed while s $\rightarrow$ d and p $\rightarrow$ f transitions are not allowed. This apparent limitation is actually an advantage: in addition to being element-specific, NEXAFS is symmetry-specific, meaning that the density of states of p-orbitals can be probed separately from the density of states in d-orbitals. Therefore, when measuring the O 1s $\rightarrow$ 2p transition, some portion of the spectrum corresponds to partially unoccupied, hybridized O 2p - TM 3d antibonding orbitals while the remainder correspond to O 2p orbitals.[101] This can complicate the analysis while providing a glimpse into the density of states of the TM 3d orbitals. By comparing the two spectra, relative changes can be ascribed to p-symmetry or d-symmetry orbitals.

The two techniques are not mutually exclusive however, because the physical processes involved are very similar. Provided that X-rays are incident on the sample, Auger electrons and photoelectrons will be emitted. In XPS, electrons are detected according to their kinetic energy, while in NEXAFS it is sufficient to collect all the electrons (total electron yield or TEY mode), or all the electrons above some energy threshold (partial electron yield or PEY) while varying the incident energy.[95] A hybrid technique known as Resonant Photoemission (RPES)[102] involves performing the XPS experiment at several closely-spaced incident energies in order to probe the occupied valence band states with some element-specificity. In principle, the RPES and NEXAFS could be performed simultaneously, although in practice NEXAFS is faster because the electrons do not need to be sorted by kinetic energy.

2.1.3.5 Calculations of NEXAFS Spectra

The present study is experimental in nature because although the computational methods used for lithium-ion battery materials are limited in accuracy, the experimental methods currently used to determine the electronic structure of these materials are even more limited in their precision. In

ex situ studies, only a finite number of samples can be generated. Spectroscopy on these samples generally reveals a combination of smooth and abrupt changes from sample to sample,[13,103] making it difficult to follow trends as a function of delithiation. The methods developed in this study should be useful in creating high-resolution datasets with which theorists may develop superior models.

The *ab initio* calculation of hard X-ray spectra using FEFF 8[104] is well developed and is used in battery studies to improve the modeling of EXAFS.[105] However, soft X-ray spectra are much more difficult to model due to hybridization between the O 2p and metal 3d orbitals, which varies with interatomic distance.

For modeling the metal L-edges, a special tool has been developed by Dr. Frank de Groot and Dr. Eli Stavitski[106,107] called CTM4XAS. CTM4XAS is short for "Charge Transfer Multiplets for X-ray Absorption Spectroscopy." This program uses symmetry-based calculations (such as octahedral and tetrahedral coordination) to predict charge-transfer effects in metal L-edge spectra including ligand-to-metal charge transfer (LMCT) in which electron in oxygen orbitals are transferred into 3d metal orbitals, as well as d-d transitions. The term "multiplet" refers to the phenomenon of multiple charge-transfer transitions occurring simultaneously. For input, the program takes an integer oxidation state (Co^{2+} or Ni^{3+}) along with the temperature (such as 300 K), the expected crystal field splitting (the energy difference between the t_{2g} and e_g orbitals[45]) to generate an expected metal L-edge spectrum. An example of this use is seen in Figure 71.

Unfortunately, there are several shortcomings of the program. First, the program is limited to very well-known electron configurations; for example, Ni^{4+} cannot be used in calculations. Second, the energy positions of the absorption features are shifted according to literature values for the binding energies of the core electrons as a function of oxidation state;[107] the actual transition energies are not calculated. Third, the program does not take into account the metal-ligand bond distances.

2.2 Literature Review

In the literature it has long been acknowledged that lithiated transition metal oxides, which are highly stable when synthesized at 800°C,[47] become thermally unstable at temperatures below 300°C as a result of delithiation.[73] If this instability were limited to the phase separation of a mixed metal oxide into simple oxides such as Mn_2O_3 and NiO, or the dissolution of the transition metal

into the electrolyte (which has been measured[71]), the problem would merely be a loss of capacity. However, a frequent consequence of overcharge, especially above room temperature, is the release of oxygen gas from the cathode which may ignite the electrolyte. High profile battery recalls by major companies including Dell, Inc.[38] have resulted when manufacturing defects, such as high-resistance electrical contacts, overheat the cell. Thermal runaway, which can start at only 60°C[37] then leads to an explosion.

The direct approach to this problem is simply to charge a cell while detecting the gases which evolve from the cell while preventing the electrolyte from evaporating as well as preventing atmospheric moisture from entering the cell. As described below, multiple studies have detected oxygen gas evolution. However, these studies invariably detect much larger amounts of CO_2 gas due to the breakdown of the electrolyte. Worse, some of the oxygen gas detected has been attributed to the breakdown of the electrolyte, while in some cases oxygen gas is not detected due the reaction of oxygen with the unoxidized electrolyte. The standard solvent-based liquid electrolyte is a hindrance in these studies.

To get at the root of the problem, the electronic structure of the cathode material must be studied in order to find clues that may indicate the instability of oxygen. Many studies have probed the electronic structure of cathode materials using *in operando* hard X-ray techniques using the same liquid electrolyte as standard batteries. Soft X-ray techniques, which heretofore have always been *ex situ*, have also used liquid electrolyte batteries to delithiate the material. In such studies it can be assumed that during charging, the cathode material reacted with the liquid electrolyte prior to battery disassembly. In this study, solid electrolyte cells are used not only to enable soft X-ray spectroscopy, but to eliminate the effect of the electrolyte on the cathode material. Future studies may use the same cells to perform oxygen evolution experiments, also without the interference of liquid electrolytes.

2.2.1 Anomalous Capacity in Transition Metal Oxide Cathodes

Three mysteries regarding transition metal oxide cathode materials serve to promote research into charge compensation, apart from the practical necessity of improving energy storage. First, in the first charge cycle many materials require excess electrical charge to reach a high cell voltage.

During the first discharge and subsequent cycles, of, for instance, the overlithiated material studied in chapters 4 and 5, the reaction is nearly 99% charge efficient.[17] Due to resistive losses, the energy efficiency is less than 99%, but the transfer of lithium ions across the cell is highly efficient in the early cycles; over hundreds of cycles, the charge capacity fades gradually. This initial loss of capacity is attributed to oxygen evolution, which is dicussed in the next subsection.

A more fascinating mystery in battery technology is the tendency for some overlithiated cathode materials to gain capacity over many cycles. It was found[108] that overlithiated nickel manganese oxide, which contains lithium both in the lithium planes and in the transition metal oxide planes, gains capacity above its theoretical capacity after the first cycle. One such nickel manganese oxide is closely related to the overlithiated material studied in this work: $Li_{1.27}Ni_{0.1}Mn_{0.63}O_2$. West et al.[17] studied both materials. They showed that the capacity gains (in spite of the first-cycle loss of capacity) continued monotonically for fifty cycles up to double the initial capacity. However, ultimately the capacity did not surpass that of $Li_{1.27}Ni_{0.10}Mn_{0.63}O_2$.

A third mystery is an increase in reversible capacity achieved at 50°C. This is nonintuitive because at such temperatures, the organic electrolyte tends to react irreversibly with both the anode and cathode, effectively reducing energy storage.[8,36] Johnson et al.[14] found that a range of materials including $LiNi_{0.1}Mn_{0.8}Co_{0.01}O_2$ exhibited *more* capacity below the voltage cutoff of 4.6 V at 50°C as compared to room temperature. Although they speculate that the liquid electrolyte could *contribute* to the battery capacity, they propose to use XAS to study the problem.

It can be speculated the anomalous capacity found at high temperatures could be due to ligand-to-metal charge transfer (LMCT), mentioned in section 2.1.1.3. By this process, electrons could be transferred from oxygen to transition metal ions, effectively preventing them from reaching their maximum oxidation states by replenishing their 3d orbitals. In this study, and in the XAS studies referenced below, all experiments were performed at room temperature. Possible future experiments at elevated temperatures are discussed in section 6.4.3.

2.2.2 Oxygen Evolution from Transition Metal Oxide Cathodes

Armstrong et al.[16] developed a technique called differential electrochemical mass spectroscopy (DEMS) in which a cell is charged while gases are siphoned off using a tube. Using mass spectroscopy, specific gases are detected according to their molecular mass, including CO_2 and O_2 along with a carrier gas, Ar. It was concluded that for $Li_{1.2}Ni_{0.2}Mn_{0.6}O_2$ (an overlithiated compound very similiar to one studied in this work), oxygen evolution begins above 4.V, although the amount of oxygen loss could not be quantified. *Ex situ* neutron diffraction was used in an attempt to determine the resulting crystal structure, given a calculated loss of 0.365 oxygen ions per formula unit. The analysis left some uncertainty as to whether the oxygen was lost from vacancies throughout the structure or from the surface of the crystals. The latter explanation is more convincing, although it requires that the transition metal ions diffuse from the surface of the crystal as oxygen is lost, leading to a fully-packed lattice with few oxygen vacancies. Furthermore, it was determined that lithium ions were preferentially lost from the overlithiated layer, leaving lithium vacancies to be filled by transition metal ions. Logically, if the lithium ions in the transition metal layer are replaced by additional transition metal ions, then from the perspective of the transition metal ions, the number of transition metal nearest neighbors should increase. The ideal experiment for testing this hypothesis, which is the technique used in this work, is EXAFS

Another very similar compound, $Li[Li_{1/9}Ni_{1/3}Mn_{5/9}]O_2$, was studied by Jiang et al.[109] Oxygen gas was, unfortunately, not detected in their experiment. This was attributed to simple combustion in which the oxygen gas reacted with the volatile liquid electrolyte, leaving no oxygen gas to detect.

2.2.3 Hard X-ray Absorption Spectroscopy

In the literature, papers using *in situ* or *in operando* XAS in the title invariably refer to hard X-ray *in operando* studies due to the difficulties of designing a vacuum-compatible cell for soft X-ray studies. In each study, the XANES edges for each transition metal element are examined for shifts to higher energies. In most cases, the Ni K-edge is found to shift rapidly with delithiation while only subtle changes are seen in the Mn K-edge. All too often, when the measured charge capacity of the cathode material exceeds its theoretically reversible capacity, the excess capacity is "blamed" on the oxidation of cobalt, in spite of only modest shifts in the Co K-edge. In all such cases, the

XANES represents an electron transition of the 1s electrons into the metal 4sp orbitals, which are empty. Shifts in the XANES reflect the motion of neighboring ligands[110] in addition to changes in the shielding of the core electron states by the valence electrons. Attempts to correlate the XANES edge position with the 3d electron configuration have been confounded by differences in metal-ligand bond distances.[111]

Mansour et al.[112] performed *in operando* XAS on lithium nickel iron cobalt oxide. The K-edges of cobalt, iron, and nickel were characterized by EXAFS and XANES. They found that upon charging, nickel oxidizes preferentially, followed by iron, while cobalt did not oxidize significantly. This conclusion was based on the lack of a change in the inflection point of the absorption edge, indicating that cobalt's valence state had not changed. However, the XANES information showed more subtle changes in cobalt's bonding environment.

Similar experiments were performed[113] on lithium nickel cobalt manganese oxide, coated with lithium cobalt oxide, at the transition metal K-edges. They found that in this material, manganese shows no shift in the position of the inflection point of the K-edge, indicating that its oxidation state did not change.

Another *in operando XAS* study of cathode materials was carried out by[90] on lithium nickel manganese oxide. They found that upon charging, nickel oxides from 2+ to 3+ to 4+, while manganese remains at 4+. However, upon deep discharge to 1 V, manganese is reduced preferentially. While current synchrotron equipment is not designed for a photon energy low enough to probe lithium directly, lithium may act as a backscatterer of the internal photoelectron. Using EXAFS, they found that manganese has lithium ions as second nearest neighbors, indicating that lithium migrated into the transition metal layer.

Ito et al.[114] studied a complex overlithiated material, $LiNi_{0.17}Li_{0.2}Co_{0.07}Mn_{0.56}O_2$, *in operando* with hard X-rays over the course of two cycles. The signal-to-noise ratio for the Co K-edge was low due to the low concentration of cobalt. The Ni K-edge shifted to higher energies in the first charge, although in the second charge the shift was not as great as in the first cycle. The Mn K-edge showed no XANES shift in the first cycle, but shifted to lower energies during discharge and shifted to higher energies during the second charge cycle. However, the reversible charge capacity could not be accounted for by the combined oxidation of nickel and manganese.

In contrast to these studies of ever-more-complex cathode materials, Alamgir et al.[54] used *in operando* XAS on a solid-state thin-film lithium cobalt oxide battery. Because only one transition metal species was present, charge compensation could only occur due to cobalt or oxygen oxidation. Using principal component analysis,[115] to relate spectroscopic peak shapes to experimental variables, they were able to deconvolute the spectrum into three principal components whose magnitudes changed as a function of the state of charge. This showed that two reactions, presumably the formation of both cobalt holes and oxygen holes, occurred simultaneously at some states of charge. At other states of charge, only one reaction occurred. EXAFS showed that the Co–O bond distance contracted during delithiation, indicating a reduction in Coulombic repulsion between Co and O due to a loss of electrons. Ultimately, it could not be determined whether the electron was lost from the Co 3d orbitals or from the O 2p orbitals, or from both. Also, because the thin-film battery was constructed with the cathode material between the substrate and the solid electrolyte, soft X-ray absorption could not be peformed on the cathode.

2.2.4 Soft X-ray Absorption Spectroscopy

The direct XAS study of the oxygen K-edge of liquid water,[116] was accomplished using a silicon nitride window to separate the beamline, held under vacuum, from the endstation, which was filled with helium gas.[117] This endstation at the Advanced Light Source was specifically designed for environmental observations. Their ingenious design is not practical for in situ battery work because where their design involved a gas held back by a nonconductive window, liquid-electrolyte batteries require a liquid-impregnated cathode to be sealed from vacuum using a conductive material. In the proposed work, the battery must be compatible with any soft X-ray beamline.

An *ex situ* study of chemically deintercalated lithium cobalt oxide was performed.[118] It was found that the cathode material, at different states of charge, showed no change in oxidation state for cobalt. Instead, they found a small peak in the oxygen K-edge band which reduces in height with increasing state of charge. This conflicts with the intuitive theory that cobalt acts to compensate the intercalation and deintercalation of lithium in this material, and differs from the behavior of nickel in such materials, as described below.

2.2.4.1 *Oxygen Holes versus Oxygen Vacancies*

Oxygen holes, which are electronic holes in the valence band of an oxide, are much less common than oxygen vacancies, which are vacancies on the oxygen sublattice of a crystalline oxide. The former is a missing electron while the latter is a missing ion. They are related, however, as shown by Kuiper et al.[119] The high-temperature superconductor $YBa_2Cu_3O_x$ was heated to temperatures from 500 to 1000°C in flowing oxygen gas to achieve a wide range of different concentrations of oxygen vacancies. The resulting O K-edge NEXAFS spectra are shown in Figure 10. It was found that higher temperatures yielded lower oxygen stoichiometries, or higher levels of oxygen vacancies, and that this led to higher concentrations of oxygen holes near the Fermi level. Conversely, at lower temperatures, very low levels of oxygen vacancies were found, and very little X-ray absorption occurs near the Fermi level.

A complicating factor in the analysis is the hybridization of Cu 3d orbitals with O 2p orbitals in this material. Cu L-edge NEXAFS[119] showed that with increasing temperature (increasing oxygen vacancies) some portion of the O K-edge NEXAFS spectrum can be explained by holes in the Cu 3d orbitals. Conversely, at lower temperatures (increasing x in Figure 10) the absorption features near the Fermi level are attributed to O 2p holes. The precise balance between the two types of electronic holes could not be determined due to limited spectral resolution, but the trend was clear: charge compensation occurred partially in the O 2p bands, and the amount of charge per oxygen ion depended inversely on the amount of oxygen ions. Therefore, the concentration of oxygen holes is inversely related to the concentration of oxygen vacancies. The implication for battery materials is that oxygen evolution can lessen the need for oxygen holes, thereby shifting the burden of charge compensation onto the transition metal ions.

2.2.4.2 Ex Situ *Soft X-ray Battery Studies*

Because NEXAFS reveals the symmetry-selected partial density of states for each desired element including oxygen, it is the ideal tool for determining charge compensation mechanisms. Although the O 2p orbitals are large and thereby overlap with transition metal d-orbitals, holes of exclusively O 2p character can be detected by comparing the O K-edge NEXAFS to the metal L-edge NEXAFS. During delithiation, holes which appear in the O K-edge but not in the metal L-edges can be deduced

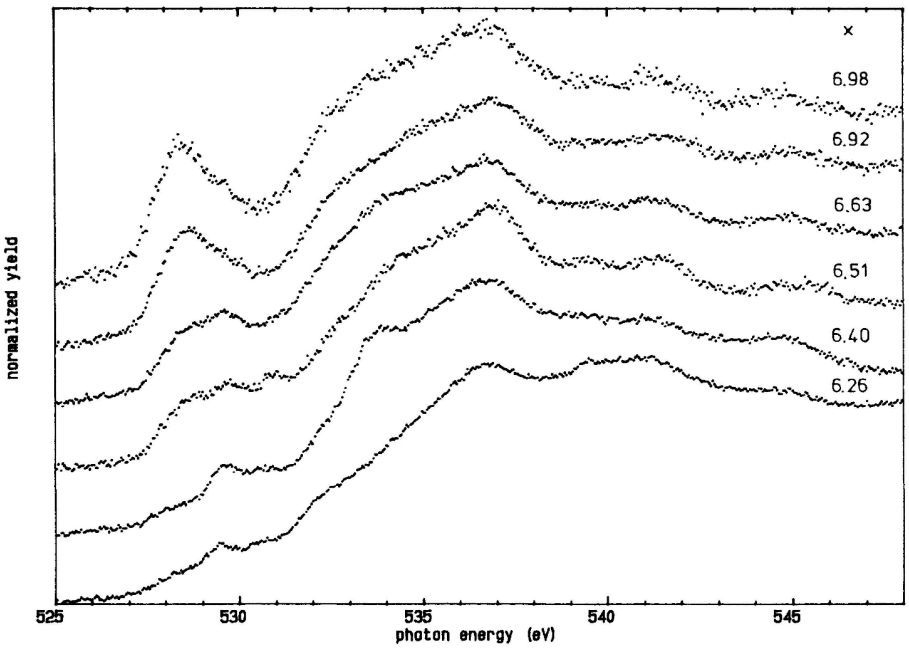

Figure 10: O K-edge NEXAFS (TEY mode) of $YBa_2Cu_3O_x$ samples, after scraping under vacuum, from Kuiper et al.[119]

to be of O 2p character rather than being of d character. The deductive procedure of Kuiper et al.[119] described in section 2.2.4.1 can be applied to battery materials except that the lithium content is changed during the experiment instead of the oxygen content.

The landmark study of oxygen oxidation by Yoon et al.[13] in 2002 came to similar conclusions as previous researchers who published slightly less detailed work at about the same time.[118,120] As in the present study, Yoon et al. utilized NIST beamline U7A due to its virtually unique combination of surface-sensitive PEY detection and its subsurface-sensitive FY detection mode. (See section 3.1 for details.) In that study, *ex situ* hard X-ray spectroscopy at the Co K-edge yielded the same conclusions as Alamgir et al.[54] in that the oxidation of cobalt was not sufficient to explain the measured capacity of the material. Additionally, *ex situ* soft X-ray spectroscopy at the Co L-edge, shown in Figure 11, found no evidence that any amount of Co^{4+} was forming as a result of lithium extraction. In this spectrum, two groups of absorption features are found, including the L_{III} at 778 eV and the L_{II} at 795 eV. Although each group of features indicates the $2p \rightarrow 3d$ electron transition, they differ in terms of the aggregate spin of the electrons remaining in the 2p orbitals after one of these core electrons is ejected. Although in principle either set of features can be used to understand

d-symmetry partial density of states in the valence band, in practice only the L_{III} is used due to its higher intensity. In Figure 11, the single peak seen at 778 eV represents the absorption of the empty Co e_g band.

As delithiation progresses, the Co L_{III} is seen to shift to higher energies, suggesting that the Co 2p orbitals are become more bound to the nucleus due to the loss of valence band electrons. At 50% delithiation, a mixture of Co^{3+} and Co^{4+} was expected. However, Co^{4+} has an electron configuration of $t_{2g}{}^5$ $e_g{}^0$, which should lead to the formation of a distinct peak below 778 eV. Instead, only a small shoulder develops in this region, even when 75% of the lithium ions are removed. It was concluded by Yoon et al. that although some charge compensation could be attributed to cobalt, the oxidation of cobalt was not sufficient to explain charge compensation in $LiCoO_2$. Necessarily, because cobalt is the only transition metal in this material, oxygen must oxidize to balance charge.

In Figure 12, the evolution of the oxygen K-edge with delithiation is shown. Here, the trends are much more apparent than in the Co L-edge. In the pristine material, the pre-edge associated with the Co $e_g{}^0$ orbital is initially very sharp, but this feature becomes blunt with delithiation. Furthermore, new features (A_3, A_2, and an arrow) appear in the spectrum both below and above this peak. Unfortunately, these peaks could not be assigned to any particular orbital configuration because they could not be predicted by theoretical methods. As can be seen in the figures, these new features were much more pronounced in the O K-edge than in the Co L-edge. In particular, the A_3 feature is half the height of the A_1 feature and is approximately 4 eV below it; the features in the Co L-edge spectrum are far less intense than the main peak and extend only 3 eV below it. It is thus inferred that although some of the new features in the O K-edge are the same as the new features in the Co L-edge, much of the intensity of the spectrum can be attributed to holes of exclusively O 2p character.

At higher energies, the features marked B and C, indicate that the empty 4sp orbitals are changing both in intensity and in energy. Because these orbitals are empty at all times, any change in these features is exclusively due to geometrical changes, including contraction of the Co–O bond. This highlights a problem with NEXAFS analysis: as the degree of hybridization changes, the appearance of the electronic structure changes. This makes it difficult to quantify the electronic structure of the oxygen orbitals in these materials.

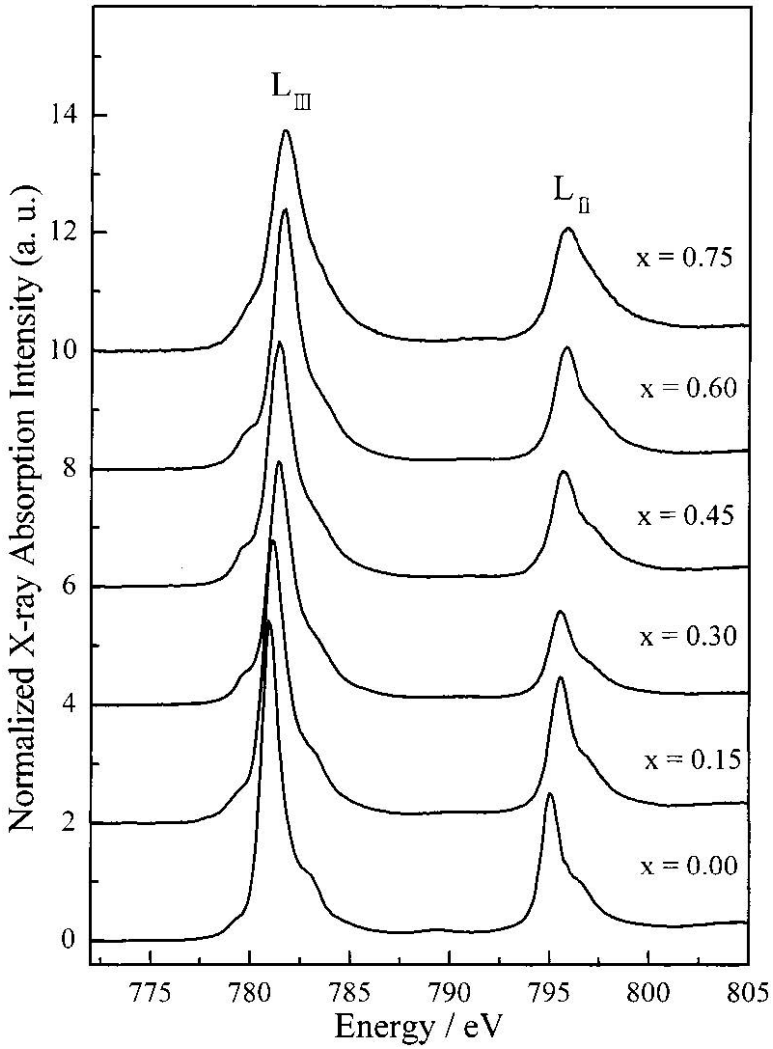

Figure 11: *Ex Situ* Co L-edge NEXAFS of $Li_{1-x}CoO_2$ from Yoon et al.[13]

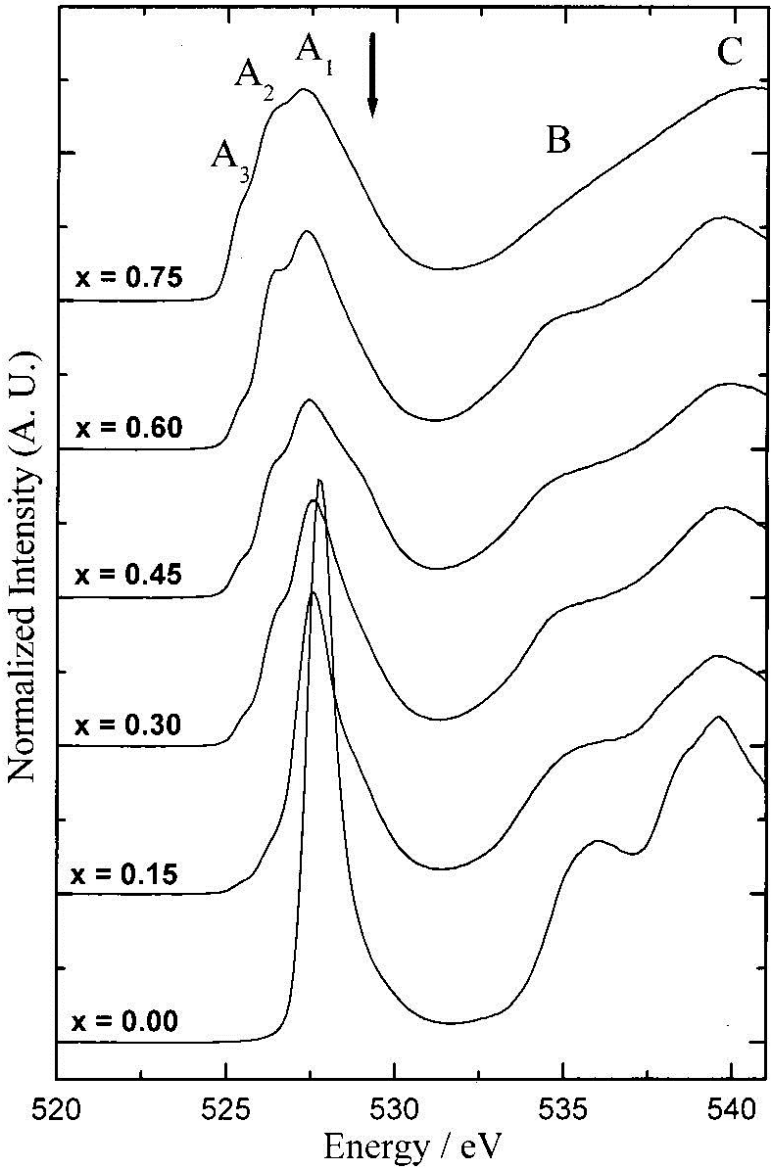

Figure 12: *Ex situ* O K-edge NEXAFS of $Li_{1-x}CoO_2$ from Yoon et al.[13]

CHAPTER III

EXPERIMENTAL METHODS

In this chapter, *in operando* battery characterization methods are discussed in light of the spectroscopic constraints (section 3.1) inherent in soft X-ray and hard X-ray absorption experiments. The advantages and disadvantages of *in operando* experiments (section 3.2), in which many spectra are taken using a single battery, are discussed. The fastidious methods which were developed to analyze the fine-grained EXAFS data obtained from such experiments ar discussed in section 3.3. Battery construction methods are discussed in sections 3.4 and 3.5. The sample holders which were designed for soft X-ray spectroscopy on pellet batteries and thin film memristors are discussed in section 3.6.

One much-used battery design stands out as being the antithesis of the cell designs developed in this study: the coin cell battery. These cells utilize two discs of stainless steel separated by a plastic ring which both seals the cell and separates the discs electrically. Stainless steel is virtually opaque to all useful wavelengths of radiation from radio waves to gamma rays. An early goal was to create a "windowed" coin cell which could transmit a focused beam of X-rays through two $^{9}/_{32}$" holes covered by aluminum foil and, *moreover*, to create such a cell which could be cycled for several days or a week without leaking. All attempts to seal an aluminum foil "window" to punctured pouch cell parts failed, sooner or later, due to chemical incompatibility with the electrolyte. First, as with any electrolyte, solder will tend to corrode when placed in a galvanic circuit either with the anode or the cathode material. Second, because the solvent used in the electrolyte is highly polar, various glues and two-part epoxies tended to swell and eventually dissolve.

A much more adaptable solution was that of the pouch cell, described in Section 3.4, in which the inner surface of the cell is entirely polyethylene. Such a cell was used for an *in operando* hard X-ray transmission experiment which spanned a full charge, a full discharge, and a full recharge step.

A pouch cell, however, is still not transparent to soft X-rays or to low-energy electrons. Therefore, the method of solid state batteries was adapted for NEXAFS experiments as described in section 3.5. A second cathode characterization method is also amenable to soft X-ray and electron spectroscopies: thin film memristors. In this method there is no electrolyte and no open circuit voltage and therefore, no battery. However, the *in situ* application of an electric field across a cathode material can disturb the distribution of lithium ions sufficiently for characterization methods to detect the effects on the electron configuration in transition metals and in oxygen ions.

3.1 Spectroscopic Constraints

In any spectroscopic investigation, the limitations of the probe must be taken into account prior to designing the experiment. In Figure 13, the calculated attenuation length of X-rays through $LiCoO_2$ is given. At the soft X-ray limit, the intensity of a beam decreases by $1/e$ after passing through only tens of nanometers of $LiCoO_2$. As the beam energy is tuned past the O K-edge near 540 eV, the attenuation length drops suddenly as oxygen ions are ionized. A similar effect is seen at the Co L-edge; at both edges the attenuation length is hundreds of nanometers. For particles of 5–10 micron size, only the surface is irradiated by the beam. (Any scattered or fluorescent beam is also absorbed.) At the Co K-edge, however, the attenuation length is tens of microns, making it possible for X-rays to easily pass through 5–10 micron particles. This renders hard X-ray measurements bulk-sensitive, but not very surface sensitive, while soft X-ray measurements are very surface sensitive. In this section, the implications of the probe depth for hard X-ray and soft X-ray experiments are discussed.

In practice, the calculated spectrum in Figure 13 can never be measured using one piece of synchrotron equipment because as the electrons circulating in the ring are redirected by magnets, the angle of the directional change and the strength of the magnets produce a limited spectrum of broadband X-rays.[96] At the National Synchrotron Light Source (NSLS), these limitations are overcome, in part, by using two separate electron storage rings. In the soft X-ray (or Vacuum Ultraviolet (VUV)) ring, a lower kinetic energy for the electrons and a large angle change at each bending magnetic provides a narrower spectrum of soft X-rays. In the larger hard X-ray ring, electrons of higher kinetic energy circulate in a larger ring with many smaller bends in the electron path, yielding a broader spectrum of hard X-rays which drops off below the gamma ray region.[121]

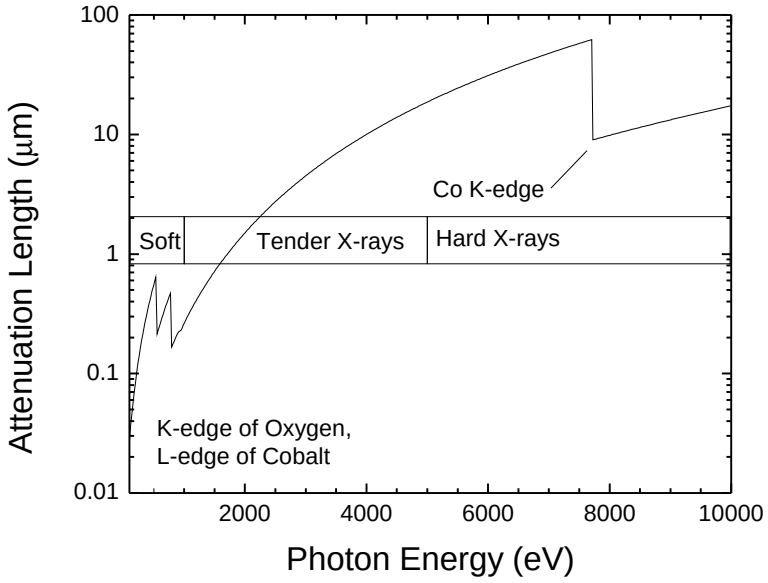

Figure 13: Calculated[96] Attenuation Length of Soft, Tend, and Hard X-rays in $LiCoO_2$

Table 7: Characteristics and Capabilities of NSLS Beamlines used in this Study[122]

Beamline	Management	Energy Range	Detection Mode
U7A	NIST	180 - 1200 eV	FY & PEY
X11A	NRL	2.6 - 26 keV	Trans.
X23A2	NIST	4.9 - 30 keV	Trans.

Three beamlines used in this work are detailed in Table 7. The National Institute of Standards and Technology (NIST) beamline U7A carries the prefix "U" for "ultraviolet" and utilizes soft X-rays in combination with surface-sensitive detectors; because the transmitted beam is totally absorbed in every experiment, no detector is provided for it. The hard X-ray beamlines X11A and X23A2, operated by the Naval Research Laboratory (NRL) and NIST respectively, primarily utilize transmission detection. However, fluorescence detection is also used for samples on thick substrates.

3.1.1 Hard X-ray Probe

For sol-gel derived particles of 5–10 micron diameter, hard X-rays are capable of penetrating a few layers of particles in addition to an aluminum foil substrate and other packaging. This constraint is very well suited to battery studies. For the cathode of a lithium ion battery, aluminum foil is ideal because it passivates to AlF_3 . The penetration of the liquid electrolyte into the composite cathode

deposit requires fairly thin layers of about 15 mg/cm^2, which is thin enough to be penetrated by the hard X-ray probe.[17] Battery cathode samples can simply be removed from batteries, washed, and placed in a hard X-ray beam. For *in operando* experiments, however, the packaging must be well chosen to minimize absorption as discussed in section 3.4.

In terms of information depth, almost 100% of the signal is bulk-sensitive rather than surface-sensitive. This is only slightly modified by the use of fluorescence detection modes, in which the (bulky) detector is frequently placed 90° from the beam. If the sample is also angled to 45° from the incident beam, the attenuation length for both the incident and fluorescent beams is reduced, although this length is still multiple microns.[96] Surface sensitivity is only possible at glancing angles.

The width of the hard X-ray probe is very large in most cases, spanning thousands of solid particles. Although Kirkpatrick-Baez[123] optics can be used to focus X-rays to a small point, their use is not widespread. At the NSLS, the beam can be as much as 15 mm wide, although that can be reduced using baffles which absorb the edge of the beam. The height of the beam can be 1–4 millimeters.

3.1.2 Soft X-ray Probe

Whereas the hard X-ray probe travels through the bulk of several layers of particles, the soft X-ray probe is incapable of penetrating a significant fraction of a single particle. Furthermore, the electrons and photons which are ejected from the surface can penetrate even less material, rendering the entire measurement very surface sensitive. As seen in Figure 13, the attenuation length for soft X-rays is only a few hundred nanometers. In the case of fluorescence, the photon energy will be less than the photon energy of the incident beam and therefore, the attenuation length will be even shorter.

For electrons ejected from the surface, the relevant measurement is the inelastic mean free path (IMFP). The IMFP can be used to estimate the depth from which an electron can escape from a solid. This depth is estimated by the use of an equation developed by Seah & Dench.[124] This equation can be applied to a solid material using a web applet.[125] The results of such a calculation for $LiCoO_2$ are shown in Figure 14. This figure shows that as the kinetic energy of an electron increases, electrons from deeper in the material can be ejected out of the material.

The kinetic energy of the electron depends on whether it is a photoelectron (a core level electron ejected from the surface) or an Auger electron (a valence band electron ejected from the surface). If the photon energy of the incident beam is 600 eV, the kinetic energy of the O 1s photoelectron (which has a binding energy of about 546 eV) will be $600 - 546 = 54$ eV. Most of these electrons will not escape the sample. However, the excitation of this core electron leaves a core hole which is re-filled by a valence-band electron. The kinetic energy gained by the valence-band electron is given to another electron in the valence band; this new electron is termed an Auger electron and carries a kinetic energy comparable to the binding energy of the photoelectron.[46] By detecting Auger electrons, it is possible to obtain information from several nanometers within the sample.

For a pellet battery, therefore, only the active material which is exposed at the surface and free of corrosion or coatings can be studied using Auger electron emission. By using fluorescence yield measurements, hundreds of nanometers of material can be probed, making it possible to study coated samples and/or compare differences between the surface and the bulk of the material. However, given a particle size of 5–10 microns, only a small portion of the material is probed. It would be preferable to perform both soft X-ray and hard X-ray bulk-sensitive measurements in order to make direct comparisons. Failing that, a combination of surface-sensitive soft X-ray and hard X-ray measurements would also be desirable. Instead, hard X-ray measurements are largely limited to providing bulk-sensitive information while soft X-ray measurements are limited to surface-sensitive information.

Although the soft X-ray beam at U7A is refocused to a small spot, it still cannot be focused smaller than 1 mm^2. In addition to this mode of operation, however, two-dimensional Auger electron detectors are also being developed at U7A. The first detector of its type, the Lariat Mk I, detects electrons emitted from sample while the soft X-ray beam is rastered across a 1 cm^2 area. The effective pixel size for this detector is 75 microns or 0.075 mm. The next model, the Lariat MK II, will have a resolution of 5 microns or 0.005 mm. In the future, although 5–10 micron particles may be singled out by the new detector, future battery research is expected to utilize nanoparticles. Therefore, as with hard X-ray beams, very many particles (at the surface) are sampled simultaneously.

The implication of the probe size, coupled with the necessity of studying the oxygen absorption edge, is that any solid electrolyte, binder, and conductive additive used in a soft X-ray *in operando*

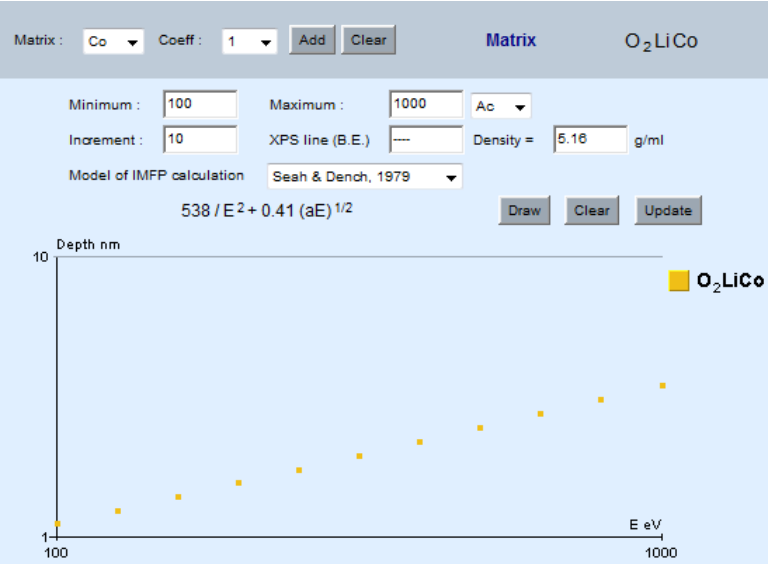

Figure 14: Calculated[124] Inelastic Mean Free Path for electrons as a function of kinetic energy in $LiCoO_2$

battery must be oxygen-free to ensure that the spectroscopic results only correspond to the active material. That being said, any stray oxygen included in an *in operando* sample due to impurities or corrosion will be present in every spectrum. Small changes in the spectrum due to delithiation will still be apparent.

3.2 In Operando *Approach*

Three experimental strategies used in this work are denoted by Latin phrases: *ex situ*, *in situ*, and *in operando*. The first, *ex situ*, simply means that the samples are prepared prior to the experiment. Typically, several samples are prepared under carefully controlled conditions. This strategy would not require a Latin phrase if not for the use of *in situ* strategies, which require that the sample be altered or even created during the characterization experiment. The third strategy goes a step further by requiring that the sample perform some chemical task which might, in theory, be useful. For catalysts this means promoting a reaction while for batteries this means transferring lithium from electrode to the other.

This progression from *ex situ* to *in operando* experimentation represents both increased scientific rewards and increased risks. In an *ex situ* experiment, samples are prepared ahead of time, and poorly-processed samples can be replaced until a full set is ready for characterization. Each

sample could represent a different chemical formula or a different heat treatment process, for example. Characterization can then proceed with no further processing. In contrast, *in situ* experiments require heating, cooling, or gas exposure equipment inside the analysis chamber. This allows the researcher much finer control over the experimental variables, but it comes with costs. Typically, only one sample can be heated or cooled in a controlled way. Furthermore, many types of samples are sensitive to air exposure, especially at high temperatures and especially when highly surface-sensitive experiments are performed. Therefore, usually only one sample at a time can be installed in the analysis chamber at a time. There is a risk that this single sample may have been prepared incorrectly, or that the heating and cooling apparatus may fail.

3.2.1 Disadvantages of *In Operando* Experiments

In operando battery experiments involve a single cell in which only one parameter, such as state of charge, changes during the experiment. This exemplifies the principle of *ceteris paribus*, or "all else being equal." However, there are many characterization techniques which cannot be performed simultaneously with, for instance, hard X-ray transmission experiments. Although it is possible in principle to perform *in operando* X-ray diffraction while also measuring the X-ray absorption spectrum, such an experiment would be complex and cumbersome. The advantage of *ex situ* experiments is the possibility of characterizing each sample using microscopy, optical spectroscopy, magnetic measurements, and composition measurements on the same set of samples. A full array of *ex situ* experiments can take place over a series of months.

An additional limitation of *in operando* experiments is that they are necessarily non-equilibrium measurements. Whereas *ex situ* samples may be charged to a certain voltage and held at the voltage for days[109] to equilibrate the lithium content throughout the cathode, such long experiments are not possible at a synchrotron where the beamtime is typically limited to 2–5 days. Instead, a cell is charged at a constant, slow rate over the course of 12 hours or more. Although this will result in some diffusion gradient through an intercalation cathode particle, in a transmission experiment the beam probes the entire bulk of the sample, effectively taking an average throughout the crystal. In soft X-ray experiments, although only the surface is probed, in this study the experiment is generally an order of magnitude slower, so each spectrum can be assumed to be near-equilibrium in terms of

composition.

3.2.2 Advantages of *In Operando* Experiments

In operando experiments are well-suited to synchrotron characterization methods because a highly detailed data set may be obtained within a small amount of beamtime, such as a few days. The resulting data set will represent a monotonic series of compositions even if the number of scans per hour becomes very high. In an *ex situ* study with the same number of battery compositions, problems with individual samples create uncertainty as to the correlation between the intended composition and the resulting electronic structure. By using *in operando* methods, charge compensation trends can be clearly identified.

A more insidious problem is the fact that X-ray absorption experiments cannot be performed without a synchrotron. Whereas X-ray diffraction experiments can be performed at one's home institution and then repeated at a synchrotron, *ex situ* sample intended for X-ray absorption experiments cannot be spot-checked in terms of their electronic structure. (Although XPS measurements can check for sample cleanliness, the valence band spectra will not be helpful in determining element-specific problems.) This means that, especially for electrochemically produced samples for soft X-ray analysis, the sample preparation can fail prior to shipping the samples, and there is no way to check. Samples may become coated with contaminants, or react with those contaminants to form a thin surface layer which is chemically different from the underlying sample. Even when this surface coating is thin enough to be transparent to soft X-rays, its thickness will tend to vary from sample to sample in an unsystematic way. Where cleaning is attempted, the extent of cleaning will also vary unsystematically.

Figures 15 and 16 show six *ex situ* O K-edge spectra each (in PEY mode and FY mode, respectively) for a series of composite cathodes ($Li_{1.17}Ni_{0.25}Mn_{0.58}O_2$) removed from six liquid-electrolyte coin cells. The surface-sensitive PEY scans show dramatic, and disorganized, differences from sample to sample. Compared to the pristine material, the pre-edge features are much less intense than expected, and apart from the 4.2V sample, the expected pre-edge features are absent. Comparison with the near-bulk-sensitive FY scans reveals the electronic structure of the cathode material. Based on this surface-to-bulk difference in absorption, the exposed surface of the cathode particles is likely

coated with a combination of ethylene carbonate (from the electrolyte) and Li_2CO_3 (from exposure to moist air). Unfortunately, even the FY scans vary greatly in the intensity of the pre-peaks. Trends from sample-to-sample could not be determined.

X-ray absorption experiments are repeatable in the sense that after background subtraction and alignment is performed, the results from two duplicate experiments at the same beamline will be identical. However, because the exact signal levels are sensitive to sample preparation and mounting, the total amount of absorption, peak shape, and noise level are not identical from sample to sample at the same beamline. Surface contamination is much less of an issue where hard X-rays are used. When the beam penetrates the entire sample, thin surface layers contribute nothing to the X-ray absorption signal.

3.2.3 Combination of Multiple Elements per Scan

The scientific advantages of gathering data from as many elements as possible are obvious. Scanning multiple elemental absorption edges in a single scan can be a practical necessity, however, at beamlines which lack effective scripting capability. At U7A, the XDAC software is well-configured and sophisticated scripts are readily available. The acquisition of oxygen K-edge, Mn L-edge, Co L-edge, and Ni L-edge data, and the naming of files, can be customized. However, beamline X10C uses the VMS operating system along with a custom-written data acquisition program. Also, at X11A although XDAC is used, no tested scripts are available. At X11B, the optical design of the beamline does not permit the Mn K-edge and the Ni K-edge to be acquired using the same monochromator alignment.

A multi-element strategy was developed at X11A and was later used at X10C. First, a scan specification was designed which collects data from below the manganese edge to above the nickel edge. This includes low-point-density regions for the pre-edge, high-point-density regions for the edge, and k-spaced-point regions for the EXAFS region. (The spacing between data points is small just above the edge and becomes quadratically larger above the edge.) Between the two edges, an especially low-point-density region is used to save time. Second, elemental reference foils are

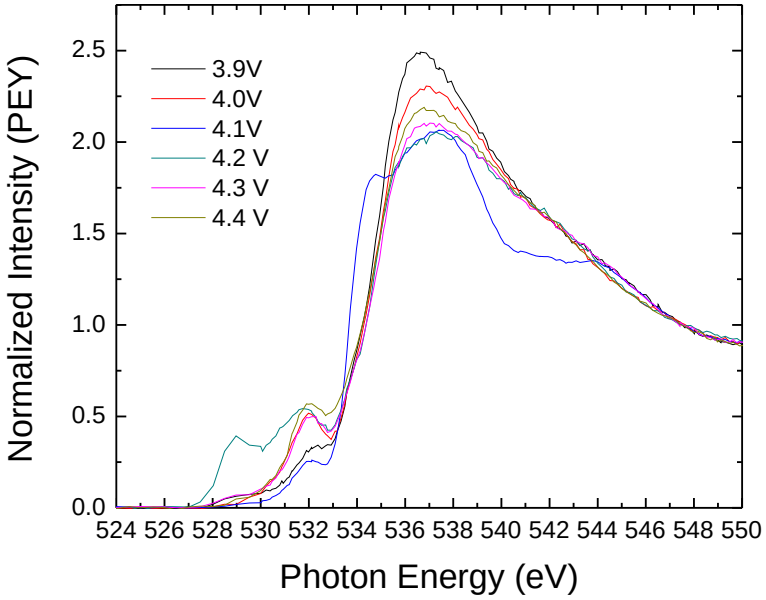

Figure 15: Surface-Sensitive O K-edge NEXAFS of *Ex Situ* Cathodes, PEY mode

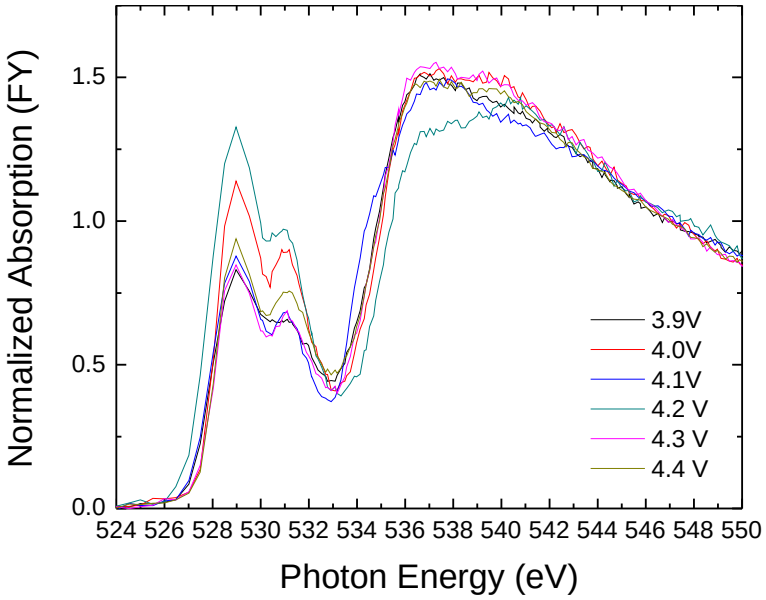

Figure 16: Near-Bulk-Sensitive O K-edge NEXAFS of *Ex Situ* Cathodes, FY mode

inserted for each element. Third, the signal levels are checked above and below each absorption edge to ensure that none of the detectors are overloaded or underloaded throughout the entire scan. Fourth, the software is programmed to repeat this scan for a large number of times.

A pitfall in this strategy was found in the specification of the scan. When k-spaced points are calculated by XDAC, the program uses the first absorption edge as the point of reference for k-point spacing. The result is that the first absorption edge has correct k-spaced points, while subsequent edges have excessively low point-density in the EXAFS region. Fortunately, the most important data in EXAFS are low-frequency data, and this requires only widely-spaced points. The simplest solution to this problem is to reduce the k-spacing such that it will be excessive at the lower edge, and just right at the higher edge. At X10C, although the software is not scriptable, it was written to be more powerful, and k-spacing regions for each edge could be calculated independently.

3.2.4 Automation without Synchronization

When a novel experiment requires two different techniques to be performed, it is rare that the two types of electronics will be able to communicate with each other in any way. While there may be some situations where all of the electronics communicate using the National Instruments GPIB protocol, and can be scripted using LabView, such situations did not present themselves in this work. Although two Solartron potentiostat systems were available, the software license provided with them precluded multiple potentiostats from being controlled, simultaneously, by one computer. Therefore, experiments were designed which could proceed independently.

This requires that simple, predictable experiments be designed. Table 8 gives the four combinations of electronics used in this study. (A discussion of the programmability of different potentiostats is included in section C.7) In the case of *in operando* NEXAFS at beamline U7A, either the Solartron or the Pine potentiostat was used to charge the sample in 55 minute increments with 5 minute rests, or in 58 minute increments with 2 minute rests. Such a scheme included time for measuring the open circuit voltage periodically while simplifying the calculation of the amount of charge passed over time. This charging scheme was started simultaneously with the beginning of the spectroscopic experiment, and time stamps on the files were compared during data analysis. Truncated spectra (caused by scheduled or unscheduled beam dumps) were discarded. In this scheme,

Table 8: Experiments Requiring Multiple Electronics Units

In Operando	Sample	Independent Variable	Dependent Variable
NEXAFS	Pellet Battery	Solartron or Pine	PEY/FY, XDAC
XANES	Pouch Cell	Pine, Aftermath	XAS Transmission, XDAC
Resistivity	Thin film	Arbin, MITS Pro	Solartron, Corrware
High Temperature	Pellet Battery	Eurotherm PID	Solartron, Zplot

the schedule of the synchrotron ring does not need to be included in the programming of either the battery charging or the spectroscopy. In the case of hard X-ray transmission experiments on liquid-electrolyte pouch cells, the cell could be charged at a constant current until a limiting voltage of 4.8V was reached. As in the soft X-ray case, only the start times of each side of the experiment were required in order to correlate state of charge with spectroscopic changes.

The *in operando* resistivity experiment on a thin film (see section A.1) required a potentiostat of great sensitivity, namely the Solartron 1287, for the thin film resistivity portion of the experiment. Although in theory a second Solartron 1287 could have been used to delithiate the cell as well (potentially simplifying data organization), the Corrware software license precluded this. An Arbin potentiostat, and a second computer, was used to delithiate the thin film via the liquid electrolyte.

In the high temperature *in operando* experiment, the independent variable was temperature, and this was controlled by a Eurotherm PID controller. Although this controller lacked a computer connection, a series of slow ramps and holds could be programmed so long as the ramps always increased the temperature. The cooling of the furnace was found to be both extremely slow, and unpredictable. Therefore, if multiple heating cycles were required, the furnace was allowed to cool overnight before starting the next cycle manually.

3.3 EXAFS Extraction and ARTEMIS *Modeling*

In this section, XAS data reduction procedures are discussed. Detailed procedures are provided in Section D.1. Although standard tools including ATHENA and ARTEMIS software by Matt Newville and Bruce Ravel[99] were used, the order of the procedures has been streamlined to enhance the repeatability of the analysis and to save time. Also, the procedures detailed here are designed to keep as many parameters constant as possible to allow for the accurate analysis of fine changes seen in data from *in operando* battery experiments. Ultimately, although XANES and EXAFS do not

provide absolute oxidation states and absolute nearest neighbor distances, these techniques can be used to identify element-specific electronic and structural trends. Soft X-ray NEXAFS experiments, however, can be used to identify absolute oxidation states as well as redox trends.

Figure 17 gives the normalized Mn K-edge absorption spectrum along with correct and incorrect background curves. The spectrum was measured in transmission, although hard X-ray fluorescence detectors are available for samples deposited on thick substrates. At approximately, 6,539 eV a pair of small absorption features is seen which indicates the dipole-forbidden 1s $\rightarrow$ 3d transition. (The dipole selection rule is relaxed due to Mn 3d - O 2p hybridization in addition to tetragonal distortion away from octahedral symmetry in the crystal.) Coincidentally, this feature appears at the same energy as the 1s $\rightarrow$ 4sp transition for Mn metal; the absorption of an Mn metal foil is measured downstream from the sample and is used for data alignment, but is not shown. Because manganese adopts an Mn^{4+} state, however, its 1s $\rightarrow$ 4sp transition is approximately 20 eV higher. This transition is termed the "white line" because early studies used black and white negative film to measure absorption; in the negative, the absorption peak would be more transparent. Above this white line are EXAFS oscillations which decay rapidly. Unfortunately, this modulation is not mutually exclusive with electronic transitions and the two regions overlap.

It should be noted that although the spectrum is normalized to unit absorption, the extraction of EXAFS requires a choice of background spline which, ideally, is independent of the structural information.[98] The shape of the background spline depends on the choice of E_0 which unfortunately cannot be extracted directly from any one feature of the absorption spectrum, and instead must be refined as described below. In Figure 17, the red line indicates a poorly chosen spline which does not follow the EXAFS oscillations. The blue line, however, starts at the half-edge-jump where the normalized absorption is 50%; although this starting point may be refined further, it is a good initial choice because it follows the EXAFS oscillations. In subsequent steps, the oscillations about this spline will be Fourier transformed to yield nearest neighbor distances.

Within the spline the two regions overlap, however, and the nature of this overlap differs from one element to the next, and depends heavily on the type of absorption edge, the oxidation state, and the ligands bonded the absorbing atom. The data reduction process attempts to separate the two regions and present, firstly, a well-normalized XANES region and secondly, an EXAFS region

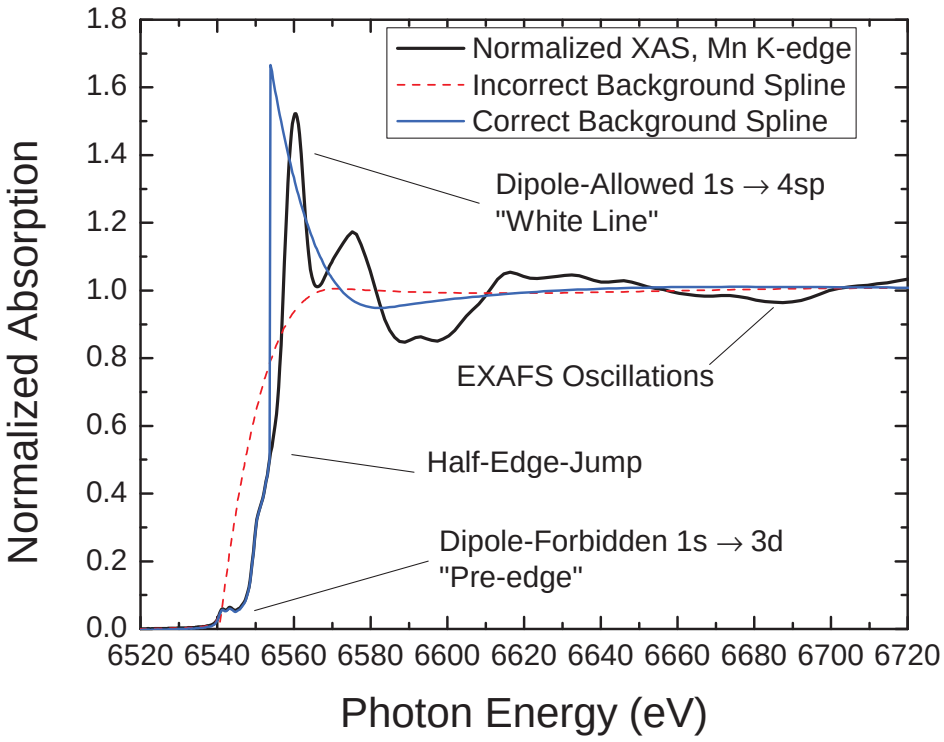

Figure 17: XAS spectrum for the Mn K-edge after normalization with correct and incorrect background splines

with the background absorption (and no structural information) subtracted from it. The XANES region is easy to normalize, but difficult to analyze. The EXAFS information, in contrast, can easily be analyzed provided that an accurate background curve is subtracted. Background subtraction is sufficiently uncertain that iterative refinements, followed by simulations, are required to determine the optimal parameters for the background curve.

The spectral overlap of the XANES and EXAFS regions makes it difficult to develop a standard method of data reduction. Separation of the XANES and EXAFS regions requires parameter choices which are chosen by the analyst and then refined; the parameters are not extracted directly from the data. However, unless the parameter choices are very far off, the final analysis can remain accurate, especially if EXAFS fitting is performed and used to correct the inital values.[126] To extract accurate electronic and structural trends, the initial parameters must be well chosen and should remain constant from scan to scan. Because each scan is a different shape, certain parameters which do not affect the final result must be adjusted to compensate for meaningful changes from scan to scan. Finally, these initial choices should be corrected using EXAFS fitting.

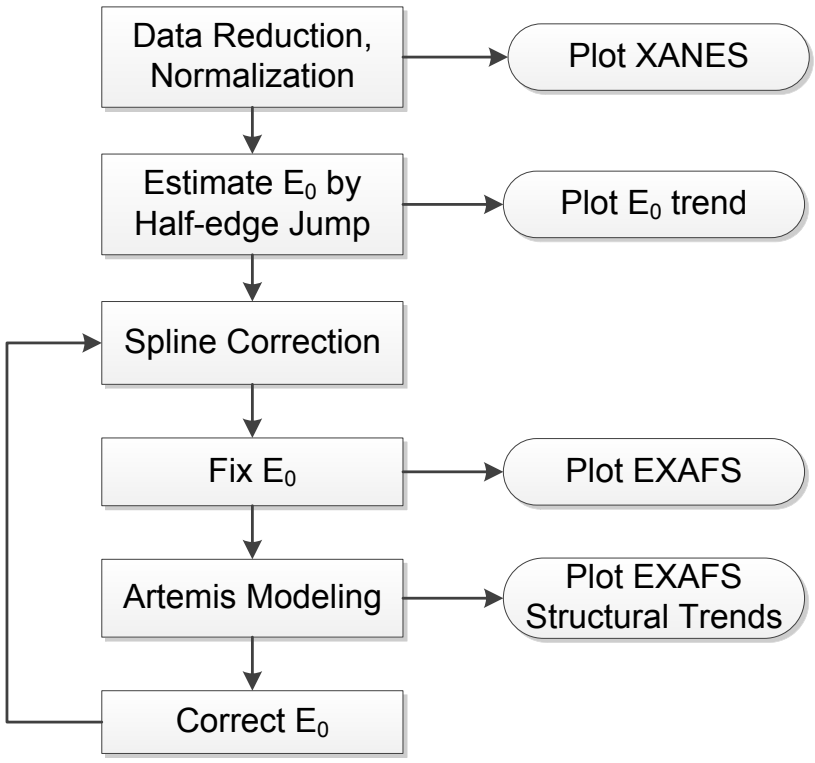

Figure 18: Flowchart of Procedures for Hard X-ray Data Reduction, XANES and EXAFS extraction, and the extraction of structural trends.

In Figure 18, a flowchart for data reduction is given. First the scans are inspected and normalized according to the streamlined procedures given in Section D.1, and the XANES region can be plotted. Second, as described in Section D.1.1, the E_0 parameter, which is the basis for background subtraction as well as the zero point for k-space plotting, is estimated as the point at which the absorption is 50% of the normalized intensity of each scan; a trend can be plotted to indicate redox trends. Third, the background subtraction spline range is adjusted to counteract the movement of the absorption edge to higher energies; the E_0 can then be set to a constant value and a consistent EXAFS dataset may be plotted. Fourth, the EXAFS data are fitted in k-space (see Section D.2) to extract structural shifts, peak height and width, and a correction to E_0. This correction to E_0 is then used to improve the background subtraction and the definition of k-space. Finally, structural trends can be extracted which depend only on structural changes and not on parameter adjustments.

3.4 Hard X-ray Transmission Pouch Cells

Pouch cells resemble ketchup packets and other food packaging and can easily be constructed from commercially-available food-service materials. European scientists refer to pouch cells as coffee-bag cells;[127] indeed, the pouch cell material is as thick as that used in coffee bean packaging. The material consists of three layers: an outer layer of non-heat-sealable polyethylene, a very thin layer of moisture-blocking aluminum, and an inner layer of heat-sealable polyethylene.

A working battery, unlike a ketchup packet, requires an electrical connection between the inside and outside of the pouch in spite of the need for moisture sealing. The best current collectors are very thin metal foils of 0.001" or lesser thickness with no roughness. Thicker foils create wicking edges while rough foils create a wicking surface, and both must be avoided.

Standard methods[17] were used to spray a cathode slurry, consisting of 10 wt% PVDF, 10 wt% acetylene black, and 80 wt% cathode powder dispersed in n-Methyl-2-pyrrolidone, onto 0.0005" thick aluminum foil. For hard X-ray transmission experiments, the composite electrode was cut to a large rectangular size (15 mm wide) in order to accept the wide, unfocussed X-ray beam at beamlines X11A and X10C which are approximately 10 mm wide and 1–3 mm tall. Because this rectangular beam tends to change shape as the X-ray wavelength varies from the Mn K-edge to the Ni K-edge (from a "smile" to a "frown" or vice versa), the electrode was 10 mm tall. The pouch cell construction process is detailed in Section B.1.

In an X-ray absorption experiment carried out in transmission mode, the intensity of the X-ray beam is measured before and after it passes through the sample, and again after passing through a reference sample. By dividing the intensity of the beam after the sample by the intensity of the beam before the sample, and taking the natural logarithm, variations in the intensity of the beam over time and as a function of photon energy can be cancelled out. However, the packaging of an *in operando* cell will absorb X-rays in a way that varies with photon energy, and this cannot be accounted for in the same way. Provided that the packaging contains none of the materials to be studied, this variation should be smooth and can be accounted for during the normalization of the data. However, the total amount of absorption should be minimized so that the transmitted beam has sufficient intensity to be measured with an acceptable signal-to-noise ratio.

Table 9: Layered moisture barrier material manufactured bys Shield Pack, Inc.[128]

Material	Thickness	Formula	Density (g/cm^3)	Layers
Aluminum Interlayer	8.9 μm	Al	2.7	2
Polyethylene Terephthalate	12 μm	$C_{10}H_8O_4$	1.4	2
Polyethylene	25 μm	CH_2	0.9	2
Polyethylene	53 μm	CH_2	0.9	2
Aluminum Foil	12.7 μm	Al	2.7	1

The X-ray absorption of each material depends on the path length of the beam through the material, its density, and its composition. By using the Filter Transmission program developed by Gullickson et al.,[96] the total absorption can be estimated. (Fine structure is not included in this calculation.) Table 9 below lists the thickness and density of the moisture barrier material obtained by Shield Pack, Inc.[128] which was used to create pouch cells for this study. Because the beam passes through the pouch cell material twice, two layers were included. Although the moisture-blocking aluminum layers are dense, they are also thin. In contrast, the polymer layers are much thicker, although they are less dense. The calculated absorption of these materials, as well as the lithium anode, but not including the cathode material or cathode current collector, is given in Figure 19. Although the absorption of X-rays at the Mn K-edge was greater than 50%, the signal-to-noise ratio was nonetheless more than acceptable for this study. Over the range from the Mn K-edge to the Ni K-edge, the X-ray absorption of the pouch cell material is a smoothly-varying function of photon energy that does not interfere with data normalization. Remarkably, the very thick lithium foil anode is estimated to have absorbed a negligible amount of X-ray intensity.

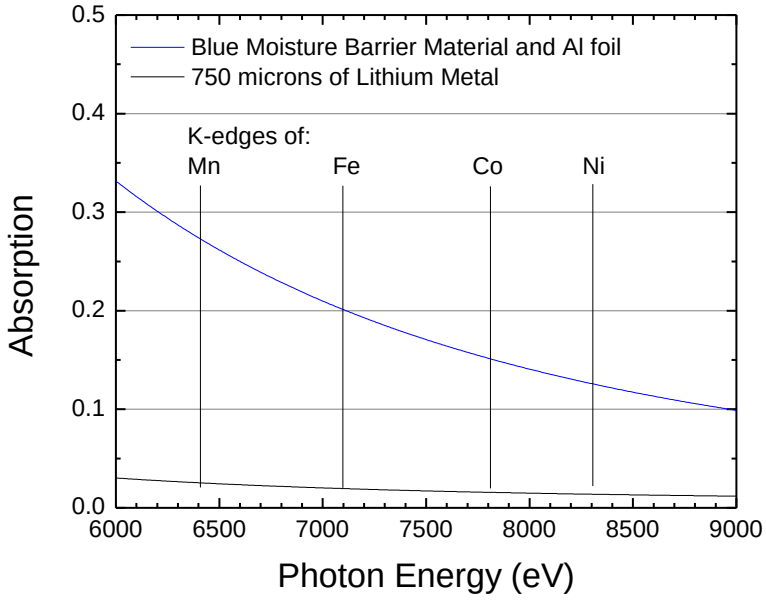

Figure 19: Calculated[96] absorption of a pouch cell, excluding liquid electrolyte and cathode

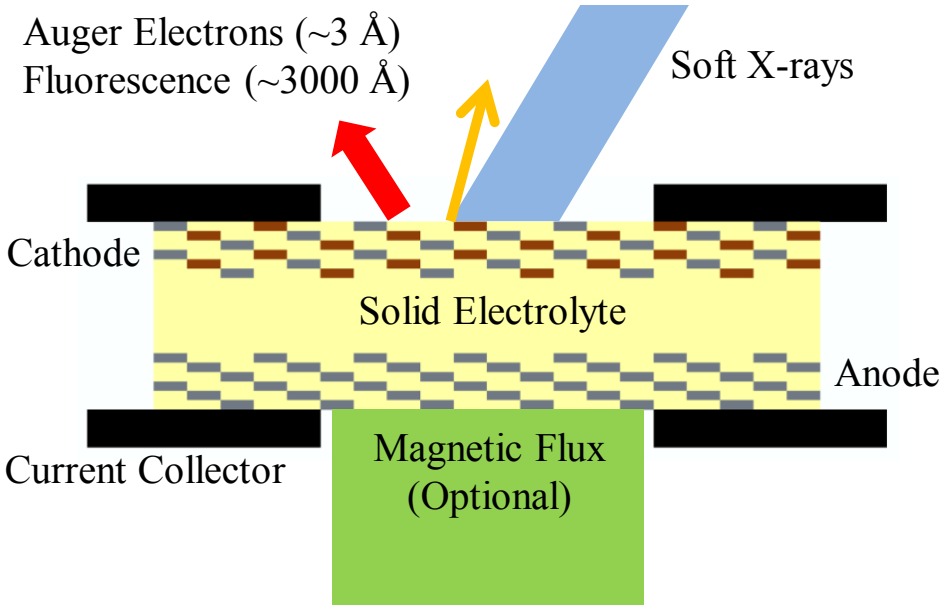

Figure 20: Schematic of soft X-ray *in operando* cell, including solid electrolyte layer and composite anode and cathode in which the solid electrolyte is a continuous matrix phase and provides for cathode-vacuum and anode-vacuum interfaces, mounted between nonmagnetic perforated plates

3.5 Soft X-ray Pellet Battery Methods

Before *in operando* soft X-ray experiments could proceed, it was necessary to adapt the technology of sulfide-electrolyte batteries to operate well in a vacuum chamber by creating a free-standing battery. Whereas early solid state batteries described in the literature[129] used an indium foil or lithium metal foil as the anode, it was found necessary to use a composite anode for two reasons. Firstly, lithium metal has a high vapor pressure and its use is discouraged in vacuum chambers. (At high temperatures it could quickly coat the inside the of chamber with lithium.) Secondly, solid state batteries have a tendency to form dendrites when charged at high current levels. Although improvements in the conductivity of the electrolyte diminishes the tendency to form dendrites, composite graphite anodes were found to be highly effective in preventing dendrites from forming due the thermodynamic tendency for lithium ions to intercalate into graphite rather than form lithium metal.

In this section, the optimization of the electrolyte, the anode, and of the cathode are discussed. Finally, SEM investigations reveal the spatial distribution of graphite, solid electrolyte, and active material in the electrodes.

3.5.1 Pelletization Method

Although prior researchers have studied solid state pellet batteries in detail[130] and obtained patents on the topic,[131] the process of producing the three-layer pellet shown in Figure 20 is conspicuously absent from published work. The process developed at Georgia Institute of Technology is described step-by-step in section B.2.3. In contrast to methods used for solid oxide fuel cells (SOFCs) developed in Prof. Meilin Liu's group[132] at Georgia Institute of Technology, it was not possible to prepress multiple pellets and then join them by pressing because the springback of the sulfide electrolyte was too great. Using a 12.7 mm die set, the resulting pellets were consistently 12.82 mm, preventing their reinsertion into the die set. Instead, an elegant slurry method was developed which created a three-layer pellet in a single pressing step using a single die set. Heat-curing steps are not required.

In an early method of this type, a tamping process was employed in which each layer was added to the die and subsequently pre-pressed by the upper punch of the die set. Pressure was applied while rotating the punch to create even layers. This method was found to be limited to powder charges larger than 30 mg (for electrodes) distributed over a $1/2$" anvil; smaller charges would not form a continuous layer. This is disadvantageous because in cathode layers, a thicker layer creates more resistance and adds more capacity to the battery, lengthening the time to charge a cell. Larger powder charges would form a smooth deposit after rotating the punch, but two problems appeared. Firstly, if tamping was applied both to the electrode and also to the electrolyte layer above it, the two layers would tend to mix, likely leading to a shorted pellet. Secondly, composite cathode mixtures containing significant volume percentages of graphite would take on a smeared appearance after the punch was rotated. This suggested that graphite in the mixture was spreading across the interface with the electrolyte layer. Indeed, in cyclic voltammetry on two cathode half cells constructed in this way, the intensity of the total current through the cell was found to be much less in the case of 20 vol% graphite than it was in the case of 8 vol% graphite. Correspondingly, an anode half cell constructed in this way was found to be greatly inferior in current handling compared to an anode half cell constructed using the slurry method. It was concluded that the tamping method is incompatible with the use of graphite as a conductive additive.

In the slurry method, a mixture of sulfide electrolyte, graphite, and active material (or electrolyte and graphite for the anode) was combined with ultra-dry hexane to form a thick suspension of particles. Although this mixture required periodic agitation to prevent settling of the particles, the suspension could be successfully pipetted onto the pressing anvils before settling occured. By performing this slurry deposition procedure on a sensitive balance, the mass of the electrodes could be measured directly and precisely after the evaporation of the hexane. Slurries cast in this way onto the anvils had three further advantages. Firstly, the dried deposit formed a meniscus shape on the stainless steel anvil. Secondly, and crucially, the dried deposit adhered strongly to the polished anvil, making it possible to invert the anvil and insert it into the die set. Thirdly, the mixture of electrolyte, graphite, and active material was well-mixed at the micron scale. These three advantages are evident in the cross-section micrographs of Section 3.5.5.

To assemble a full cell, the cathode composite anvil was inserted into the die set, followed by the solid electrolyte powder charge. The entire die set was then tapped vertically against the glovebox floor to even out the powder charge. The anode composite anvil was then carefully inverted and added to the die set. Pressing was performed gradually as described in Section B.2.3. Upon ejection, defects were common in the circumference of the top electrode, but absent in the bottom electrode. (Although ring-type delamination from residual stresses is expected in the first pellet surface to exit the die set, the opposite trend was observed.) To ensure an accurate measurement of the mass of the cathode composite electrode, the cathode composite anvil was always inserted in the bottom of the die set.

3.5.2 Sulfide Electrolyte Optimization

In powder compact batteries, the mode of ionic conduction is of interest in determining the optimal microstructure. Although the heat treatment of the material has been well studied,[130] it is not clear whether the conductivity is grain-boundary dominated or bulk-dominated. The conductivity can depend on interstitial ions or on the presence of vacancies. In the case of yttria-stabilized zirconia, both the grain size and the partial pressure of oxygen can alter the apparent conductivity. However, in an uncrystallized sulfide glass, there are neither interstitial sites nor crystalline vacancies and furthermore, sulfur is not gaseous at room temperature and so it is difficult to evaporate sulfide ions

out of the material. Ultimately though, if a sulfide glass powder pellet is not fully dense, there is some surface area on which ions may travel. It is interesting to determine whether the conductivity scales linearly with apparent density.

A tightly intertwined issue is the effect of heat treatment. In this material system, the rate of sintering and the rate of crystallization both rise dramatically just above the glass transition. According to DSC, the T_g is approximately 170°C; sintering and crystallization are both slow at 180°C and are both faster at 190°C. To separate the two effects one can heat the powder to 190°C for approximately 10 h, and then deagglomerate the powder before pressing a pellet. Section 3.5.2.2 discusses how total conductivity (with Li foil contacts) depends on heat treatment temperature given heat treatment times of 5 h, 10h, and 15 h, respectively. The surprising result is that while conductivity is enhanced at 260°C, the enhancement is less than the enhancement at 200°C for the same heat treatment time. Also, at the low temperature of 190°C, the conductivity is highest after a 10 h heat treatment, rather than after a 15 h heat treatment. This suggests either that the chemical stochiometry of the material changes due to evaporation, or that over-crystallization can be harmful to the material even when sintering is prevented. Because the weight loss on heat treatment seems to be constant versus temperature, it can be deduced that the loss of ionic conductivity with time at higher temperatures is due to a change in microstructure. This change in microstructure could be coarsening which could lead to the loss of grain boundary area, or could be a completion of crystallization which eliminates glassy regions between crystalline grains. Either explanation, if true, would suggest that the crystals themselves are of lower conductivity and yet that the conductivity of the sulfide glass is enhanced by their presence. The crystallization process could alter the glass composition or bonding arrangement in a way that increases molar volume.

3.5.2.1 Characterization of Amorphized Solid Electrolyte

In agreement with the pioneering work of Prof. Hayashi,[61] ball milling according to the methods detailed in Appendix B yielded a totally amorphous sulfide glass, as demonstrated by the X-ray diffractogram given in Figure 21. The results given in this figure are exceptional in that no trace of the Li_2S peak at ~45° 2θ. Although this level of amorphization is not required to obtain high

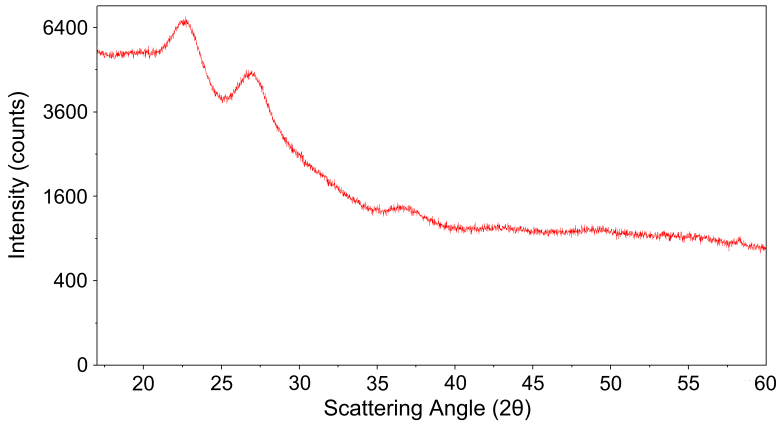

Figure 21: X-ray Diffractogram for Amorphized $70Li_2S{\cdot}30P_2S_5$

conductivity, the effectiveness of the ball milling process is demonstrated. The glass transition temperature T_g is shown as a negative sloping region above 180°C while the crystallization temperature T_x is found to extend from 240°C to a peak at 260°C, given a ramp rate of 10°C/min. Further DSC studies showed little variation in T_g, although the crystallization temperature could be reduced greatly by heat treatment near T_g.

3.5.2.2 Pre-Pressing Heat Treatment

The crystallization of the sulfide glass was investigated over a wide range of temperatures using fixed heat-treatment times. Related studies by Minami et al.[130] in Prof. Hayashi's group were limited to temperatures of 200°C and higher; this range was extended down to 170°C. In Minami et al., sophisticated DSC techniques were used to generate a two-step heat treatment which optimized the nucleation and crystallization of the glass in order to maximize the conductivity. It was undertaken to develop a simpler method, however, which consisted of heat treatments of loose powder for a fixed time. Although results superior to those of Minami et al. were not obtained, a mysterious trend was discovered. In Figure 23, AC conductivities (using non-blocking Li-metal electrodes) are given for pre-pressing heat treatment times of 5 h, 10 h, and 15 h. From the 5 h heat treatment data, in blue diamonds, a clear change is seen just above 190°C. In the 10 h data series, in red squares, the change is seen above 180°C. Although the 10 h heat treatments generated superior conductivity at lower temperatures, this was not the case at 200°C. Furthermore, the data point at 15 h (green triangle) yielded somewhat lower conductivity compared to the 10 h heat treatment. More strange

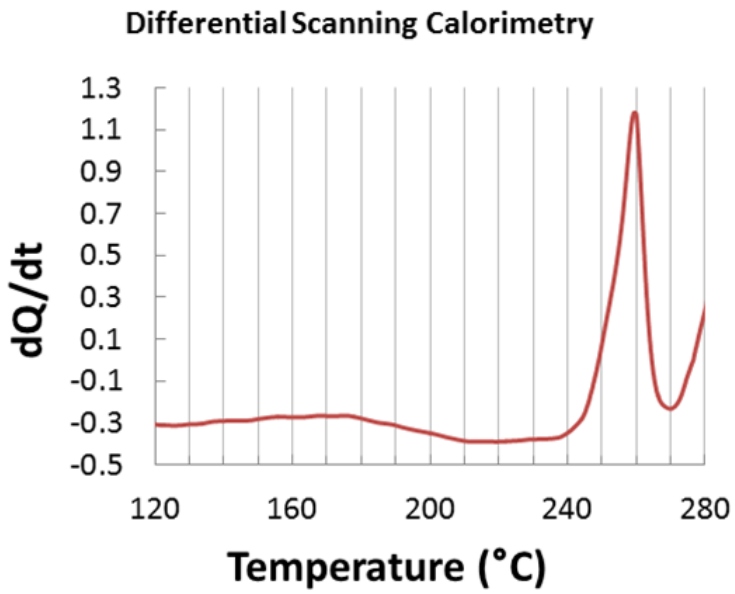

Figure 22: Differential Scanning Calorimetry for $70Li_2S{\cdot}30P_2S_5$

is the trend in the 5 h data series above 200°C, which clearly shows that heat treatments at higher temperatures are less effective than heat treatments near T_g. From a practical perspective, it can be concluded that heat treatments near the T_g are desireable. However, no theory provided by Minami et al.[130] could explain a detrimental effect of excessive heat treatment. If the cause were grain growth, it would suggest a grain boundary conduction mechanism in the material. If the cause were to be determined as over-crystallization, it would suggest that a bulk conduction mechanism based on a continuous glassy phase is dominant. These results suggested further study using Raman techniques in the next Subsection as well as the *in operando* heat treatment experiments in the next Chapter.

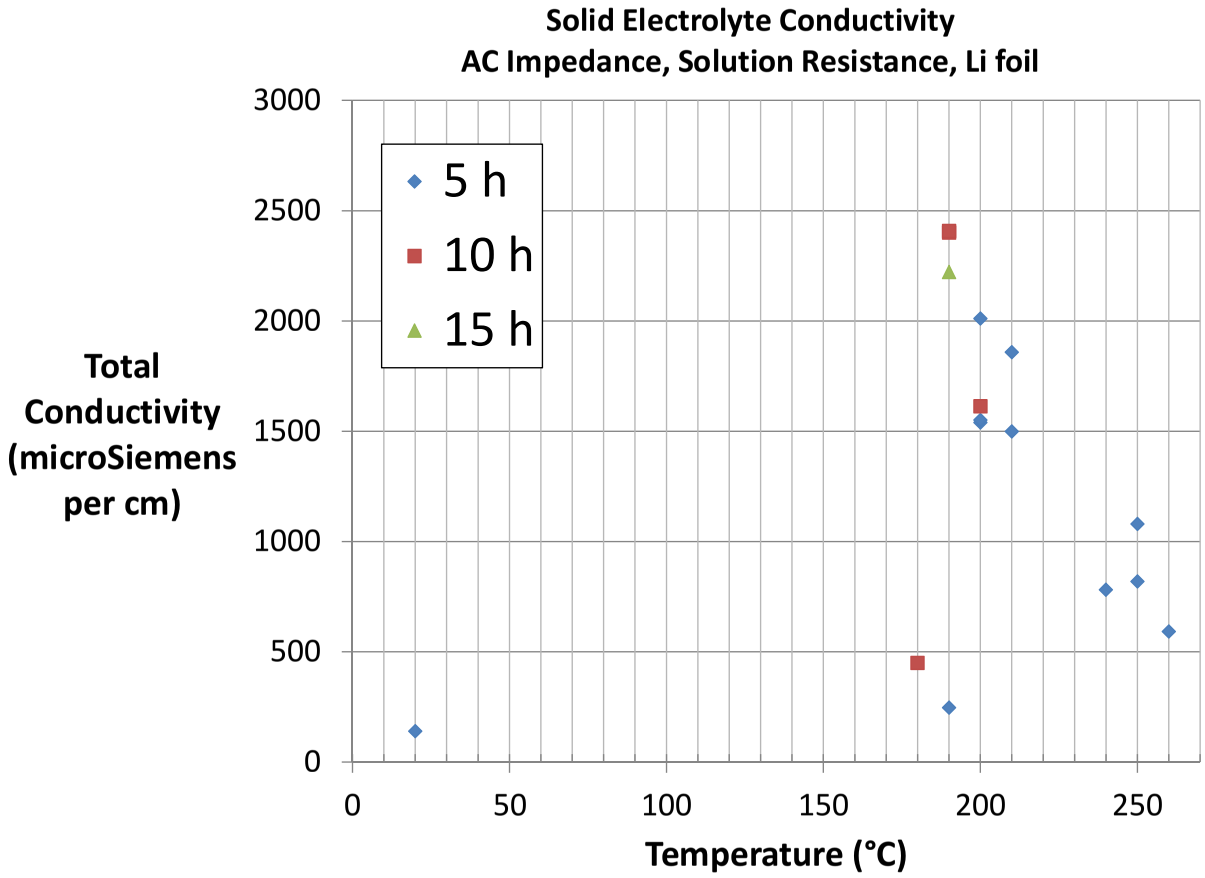

Figure 23: AC Conductivity for $70Li_2S{\cdot}30P_2S_5$ vs. Heat Treatment Temperature

3.5.3 Anode Optimization

For research purposes, a lithium metal anode is ideal because it establishes a reference potential for the lithium ion. In fact, in contrast with aqueous electrochemistry which uses a cornucopia of reference electrodes, in three-electrode lithium-ion cells both the counterelectrode and reference electrode are made from lithium foil, lithium paste, or lithium metal plated onto nickel because a superior reference electrode has not been established.[133] Ideally, lithium ions diffuse through a surface-electrolyte interphase which forms from the spontaneous reduction of solvent molecules and join the underlying lithium metal. In reality, as lithium metal is deposited on lithium metal, solid deposits form at the least-resistive points on the surface, which are usually pointed asperities which have previously broken through the surface-electrolyte interphase. This leads to the formation of dendrites which may short out the battery. Therefore, in commercial batteries, lithium metal anodes are only used in nonrechargeable cells.

In powder-compact batteries, the surface-electrolyte interphase never forms because no solvent is present. Worse, the porosity of the pellet allows lithium dendrites to grow to millimeter lengths, completely shorting the sample. The dendrites thus formed are visible as a gray tinge on the opposite surface of the cell; they can be confirmed as metallic dendrites by their very high conductivity which can be measured using two-point probe measurements.

A completely nonporous pellet[130] may physically block dendrites using the strategy used by Prof. Balsara to block dendrites in polymer electrolytes,[134] but nonporous pellets were found to be difficult to fabricate. Instead, a graphite electrode was employed due to its low thermodynamic potential for intercalated lithium ions. In half cells, graphite electrodes exhibited a potential just above 2.0 V vs Li/Li^+ across a wide range of graphite loading levels. As is the case for liquid-electrolyte batteries, the first intercalation cycle permanently reduces this potential, i.e., subsequent delithiation would not cause the potential to return to 2.0 V. Due to this initial potential, full cells could exhibit a negative potential before charging began.

Two types of conductive additives were tested over a variety of loadings: natural graphite and acetylene black. Although it was possible to press an anode using 100% graphite powder, better powder compacts were formed at 60 wt% or less of graphite. In the case of acetylene black,

however, it was difficult to create an adherent layer with enough acetylene black powder to ensure conductivity. The use of acetylene black was abandoned.

3.5.3.1 Ex Situ *EIS of Anode Half Cells*

The composite anode mixture, in terms of mass percentages of graphite and electrolyte powder, was optimized through electrochemical tests on a range of half cells. The cell structure included a composite anode layer, a solid electrolyte layer, and a circular foil of lithium metal. The range of compositions included 100%, 60%, 40%, 32%, and 16 wt% graphite, 32% being the optimal choice. These results were presented at the 220th Meeting of the Electrochemical Society in Boston, MA[135] in 2011. The electrochemical results were suboptimal because although the electrolyte was well-amorphized, it was not heat treated as described in the previous Section.

Objectives Solid state batteries are useful for *in situ* experiments utilizing both photon and electron probes. Neither XPS nor SEM can be performed *in situ* on a battery with a liquid electrolyte. Furthermore, thin film batteries typically require a metal current collector which covers the thin film cathode material. A powder compact battery, then, which mixes a solid electrolyte with an intercalation material and a conductive additive, can enable new types of experiments.

Similar to XPS, soft X-ray NEXAFS (near-edge X-ray absorption fine structure) utilizes a non-penetrating x-ray beam to investigate the electronic structure of solid materials. Soft X-rays are extremely sensitive to the 3d orbital occupation of transition metals as well as to the charge on oxygen.[136] Performing this experiment *in situ* allows the determination of the oxidation state of the nickel, manganese, cobalt, and oxygen in a lithium intercalation cathode to be measured smoothly as a function of lithium content. However, the cathode surface of the solid state battery must delithiate smoothly and fully in spite of the spectroscopic hole in the current collector which allows X-rays and/or electrons through. Typically, the anode of a full cell has no window. The challenge here is to optimize the rate of intercalation of lithium into graphite by maximizing the interfacial area without losing electrical connectivity between graphite particles, e.g., by using less than 16 wt% graphite.

Method Electrochemical impedance spectroscopy (EIS)is a proven technique for the determination of solution resistance, charge transfer resistance, double layer capacitances, and for determining

the type of diffusion occurring at electrodes.

Usually, a high-performance lithium ion battery requires fast diffusion in one dimension while current collectors on each side of the cell distribute electrical charge evenly in two dimensions. A powder compact battery designed for spectroscopy at the bare electrode surfaces, however, must have an electrically conductive network embedded into the cell. Simultaneously, an ionic conducting network of electrolyte particles must allow lithium ions to diffuse out of the full thickness of the cathode. The anode must then receive the lithium ions at a rate sufficient to prevent the growth of lithium metal dendrites.

Results

Electrochemical Impedance Spectroscopy Low-frequency impedance measurements were performed on full cells comprising a composite anode made from a graphite-electrolyte mixture, solid electrolyte, and a composite cathode made from graphite, electrolyte, and an overlithiated lithium nickel manganese oxide. In addition, impedance was performed on anode half cells comprising a graphite-electrolyte mixture, solid electrolyte, and lithium metal. Figure 24 gives electrochemical impedance spectra for three anode half-cells, at a DC bias of 500 mV vs Li/Li^+. As the volume percentage of graphite is varied, the interfacial resistance is minimized at 32 wt% graphite. Also, the low-frequency tail of the spectra also vary with graphite loading. At 100% graphite loading, a 45° slope indicates Warburg diffusion in which case the lithium ion diffuses into an effectively "infinite" electrode; this suggests long diffusion paths and large (effective) particle sizes. However, at 32 vol% graphite there is a slight change in slope at ~4Hz indicating that on sufficiently long time scales, the electrode is not "infinite". At 16 wt% the low frequency spectrum has a slope of less than 45° along with a curved region, which indicates a finite diffusion case along with a non-diffusive resistance in parallel with diffusion. These results suggest that at 16 wt%, the ionic network is very "open", containing much surface area and giving rise to higher capacitance. Fitting results are given in Figure 27.

Windowless solid state batteries face the unique requirement that the absence of a current collector in the open "window" should not electrically isolate the cathode material in that area. Therefore,

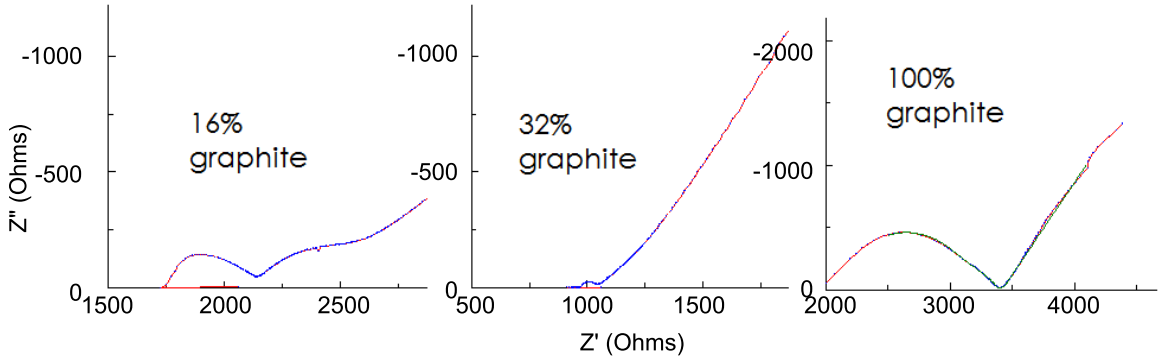

Figure 24: Nyquist plots for anode half cells produced with three different weight percentages of graphite

an impedance spectrum taken with a windowed current collector should differ minimally from a spectrum taken with a non-windowed current collector. Full cells made with 4 wt% and 8 wt% graphite additive showed greater solution resistance and decreased double layer capacitance when a windowed current collector was used, indicating that some of the cathode was isolated. At 16 wt% graphite additive, however, the equivalent circuit parameters stayed within a few percent, indicating that electrical conductivity across the exposed surface of the pellet was achieved. Soft x-ray NEXAFS showed that the lithium nickel manganese oxide was not obscured by graphite or electrolyte.

Cyclic Voltammetry Although impedance results are valuable in optimizing a battery, the cell must also support direct current. Cyclic voltammograms at 400 $\mu V/s$ are given in Figure 25. Here, negative current indicates lithiation of the graphite anode while positive current indicates delithiation. Additionally, the delithiation peak between 2 V and 3 V may indicate a limited reaction in which the solid electrolyte is partly delithiated at the electrolyte/graphite interface. The graph for 32 wt% graphite is limited to $\pm$ 100 μA by the Arbin BT2000 potentiostat, which does not include an auto-range function. Results for 16 wt% graphite were similar to those for 40 wt% graphite.

Full lithiation of the graphite layer is evidenced in Figure 26 below. The iridescent golden color, as opposed to the light yellow color of the sulfide electrolyte, is indicative of LiC_6.[64] This compound represents graphite saturated with lithium. Although the cell in the figure was not charged using a windowed cell, in principle the same result would be obtained with a windowed cell due to the electronic conductivity of the composite layer. Future Raman and XRD studies on graphite

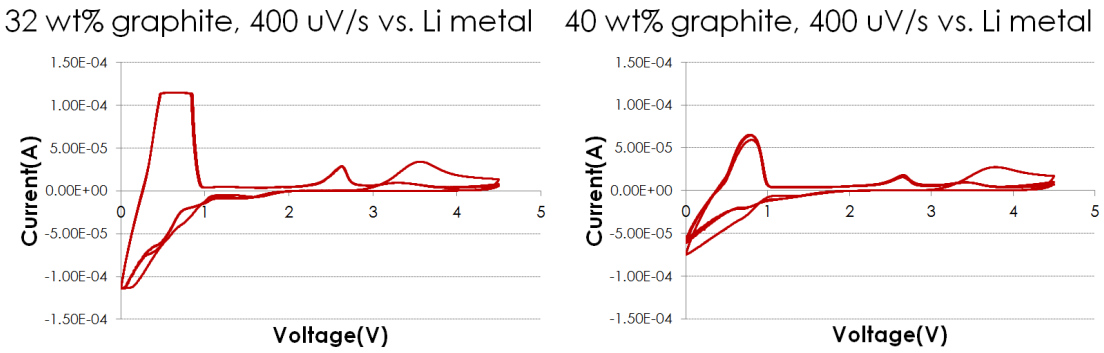

Figure 25: Cyclic voltammetry on anode half cells at two levels of graphite concentration

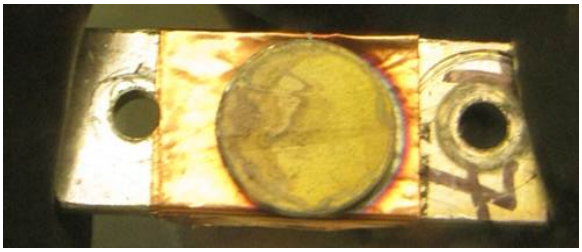

Figure 26: Formation of LiC_6 in composite graphite anode due to electrochemical lithiation

lithiation should be performed on this system because, in the absence of liquid electrolyte, no Solid Electrolyte Interphase forms on the graphite surface.

Conclusions By substituting electrolyte powder for graphite powder in the anode, the interfacial surface area is increased, and the impedance behavior of the cell is enhanced. Electrochemical impedance spectroscopy at both high and low frequencies is an excellent tool for optimizing the interfacial characteristics of solid state batteries. The optimization of powder compact batteries will enable *in situ* XPS, *in situ* SEM, and *in situ* surface-sensitive synchrotron studies with soft X-rays which are impossible using thin film batteries. Composite anodes with 32 wt% graphite have superior interfacial resistance and a relatively low Warburg time constant for diffusion. Although the 16 wt% composition is promising, such low loadings are better suited to be conductive additives for composite cathode layers.

Summary of EIS parameters

wt%	C_{int} (F)	R_{CT} (Ω)	W_o (Ω)	τ (s)	R_{BIS} (Ω)	C_{BIS} (F)
16	$1.9x10^{-9}$	300	10803	11	850	$1.5x10^{-4}$
24	$1.5x10^{-9}$	360	483	0.06	194	$1.3x10^{-6}$
32	$2.5x10^{-8}$	50	700	0.25	0	$2x10^{-4}$
40	$6.7x10^{-10}$	483	$2.1x10^{4}$	43	300	$1.7x10^{-4}$
60	$1.1x10^{-9}$	415	$2.3x10^{5}$	559	700	$2.5x10^{-6}$
100	$6.7x10^{-10}$	812	$1.7x10^{6}$	(inf)	300	$1.3x10^{-6}$

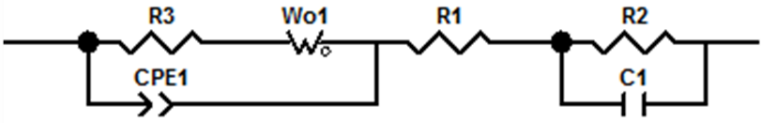

Figure 27: EIS Model incorporating Bisquert Element and Fitting Results

3.5.4 Cathode Optimization

Ideally, a lithium-ion cathode would consist of a solid single crystal or multicrystalline thin film of $LiCoO_2$ oriented with the high-ionic conductivity plane perpendicular to the surface. Most cathode materials, however, are semiconductors with low conductivity for either electrons or holes. This low conductivity, in conjunction with low lithium-ion diffusion coefficients, requires the use of finely divided cathode powders. (Micron-scale particles are common, although nanoscale particles may have higher performance.) In commercial batteries, carbon coating or acetylene black, is used as a conductive additive to create a conductive network in the cathode layer. When liquid electrolytes are used, the surface tension of the electrolyte causes it to thoroughly coat the exposed surfaces and enable ion transfer. In a powder-compact battery, the design is similar but the cathode-electrolyte interface must be created manually.

A wide variety of composite anode and cathode compositions were tried and are summarized in Figure 28. This ternary diagram gives composite cathode compositions in terms of volume percentages; at any point on the diagram, the composition adds to unity and porosity is not included.

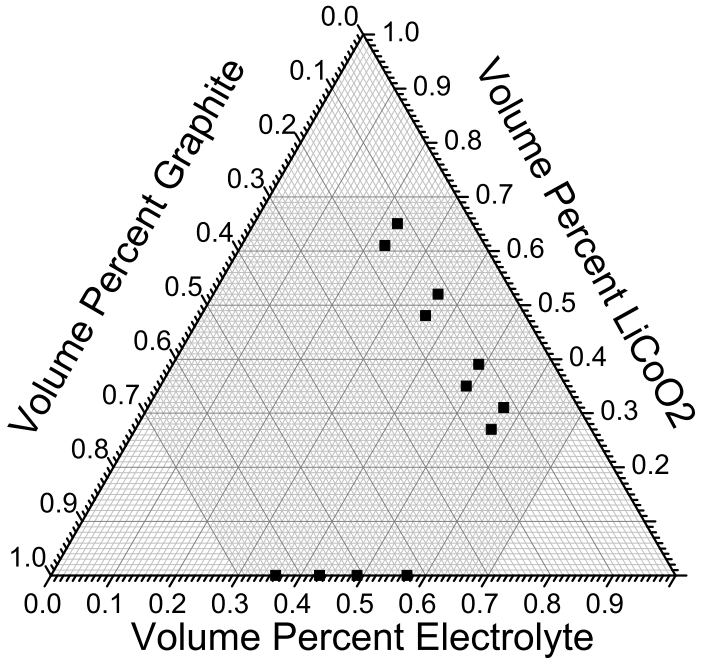

Figure 28: Ternary diagram of investigated composite electrodes

At the extremes of the diagram are pure solid electrolyte, pure graphite, and pure $LiCoO_2$ or other active material. Although pure solid electrolyte easily forms a powder compact, pure graphite anode compositions had a tendency to fracture, leaving adherent fragments of graphite attached to a solid electrolyte pellet. Electrode compositions with greater than 30 vol% $LiCoO_2$ could not be consolidated by pressing. Additionally, compositions with high levels of graphite or active material tended not to form a viscous slurry with hexane. Along the bottom of Figure 29 are the graphite-electrolyte mixtures used as anodes in the previous Section, with the mass percentages recalculated as volume percentages. In improving composite electrode compositions, both anodes and cathodes tended towards higher levels of solid electrolyte.

The key to *in operando* soft X-ray spectroscopy is the design of a composite cathode layer that simultaneously presents the active material to the exterior surface while maintaining contact with the solid electrolyte and maintaining electrical continuity using conductive additives. To that end, two conductive 3D networks must be created: one for lithium ions and one for conductive additive particles. Furthermore, the conductive additive network must not block the conduction of lithium ions. These two networks must both connect to cathode particles over a short length scale, i.e., conductive

particles should form a tight web without excessively long chains and without completely surrounding any cathode particles. A cathode particle surrounded with electrolyte particles is electrically isolated, and a cathode particle surrounded by graphite particles will have a low-ionic-conductivity path for lithium ion diffusion.

According to percolation theory, for randomly packed hard spheres of two different species, the continuous phase must represent approximately 30% of the volume of the material. (Platelike or acicular materials can potentially comprise less than 30% of the volume while maintaining a continuous network.) In a three-component network of electrolyte, conductive additive, and active material, however, the system can be simplified into two groups: ion-conducting electrolyte and electron-conducting active material and conductive additive. The guiding principle in ensuring ionic conductivity is the determination of an optimal volume percentage of solid electrolyte. Via anode studies, it was found that 32 wt% graphite yielded excellent overall results. For cathode mixtures, however, a greater proportion of electrolyte was advantageous. It was concluded that at least 66 vol% of electrolyte was required to provide good performance.

Simultaneously, electronic conductivity across the pellet, and through the thick composite electrodes, was provided by graphite powder. A volume percentage of at least 16% graphite was required to achieve a quick response in current pulse testing, while volume percentages above 24% were found to be highly detrimental. The volume percentage of active material, necessarily, formed the remainder of the composite cathode layer but, even at high loadings but without graphite additives, it contributed no measureable electronic conductivity. For spectroscopic purposes, 10 vol% of active material was found to be quite low (see Section 4.2), leading to spectra of low intensity. Because the soft X-ray beam size was focused down to 1 mm^2, and not to 1 μm^2, much of the signal was derived from the solid electrolyte, which contained only a small amount of oxygen derived from minor moisture contamination.

The optimized cathode mixture used in Section 4.2 was 74:10:16, i.e., 74 vol% solid electrolyte, 10 vol% active material, and 16 vol% graphite. (These formulae assume literature values for the component densities, and zero porosity.) In future studies, the volume percentage of active material should be increased to 16 vol%. A target composition of 66:16:18 should be further developed, although the increase in active material will increase the battery capacity, thereby lengthening the

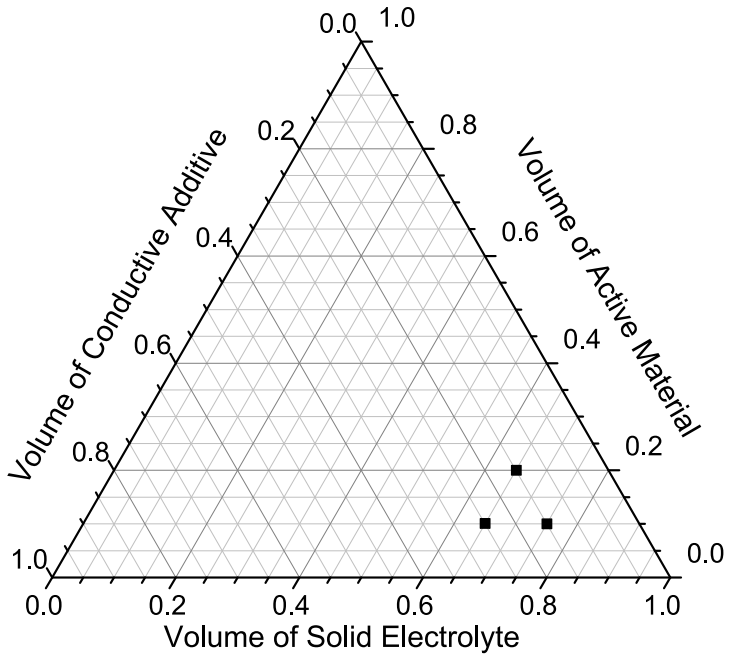

Figure 29: Ternary diagram of optimal composite cathodes

experiment. Further optimization of the composite cathode microstructure should be possible, and high temperature *in operando* studies will also shorten the experimental time.

In Figure 29 below, a ternary diagram is given for the composite cathode mixture. The optimal region for battery experiments is a triangle bounded by three points indicating 16–24 vol% graphite, 10–20 vol% active material, and 66–74% solid electrolyte. Optimization of the mixture will also require SEM studies in addition to that presented in the next Section. As seen in the next section, the morphology of the graphite is not spherical, and active material particle size is excessively large. Furthermore, helium pycnometric measurements of the true density of the solid electrolyte powder, and similar studies of the porosity of a pellet battery, will help optimize the accurate calculation of the mass and volume ratios.

3.5.5 Scanning Electron Microscopy

Scanning electron microscopy, especially when Energy Dispersive X-ray Spectroscopy is employed, can be seen as virtually the reverse of the NEXAFS process. Whereas in the SEM the high-energy electron beam creates soft X-ray fluorescence as well as secondary electrons and Auger electrons, in NEXAFS a soft X-ray beam generates Auger electrons as well as soft X-ray fluorescence. The energy range spanned by the X-ray fluorescence in the SEM covers the energy range that would otherwise be covered by several beamlines at the synchrotron, albeit at lower intensity and much lower energy resolution. While in NEXAFS experiments on V_2O_5[137] the vanadium L-edge can be differentiated from the oxygen K-edge only a few electron-volts higher in energy, the same level of resolution is unthinkable in EDS because the fluorescence peaks are hundreds of electron-volts in width. Therefore, in practice, fine chemical shifts must be detected at synchrotron facilities and not in EDS-equipped SEMs. Instead, the superior spatial resolution of the SEM can be used to assess particle sizes and particle distribution.

A key problem in optimizing a solid state battery is ensuring an even distribution of active material and conductive additive across the surface of the pellet as well as through the cross section of the pellet. This distribution arises from the slurry deposition of the electrode on the stainless steel anvils. If, during the drying process, the relatively dense active material sinks toward the anvil, the active material will appear on the outer surface of the electrode while the lighter graphite will form a blocking layer at the interface with the electrolyte layer. In this Section it is shown that such a distribution did not arise; instead, the different types of particles are evenly distributed in both the cathode and anode layers. However, the loading of active material particles is very low and the active material particle size is quite large. Also shown in this Section is the distribution of particles across the surface of the cathode layer

A related problem is the necessity of a conductive network of graphite particles across the sample surface. While the conductivity of the network was separately tested using two-point probe measurements, the tendency of certain regions of the sample to accumulate charge was also gauged by SEM experiments. At an accelerating voltage of 10 kV, no charging was seen in SEM images

although at 20 kV a limited amount of charging was seen in very small regions.

Scanning Electron Microscopy (SEM) was chosen over optical microscopy for its ability to resolve the small particles used in solid state batteries and especially for its high depth of field. A potential drawback was its sensitivity to electrical charging at the surface which could be caused by a lack of conductivity in the electrode layers or by nonconductive dust from inside the glovebox. However, the high quality of the resulting micrographs proves that the electrode layers are conductive and that amount of dust was extremely low.

3.5.5.1 Ex Situ *SEM Experiments*

In the first SEM investigations using a Hitachi 4700 SEM, a solid state battery was mounted between metal plates in the same manner as at the synchrotron. As at the synchrotron, it was important to ground the top surface and not the bottom surface in order to prevent changes to the battery *in situ*. In principle, *in operando* SEM studies should be straightforward using this method. One of the two stainless steel screws, size #2, was inserted into a standard SEM stub hole and fixed in place by a set screw. This had the effect of grounding the top surface while a ceramic "hat" washer insulated the bottom plate, although unfortunately the (aluminum) inner surface of the stub hole was imprinted with the thread pattern of the screw, making removal difficult.

In subsequent tests using a Zeiss Ultra60 field-emission SEM, some of the same pellets were fractured in half and mounted on 90° angle stubs such that each pellet could be viewed in cross section as well as on the cathode surface. Grounding was achieved using double-sided carbon tape and single-sided copper tape. In this case both surfaces were grounded in spite of a small residual voltage.

The sample transfer method was very similar to that used for synchrotron studies. First, a sample mount for the specific SEM was obtained; for one brand of SEM, a bevel on the sample mount slid into a groove on the stage; for another brand the groove was on the mount, and the bevel was on the stage. In either case, a pin stub fit into the mount and thereby consumed part of the working distance inside the machine, leaving less space under the objective lens for the samples themselves. Worse, the sample mounts are extremely expensive to purchase and are highly in demand by other users. For that reason, only the especially bulky sample mounts were available for the experiments.

Once the sample mounts were introduced into the glovebox, the samples were attached via the pin stub hole and the assembly was packaged in a square-sided glass jar and sealed. The glass jar was removed from the glovebox, carried across campus, and placed inside a very large plastic bag. For the Hitachi 4700 which has a loadlock with a short transfer arm, the Sigma Aldrich Glovebag was used. For the Zeiss Ultra60, which has a loadlock with a long transfer arm, a plain (but enormous) polyethylene bag with no molded-in gloves was used. This bag was inflated with nitrogen while the Omega USB humidity gauge[1] monitored the humidity until the gauge read 0% humidity. (This level of humidity cannot be taken at face value because firstly, it is impossible and secondly, the gauge is only rated for accuracy down to 4% RH). When the humidity was reduced sufficiently, it was found that the Bakelite lid of the square-side glass jar was impossible to open while it was inside the slippery polyethylene bag. Ultimately, a very large rubber band was wrapped tightly around the lid to increase the level of friction. At that point, the sample mount was easily attached to the stage.

While the sample was inside the SEM, the humidity level in the bag increased only partially. In the final run, the edge of the bag was taped very tightly to the loadlock of the SEM and the relative humidity was maintained at single-digit percentages for many hours without nitrogen flow. After SEM investigations, the bag was easily reinflated and the entire process was reversed. Multiple SEM investigations of the same samples showed no ill effects on the sulfide material due to any moisture contamination from the sample transfer process.

3.5.5.2 SEM Micrographs

Two samples were imaged using the ZEISS Ultra60 field emission SEM. One full cell had been heat treated and partially charged at 180°C. Also, at the end of the soft X-ray *in operando* experiment described in section 4.2, the partly charged full cell was repackaged under dry conditions and shipped back to Georgia Institute of Technology for further SEM experiments. This cell had been constructed from heat-treated electrolyte powder but had not been heat treated after pressing. Figure 30 shows a low-magnification cross section of the heat-treated cell after it had been fractured in half. At the bottom of the figure is the carbon-rich anode, containing 24% by mass graphite powder.

[1] OM-EL-USB-RT communicates in real time via USB cable but requires Windows XP.

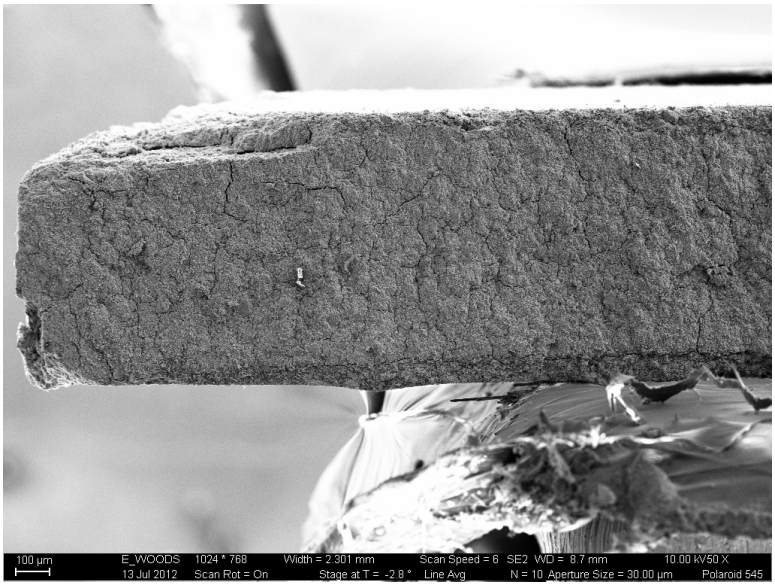

Figure 30: Low Magnification Cross Section of Heat-Treated Full Cell, 50X

The thickness of this layer can be seen to taper towards the edge. This is an effect of the slurry-based deposition process in which a hexane, graphite, and electrolyte slurry is added dropwise to a stainless steel anvil and allowed to dry. The lack of graphite at the edge of the pellet is a crucial advantage of the process because upon pellet ejection, graphite can otherwise smear along the edge of the cell, shorting it. At the top of the figure, however, the cathode layer is barely visible due to its much lower graphite loading.

The electrolyte layer of the non-heat-treated cell is shown at 2000X magnification in Figure 31. The sulfide electrolyte exhibits a variety of particle sizes including submicron particles and fused particles tens of microns across. The large particles likely formed during pellet pressing. In Figure 32, the same region is examined at 16,000X, revealing well-connected, smooth particles. In comparison with the electrolyte layer of the heat-treated cell shown in Figure 33, the heat-treated cell has similarly-sized small particles, although the small particles take on a rounder microstructure. This suggests that the small particles reached the glass transition temperature and deformed to reduce their surface area to volume ratio. At the bottom of Figure 33, the darker anode layer is seen to contain twisted flakes of graphite. Due to their low atomic mass, they appear darker in SEM micrographs.

In Figure 34, the twisted graphite flakes are seen protruding from between sulfide electrolyte

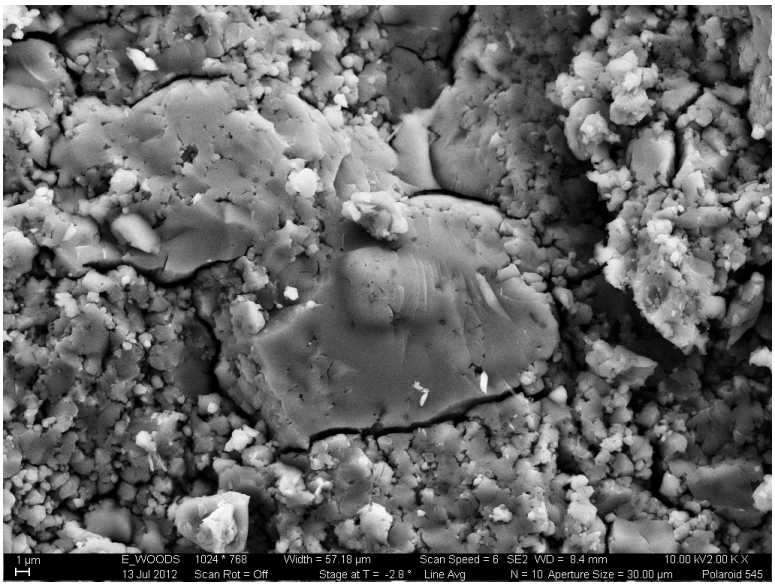

Figure 31: Medium Magnification Micrograph of Sulfide Electrolyte Layer, 2000X

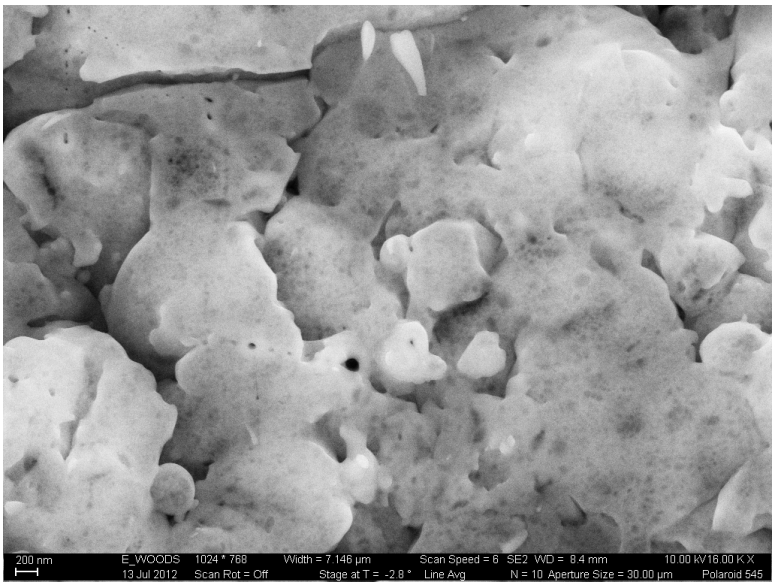

Figure 32: High Magnification Micrograph of Solid State Battery Anode, 16000X

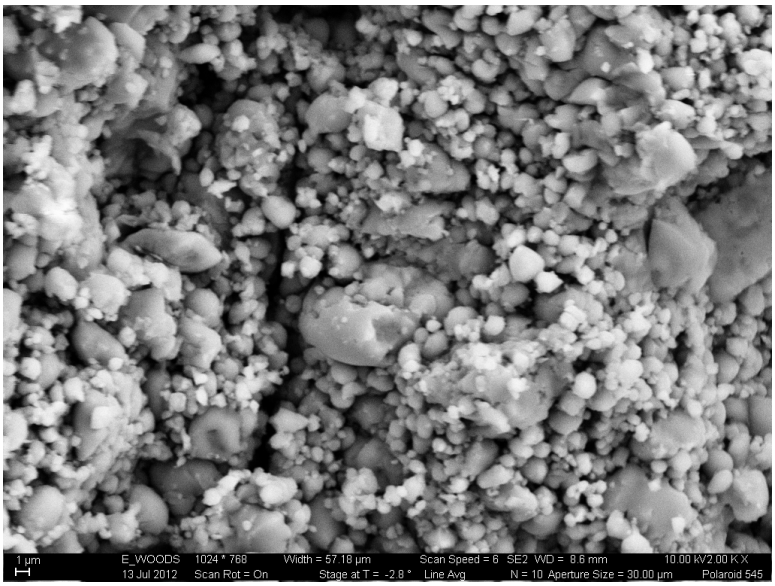

Figure 33: Medium Magnification Micrograph of Solid State Battery Anode, 2000X

particles. The 24% by mass loading of graphite particles appears to be sufficient to provide graphite-graphite contacts, yielding high electrical conductivity across the a pellet. The loading is not so high, however, to cause agglomeration of a graphite-only layer. The cathode layer shown at the top of Figure 35 (heat-treated full cell) shows the lower loading of graphite. This layer is 20–30 microns thick, as expected from density considerations. There is no evidence of particle segregation towards or away from the electrolyte layer. At medium magnification, only one particle of active material is identified at the top of Figure 36. This sol-gel-synthesized particle has a porous surface, is approximately 15 microns in diameter, and appears to be isolated. The loading of graphite is also low, limiting the electrical conductivity. For electrochemistry and for spectroscopy, a higher loading of smaller particles of active material is desirable.

3.5.5.3 EDS Elemental Maps

EDS mapping was performed at an accelerating voltage of 10 kV in order to obtain more surface sensitivity than that obtained at 20 kV. In either case, however, signals for sulfur and phosphorous were almost ubiquitous. Oxygen and carbon signals were also widespread, but were less intense. The 10 kV electron beam limited the spectral range for the fluorescence, however, meaning that the Mn K-edge, but not the Ni K-edge characteristic lines could be seen. The Mn L-edge and O K-edge, which are very widely spaced in NEXAFS studies, are indistinguishable in EDS spectra. In

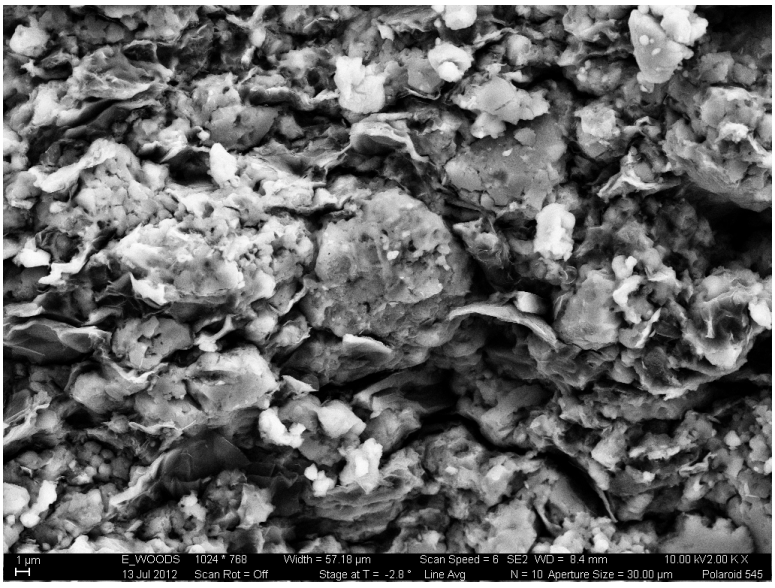

Figure 34: Medium Magnification Micrograph of Solid State Battery Anode, 2000X

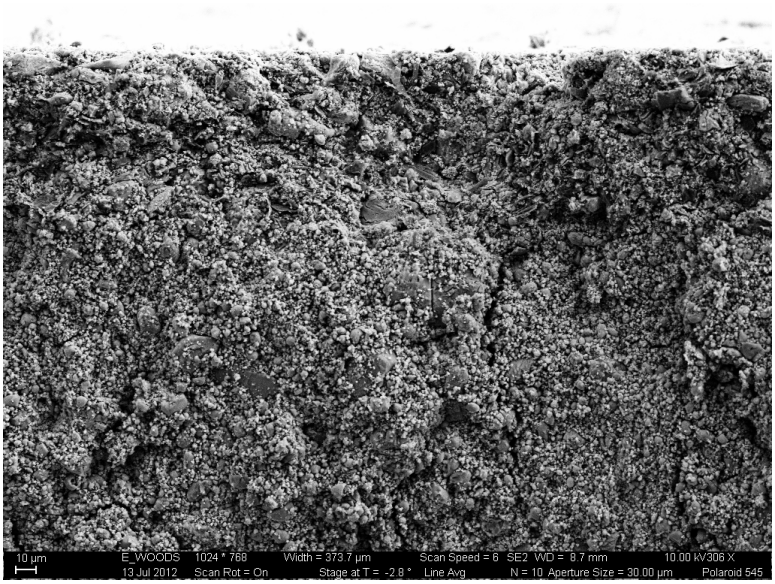

Figure 35: Low Magnification Micrograph of Solid State Battery Cathode, 306X

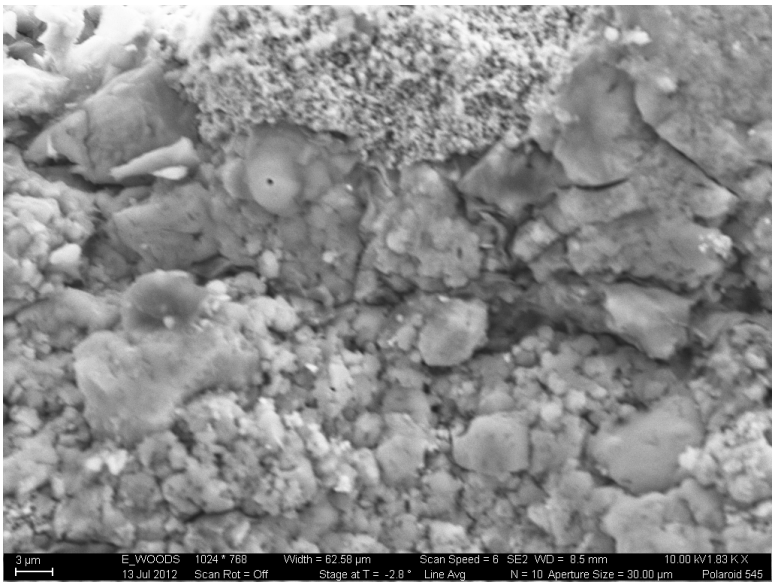

Figure 36: Medium Magnification Micrograph of Solid State Battery Cathode, 1830X

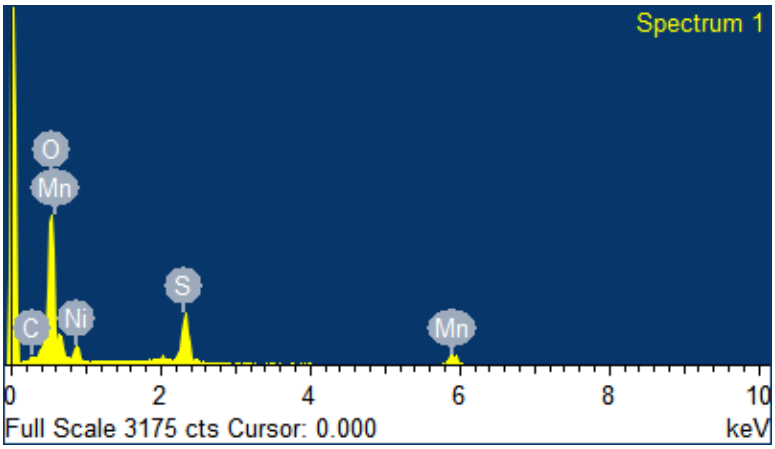

Figure 37: EDS Spectrum for Cathode Particle

Figure 37, an EDS spectrum taken from a spot on the large cathode particle in Figure 36 illustrates the presence of a low carbon signal, a large Mn L-edge signal overlapping the O K-edge, a small Ni L-edge signal, followed by a small S K-edge signal and a small Mn K-edge signal just below 6 keV. This peak is far lower in energy than the Mn K-edge absorption edge at 6539 eV; energy-loss processes within the electronic structure of the cathode particle account for the difference. The cross section for this signal is also low compared to the same peak under a 20 kV electron beam. However, this peak was essential in generating an EDS map (Figure 38) of Mn K-edge fluorescence across the region shown in section 36.

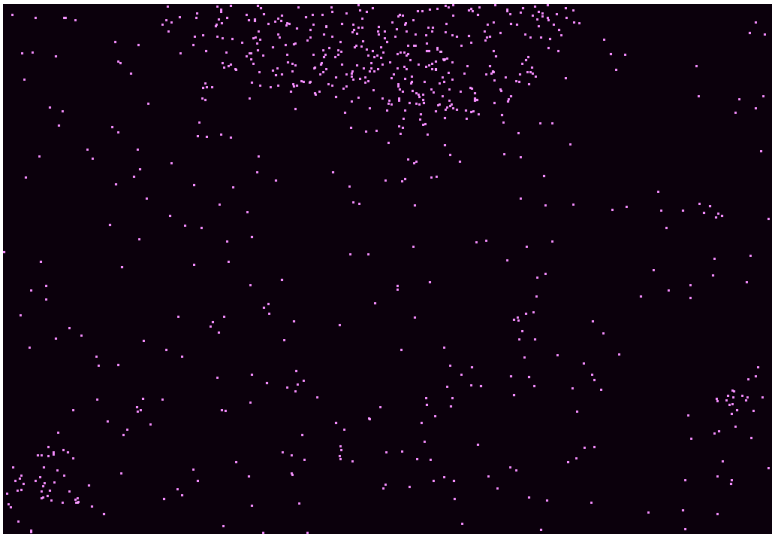

Figure 38: EDS map of Cathode Region, Mn K-edge Fluorescence

3.6 Soft X-ray In Operando *Sample Fixtures*

The soft X-ray *in operando* pellet battery (see 3.6.3) experiments leave the cathode and anode layers fully exposed to electrons and photons. This creates a second, photoelectric circuit which branches off of the battery circuit. It is important to ensure that the battery charging circuit does not provide current to the photoelectric circuit so that the spectroscopic results are unaffected. To that end, the exposed sample surface should be grounded in a way that is compatible with the potentiostat used for the experiment. Furthermore, ground loops involving the potentiostat should be tested for and avoided.

3.6.1 Electrical Considerations for *In Operando* Sample Fixtures

Circuit Laws Kirchhoff's Voltage Law states that around any circuit loop, the sum of the voltages is zero. Kirchhoff's related Current Law states that at any node of a circuit, the sum of currents flowing in and out of that junction sum to zero. Note that Kirchhoff's Current Law is not stated in terms of a loop of current, although it should be true that because charge can neither be created nor destroyed, the current around an *isolated* loop is the same at every point in the loop. The problem, typically, is identifying which loop of a larger circuit is carrying current.

Although currents and voltages are measured at nodes of a circuit, which are typically highly

conductive metal wires, the sample is typically less conductive. In resistive materials, electric or ionic current will spread out in all available directions; the current density will therefore drop to maintain the total level of current around the circuit. In thin film materials in which the contacts are deposited on top of the film to be measured, it is important to place the contacts such that current can only travel through the desired path. As discussed in in Section C.5, the current from one metal electrode to a second electrode may travel perpendicular to the desired direction into a third electrode. Current may also flow underneath one electrode to reach another electrode to complete the circuit. This can be prevented by careful separation of the external circuits.

The Photoelectric Effect When ultraviolet and vacuum ultraviolet (VUV) photons strike an atom, electrons are given enough kinetic energy to either move to a less-tightly-bound orbital or to leave the atom altogether. In most cases, an escaping electron reflects off of neighboring atoms and is reincorporated into the original absorbing atom. This is the physical basis for XANES and EXAFS. If a high vacuum exists adjacent to the atom, however, the electron can leave the atom. To satisfy Kirchhoff's Current Law, the electron must return to the sample, although in practice the electron must travel through "ground" or some other return path. This return path, which is always grounded, is the stainless steel vacuum chamber itself. If the sample is not grounded or bonded to the vacuum chamber, the exposed surface will accumulate positive charge and the electron yield will drop.

In soft X-ray spectroscopy (including X-ray absorption and X-ray Photoelectron Spectroscopy), the sample is held in high or ultrahigh vacuum to allow the soft X-ray incident beam to reach the sample, to ensure sample cleanliness, and to enable electron detection including photoelectron spectroscopy (XPS), Partial Electron Yield (PEY), and Total Electron Yield (TEY). In photoelectron spectroscopy, grounding the sample is necessary both to complete the circuit and to create an energy reference. In PEY detection (see 2.1.3.1), the photon energy reference is provided by the monochromator and grounding the sample serves only to complete the circuit. In TEY detection, the sample is connected to a picoammeter which measures the current flowing from the sample which returns to the detector through the ground connection.

An additional wrinkle is that in a vacuum chamber, an electron of high kinetic energy will impinge upon the stainless steel wall with enough energy to generate more electrons. In cases where

the sample is not grounded, such as in Figure 39, charge can return to the sample via this route. For an ungrounded or insulating sample, an electron flood gun is available to provide even more charge with which to neutralize the sample. However, grounding a conductive sample is always possible and will give more reliable and consistent results.

Earth Ground To satisfy Kirchhoff's Current Law, a return path must be provided for each circuit. This return path is frequently termed *ground*, although moistened earth itself is relatively resistive to electrical current. In actual practice, earth ground involves referencing several pieces of electronics to a single point on the earth via a common metallic conductor. The true return path for the circuits, then, is the common metallic conductor which leads to the reference point. Both communication circuits and power circuits are referenced to the same conductor.

In the NSLS II,[138] the earth grounding system will include a Ufer ground[139] which will utilize the moisture content of the concrete foundation to reduce the impedance between the rebar and the earth. The grounding electrodes will be welded to the rebar embedded in the concrete. This will achieve a ground impedance of less than 5 ohms. The primary benefit of this low impedance is to conduct lighting, and induced current due to nearby lighting, to ground without generating an induced voltage in the grounding system.

More importantly, each beamline will have an instrument reference ground point to which multiple pieces of electronics may be referenced. Inevitably, however, the stainless steel vacuum chambers, which are connected together with copper gaskets and stainless steel bolts, will also be grounded via several vacuum pumps as well as in-vacuum detectors. It is the vacuum chamber itself which is most likely to return charge from the sample to the detector.

Grounding the sample As discussed above, a surface in a vacuum which absorbs soft X-rays will emit electrons of high kinetic energy. It is this surface which must be grounded. In the case of an electronic device such as a battery, thin film, or fuel cell, only one electrode may be grounded. This may be complicated by the design of the potentiostat in which one of its electrodes is not allowed to be grounded, but solutions to that problem are discussed below. A further problem is the attachment of multiple samples to the same sample bar. The sample bar should be designed (See

section 3.6.3) such that multiple samples may share a common grounded electrode on one side, and separate, isolated, electrodes on the opposite side. In order to view the commonly grounded side of the batteries, holes should be cut in the grounded sample bar.

The sample bar is connected to the potentiostat via electrical feedthroughs in the vacuum chamber. A feedthrough includes a metal collar bolted to the chamber, metal rods passing through the collar into the vacuum chamber, and nonporous ceramic material filling the space between the rods and the collar. If these rods are part of a sample manipulator, their isolation can be called into question. An initial testing method is to measure a voltage between the rod and a known grounded point; this voltage reading should vary randomly and not remain at 0 mV, which would indicate a short. The best testing method, however, is to apply a current between the aforementioned points. If there is any unknown connection, the current will find its own path between the two points. If not, the current source will quickly reach its upper voltage limit.

Ground loops A ground loop is created when two points in a circuit are connected to different ground reference points. Any voltage difference between these two points can generate a current which will appear as noise in experimental data, be it electrochemical or spectroscopic. These can be minimized by using potentiostats and laptops with two-prong electrical plugs, and by choosing potentiostats which include DC isolation between the neutral wire and the electrode connections.

Grounding the electronics For *in operando* soft X-ray spectroscopy, grounding the sample also means grounding the potentiostat. Despite the apparent similarities between different brands of potentiostats, the procedure for grounding the potentiostat varies greatly according to its internal design. In the case of the traditional Solartron 1287, the working electrode is provided with a "virtual ground" in which an amplifier, referenced to earth ground, provides a controlled current which holds the working electrode potential near to that of earth ground. This is not a true ground, however, and Kirchhoff's Current Law is not satisfied. Virtual ground must be disabled and replaced with a true ground connection to the counterelectrode; under no circumstances can the working electrode be directly connected to earth ground lest the virtual ground circuit be shorted. (Conversely, disabling the virtual ground link without grounding the CE renders the machine unable to measure

voltage accurately.) Grounding the CE is inconvenient for soft X-ray spectroscopy on the exposed working electrode of a solid state cell, however, because the side of the sample which faces the PEY detector should be grounded. Fortunately, the Solartron can operate over a -16V to +16V range; the simple remedy is to add a negative sign in the Corrware program. The same solution would not work with an Arbin, whose voltage range is -2V to +5V.

The connection between a computer and the electronics is potentially problematic. A personal computer generally has a metal cases which, by law, necessitates a third prong on the power plug. The metal case is also connected to the data wires of a USB, RS-232, or GPIB connector as well as to ground pins included in the connector. ([1]) This can potentially create a ground loop between the PC and one of the battery electrodes. If this ground loop is in place while the opposite electrode is shorted intentionally, the battery could be shorted. To prevent unintentional grounding, a laptop with a two-prong plug should be used and the potentiostat should have been designed with an isolated signal connection.

With the Pine WavenowXV, grounding either the WE or the CE was impractical until Pine developed a metal-cased version with an optically isolated USB port. After this upgrade, the CE could be grounded with no difficulties although fully-floating operation seemed to lead to noise issues. However, grounding the WE led to extremely large excursions in measured current which seemed to have no effect on attached electrochemical cells. These excursions initially resembled very low-frequency noise induced on the circuit, but it was soon noticed that the excursions were not regular in time. Instead, the excursions seemed to represent a loss of stability in the op-amp circuits, but this was not confirmed by Pine. It was concluded that grounding the CE was both necessary and satisfactory in grounding the electrode. Unfortunately, the voltage cannot be reversed in the Aftermath program, so studies on grounded cathodes will necessitate the application of negative voltages and negative currents.

[1] In theory, USB devices do not connect to the cable shield, which is grounded only at the host. The data lines are not isolated.[140]

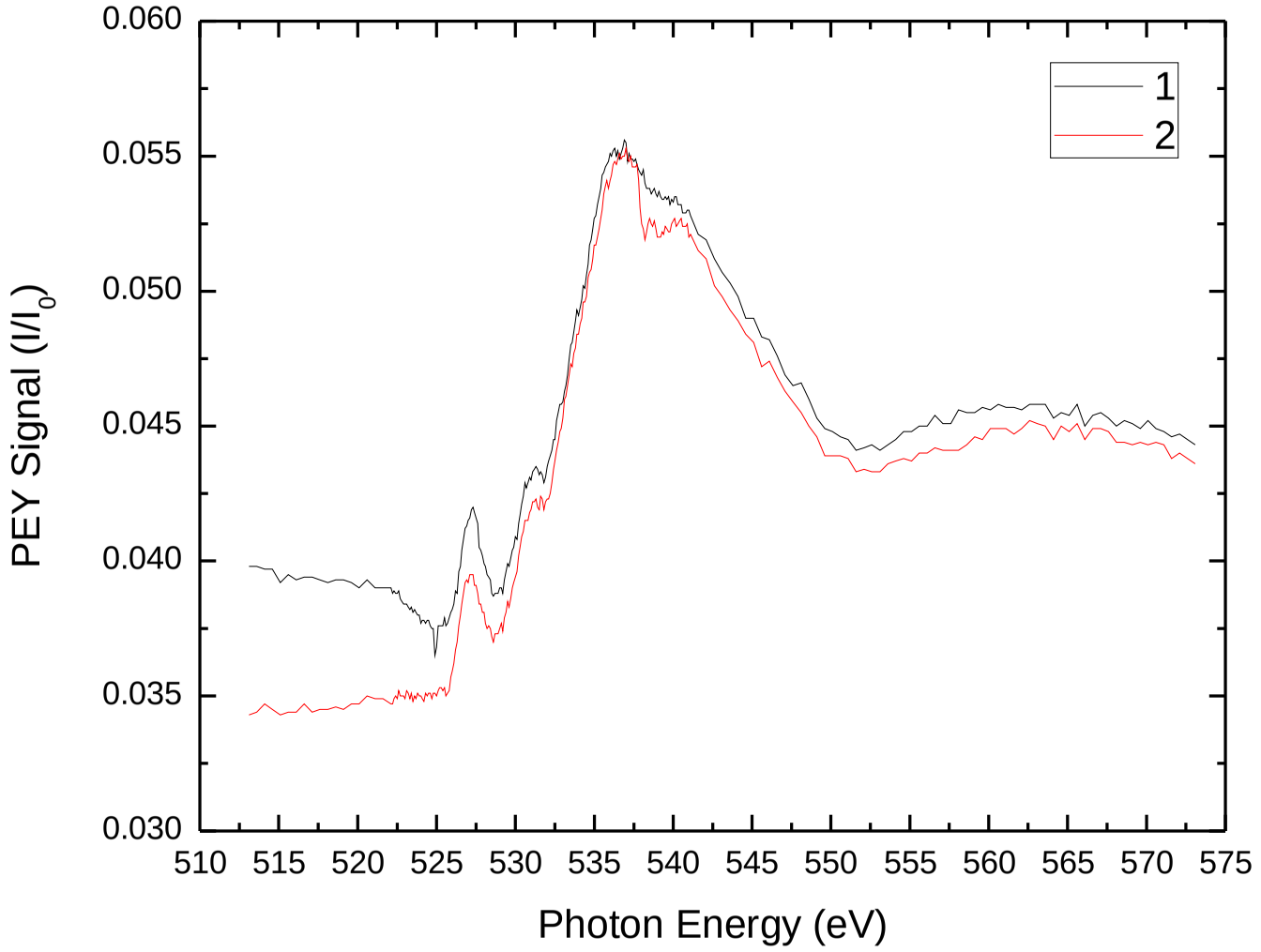

Figure 39: Sequential O K-edge NEXAFS scans (PEY mode) without grounding, resulting in spurious scan-to-scan variation

3.6.2 Sample Holder for Thin Film Memristors

An *in operando* sample bar was designed to electrically polarize thin film samples of $LiCoO_2$ and $LiNbO_2$ within the main chamber or imaging chamber. The primary constraint for the imaging chamber was the ability to apply a maximum magnetic field at the sample; this meant not only the exclusion of ferromagnetic material, but also a minimum thickness of paramagnetic or diamagnetic material. Ceramic materials were considered for their high stiffness at low thicknesses, but the danger of breakage within the vacuum chamber was deemed too great. Polymeric materials, being flexible, would preclude accurate and stable positioning of the sample. Aluminum was chosen as a stiff, lightweight, machinable and economical material. In keeping with the *ex situ* sample bars at U7A, a 10" x $1/2$" x $1/8$" aluminum bar was thinned to $1/16$" thick over a 5" region at the bottom of the bar for sample mounting.

The "guitar bar" sample holder resembles a guitar in that it has several parallel wires which terminate at three diagonally-spaced screws. Below these three screws, copper tape with conductive (copper-filled) adhesive runs over layers of insulating polyimide tape to three thin film samples. It was quickly found that the conductive adhesive was not sufficiently adherent to make a solid contact with the metallized thin films. Size 2-56 screws of nylon, PEEK, and stainless steel were screwed into threaded holes in the bar after shortening them to limit protrusion on the opposite side.

Typically, the aluminum bar itself is used as a common contact. However, electrical noise can be reduced by grounding the bar and making electrical contact only to the copper foil pieces. With one copper contact used as a common connection, only two samples can be independently polarized. Thin film samples of $LiCoO_2$ and $LiNbO_2$ on sapphire substrates were provided by Jordan Greenlee. Metal contacts were deposited on top of the thin film sample.

3.6.3 Sample Holder for Powder Pellet Batteries

In creating a solid state battery suited to *in operando* spectroscopy the goal was to produce an electronic device which removes or adds lithium ions, in a controlled way, to or from the material of interest. It is the change in lithium stoichiometry which drives changes in the spectroscopy. Therefore, although some devices may have one lithium metal electrode and one intercalation electrode, a carbon-based counterelectrode is completely acceptable. The advantage of an intercalation

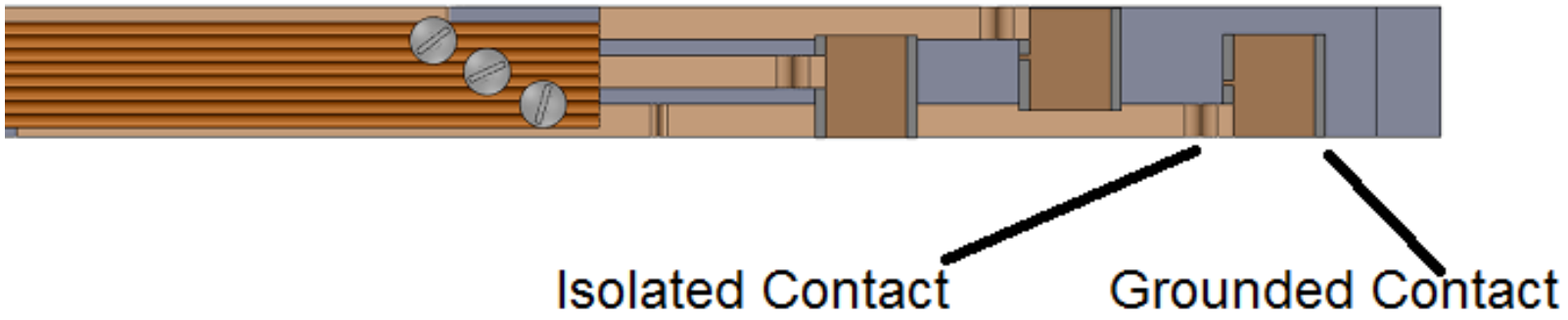

Figure 40: Schematic of "Guitar Bar" used for *in operando* experiments on thin film memristors

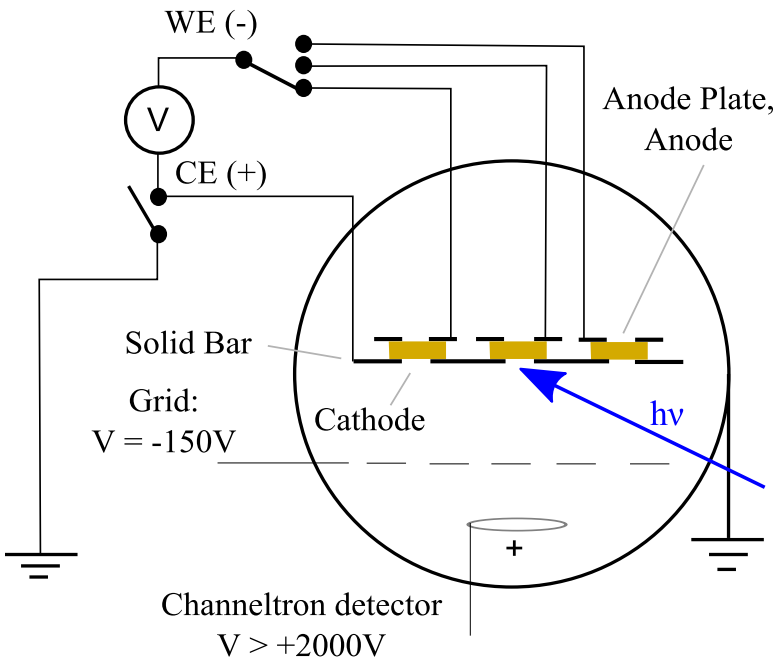

Figure 41: Circuit Diagram for *In Operando* Soft X-ray Spectroscopy

counterelectrode is that it can absorb a great deal more lithium ions than can lithium metal if dendrite formation is to be avoided. The chemical potential of lithium in graphite is favorable enough to absorb any metallic lithium that can be formed. Therefore, most devices of interest will have carbon-based counterelectrodes.

Although the solid-state intercalation battery generates an open-circuit voltage (OCV) which is very similar to that produced by the same materials in contact with a liquid electrolyte, the electrochemical voltage will not be identical because the electrolyte is different. In a liquid electrolyte, the potential of an electrode depends in part on the chemical potential of lithium ion the intercalation material and in part on the chemical potential of the Li^+ ions solvated by solvent molecules. The OCV, then, cannot be and is not the essential measure of the progress of deintercalation during the *in situ* spectroscopic experiment. Instead, delithiation is driven by a constant current. The spectroscopic results are then correlated with number of lithium ions removed from the active material.

To charge a battery while simultaneously allowing Auger electrons and photoelectrons to leave the surface, two connected circuits were assembled. The circuit diagram in Figure 41illustrates the interconnection of each current loop. In this Figure the circle represents the grounded, stainless steel vacuum chamber. The solid state cells, in yellow, are exposed on both the top (anode) and bottom

(cathode) through perforations in the metal plates. Synchrotron radiation incident on the cathode generates Auger electrons which travel from the cathode to the positively charged channeltron detector. Electrons with less than 150 eV of kinetic energy are repelled by a grid biased to -150 V. The electrons reaching the channeltron detector travel to ground and return to the cathode layer via the grounded counterelectrode.

Although for electrochemical purposes the cathode of the cell is the working electrode, the potentiostats used in this work were incompatible with a grounded working electrode lead. The experiment was then performed either without grounding, leading to electrostatic charging problems, or with the counterelectrode lead grounded and connected to the cathode layer. The working electrode lead of the potentiostat could then be connected to either of three anodes while leaving the other two isolated.

In addition to designing a freestanding cell with exposed (yet electrically connected) active material, an additional challenge was designing a mounting system that satisfied the requirements of both the electrochemistry and the spectroscopy. In case of a failed cell, redundant cells were included on the sample bar. In order to include three independent cells on a bar connected by four terminals, the positive terminals were made common and the negative terminals were connected separately. For spectroscopy, however, the cathode layers needed to be both exposed to the synchrotron beam and grounded in order to provide a return path for the photoelectron current. In the initial design, these requirements were satisfied by first sandwiching each cell between a pair of aluminum plates (with the cathode side perforated) and then bolting them onto a long sample bar. In this design, the (metallic) bolts themselves connected the perforated plate and cathode layers to the grounded sample bar and carried current. Ceramic "hat" washers insulated the stainless steel bolts, but no polymers, were used, enabling quicker pump-down. This design is seen in Figure 42 at the left-hand-side of each view.

Later, to reduce bulk and to enable magnetic imaging experiments, a simpler design was created. In this design, the sample bar itself is perforated and the cathode layer of each cell contacted the sample bar directly, simplifying cell mounting. Perforated plates were bolted onto the long bar using insulating screws. With each electrode exposed, the bar could be reversed for spectroscopy on the opposite electrode. Furthermore, magnetic imaging experiments using the LARIAT detector

could be performed because the magnetic flux could pass through the entire pellet. Thus, a three-plate design with the batteries facing "forwards" was replaced by a superior two-plate design with the batteries facing "backwards." Both nylon and PEEK screws were used successfully without compromising high vacuum performance. This design is seen in Figure 42 at the right-hand-side of each view.

In Figure 43, an illustration and a photograph show a sample bar with solid state batteries installed. In each case, the cathode plates are bolted to the sample bar while the anode plates are wired separately. In the illustration, silica cloth tubing insulates one of the wires. In the photograph, the anode plates are connected in a solder-free "wire-wrap" style to create a highly reliable and ultra-high-vacuum-compatible connection.

In Figure 44, the battery bar is shown installed into the main analysis chamber at NIST beamline U7A. In this chamber, the refocused synchrotron beam enters from the right-hand side (this connection uses edge-welded bellows) at an angle of 5° from the vertical to impinge upon the uppermost sample. The refocusing of the beam achieves a spot side of approximately 1 mm^2; the sample bar is moved vertically to aim this beam in a 5 mm x 10 mm window in the positive plate. The detectors include the PEY (from above, with internal tube) and FY detectors (below) on the right-hand side above and below the sample. The sample bar is rotated towards these detectors to improve signal collection. Finally, the beam spot on the cathode layer of the sample is shown in Figure 45.

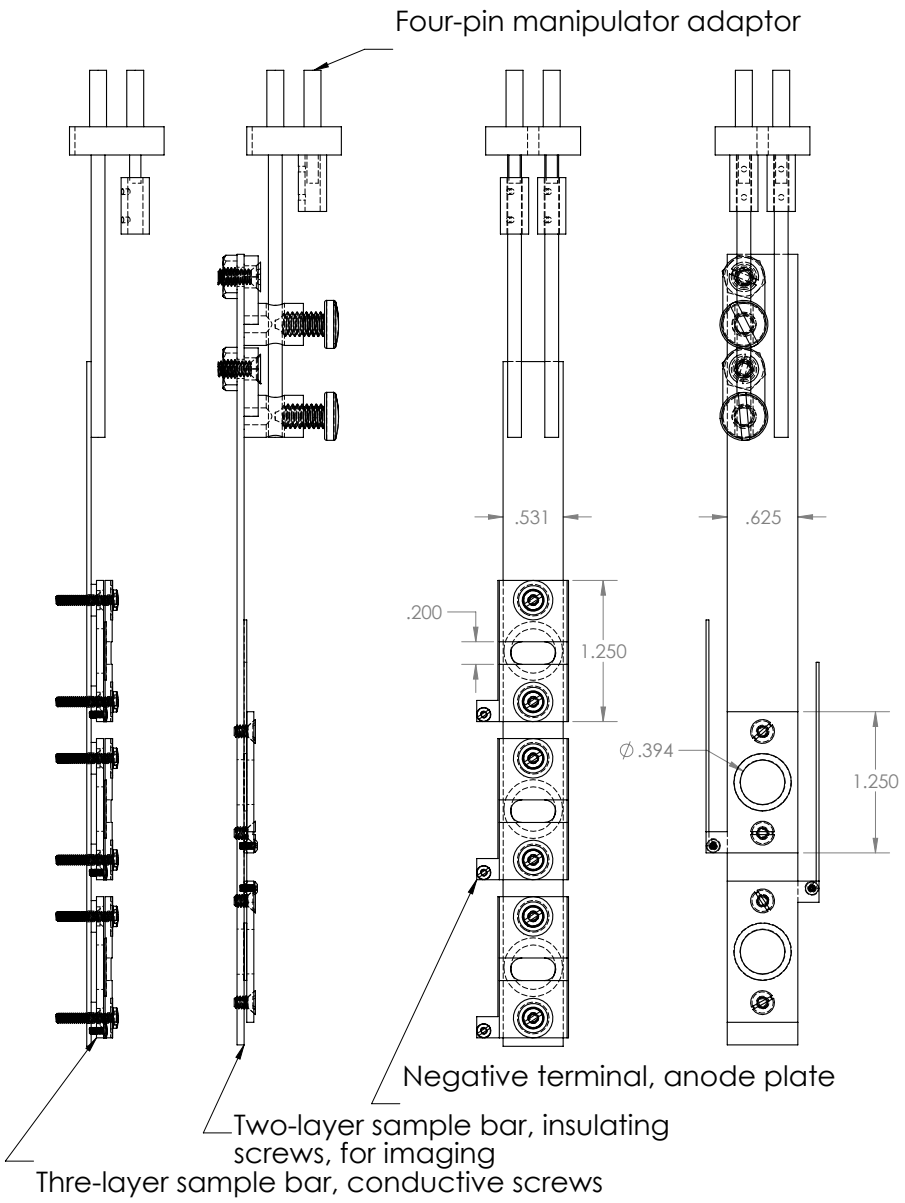

Figure 42: Diagrams of Two *In Operando* Sample Bars

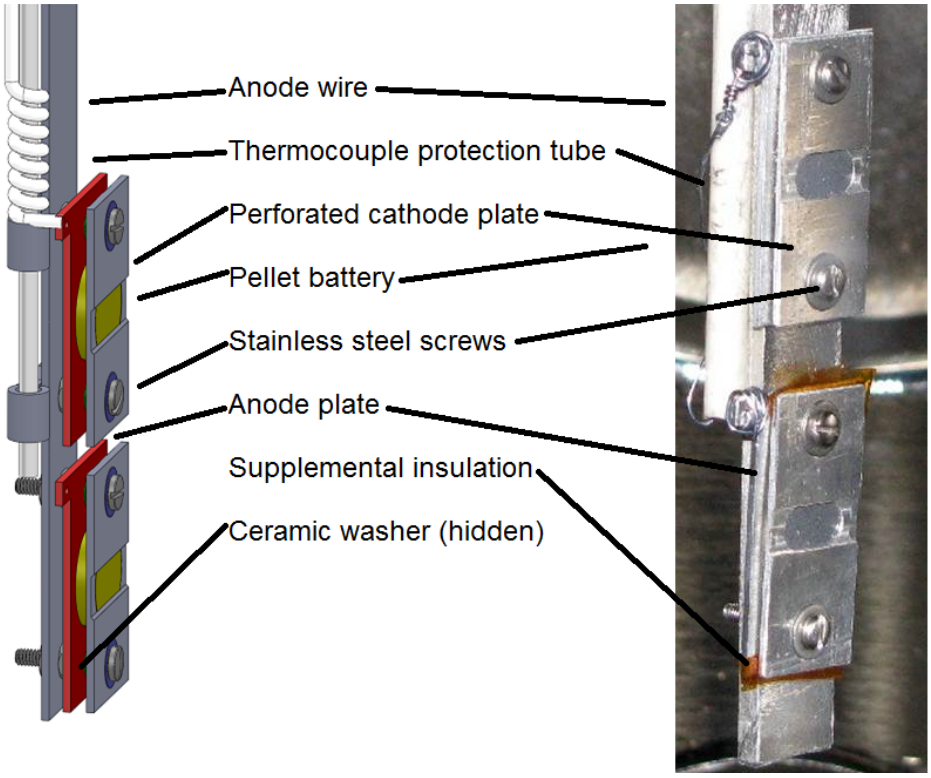

Figure 43: Illustration and Photograph of Solid State Battery Sample Bar

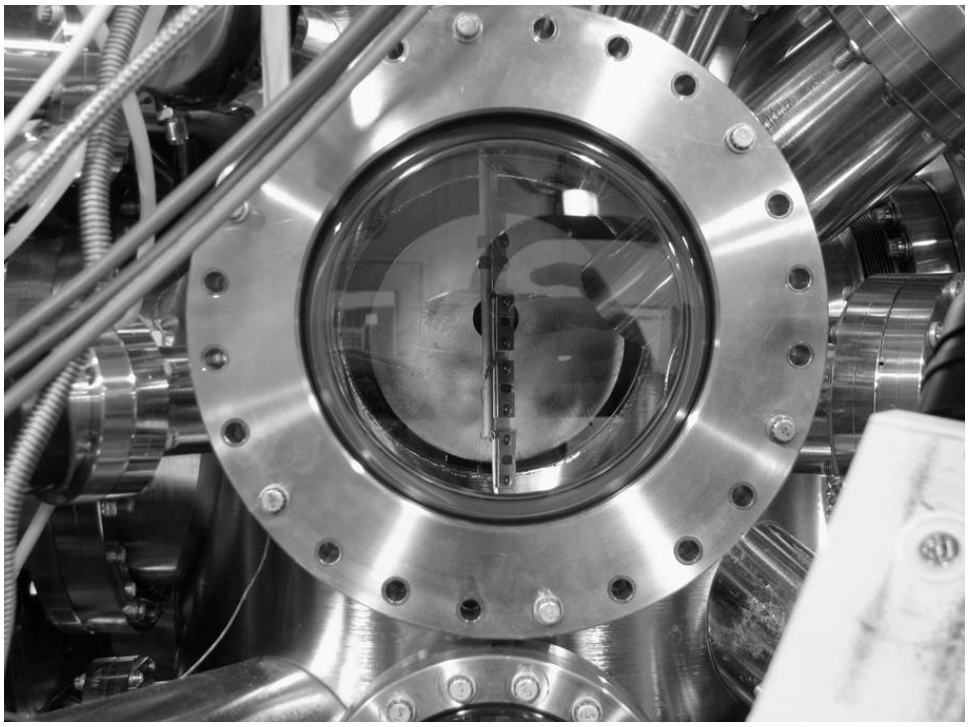

Figure 44: Photograph of solid state battery bar in main chamber of NIST beamline U7A with, clockwise from upper-right to bottom-right, the PEY detector, incident beam, and FY detector

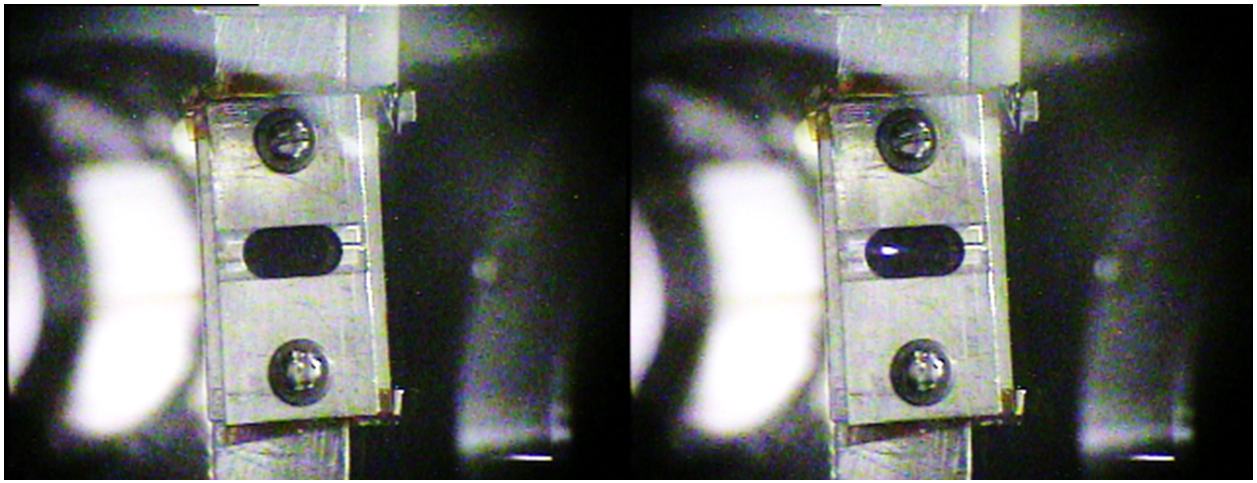

Figure 45: Solid state battery mounted in main chamber, NIST beamline U7A, without and with refocused, 1 mm^2 synchrotron beam

CHAPTER IV

HARD X-RAY ABSORPTION SPECTROSCOPY

In this chapter, two hard X-ray absorption experiments are discussed. In the first study, the well-known 333 compound ($LiNi_{1/3}Mn_{1/3}Co_{1/3}O_2$) is studied in light of recent results of Li et al.[76] showing that the magnetic susceptibility of the material as a function of delithiation cannot be explained by the oxidation of nickel ions alone. Instead, it was deduced in that study that cobalt participates in charge compensation. *Ex situ* XANES and EXAFS by Petersburg et al.,[92] however, show that cobalt does not participate directly in charge compensation. Instead, it is deduced that the oxygen ions bonded to cobalt oxidize, thereby generating the weak magnetic moment previously observed.

In section 4.2, *in operando* XAS on the overlithiated compound $Li_{1.17}Ni_{0.25}Mn_{0.58}O_2$ for the first two charge cycles is presented. It is shown that although nickel charge compensates for most of the reversible charge capacity measured by West et al.,[17] much of the capacity is not compensated by nickel oxidation. It is deduced that the anomalous capacity is due to oxygen oxidation, as was found for the 333 compound. Furthermore, in spite of the irreversible capacity lost in the first cycle,[17] which is attributed to oxygen loss,[16] a significant portion of the anomalous capacity is found over the course of many cycles.[17] In section 4.2.2, it is shown that even after the first cycle, the remaining oxygen continues to play a role in charge compensation. This accounts for the anomalous capacity found after the first cycle.

Soft X-ray *in operando* results for the same compound, synthesized in the same manner, are given in section 5.3. In this chapter, all data were obtained in transmission mode using pouch cell batteries.

4.1 Ex Situ *XAS on* $LiNi_{1/3}Mn_{1/3}Co_{1/3}O_2$

In collaboration with Prof. M. Stanley Whittingham's group at SUNY Binghamton, the intercalation cathode compound $LiNi_{1/3}Mn_{1/3}Co_{1/3}O_2$ was studied *ex situ* at several states of delithiation. In a

comprehensive study of several related stoichiometries, their rate capabilities, and magnetic moments, it was found that in $LiNi_{1/3}Mn_{1/3}Co_{1/3}O_2$, the trend of total magnetic moment versus delithiation was anomalous. Of several models considered for the magnetic moment, the best model assumed the oxidation of Co^{3+} to Co^{4+}. Although Co^{4+} has been detected in $SrCoO_2$ using *ex situ* NEXAFS, which has a large lattice spacing, it has not been seen in $LiCoO_2$ in which the Co–O bond is generally too short (and therefore hybridized) to allow cobalt to reach the 4+ state. Furthermore, this conclusion was not supported by hard X-ray XANES or EXAFS at the Co K-edge.[76]

The XANES and EXAFS results summarized in Li et al.[76] were carefully re-analyzed in great detail. It was found that although the Mn–O and Ni–O bond distances were relatively static over most of the intercalation range, the Co–O bond length continued to shrink throughout delithiation. This suggested that positive holes, and therefore unpaired magnetic moments, were present in the hybridized Co–O bond and not localized at the cobalt site.[92]

X-ray Absorption Spectroscopy at the Ni, Mn, and Co K-edges is used to investigate the charge compensation mechanism and its relationship to the magnetic moments in $Li_{1-x}Ni_{1/3}Mn_{1/3}Co_{1/3}O_2$. Multiple analytical methods are compared to separate element-specific redox trends from collective effects. EXAFS is used not only for structural, but also for chemical information while XANES is used not only for chemical, but also for structural information. While Ni is found to be the only transition metal involved in the charge compensation reaction until half the Li is removed, the second half of the deintercalation reaction is not accompanied by transition-metal oxidation. It is deduced that over the second half of Li deintercalation, the oxidation of oxygen ions bonded to cobalt is responsible for charge compensation and for an increase in the magnetic moment.

Introduction Recently, manufacturers of rechargeable lithium ion batteries have begun to replace the $LiCoO_2$ cathode material with cheaper, more cycleable alternatives. Unfortunately, although the cheaper oxides $LiNiO_2$ and $LiMnO_2$ can be synthesized, their structures break down upon delithiation. Instead, mixed transition metal (TM) oxides are being utilized in which some, but not all of the cobalt is replaced with nickel and manganese. Some mixtures exhibit greater capacity for delithiation while also enduring more cycles before $R\bar{3}m$ failure.

The optimum ratio of nickel to manganese to cobalt is not obvious, and discovering this ratio

is an area of active research. X-ray diffraction on lithium ion batteries is commonly employed, yet this technique is sensitive only to the symmetry and spacing of crystal planes. Because nickel, manganese, and cobalt tend to share the same crystal plane, the behavior of each cannot be differentiated. To obtain local electronic and atomic structure around each TM element in Li battery cathodes, X-ray Absorption Spectroscopy is employed[54,141,142] due to its element-specificity. Using this technique, oxidation states can be approximated using X-ray Absorption Near Edge Structure (XANES). Also, by using Extended X-ray Absorption Fine Structure (EXAFS), structural information can show cooperative effects between electronic and atomic structure such as Jahn-Teller distortion, which changes as a function of lithium content. By making cross comparisons, EXAFS can be used to verify oxidation states which are approximated by XANES.

A previous XAS study of this material[55] concluded that two thirds of the charge compensation was provided by the oxidation of Ni^{2+} ions to Ni^{3+} and then to Ni^{4+}. Manganese and cobalt were found to remain as Mn^{4+} and Co^{3+} over the entire range of delithiation. However, EXAFS showed a strong contraction between cobalt and oxygen, suggesting the formation of oxygen holes in oxygen ions neighboring cobalt. Simultaneously, though, an expansion of the nickel-oxygen distance during delithiation, which is not plausible if nickel is oxidizing. A more detailed EXAFS analysis may resolve the difficulties.

In the same study, near-edge X-ray absorption spectroscopy fine structure (NEXAFS) at the oxygen K-edge was used to measure the electron occupation of the O 2p orbitals, but the conclusion that oxygen holes formed around cobalt was not clearly supported. Surprisingly, *ex situ* NEXAFS showed an initial oxidation at the O K-edge, a small change between 60% and 80%, and an unchanged spectrum between 80% and 100% delithiation. The loss of oxygen gas from the overlithiated analogue of this compound has been demonstrated at high potentials.[143] This effect would explain an unchanging O K-edge spectrum for the oxygen remaining in the solid material. However, on discharge, 96% of the lithium ions return to the cathode[76] meaning that only 4% or less of the charge capacity can be explained by oxygen oxidation to O_2.

More recently, Li et al.[76] used magnetic measurement to study four cathode compositions in the $Li_{1-x}Ni_yMn_yCo_{1-2y}O_2$ system to ascertain the optimum level of cobalt. (Metal-metal distances derived from EXAFS were reported; the same dataset is analyzed in detail here with the addition of

metal-oxygen distances.) Superior rate performance was found for $y = 1/3$ at the cost of a higher charging voltage, which limited the capacity for a given voltage cut-off. Magnetic measurements showed a decreasing number of unpaired electrons with delithiation to 50%, followed by a slight increase. Assuming Ni^{2+} oxidizes to Ni^{4+}, and that Mn^{4+} cannot oxidize further, it was deduced that the increase in moment was due to Co^{3+} oxidizing to Co^{4+} beyond 55% delithiation. However, X-ray Absorption Spectroscopy showed no significant shifts in the Co or Mn K-edges. The partial oxidation of oxygen was proposed to explain the magnetic moments, the high cell voltage, and the stabilization of the crystal structure with delithiation beyond 50%. The question that remains, however, is whether all oxygen ions oxidize or whether only oxygen ions near specific TM ions become oxidized. In this study we carefully compare multiple additional complementary methods of extracting oxidation states from the XANES and EXAFS in order to detect oxygen holes around each TM element in $Li_{1-x}Ni_{1/3}Mn_{1/3}Co_{1/3}O_2$ and thereby explain the trend in magnetic moments.

In the literature on X-ray Absorption Spectroscopy, several approaches are commonly taken to extract oxidation states from TM K-edges, only some of which have a physical basis. In particular, the 50% edge jump method, in which the energy position at which 50% of the beam is absorbed is taken to be the edge position, is troublesome not only because it oversimplifies the shape of the absorption edge, but also because it does not account for the shrinkage of the first nearest neighbor distance, which can move the absorption edge to higher energies.[144] It will be shown that some portion of the evolution of the Mn XANES in this compound is due solely to contraction of the crystal with delithiation, and that the remainder is due to oxidation. In the EXAFS, differences between the magnitude and imaginary parts of the Fourier transform can be used. In the case of nickel, Jahn-Teller distortion clearly shows the coexistence of Ni^{2+} with Ni^{3+}, and Ni^{3+} with Ni^{4+}.

Methods $LiNi_{1/3}Mn_{1/3}Co_{1/3}O_2$was synthesized by the co-precipitation method followed by solid-state reaction as described previously. A 5% excess of lithium hydroxide was added to ensure that the molar ratio for Li/(Ni+Mn+Co) was near unity as measured by direct current plasma spectroscopy.[47,76] The precipitate was heated at 800°C for 8 h and then quenched to room temperature by sandwiching between copper plates. For comparison, Yoon et al. heated the same precursors at 900°C for 24 h.[55] In a previous study, Rietveld refinement indicated very little Li/Ni exchange,[76]

meaning that lithium remains in the lithium layer while nickel remains in the TM layer.

X-ray absorption data for samples at several states of charge was acquired in transmission mode at NIST beamline X23A2 at the National Synchrotron Light Source, Brookhaven National Laboratory as previously described.[76] The X-ray absorption spectra of the Mn K-edge, Co K-edge, and Ni K-edge were analyzed using ATHENA software. Reference foil spectra were used to calibrate the energy scale, and the spectra for each element were aligned to the reference spectra. The spectra were normalized by subtracting pre-edge and post-edge lines, taking care to choose a post-edge energy range which was suitable at all levels of lithium content. For each spectrum, the E_0 point was chosen to be the first inflection point in the pre-edge features at each level of delithiation. The background function range was adjusted to minimize Fourier transform artifacts in the real-space radial distribution function as described in Newville et al.[98] The Fourier Transform range Δk, which is the Fourier bandwidth, was held constant across the full range of delithiation. For each element, a k-weighting of 2 was used.

The real-space EXAFS data are shown using an uncorrected distance scale in Figure 52a. For comparison with XRD data in Figure 52 on page 127, the EXAFS distance scale for metal-metal peaks was calibrated such that all distances match in the pristine compound. Also, for each EXAFS dataset, the metal-metal peaks were approximated to be a single scattering path (neglecting weak metal-Li scattering at the same distance) and were successfully fit with Gaussian peaks. The standard errors were less than 0.12 pm.

To fit the more complex, asymmetric metal-oxygen peaks and to deconvolute Jahn-Teller distortion, however, it was necessary to use the full theory of plane-wave scattering from the nearest oxygen and metal neighbors using Equations 9 and 10 in ARTEMIS. Four parameters for each scattering path were used: an amplitude, a radial shift, a Debye-Waller factor σ^2, and energy shift ΔE_0. To improve the physical rigor of the fit, multiple datasets were fit simultaneously, and correlated parameters were not allowed to vary simultaneously. The R-range spanned the metal-oxygen and the first metal-metal peak due to the overlap of the tails of these peaks.

XRD Results *Ex situ* X-ray diffraction with Cu $K\alpha$ radiation was performed at multiple levels of delithiation. The diffractogram in Figure 46 indicates a single-phase structure at all levels

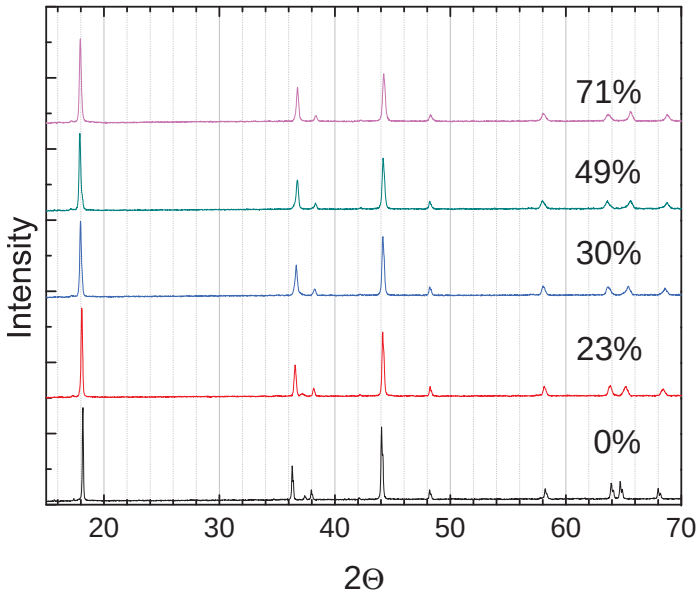

Figure 46: X-ray diffractograms[92] at five stages of delithiation, 333 compound

Table 10: XRD-derived plane spacings and unit cell volumes for $Li_{1-x}Ni_{1/3}Mn_{1/3}Co_{1/3}O_2$

x	a (Å)	c(Å)	V (Å^3)
0.00	2.859(5)	14.236(7)	100.774
0.23	2.841(5)	14.310(6)	100.026
0.30	2.831(5)	14.380(6)	99.809
0.49	2.823(5)	14.432(7)	99.604
0.71	2.823(5)	14.405(6)	99.418

of delithiation. Furthermore, the peak widths and heights do not change with delithiation. No superlattice reflections were seen, indicating a non-ordered crystal structure, meaning that nickel, manganese, and cobalt were randomly distributed. Delithiation up to 49% causes contraction in the a-axis simultaneous with expansion on the c-axis. (See Table 120) After 49% delithiation, the a-axis remains static while, notably, the c-axis contracts slightly. Across the entire range of lithium content, the unit cell volume decreases with delithiation.

XANES Results and Analysis At the K-edge for a 3d transition metal and assuming an octahedral arrangement of ligands, the X-ray absorption results from the excitation of a 1s core electron to the unoccupied 4sp orbitals. The 1s $\rightarrow$ 3d transition is only slightly allowed due to distortion from centrosymmetric symmetry and due to hybridization with the O 2p ligands.[145] Therefore, the pre-edge features in XANES can roughly indicate the configuration of 3d orbitals, although the

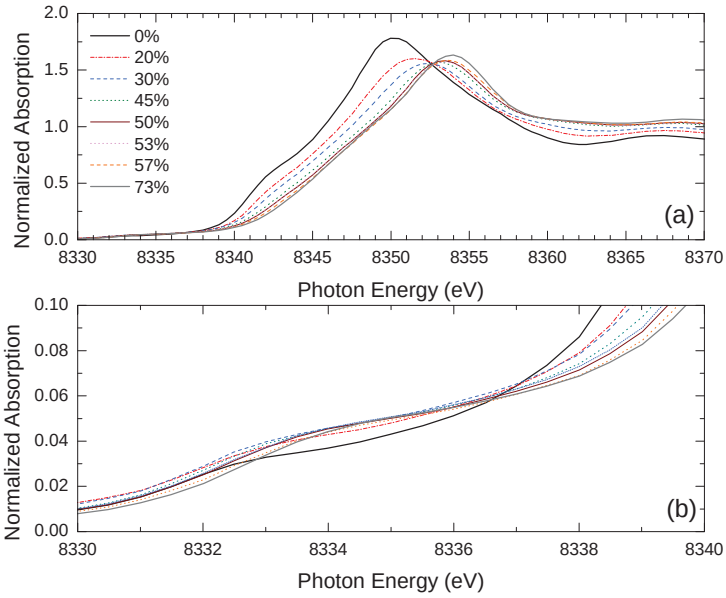

Figure 47: (a) Nickel XANES (b) 1s to 3d pre-edge at each level of delithiation[92]

core-hole lifetime effect limits the resolution compared to soft X-ray absorption at the TM L-edges.

As noted by previous researchers, EXAFS oscillations above the Co K-edge are visible ~100 eV below the Ni K-edge.[55] However, these oscillations are small and rapidly decaying and, furthermore, do not change during delithiation. They did not affect the analysis. In Figure 47, the Ni K-edge is shown with the pre-edge magnified in Figure 47b. The main peak in Figure 47a is known as the white line; this term is explained in section 3.3. The pre-edge absorption region is highly sloped, making it difficult to separate it from the white line, but indicates a single spectral feature which can be attributed to the Ni e_g orbital. In agreement with Ni L-edge results,[145] the nickel pre-edge region moves to higher energies at the early stages of delithiation. The white line shifts dramatically to higher energies between 0% and 45% delithiation; after this point the changes are more subtle. In the pristine compound, absorption edge position, as estimated by the 50% edge jump method, is consistent with the edge position for NiO, indicating Ni^{2+} as expected based on stoichiometry. However, none of the scans has an edge position as high in energy as that of $KNiIO_6$, a known Ni^{4+} compound.[111] The accuracy of the 50% edge jump method is questioned in the discussion below.

The pre-edge region of Mn is much better resolved from the white line in the Mn K-edge. However, the spectral changes with delithiation are small, as seen in Figure 48. As expected for

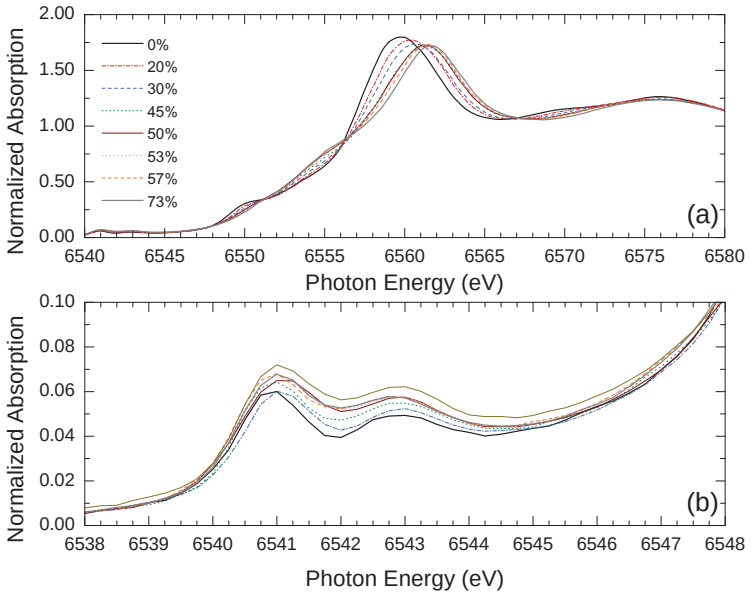

Figure 48: (a) Manganese XANES (b) 1s to 3d pre-edge at each level of delithiation[92]

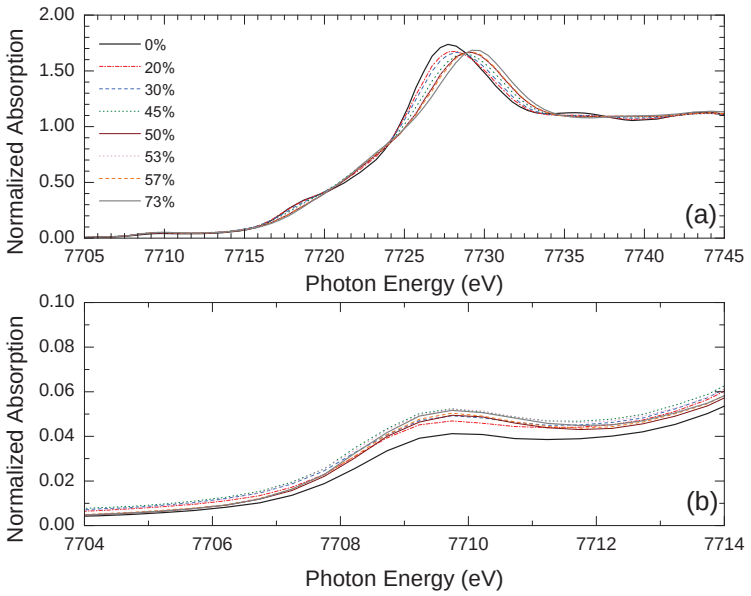

Figure 49: (a) Cobalt XANES (b) 1s to 3d pre-edge at each level of delithiation[92]

Mn^{3+} or Mn^{4+}, the manganese pre-edge shows two peaks. During delithiation, both peaks grow in height. The energy gap between the two peaks steadily shrinks with increasing delithiation from 2 eV to 1.7 eV. (Figure 50b) This suggests that, despite the contraction in the Mn–O distance which should promote a larger crystal field splitting, the crystal field splitting is actually decreasing, likely due to symmetry effects. (Figure 50a)

The cobalt pre-edge is resolved from the white line and shows no significant changes. The single peak agrees with the expected electron configuration of $t_{2g}^6\ e_g^0$. This peak moves to higher energies only in the first 20% of delithiation. (Figure 49b) However, the white line continues to shift over the whole range of delithiation. (Figure 49a)

For manganese and cobalt, the pre-edge features do not move in energy with delithiation, although the pre-edge feature in the Ni K-edge moves monotonically to higher energies.

In Figures 47–49, the evolution of the Ni, Mn, and Co K-edges is shown. For each element, all the normalized spectra up to 57% delithiation intersect through isosbestic points. An isosbestic point indicates the existence of a single reaction, and not more.[146,147] The normalized spectra for 73% delithiation fail to intersect the prior spectra at the same points. This indicates a change in the charge compensation mechanism at 73% delithiation. The existence of a single reaction which terminates at the same point for each element indicates a single coordinated reaction involving the 4sp orbitals for each element.

In Figure 47b, two prominent isosbestic points in the Ni K-edge spectrum are seen, one at the peak of the white line, and one in the EXAFS region. In the Mn K-edge spectrum in Figure 48b, at least seven isosbestic points are present, including three within the edge jump and one at the peak of the white line. Between these unchanging isosbestic points, the spectrum changes in opposite directions. Although much of the spectrum moves to higher energies, at 50% of the edge jump, the spectrum moves to lower energies. This trend is seen again in the Co K-edge, but to a lesser degree.

Figure 50b shows the only continuing trend seen in the data. The inflection point in the white line feature of each element moves to higher energies as far as 73% delithiation. This indicates the motion of unoccupied 4sp orbitals, which are hybridized to the O 2p orbitals, to higher binding energies as a result of the loss of electron density in the partly filled bonding orbitals.

According to the method used by Rumble et al.[148] and others,[149] manganese would appear

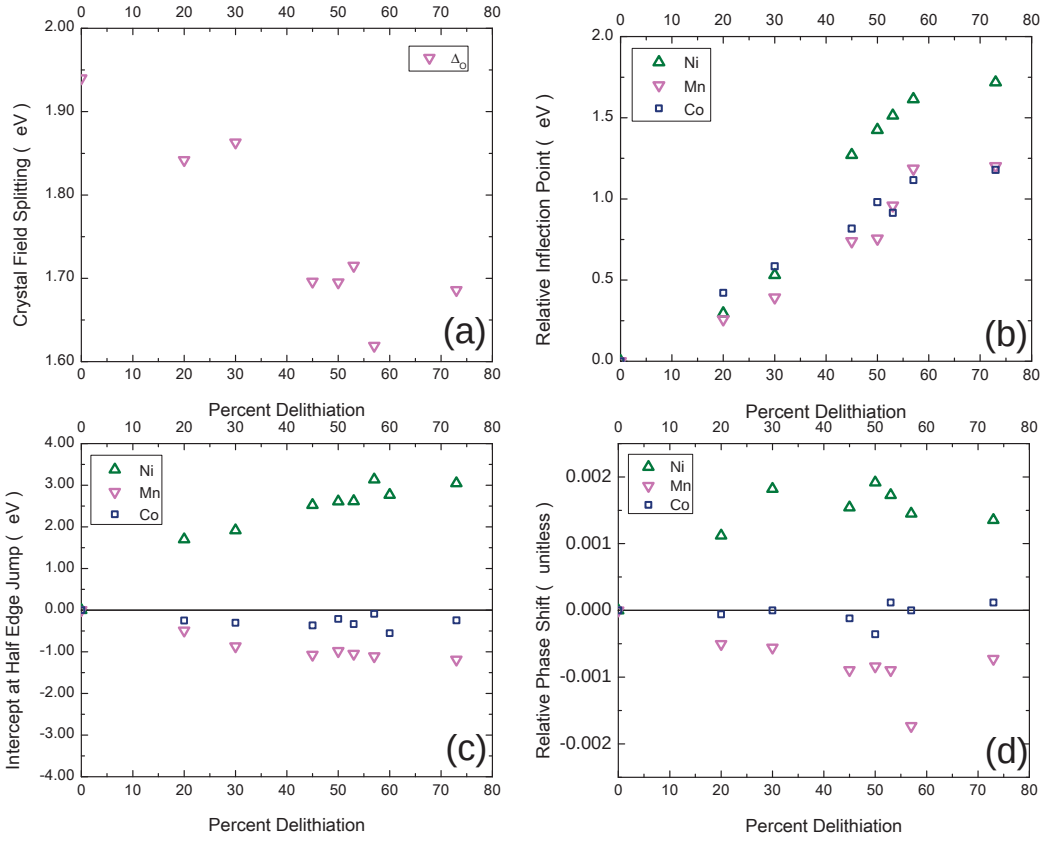

Figure 50: (a) Crystal Field Splitting of Mn, (b) Relative shift of white line inflection point, (c) Relative shift of 50% edge jump (d) Relative phase shift of EXAFS M–M peaks[92]

to be reducing (before 50% delithiation) because the energy at which 50% of the radiation is absorbed shifts to lower energies. (Figure 50d) However, the inflection point of the white line moves monotonically to higher energies over the entire range of delithiation for all three edges.

A final method extracts the unitless phase shift, $\delta_j(k, R)$ in the EXAFS equation (Eq. 9), from the EXAF metal-metal peak as a function of lithium content. The EXAFS equation accounts for a photoelectron phase shift which is sensitive to Z as well as to oxidation state.[150] Equation 10 gives the unitless phase shift which is proportional to the product of Δk, the range of k-space data used, and ΔR, the difference between the position of the peak in the real-space plot and the position of a corresponding peak in the imaginary part of the Fourier transform. The constant of proportionality, c, was taken to be unity for this analysis.

$$\chi(k) = \sum\nolimits_j S_0^2 \frac{N_k F_k \exp(-2k^2\sigma_j^2)}{kR_j^2} \sin(2kR_j + \delta_j(k)) \tag{9}$$

$$\delta_j(k, R) = c\Delta R\delta k \tag{10}$$

The results in Figure 50d), which plots the unitless phase shift, are similar to the shifts seen in the edge position in Figure 50c. Nickel appears to oxidize swiftly before reducing, cobalt shows no changes in phase shift, and manganese reduces slightly.

EXAFS Results and Analysis In Figure 51a, Ni EXAFS gives a radial distribution plot including oxygen above and below the basal plane, followed by neighboring Ni, Mn, and Co within the basal plane. In the pristine material, a single, broad peak for oxygen is consistent with Ni^{2+} (d^8). At 20% and 30% delithiation however, two overlapping peaks indicate Jahn-Teller distortion which reflects the asymmetric arrangement of electrons about Ni^{3+} (d^7). Simultaneous fitting at 20% and 30% delithiation allowed the deconvolution of the two peaks; the inclusion of 45% delithiated EXAFS was not successful. Instead, at 45% delithiation and beyond, only one peak is seen, indicating Jahn-Teller inactive Ni^{4+} (d^6). Strangely, though, this peak is much narrower than the peak in the starting compound.

A second look at the Ni–O peak in the pristine compound reveals that at its base, its width is equal to the width of the Jahn-Teller distorted peaks. Peak fitting was attempted using three

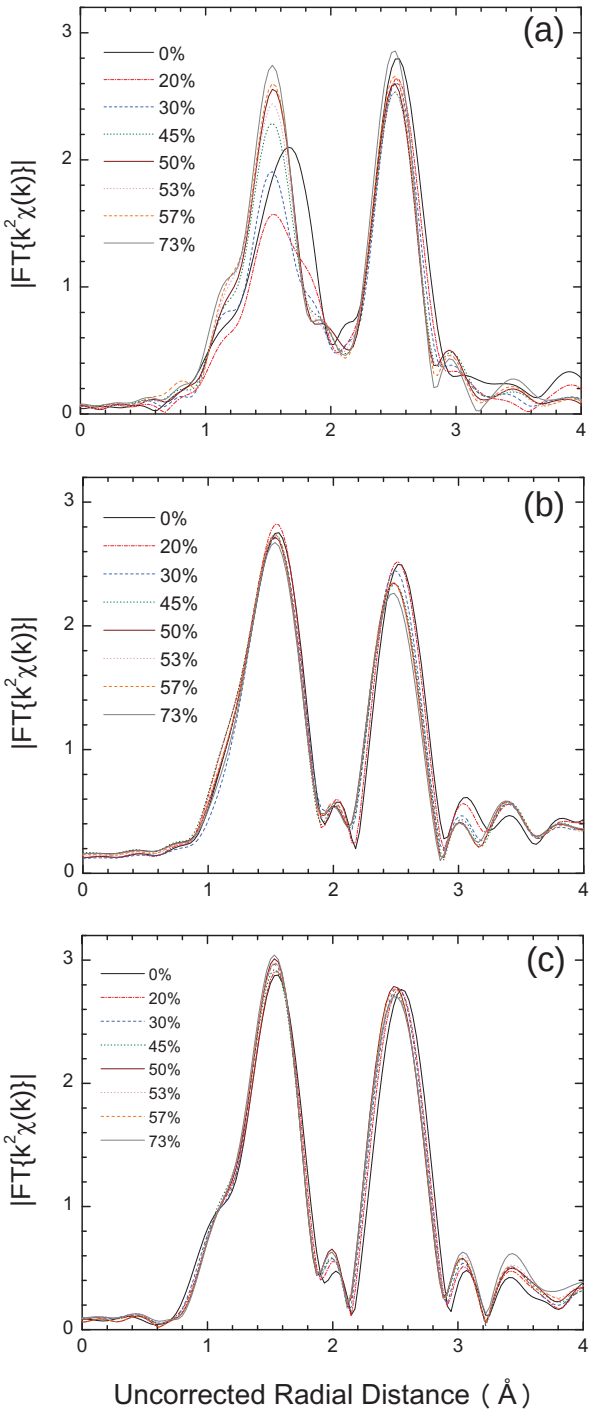

Figure 51: EXAFS for (a) nickel, (b) manganese, and (c) cobalt[92]

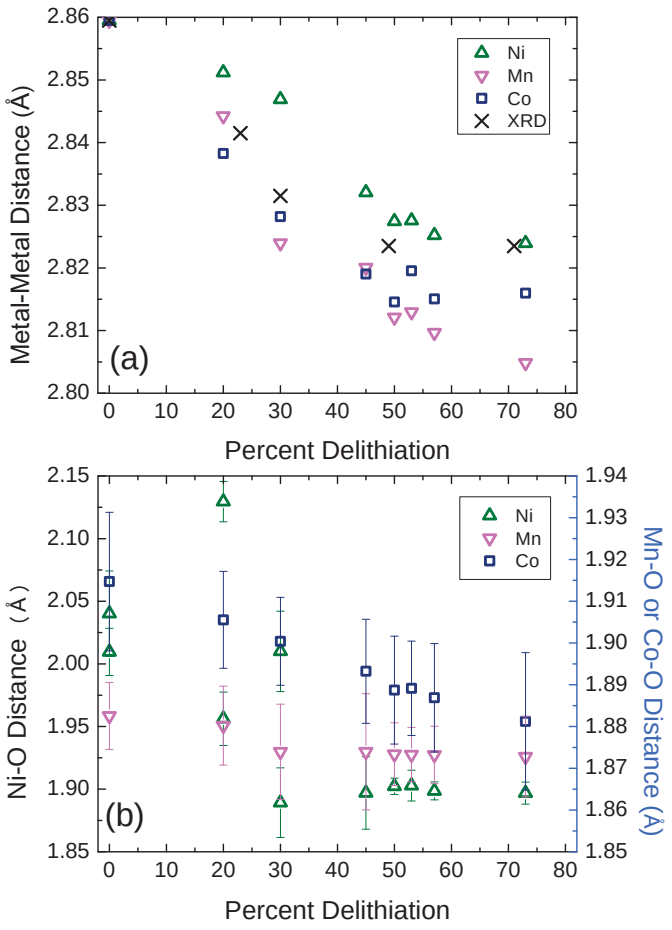

Figure 52: (a) EXAFS metal–metal distances with delithiation for each metal compared to XRD lattice parameters for the same crystalline direction. (b) EXAFS Metal-Oxygen distances around each metal.[92]

Table 11: EXAFS fitting parameters, 333 compound

Path	ΔE_0 (eV)	σ^2
Ni–O	12.24	0.00145
Mn–O	14.90	0.00190
Co–O	12.62	0.00185

different models. The first assumed a single peak of the same Debye-Waller factor as for 45% delithiation and beyond. The second assumed a single peak with a variable Debye-Waller factor. The third model assumed two peaks, each with the same Debye-Waller factor as for the narrower peaks. The first model failed to reproduce the width of the peak, while the second model found a Debye-Waller factor for the pristine compound which was twice that for the undistorted Ni–O peaks in cathodes with more than 45% or more Li removal. The third model succeeded by allowing two peaks constrained to provide a total coordination of six oxygen atoms, while also requiring the same Debye-Waller factor as for the post-45% peaks. The fitting, in this third case, was successful, and the two Ni–O peaks were found to be closer together than those for the Jahn-Teller distorted peaks at 20% and 30%.

The same trends are not seen in the Mn–O and Co–O EXAFS (Figure 51b, 51c). Instead, the Mn–O and Co–O peaks show no reduction in peak width or amplitude with delithiation, indicating a single, static coordination environment about manganese and cobalt.

In Figure 51b, the Mn EXAFS shows rapid contraction along with a loss of peak amplitude. In Figure 51c, nearest-neighbor distance changes in Co EXAFS (Figure 51c) are nearly unresolvable after 57% delithiation and the peak amplitudes are nearly constant. Neither cobalt nor manganese shows noticeable changes in peak width, indicating a single chemical environment for each element at all stages of delithiation. EXAFS fitting assumed a constant Debye-Waller factor for all Mn–O peaks, and a similar factor for Co–O peaks as seen in Table 11.

EXAFS Structural Trends Figure 52a shows the same trend for nickel and cobalt: the first metal-metal peak contracts at a constant rate followed by a stabilization while delithiation continues. Manganese, however, continues to move closer to its neighbors in the basal plane at 73% delithiation. Note that in Figure 52a, all the EXAFS distances have been calibrated such that the XRD and EXAFS data match for the pristine compound. It is interesting to note that although nickel and cobalt

see the cessation of contraction at the same time, nickel appears to move closer to its nearest neighbors at a slower rate. This suggests that nickel is initially displaced above and below the basal plan, thereby increasing the distance between nickel and its nearest neighbors.

Figure 52b shows the results of fitting the metal-oxygen peaks, including the Jahn-Teller distorted peaks for nickel. Most notably, the Mn–O peak ceases contracting at only 30% delithiation and remains at the same distance thereafter. Similarly, the closer of the Jahn-Teller peaks moves toward nickel until 30%, and then relaxes to a constant distance until 73% delithiation. Intriguingly, the Co–O peak never ceases to contract over the entire range.

Discussion The synthesis of this material achieves a nearly 1:1 ratio of lithium ions to transition metal ions. (The synthesis of Yoon et al.,[55] which used greater time and temperature, may not have achieved full lithium stoichiometry.) Therefore, the oxidation states of nickel, manganese, and cobalt must add to three to balance charge. Although XANES indicates Ni^{2+} in the pristine material, EXAFS reveals that the photoelectron backscattering distances cover a larger range in R-space than can be explained by any amount of atomic vibration, assuming the same level of vibration at the end of charge. The simple hypothesis, which suggests that the extraction of $2/3$ of the lithium is charge compensated by Ni^{2+} oxidizing to Ni^{3+} and then to Ni^{4+}, is not borne out by EXAFS. Instead, some small proportion of the nickel ions in the pristine material are Ni^{3+}. The majority Ni^{2+} is oxidized to Ni^{3+} not at 33%, but at 20% delithiation. These ions are oxidized to Ni^{4+} not at 66% delithiation, but at 45%.

To balance charge in the pristine material, Co and Mn must adopt slightly lower oxidation states than 3+ and 4+, respectively. XANES shows very small shifts in the Mn and Co K-edges before 45% delithiation which may be due to crystal contraction or to oxidation. A theory based on the effect of multiple scattering in conjunction with coordination geometry suggests that the energy gap between the pre-edge features and the inflection point of the white line depends on the inverse square of the bond length.[144] In this compound, the Mn and Co K-edges show an increasing distance between the white lines and the unmoving pre-edge feature during delithiation. This suggests that neither manganese nor cobalt necessarily oxidizes, but that the XANES merely reflects the shrinkage of the crystal.

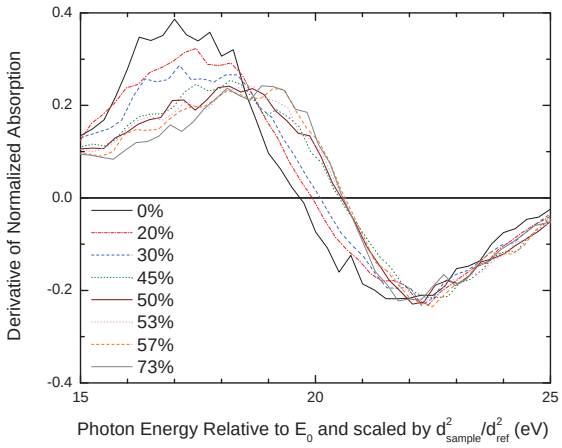

Figure 53: Derivative Mn XANES spectra scaled by the square of the EXAFS Mn–M peak distance[92]

This theory was applied to the Mn XANES data. Figure 53 shows the derivative of the white line plotted against an energy scale which is scaled by the squared ratio of the Mn–O EXAFS peak distance for each scan divided by the Mn–O EXAFS peak distance for the pristine compound. The peak in the data indicates the white line inflection point as seen in Figure 50b while the x-intercept indicates the white line peak position. The results show that this shrinkage of the energy scale brings all scans between 45% and 73% into alignment. However, there remains a continual shift in the white line from 0–45% delithiation.

Magnetic moment measurements[76] are consistent with Mn^{4+} and Co^{3+} before delithiation begins. These represent $3d^3$ (half-filled Mn t_{2g}) and $3d^6$ (filled Co and Ni t_{2g}) electron configurations. Further oxidation of any of the TM ions would lead to electron configurations which are neither half-filled nor filled; these configurations tend to be unstable.

The anomalous increase in magnetic moments after 50% delithiation found by Li et al.[76] cannot be explained by the oxidation of nickel, which is already Ni^{4+}, nor by the oxidation of cobalt or manganese, whose XANES edges are almost static after 45%. Only one trend found prior to 50% delithiation continues: the gradual but continuous contraction of the cobalt-oxygen distance. It is likely that oxygen ions bonded to cobalt ions oxidize and therefore become smaller, reducing the Co–O bond distance and creating a magnetic moment on oxygen sites. This mirrors the results of Alamgir et al.[54] for $LiCoO_2$.

Ideally, the oxidation state of transition metals would be measured by the occupation of the 3d

bonding orbitals. However, this measurement is typically only surface-sensitive and *in operando* experiments are difficult.[136] In Figure 50b, the inflection point in the white line features is used to track the binding energy of the TM 4sp orbitals, which are hybridized with the O 2p orbitals, and which are unoccupied by electrons. Although not all the TM ions oxidize with delithiation, the inflection point moves to higher energies as electrons and lithium ions are removed from the compound.

The 50% edge jump method in Figure 50d is customary, but is not based on physical theories and therefore should not apply equally well to each element at each oxidation state. As was seen in Figure 48, the manganese K-edge profile warps due to the interactions between multiple overlapping absorption features, appearing to move in opposite directions in different parts of the spectrum. The same phenomenon is seen for cobalt, but not for nickel.

The charge compensation mechanism in $LiNi_{1/3}Mn_{1/3}Co_{1/3}O_2$ is a longstanding mystery which has previously been attributed to the oxidation of Co^{3+} to Co^{4+}.[76,151] However, we have shown by multiple methods that the electronic structure of cobalt remains nearly constant over the entire range of delithiation. Although the majority of the charge compensation is provided by nickel, this process ceases at only 45% delithiation. The remaining Li+ ions cannot leave the cathode without charge compensation, and oxygen remains the only candidate. Because 96% of the charge capacity is reversible,[76] at least 46% of the capacity is attributable to oxygen oxidation without the (irreversible) loss of oxygen.

The structural changes in the material with delithiation support the hypothesis of anionic oxidation. XRD shows that even after 50% delithiation, the material remains single-phase. After the a-axis ceases to contract, the c-axis stops expanding and actually begins to contract. This would indicate that the lack of contraction is not due to the presence of a second phase, but instead to a compensation mechanism whereby the metal-oxygen bonds cease to contract. The oxidation of oxygen in this material is the best explanation because if the anion gradually loses negative charge, its coulombic attraction to the metal center will weaken. If the bond-strengthening effects of delithiation are balanced by the bond-weakening effects of oxygen oxidation, the bond strengths and bond lengths will tend to stabilize during delithiation beyond the point where oxygen begins to oxidize.

Between oxygen layers, the loss of lithium initially allows for greater repulsion between the negative charges. After oxygen begins oxidizing, however, this repulsion weakens, allowing the c-axis to contract with increased delithiation.

Because the $R\bar{3}m$ structure is composed of corner-sharing octahedra, displacements of oxygen ions around nickel should have some effect on the coordination about manganese and cobalt. Instead, the Mn–O and Co–O peaks remain as single peaks of constant FWHM even as they move to shorter distances due to delithiation. This suggests that although the material is single-phase and shows no ordering, manganese and cobalt may form randomly distributed clusters with minimal sharing of oxygen ions with nickel. Despite this clustering, the continuing shift of all three white lines demonstrates electronic continuity between clusters. Such clusters cannot be resolved by diffraction experiments due their small size.

Any charge compensation mechanism requires some change in magnetic moment. In a previous study on this compound,[76] the magnetic moment was found to decrease with delithiation up to 50% in agreement with models assuming nickel oxidation. In conflict with that model, however, delithiation beyond 50% generated a strongly increasing magnetic moment. In absence of manganese and cobalt oxidation, another explanation is required. If oxygen oxidation is reversible and also generates a magnetic moment, the formation of peroxide ions (O_2^{2-}) is a poor candidate because peroxide carries no unpaired electrons. Although the superoxide ion (O^{2-}) is magnetic, it requires an O–O bond length[91] of 1.33 Å which is less than the metal-oxygen distance in layered TM oxides. The diffusion of oxygen ions to interstitial positions would severely disrupt the structure.

A better explanation is the generation of electronic holes in the O 2p valence band[152,153] which generate a magnetic moment[154–156] by leaving unpaired spins. This scenario is illustrated in Figure 54 in which the oxygen and lithium ions are shown at three levels of delithiation. Because the oxygen ions are not sufficiently close to create peroxide or superoxide bonds, and because they do not form dioxygen gas, holes must form in the O 2p orbitals to enable charge compensation.

The ideal tool for the detection of oxygen holes is soft X-ray NEXAFS;[154] however, the adsorption of atmospheric contaminants during sample transfer in *ex situ* experiments can mask the true electronic structure. Therefore, *in operando* NEXAFS methods, with end-to-end air-free sample transfer, are needed to ensure accurate results.[136] Also, given sufficiently powerful magnets, X-ray

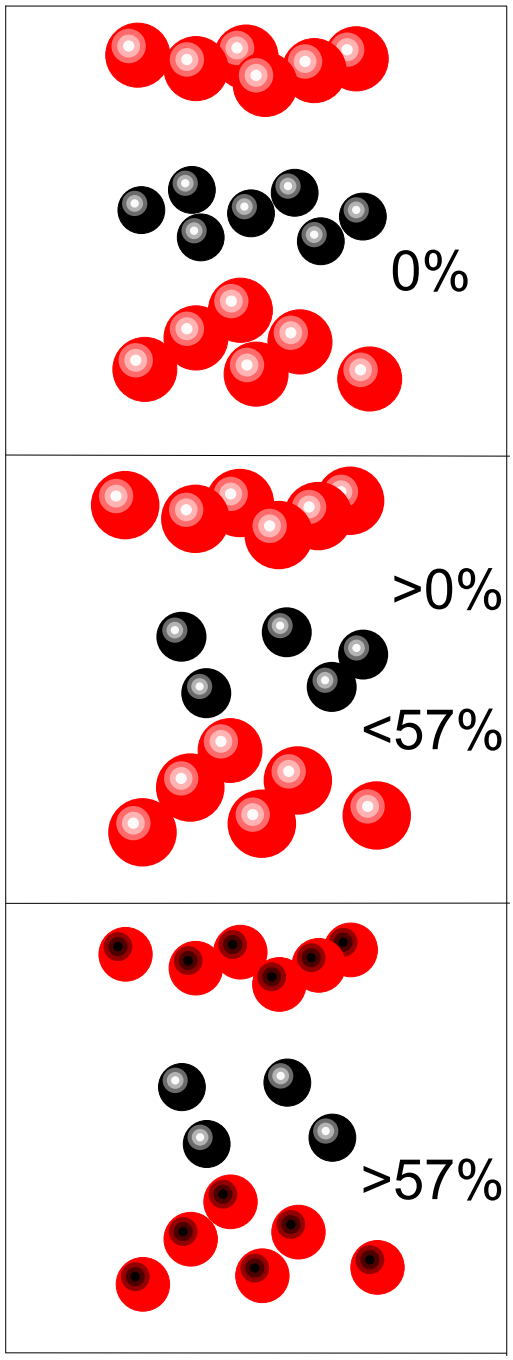

Figure 54: Schematic of delithiation between oxygen layers at three levels of delithiation with oxygen in red and lithium ions in black[92]

magnetic circular dichroism (XMCD) at the O K-edge[84] can detect magnetic moments in the O 2p valence band. A shortcoming of O K-edge NEXAFS is a lack of atomic structure information due to the interruption of the EXAFS region by TM L-edge absorptions. The oxygen oxidation mechanism is potentially crucial in the operation of lithium-air batteries which require charge compensation without transition metals.[12]

Conclusions The pristine material was found to contain nickel at an oxidation state slightly above Ni^{2+}, with cobalt and manganese slightly below Co^{3+} and Mn^{3+}, respectively. Charge compensation proceeds by the unexpectedly rapid oxidation of nickel to Ni^{4+} at 45% delithiation according to EXAFS.

Mn and Co XANES shifts up to 30% delithiation could not be explained by the effects of metal-oxygen bond contraction and are attributed to their oxidation to Co^{3+} and Mn^{4+}, respectively.

After 45%, however, each transition metal is in its maximum oxidation state and cannot oxidize further. Oxygen oxidation proceeds after that point mainly at oxygen sites bonded to Co^{3+}ions as evidenced by the continued contraction of the Co–O bond. This is proposed as an explanation for the anomalous magnetic moment increase seen by Li et al.[76]

Both XRD and EXAFS indicate a contraction of the basal plane with the removal of lithium between 0% and 57% followed by a stabilization, with the exception of the Mn–M distance. Additional lithium removal at 73% appears to occur without rearrangement of metal atomic and electronic structure. Isosbestic points in the XANES spectra indicate a single reaction proceeds for all three TM elements, but only below 57% delithiation.

The generation of oxygen holes after 45% delithiation is proposed to explain the charge compensation, the increase in the magnetic susceptibility without transition metal oxidation, and the structural trends. An *in operando* characterization method for the detection of oxygen holes in batteries, including lithium-air batteries, was suggested in which solid state powder pellet batteries are used.

4.2 In Operando *XANES and EXAFS on $Li_{1.17}Ni_{0.25}Mn_{0.58}O_2$*

In operando X-ray absorption spectroscopy was carried out on both a hard X-ray transmission cell and, for the first time, a soft X-ray-compatible cell, using cathode powder from the same production process. Transmission, near-surface fluorescence, and surface-sensitive Auger electron measurements indicate the oxidation of nickel and of oxygen. Jahn-Teller distortion in Ni EXAFS is deconvoluted, revealing the onsets of Ni^{3+} and Ni^{4+}. Hard X-ray *in operando* results are given in this section while soft X-ray results are presented in section 5.3

Introduction A variety of cathode materials for lithium-ion batteries has been studied *ex situ* at multiple states of charge using Near-Edge X-ray Absorption Spectroscopy (NEXAFS). More commonly, the same materials are studied *in operando* using a hard X-ray-transparent cell in order to study the delithiation process in greater detail and without needing to disassemble multiple batteries. Here we present a study of a single cathode material is studied *in operando* with hard X-rays, and, for the first time, is separately studied *in operando* with a soft X-ray-compatible ceramic battery as discussed in section 5.3.

Lithium-ion battery cathode materials generally require a transition metal (TM) ion which can attain multiple oxidation states in order to balance charge as lithium ions enter or exit. The higher-voltage (higher energy density) cathode materials are generally oxides. It is well known that when the TM ion reaches its maximum oxidation state, the oxidation state of oxygen can change, either leading to the loss of dioxygen gas, or at least to spectroscopic changes in NEXAFS at the O K-edge.

The necessity of studying the charge compensation mechanism of the overlithiated cathode material can be seen by analyzing the chemical formula: $Li[Li_{(1/3-2y/3)}Ni_yMn_{(2/3-y/3)}]O_2$. Table 12 illustrates the case for $y = 0.25$. Nickel appears in its lowest oxidation state while manganese appears in its highest oxidation state in common with similar materials.[92] However, the quantity of lithium greatly exceeds the capacity of the $Ni^{2+} \rightarrow Ni^{4+}$ redox couple. Full extraction of lithium requires further charge compensation.

As delithiation progresses, nickel oxidizes to balance charge, but manganese cannot oxidize further. Nickel must reach its tetravalent state long before delithiation is complete, and oxygen must then oxidize to balance charge, as shown in Table 13. The crossover point differs from one

Table 12: Charge Balance, Pristine compound

	Stoich.	Ox. State	Charge
Li	1.17	1	1.17
Ni	0.25	2	0.50
Mn	0.5825	4	2.33
O	2	-2	-4.00
Sum			0.0

Table 13: Charge Balance, Ni^{4+} Compound

	Stoich.	Ox. State	Charge
Li	0.67	1	0.67
Ni	0.25	4	1.00
Mn	0.5825	4	2.33
O	2	-2	-4.00
Sum			0

compound to the next, however. It will be shown that in the present compound, nickel reaches its highest oxidation state prior to that expected for the stoichiometry of $Li_{0.67}Ni_{0.25}Mn_{0.58}O_2$ and yet, after this point, delithiation continues. This in contrast with $LiNi_{1/3}Mn_{1/3}Co_{1/3}O_2$ in which Ni^{4+} appeared at 45% delithiation rather than the expected 66%,[92] as demonstrated by the evolution of Jahn-Teller distortion in EXAFS data.

Experimental Methods Stoichiometric amounts of lithium acetate, nickel nitrate, and manganese acetate were dissolved in nanopure water and heat-treated as described previously.[136]

Solid state cells were made as described previously[136] using a composite graphite anode (24 wt% graphite) and a composite cathode composed of 74 vol% electrolyte ($70Li_2S{\cdot}30P_2S_5$), 16 vol% graphite and 10 vol% active material. Three cells were mounted between aluminum plates with 0.4" diameter holes on each side and charged using a Pine WavenowXV potentiostat in galvanostatic mode with un-grounded connections.

At NIST beamline U7A, NEXAFS was carried out using simultaneous PEY and FY detection at the O K-edge, Mn L-edge and Ni L-edge. The analysis chamber was maintained at 3 x 10^{-8} Torr during the experiment. The cell was charged in 1 h increments at rates from 3 μA to 125 nA in order to maintain a cell voltage below 4.8V. The depth of delithiation is calculated according to the theoretical capacity of 361 mAh/g.

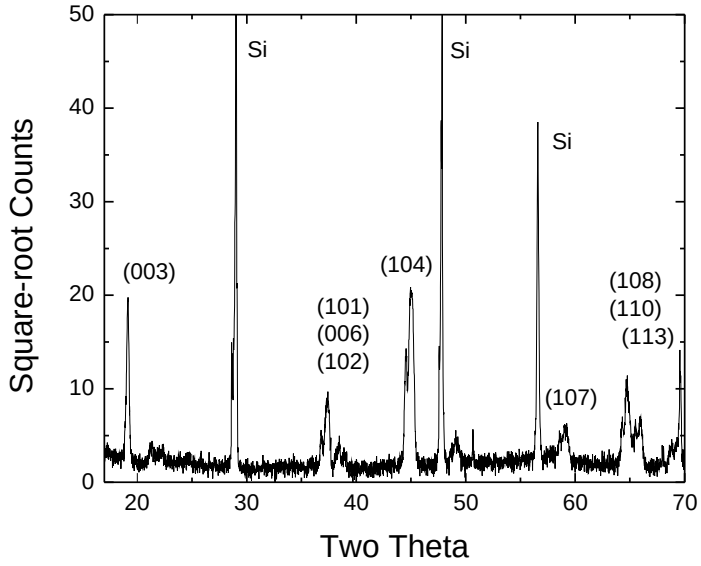

Figure 55: X-ray diffractogram, overlithiated compound, pristine

Standard methods[17] were used to spray a mixture of cathode material, PVDF, and acetylene black on aluminum foil. Pouch cells were constructed using heat-sealable moisture barrier material (Shield Pack, Inc.[128]) such that a 10 mm wide beam was absorbed by lithium metal, electrolyte, and the aluminum-foil layer but not by nickel or copper foil. Transmission experiments were performed at NRL beamline X11A at NSLS while the cell was charged at constant current using the same potentiostat. A C/12 rate was calculated based on the many-cycle reversible capacity of 220 mAh/g,[17] although the lithium concentrations are reported relative to the theoretical capacity of 361 mAh/g. Each scan took 45 minutes. After the cell reached 4.8V after approximately 12 h, the cell was allowed to rest at open circuit while subsequent transmission scans were taken.

4.2.1 Analysis of First Charge

Results

XRD, overlithiated compound The X-ray diffractogram for $Li_{1.17}Ni_{0.25}Mn_{0.58}O_2$ is given in Figure 55. Although it shares the $R\bar{3}m$ crystal structure with $LiNi_{1/3}Mn_{1/3}Co_{1/3}O_2$, additional lithium is incorporated into the transition metal ion layer. A small superlattice reflection between 21 and 25° 2θ is consistent with the results of Thackeray et al.[108] for similar compounds.[136]

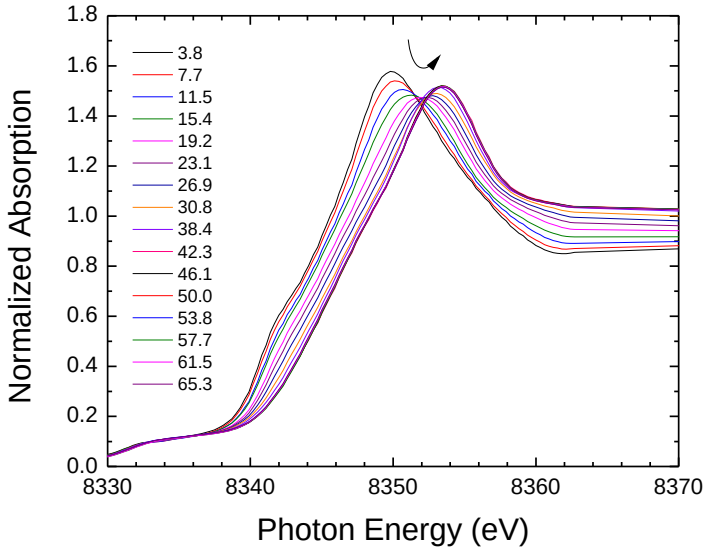

Figure 56: Ni K-edge XANES, overlithiated compound, first charge

XANES Figure 56 shows XANES results including 15 scans while charging at C/12 and two additional scans while resting the cell. In the first charge, the Ni XANES shows a significant shift to higher energies but with a near-isosbestic point in the white line. After 38% of the total amount of lithium is removed, and during the rest period, the Ni XANES shows little change.

The Mn K edge XANES (Fig. 57) shows very subtle changes while maintaining four isosbestic points, marked with carats. In similarity with Ni XANES, an additional near-isosbestic point is seen at the white line. Isosbestic points indicate a single reaction is taking place.[54] Although the lack of rigid shift in the XANES suggests the lack of oxidation, the 1s $\rightarrow$ 4sp transition is not sensitive to the Mn 3d electrons, but to the Mn–O bond distance and bond geometry. This effect can also blur an isosbestic point.[92]

EXAFS Analysis In keeping with the XANES results in Figure 56, the EXAFS results include two scans during a rest period after the first charge; however, the effect of the rest on EXAFS is more significant. In Figure 58, Ni EXAFS shows a continuous progression from a single Ni–O peak (Ni^{2+}) to a Jahn-Teller distorted pair Ni–O peaks (Ni^{3+}) followed by a sudden jump to a single, broader Ni–O peak at a nearer distance (Ni^{4+}). The jump occurs after 38% delithiation and is followed by a gradual increase in peak height followed by a decline during the rest period.

As in Mn XANES, Mn EXAFS (Fig. 59) shows minor changes with delithiation. Although

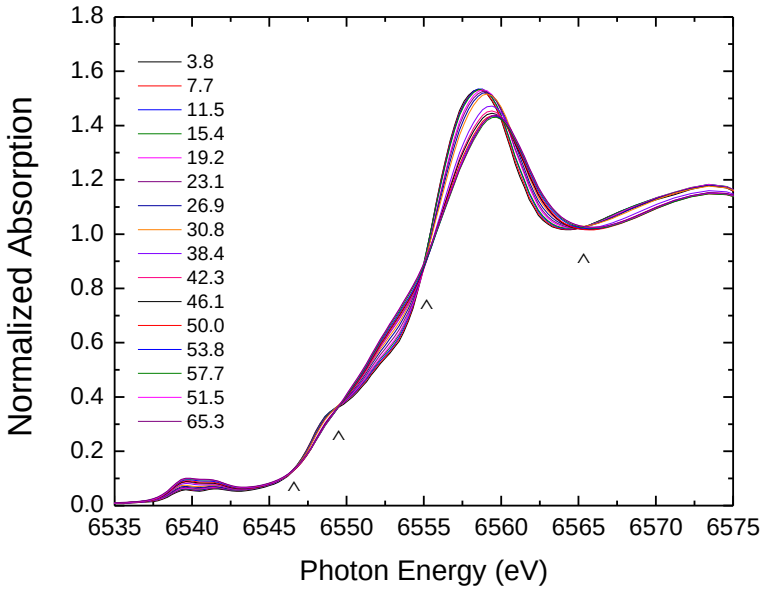

Figure 57: Mn K-edge XANES, overlithiated compound, first charge

the Mn–O peak distance changes only slightly, the peak shape does widen before stalling at 38% delithiation.

Analysis of Structural Trends ARTEMIS modeling (see Section 3.3) was used to quantify the contraction and expansion of the metal-oxygen and metal-metal peak distances while quantifying trends in the Debye-Waller factors which represent thermal and static bond-length disorder. Furthermore, the Jahn-Teller distortion about nickel was quantified during the first charge. For Ni EXAFS, S_0^2 was calibrated to be 0.75 meaning that 25% of the photoelectrons did not participate; for Mn EXAFS, S_0^2 was 0.6.

Figure 60 (top) shows the relative amplitude of the two Jahn-Teller distorted Ni–O peaks in Figure 58. The maximum amplitude is S_0^2, or 0.75. The relative amplitudes are equal near 20% delithiation; this can identified as Ni^{3+}. The positions of the two deconvoluted peaks are given in Figure 60 (bottom). The distances are relative to the crystallographic distance between Ni and O in the pristine compound. At 30%, the farther Ni–O peak is barely distinguishable from a single peak, as suggested by the error bars, and oxidation to Ni^{4+} is nearly complete. After 38% delithiation, no further contraction in the Ni–O distance is seen, indicating a stable bond between nickel and oxygen.

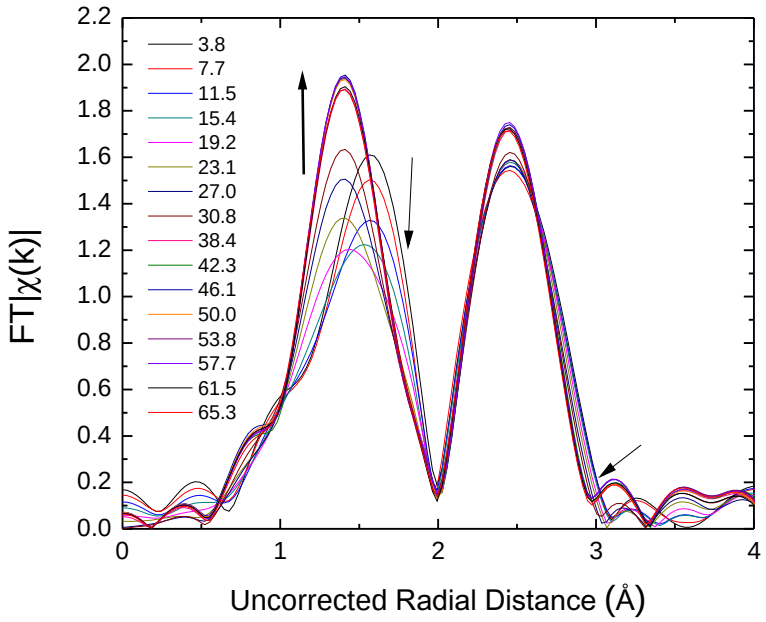

Figure 58: Ni K-edge EXAFS, overlithiated compound, first charge, with arrows indicating trends

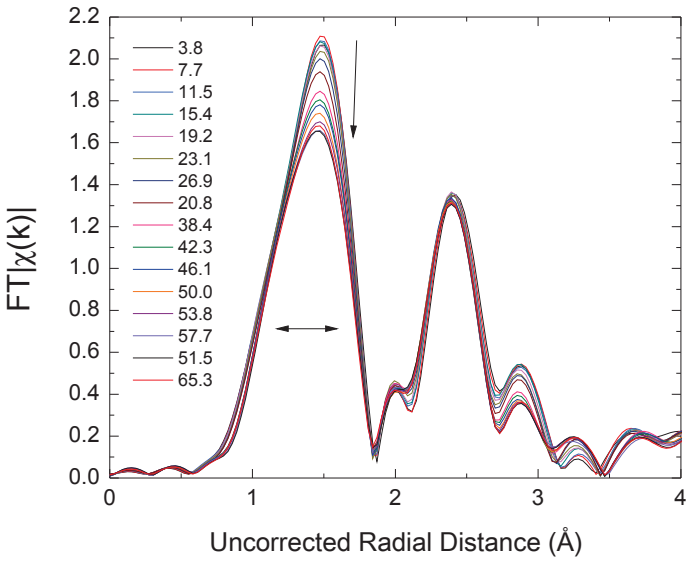

Figure 59: Mn K-edge EXAFS, overlithiated compound, first charge, with arrows indicating trends

Figure 61 summarizes a fit of the Mn EXAFS in Figure 58. The error bars represent uncertainty in the least-squares fit. While the Mn–O distance shrinks during delithiation both before and after the appearance of Ni^{4+}, the process is more rapid before 38% delithiation. Simultaneously, the Debye-Waller factor increases, quickly at first but more slowly after 38%. During the rest period, the Mn–O bond distance is stable while the bond length disorder decreases.

Figure 62 compares the fits of the Ni–M and Mn–M EXAFS peaks. Because EXAFS does not provide an absolute distance scale, both peak distances were calibrated to the crystallographic distance in the first scan. However, XRD results in Fig. 55 showed evidence of ordering in the transition metal layer, and Fig. 62 provides further evidence that the two metals are not evenly mixed. Indeed, in an overlithiated material, many of the second-nearest neighbors are lithium ions which are nearly undetectable in EXAFS; as these are removed from the structure, the Ni and Mn ions can be expected to diffuse through vacancies to new positions.[16]

In the first half of the delithiation process, the Ni–M distance contracts more rapidly than does the Mn–M distance. In the second half of delithiation, however, the difference is very stark as the error bars no longer overlap. The Mn–M distance gradually increases while Ni–M continues to shrink, indicating that the average Mn ion is in a region with an expanding a-axis. It must be kept in mind, however, that as neighboring atoms move closer to Ni, 70% of these neighboring atoms can be expected to be Mn atoms due to the stoichiometry. Clustering of Mn about Ni has been observed in similar overlithiated materials using ^{6}Li MAS-NMR.[44]

Discussion Recently developed cathode materials achieve high specific capacities by relying on the oxidation of oxygen, as evidenced by their stoichiometries. In $LiNi_{1/3}Mn_{1/3}Co_{1/3}O_2$, out of a theoretical capacity of 295 mAh/g, 172 mAh/g is reversible[76] in spite of a $Ni^{2+} \rightarrow Ni^{4+}$ redox couple which can only accomodate 133 mAh/g. In $Li_{1.17}Ni_{0.25}Mn_{0.58}O_2$, out of a theoretical capacity of 361 mAh/g, 220 mAh/g[17] is reversible even though the $Ni^{2+} \rightarrow Ni^{4+}$ redox couple can only account for 137 mAh/g. To ensure safety and reliability, the oxygen redox mechanisms is these materials must be measured directly.

In $LiNi_{1/3}Mn_{1/3}Co_{1/3}O_2$, EXAFS analysis of the Jahn-Teller distortion showed[92] that in the pristine compound, nickel was already oxidized slightly beyond Ni^{2+}. By 20% delithiation, the

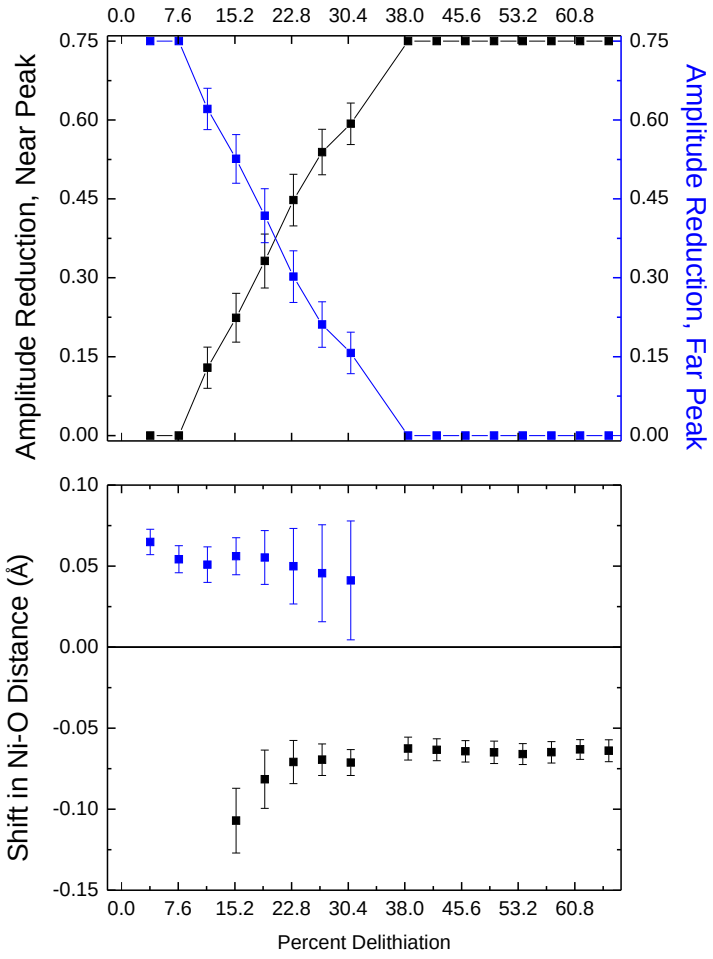

Figure 60: Deconvolution of Jahn-Teller Distortion, overlithiated compound, first charge

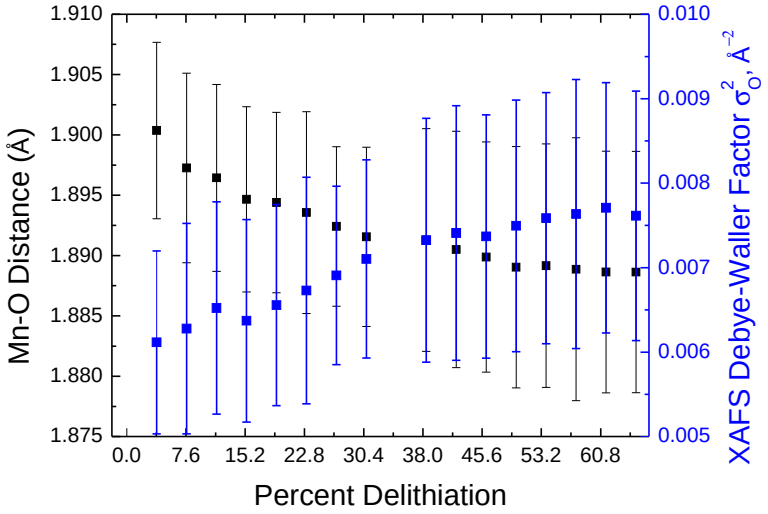

Figure 61: Mn–O Bond Length and Bond Disorder, overlithiated compound, first charge

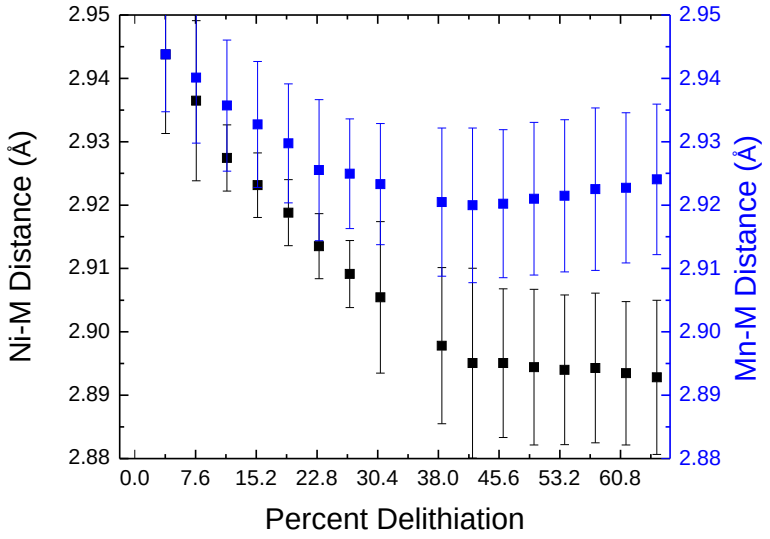

Figure 62: Ni–M and Mn–M Bond Lengths, overlithiated compound, first charge

Jahn-Teller distortion had already passed the Ni^{3+} point. However, Ni^{4+} was not reached until 45% delithiation. In the present compound, Ni^{2+} also reaches Ni^{3+} at about 20% delithiation. Ni^{4+} is reached more quickly, however, appearing by the 38% point. This indicates that although the $Ni^{2+} \rightarrow Ni^{3+}$ reaction occurrs at the same rate, the $Ni^{3+} \rightarrow Ni^{4+}$ reaction is more rapid in the present compound. In both cases, the oxidation states were determined not by the positions of K-edge XANES edges, which are always distorted by the local bonding environment, but by the evolution of Jahn-Teller distortion in Ni EXAFS which is sensitive to the 3d orbital configuration. Although Mn^{4+} is not Jahn-Teller active, the oxidation states of manganese, nickel, and oxygen can be detected, *in operando*, using soft X-ray NEXAFS.

Conclusions for first charge *In operando* EXAFS reveals that charge compensation by the oxidation of nickel proceeds faster than the stoichiometry would predict, reaching Ni^{4+} at only 38% delithiation. Although manganese is maintained in a quadrivalent state, the continous contraction of the Mn–O bond is evidence of the continued oxidation of oxygen ions. The stable bond distance between nickel and oxygen, however, suggests a high degree of covalency.

EXAFS modeling shows trends in the metal-metal distances which indicate that nickel and manganese are segregated into separate environments. However, after the appearance of Ni^{4+} and during

the inevitable formation of oxygen holes, the structure becomes highly stable while delithiation continues.

4.2.2 Analysis of Second Charge and Comparison with First Charge

In this section, *in operando* hard X-ray absorption data for the second charge of a pouch cell made with the overlithiated compound is presented. Between the first and second charge, X-ray diffraction was not performed; firstly, beamline X11A lacks diffraction capability and secondly, the packaging of the cell would have introduced spurious reflections into the signal. (Simultaneous *in operando* XAS and XRD should be possible given the necessary beamline equipment as well as an *in operando* cell with amorphous polymer windows.) In this section, the percentage of lithium in the cathode material is not calculated because the amount of lithium remaining in the cathode after discharge is not accurately known. Instead, the scan numbers are given where each scan represents 45 minutes of charging at 370 mA, just as was done for the first charge cycle.

When a cathode is delithiated, relithiated, and delithiated for a second time, it is expected that the crystal structure will not return to its pristine state. However, the nature of the irreversible capacity loss is not known, although Armstrong et al.[16] detected the loss of oxygen gas. If the crystal merely gains oxygen vacancies, the irreversible capacity may have profound effects on the EXAFS data. If, however, the defects lead to the sloughing off of Li_2O and O_2 gas, the X-ray probe may not be sensitive to the loss of those species. XRD will be less sensitive to Li_2O, while hard X-ray XAS will be totally insensitive to oxygen atoms not bound to a transition metal. Neutron diffraction analysis by Armstrong et al.,[16] however, suggested that the loss of Li_2O from the surface would be accompanied by the diffusion of transition metal elements into lithium vacancies left in the overlithiated layer. The replacement of a lithium ion by a transition metal ion should be easy to detect in the second coordination shell in EXAFS. If these transition metal ions from the surface dissolve into the electrolyte, through, they will not be easily discerned in EXAFS.

Although the cell voltage is sensitive to the chemical potential of lithium ions, which will depend in part on the level of defects in the crystal, the cell voltage is generally distorted by ohmic resistance, which changes as a function of delithiation.[17]

In this experiment, the relithiation (discharge) step was ended at 3.0 V vs V_{Li/Li^+}, which was the

same as the initial open circuit potential. Over time, however, the open circuit potential rose to 3.4 V before the second charge cycle began. While this voltage difference should indicate a higher state of charge at the beginning of the second cycle, XANES and EXAFS appear very similar in the first scan of each cycle.

XANES results for the second charge In order to follow the trend of nickel oxidation, the 50% edge jump point was measured for each normalized spectrum in the first and second charges. Each charge was ended after 4.8 V was reached, although this point was reached more quickly in the second charge due to the irreversible capacity loss in the first cycle. In Figure 63, that initially the XANES curves follow the same trend, indicating that the state of charge at the beginning of each cycle was similar. However, at the point where nickel reaches the Ni^{4+} state and ceases to oxidize, the two trends diverge. In the second charge, the Ni K-edge failed to reach the same energy position compared to the first charge. However, in each case the XANES seem to stall at a constant oxidation state.

At the end of the second cycle, the cell voltage rose above 4.8 V and the XANES edge quickly moves to higher energies. This occurred due to a limitation on of the Pine potentiostat and although voltages above 4.8 V should be avoided due to the oxidation of the liquid electrolyte which occurs at high potentials, this result is intriguing and requires further study.

The Ni K-edge XANES from the first (thin lines) and second cycle (thick lines) are compared in Figure 64. In the first scan of each charge cycle, the Ni XANES spectra are remarkably similar in shape, although some divergence appears by the twelfth scan.

EXAFS results for the second charge Figure 65 compares the Mn EXAFS from charge 1 to charge 2 in a stacked plot. The EXAFS are remarkably similar, differing mainly in the height of the Mn–O peak, which is initially higher in the second cycle, but which is eventually lower as compared to the first cycle. The feature near 2.8 Å follows the same trend, although the Mn–M is almost identical in each pair of scans. While the Mn–O peak height differs in intensity from charge 1 to charge 2, the peak widths are similar. In either charge cycle, the low height of the Mn–M peak is evidence that Mn is not fully surrounded with transition metal ions, as in the $LiNi_{1/3}Mn_{1/3}Co_{1/3}O_2$

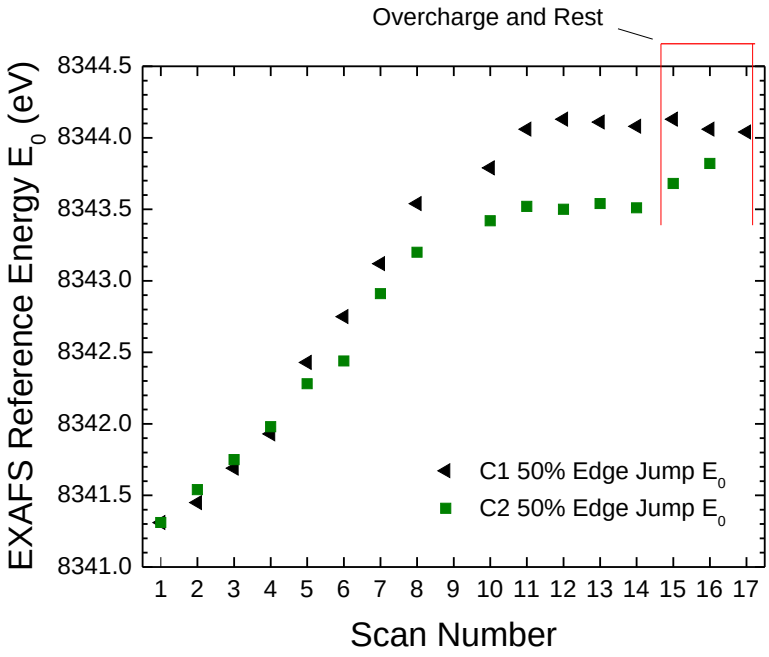

Figure 63: E_0 point for Ni K-edge, overlithiated compound, during first and second charge (C1 and C2) with overcharge and rest periods indicated

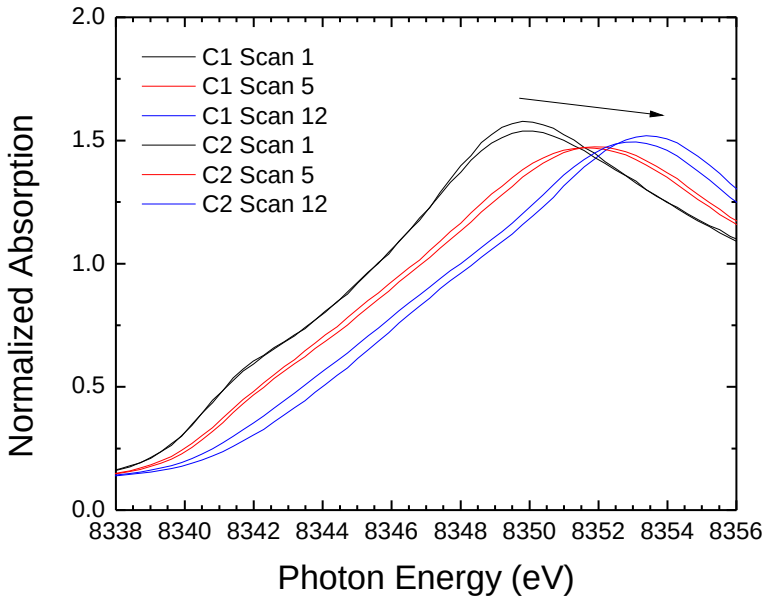

Figure 64: Selected Ni K-edge XANES, overlithiated compound, from first charge (C1, thin lines) and second charge (C2, thick lines)

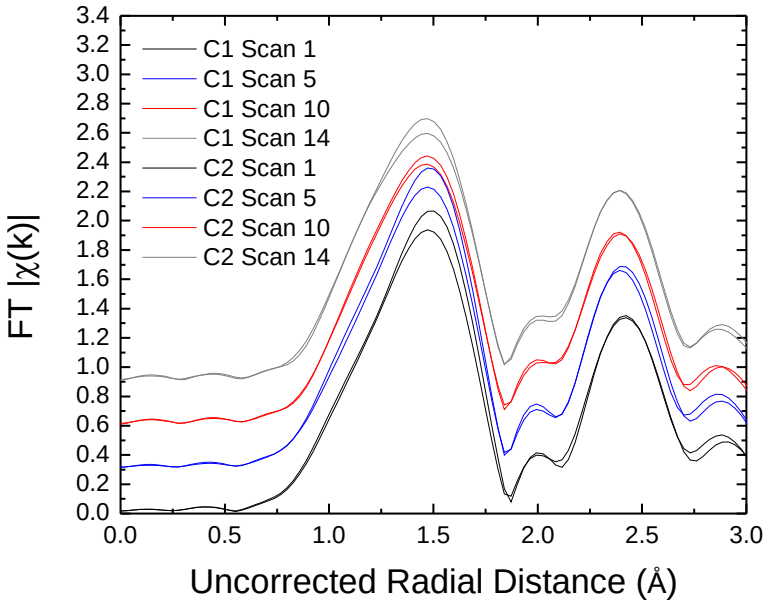

Figure 65: Comparison of stacked Mn K-edge EXAFS, overlithiated compound, from first to second charge

which has more intense Mn–M peaks. Instead, within the overlithiated transition metal ion layer, the neighboring atoms around manganese are a mixture of transition metal ions and lithium ions. Here, no increase or decrease in the Mn–M peak height is seen.

This result is in contrast to the conclusions of Armstrong et al.[16,114] whose neutron scattering results suggested that the lithium in the overlithiated layer is irreversibly extracted and, furthermore, is replaced with transition metal ions which diffuse from the edge of the crystal into the bulk. Because lithium ions are poor scatterers in EXAFS, it is possible that lithium vacancies may be indistinguishable from lithium ions. However, an increase in the Mn–M peak height is not seen, indicating that the proportion of transition metal ions about manganese does not increase.

The differences seen in the Ni K-edge XANES spectra are reflected in even larger differences in the Ni EXAFS. In Figure 66, stacked EXAFS scans from the first and second charge are compared. Jahn-Teller distortion is clearly seen in scan 5, although the progression from Ni^{2+} to Ni^{3+} is slower in the second cycle. The difference is much more dramatic in scan 10, however, in which the tall, narrow Ni–O peak associated with Ni^{4+} has not formed in the second cycle. In scan 14, at a point where the cell was below 4.8 V in each cycle, the blunted second-cycle peak has not grown further. Ultimately, a narrow Ni–O peak never forms.

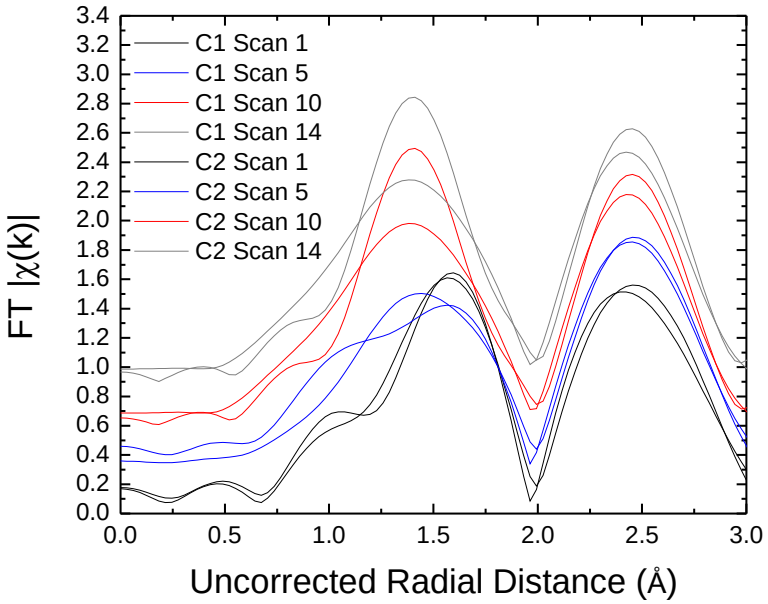

Figure 66: Comparison of stacked Ni K-edge EXAFS, overlithiated compound, from first charge (thin lines) to second charge (thick lines)

To quantify these differences, modeling in ARTEMIS was attempted. The initial hypothesis was that Ni^{3+} is retained at all states of charge in the second cycle, and that two Ni–O peaks were convoluted together. Such a deconvolution could be used to estimate the proportion of inert Ni^{3+}. This would be consistent with the formation of a second phase containing Ni^{3+} in addition to a phase containing Ni^{4+}. Unfortunately, no stastically valid deconvolution of the blunt Ni–O peak into two narrow peaks could be found.

In comparison with both the Ni and Mn EXAFS for $LiNi_{1/3}Mn_{1/3}Co_{1/3}O_2$, the height of the Ni–M peak is reasonable for nickel surrounded by (approximately) six transition metal neighbors. In Figure 66, a decrease in Ni–M peak height is seen from the first cycle to the second.

Conclusions for the second cycle In the second charge, as in the first, the charge compensation mechanism involves the oxidation of nickel up to a limit beyond which no further oxidation of nickel occurs. Beyond that point, oxidation of oxygen occurs to balance charge. However, in the second cycle the average oxidation state of nickel, throughout the bulk of the particles, becomes stagnant at a level below Ni^{4+}.

No significant changes are seen in Mn EXAFS from the first charge to the second charge, indicating that the role of manganese does not change. Although the Mn–M peak height is low in agreement with prior work indicating that manganese is surrounded by lithium in the overlithiated layer, no gain of peak height is seen in the second cycle: Neighboring lithium ions in the overlithiated plane are either not removed at all, or simply leave vacancies behind which are not filled with transition metals. Instead, Ni EXAFS shows a decrease in Ni–M peak height from the first to the second charge, suggesting that transition metals neighboring nickel diffuse away. Alternately, some percentage of nickel may diffuse into the lithium-ion plane while retaining the same number of neighboring oxygen ions.

4.3 Comparison of $LiNi_{1/3}Mn_{1/3}Co_{1/3}O_2$ to $Li_{1.17}Ni_{0.25}Mn_{0.58}O_2$

The two compounds studied in this Chapter are very similar in terms of electronic structure and crystal structure. In the respective pristine compounds, Ni^{2+} and Mn^{4+} are present in each case in spite of the difference in stoichiometry. In each case, charge compensation is achieved through the oxidation of nickel but not manganese. However, after the cessation of the oxidation of nickel, delithiation continues in each case, suggesting an alternative charge compensation scheme involving oxygen oxidation.

They also share the $R\bar{3}m$ crystal structure in which the transition metal layers contain a mixture of transition metal ions.While the crystallographic differences between the two are not pronounced in XRD because the transition metals exist in the same plane, the differences in local coordination become clear when EXAFS is employed due to its inherent element specificity. Due to the layered nature of the crystal structure, each transition metal is sensitive only to its oxygen ligands and to its second nearest neighbors within the basal plane. In the case of $LiNi_{1/3}Mn_{1/3}Co_{1/3}O_2$, the coordination environment of three different transition metal elements were compared and were found to differ. Similarly, in $Li_{1.17}Ni_{0.25}Mn_{0.58}O_2$, the structural trends with delithiation, from the perspective of each transition metal, were found to diverge.

The differences in terms of XANES, EXAFS, and in terms of element-specific structural trends are discussed in this Section.

XANES Comparison The trends seen in the manganese XANES with delithiation are very similar between the two compounds. In each case, the spectra showed no rigid shift to higher energies with delithiation, suggesting a lack of redox activity. However, the spectra were distorted about a series of isobestic points, resulting in a half-edge jump position which decreased in energy with delithiation. In each case, the movement of the white line to higher energies indicates the contraction of the oxygen coordination shell. For the first compound, a procedure developed by Grant Bunker was applied which scaled the XANES in energy to attempt to account for the Mn-O contraction seen in EXAFS. The scaled scans overlapped to form a new isosbestic points, which indicated that the only changes in Mn XANES were structural and not due to oxidation.

Strong similarities were also seen in Ni XANES, in which a simpler spectrum shifted uniformly to higher energies with delithiation. In the pristine compounds, a shoulder is seen which disappears with delithiation. No isosbestic points are seen due the shift of the edge. The 1s $\rightarrow$ 3d transition, however, remains constant in energy in spite of the motion of the 1s $\rightarrow$ 4sp band.

The investigation of the Mn 1s $\rightarrow$ 3d pre-edge features for $LiNi_{1/3}Mn_{1/3}Co_{1/3}O_2$ did not yield any significant conclusions. Because the cross section for these peaks is low, the signal to noise ratio for any changes is large. Also, because the appearance of these transitions in the K-edge spectra is only due to a combination of bond hybridization and coordination geometry, the 3d density of states is poorly represented and furthermore, subtle changes in bond geometry have large effects of the shapes of these peaks. Current analysis methods cannot extract the 3d density of states from a TM K-edge spectrum.

EXAFS Comparison For the first compound, the Mn EXAFS show tall, narrow Mn-O and Mn-M peaks. The Mn-O peak height (with k^2 weighting) is 2.8 Å^{-2} while the Mn-M peak height is initally 2.5 Å^{-2} in height; this height decreases due to peak broadening with delithiation. A similar peak height ratio is seen in Co EXAFS. During delithiation, neither the Mn EXAFS nor the Co EXAFS show large changes in peak width, indicating that bond-length disorder is low and remains low.

For the second compound, the Mn EXAFS for the pristine compound indicates a similar Mn-O peak but a much smaller Mn-M peak. This agrees with the NMR results of Yoon et al.[44] which indicate a clustering of lithium ions about manganese such that in the overlithiated plane, three

nearest neighbors are lithium and three are manganese atoms. In this case, the Mn-M peak height is approximately $4/6$ of the height of the Mn-M peak in the first compound which had no overlithiation; this is reasonable because many manganese ions will form part of a cluster about nickel.

In comparing the Ni EXAFS from the two compounds, the qualitative trends are quite similar. In the pristine compound, the Ni-O peaks are shorter and broader than the Ni-M peaks. During delithiation, the initial Ni-O peak broadens, splits, and the old Ni-O peak gives way to the new Ni-O peak which grows to become tall and narrow. The final Ni-O peak is close in height to the Ni-M peak. In comparing the two compounds, the Ni-O peaks for the overlithiated compound are generally higher throughout the process. This may indicate some degree of lithium as a second nearest neighbor to nickel in the second compound; however, the Ni-M peaks are still much larger in area and in height compared to the Mn-M peak.

Structural Trends Comparison For the first compound, XRD data indicated a contraction of the a-axis, which is along the basal plane, followed by a cessation of this contraction after 50% delithiation. This unexpected trend was inferred to depend on the oxidation of the metal atoms to their maximum oxidation states, followed by the oxidation of oxygen which should lead to a more gradual contraction. EXAFS provides an excellent element-specific in-plane comparison with this XRD peak. Although EXAFS cannot extract absolute distances, the relative distance changes were informative. While the Co-M and Ni-M bond distances followed the XRD trend exactly, the Mn-M trend did not, showing a continued contraction in the basal plane. At the same time, the Co-O bond distance continued to contract across the entire range of delithiation, while the Mn-O and Ni-O bond distances ceased to contract. This indicated that for the first compound, the presence of oxygen holes neighboring cobalt caused the Co-O bond distance to contract in the later stages of delithiation in spite of the lack of oxidation seen in Co XANES.

For the second compound, the contraction of the basal plane showed a similar contraction up to about 38% delithiation. Intriguingly, the Mn-M distance begins to expand gradually after this point. The Mn-O distance, however, contracts gradually over the entire range of delithiation. In either compound, the rate of contraction with delithiation nearly stopped when only about half of the expected lithium ion capacity was removed, suggesting a change in the charge compensation

mechanism.

For nickel, the structural trends are similar from one compound to the next. Contraction of the Ni-M distance proceeds until reaching a limit. Simultaneously, Ni-O peak quickly develops Jahn-Teller distortion followed by the formation of a new, narrower Ni-O peak which remains fairly constant during further delithiation. The undistorted single peak indicates the formation of Ni^{4+} which remains constant during further delithiation. (For the second charge of the overlithiated compound, the XANES and EXAFS indicated that Ni^{4+} was not reached, but that a limiting case was reached at the same degree of delithiation.) The cessation of contraction of the Ni-M peak distance corresponds exactly to the cessation of oxidation of nickel. After this point, only oxygen-related charge compensation mechanisms remain as possibilities.

CHAPTER V

SOFT X-RAY ABSORPTION SPECTROSCOPY

In this chapter, the results of three soft X-ray NEXAFS experiments are discussed. In these studies, the X-ray beam is quickly absorbed by most forms of matter, including the sample. In place of detecting the transmitted beam, as was the case in the last chapter, here the absorption of X-ray is evidenced by the detection of Auger electrons and fluorescence from the sample surface. As discussed in section 3.1.2, the electrons and fluorescence emanate from the near-surface regions and much of the signals are absorbed before they reach the detectors. The fluorescence is better able to penetrate matter as compared to the electrons, though, allowing for surface-to-bulk comparisons to be made.

Given the low information depth, neither gases, nor packaging, nor the condensation of atmospheric moisture and hydrocarbons is allowable, and so the sample must be mounted in a high-vacuum chamber. If the sample is a nonporous, solid thin film, it suffices merely to load the sample bar onto a robotic manipulator in a sample introduction chamber, evacuate that chamber, and then transfer the sample bar into the main analysis chamber, which is always kept under high vacuum for cleanliness. For a porous pellet, and especially for sulfide-based materials, this procedure is not sufficient and the sample must be kept as dry as possible at all times. The procedure for shipping such samples, and transferring them into a vacuum chamber, is described in section B.2.8.

In this chapter, three experiments are presented, all of which center around the O K-edge. First, an experiment on a two-terminal semiconductor device, termed a memristor, is presented. In that experiment the O K-edge absorption was used to determine the mode of charge compensation in $LiNbO_2$ as lithium ions are caused to drift from one terminal to the other. Although charge compensation could be attributed largely to niobium, this could be detected via the hybridization between niobium and oxygen. (Nb absorption edges are not conveniently accessed.) The results of this experiment are instructive in interpreting *in operando* results from lithium ion batteries, although the device itself is not a battery.

The feasibility of soft X-ray *in operando* spectroscopy on sulfide pellet batteries was demonstrated in Petersburg et al.[136] in 2009 using $LiCoO_2$. At that time the pellet battery design had numerous problems. First, the lithium metal anode was later found to cause dendrites to form through the porous structure; for this reason the relatively high rates of current passed through the cell can be explained by dendrite conduction. (See section 3.5.3.) Second, the solid electrolyte (see section 3.5.2) had not yet been fully amorphized or heat treated, leading to low ionic conductivity and contributing to the preferential formation of dendrites. Third, the cathode mixture contained far too little electroyte and far too much conductive additive to transfer lithium ions effectively. Fourth, the sample fixtures described in section 3.6 had not been developed; a sample fixture was assembled within a glovebag, described in section B.2.8, at the synchrotron beamline. This time-consuming procedure, carried out with inadequate N_2 flow, led to the contamination of the samples by atmospheric moisture. Therefore, the spectroscopic results reflect a high degree of surface contamination and a very low amount of cathode delithiation.

The improved techniques described in Chapter 3 were used for the soft X-ray *in operando* study of the overlithiated compound described in section 5.3. Using these techniques, dendrite formation was eliminated, electrolyte conductivity was greatly improved, composite electrode mixtures were optimized, and surface contamination was minimized. As a result, the spectroscopic changes over time can be attributed to the efficient delithiation of the cathode material. In that section, the soft X-ray *in operando* results are described in conjunction with the hard X-ray *in operando* results for the same material in section 4.2.

Finally, in section 5.4, a comparison is made between the O K-edge NEXAFS on memristors and on batteries in order to better understand d-p hybridization in the O K-edge spectra.

5.1 In Operando *NEXAFS using $LiNbO_2$ Memristors*

In a lithium battery, lithium ions removed from the cathode layer diffuse through the electrolyte towards the anode during charging. At the same time, to balance charge, negative electrons must pass through an external circuit from the cathode to the anode. The electrons leave behind electronic holes in the cathode material which tend to be localized in the Ni e_g orbitals and in hybridized TM 3d - O 2p orbitals such as the Co–O bond. This process of charge compensation is difficult to study, in

part, due to the slow delithiation reaction which can take a day or more to complete. A much faster alternative to *in operando* soft X-ray spectroscopy on pellet batteries, which also creates electronic holes in a cathode material, was developed using a thin film device.

This device consisted of a thin film of $LiNbO_2$ or $LiCoO_2$ (c-axis oriented but not single-crystalline, 120 nm thick) on an insulating sapphire substrate. Two nickel metal strips were deposited atop the $LiNbO_2$ or $LiCoO_2$ at either end of the 1 cm film, leaving an approximately 5 mm gap. When an electric field is applied to the device, lithium ions diffuse across the thin film and pile up[53] under one ion-blocking metal contact while being depleted near the opposite contact. Due to the electronic conductivity of the thin film, current continues to flow while a steady-state distribution of lithium ions forms across the entire thin film. This interplay between ionic and electronic conduction gives rise to a time dependent device resistance. In the present experiment, however, the steady-state distribution of ions was maintained over time for the benefit of the spectroscopy, which took over ten minutes per scan.

Because this thin film device contains no electrolyte, the thin film is not permanently delithiated and it is difficult to directly measure the degree of delithiation or overlithiation near either contact. Although the device is potentially useful in evaluating (thin film) intercalation cathode materials, it was first developed for use as a semiconductor device by Prof. Alan Doolittle and Jordan Greenlee at Georgia Institute of Technology. In that context, the two-terminal device is termed a memristor, being a resistor of time-dependent resistance. (A complementary device, the ion-gated transistor, uses three terminals and was described in Section A.1.) The potential importance of this device and applications in advanced computing are discussed in Greenlee et al.[52]

The two materials, $LiNbO_2$ and $LiCoO_2$, share the same $R\bar{3}m$ crystal structure as well as the same formal charge on the transition metal ion, 3+. However, where Co^{3+} has a $3d^6$ (or 3d $t_{2g}{}^6$ low spin) configuration, Nb^{3+} has a $4d^2$(likely 4d $t_{2g}{}^2$ with unpaired spins) configuration. The degree of covalency of the Nb–O bond as compared to the Co–O bond is not known. In spite of its high conductivity, $LiNbO_2$ has not yet been studied in a lithium battery context. In contrast to lithium niobate, $LiNbO_3$ which is widely used as an optical material, $LiNbO_2$ is difficult to synthesize, especially in thin film form. A wide variety of further developments on this material can be expected from the Doolittle-Alamgir collaboration in the future.

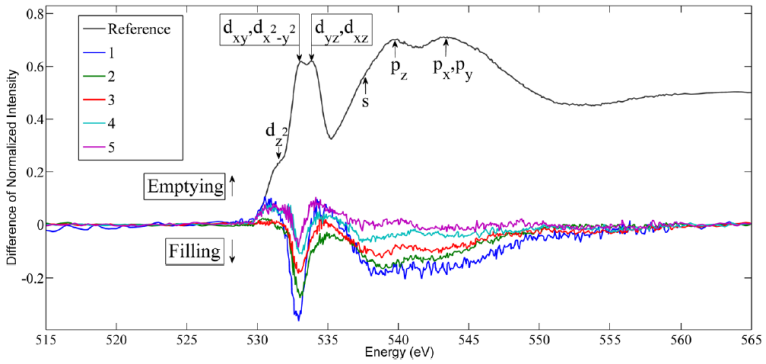

Figure 67: Difference NEXAFS Spectra of Biased $LiNbO_2$along the Electric Field Direction vs. As-Grown Film[52]

Experimental Methods A sample bar was developed to hold up to three thin film memristors at a time while allowing any one of the three devices to be polarized. The sample bar design is described in Section 3.6.2. Electrically, the sample bar was common and was attached to the counterelectrode lead of the Pine potentiostat. A vertical electric field, either positive or negative, could be applied across the thin film. Constant voltages were applied, and lithium diffusion profiles across the samples reached steady state in under an hour. Because the resistivity of $LiCoO_2$ is much greater than that of $LiNbO_2$, the current required to maintain a voltage was much higher in $LiNbO_2$. The spatial effect on the O K-edge was much greater for $LiNbO_2$ however, and only the results for this material were published in Greenlee et al.[52]

Results The application of 2.0 V DC across a $LiNbO_2$ thin film yielded a surprisingly uniform spatial trend across the surface, with oxygen holes forming near the negative contact and none forming at the positive contact. In Figure 67 from Greenlee et al.,[52] O K-edge NEXAFS are given for the as-grown $LiNbO_2$ film (in black) along with difference spectra for five positions along the 5 mm gap between the nickel electrodes. The highest-energy absorption features represent hybridized O 2p - Nb 5sp orbitals. The lowest-energy absorption features are hybridized O 2p - Nb 4d orbitals. Although some oxygen holes are seen as enhanced absorption at the Fermi level (near the negative electrode), the d_{xy},$d_{x^2-y^2}$ orbitals are actually filled near the positive electrode.

First, it must be remarked that adding or subtracting 2.0 V DC from the open-circuit voltage of a lithium battery would be catastrophic, leading either to a rapid overlithiation of the surface of the

cathode material or the rapid overdelithiation of the cathode material. Overlithiation can lead to the formation of nonconductive Li_2O while overdelithiation leads to the breakdown of the intercalation cathode material. However, because the nickel metal contacts were blocking, lithium could not be removed from the material and very little lithium could, therefore, be removed from the vicinity of the opposite contact.

Second, the appearance of oxygen holes at the negative contact was striking. These holes were evidenced by an increase in the height of pre-peaks in the O K-edge spectrum near the Fermi level, much like the expected effect of removing lithium ions from the *positive* contact of a battery. Again, because the contacts were blocking, the (positive) oxygen holes formed at the negative contact to balance the negative charge. These holes dissipated when the field was removed.

Third, reduction was seen at the positive contact. At that contact, lithium ions were repelled from the region while electrons were attracted to it. Therefore, electrons occupied some of the Nb 4d orbitals, presumably reducing Nb^{3+} to Nb^{2+}. This could not be directly measured at NIST beamline U7A because the Nb L_{III} resonance ($3p \rightarrow 4d$) binding energy is at 2371 eV, far above its energy range. (Nb M edge NEXAFS was attempted but the edge was extremely broad and lacked intensity.) The Nb L-edge energy is simultaneously below the lower limit for most hard X-ray beamlines, which is in the region of 4 keV. At the NSLS, only NIST beamline X24A is capable of measuring this edge. If the localized reduction of Nb^{3+} could be measured and compared to niobium oxide reference compounds, the degree of localized delithiation could be more easily quantified as compared to the oxygen K-edge. However, the ability to detect changes in the Nb 4d orbitals via the oxygen edge demonstrates the versatility of O K-edge techniques.

Finally, from a battery perspective the results of this experiment can be used to rapidly screen new (thin film) cathode compositions. Provided the depth of delithiation can be estimated, and is sufficiently deep, the charge compensation mechanism can be approximated using thin films. Although in this case the film was fully lithiated and no pre-existing oxygen holes were present, thin films can be delithiated and then biased. Especially in cases where only 3d metals are present, the charge compensation at both the oxygen K-edge and the TM L-edges can be studied over the course of a few hours of beamtime. However, as with all thin film battery methods, the technique is limited to those thin films which can be fabricated with the correct stoichiometry and crystal structure on a

suitable substrate. The vast majority of lithium battery cathode materials are synthesized as powders and heat treated at high temperatures to achieve the desired crystal structure. Therefore, the pellet battery method applied in the next two Sections is the more widely applicable technique.

5.2 In Operando *Soft X-ray Absorption on $LiCoO_2$*

Surface-sensitive and bulk-sensitive NEXAFS measurements of the cathode of an intact, packaging-free solid state lithium battery are presented. Partial electron yield and fluorescence yield techniques reveal that the chemical environments of oxygen and of cobalt at the surface differ from those in the bulk in $LiCoO_2$. The cell was successfully charged in a vacuum synchrotron endstation under high vacuum conditions with simultaneous collection of surface-sensitive and bulk-sensitive signals. This is the first-ever reported *in operando* soft X-ray absorption study of a working lithium battery.

Cell Design and Assembly The cathode layer consisted of a mixture of 14 wt% $LiCoO_2$, (7–10 μm, Sigma-Aldrich), 41 wt% solid electrolyte powder and 45 wt% acetylene black (Sigma-Aldrich) mixed in a SPEX 8000 planetary ball mill (without grinding media). The electrolyte layer consisted of partially amorphized lithium phosphorous sulfide glass of the formula $75Li_2S{\cdot}25P_2S_5$. The electrolyte was mixed in an argon-filled glovebox, vacuum sealed into an agate vial equipped with Viton^{TM} o-rings and three 12 mm agate balls, and amorphized in a SPEX 8000 mill for 20 hours. XRD showed the powder to contain a large amorphous fraction, indicating its lithium ion conductivity.[61] The cathode and electrolyte layers were pressed in a 13mm die at 2050 kg/cm^2 in an argon-filled glovebox containing less than 1 ppm of moisture. A reference pellet consisting of as-received 95 wt% $LiCoO_2$ and 5 wt% PVDF was used for comparison.

The fixture providing electrical contact consists of a metal backplate in contact with an 11 mm disc of scraped lithium foil which in turn contacts the electrolyte-and-cathode pellet. The 4 mm thickness front plate contained an 8 mm hole for the benefit of spectroscopic experiments. The pellet side contained a shallow counterbore to hold the pellet in place. On the incident beam side, a 45° countersink allowed for wide collection angles. Nylon screws held the current collector plates together. Only double-sided conductive tape was required to affix the reference sample. Figure 68a shows a schematic of the profile of this assembly together with a schematic of the profile of the three-layer battery. Figure 68b shows a 3D rendition of the assembly as well as a photograph of the actual

assembly. The assembly was inserted into the loadlock of the analysis chamber at beamline U7A via a nitrogen-filled glovebag. In this photograph, the yellow screws are nylon which have absorbed sufficient H_2S gas during sample shipping to turn yellow, while the black strip below the pellet is copper tape which has also reacted with sulfur. Such reactions do not occur in a dry glovebox or in a vacuum chamber, but instead are due to moisture reacting with the sulfide electrolyte and generating H_2S. The procedures developed in section B.2.8 were later developed to limit the level of moisture in shipping containers and to greatly reduce the level of moisture in the nitrogen-filled glovebag.

Electrochemical Cycling The battery was transferred from the loadlock to the soft X-ray analysis chamber and pumped down to $3x10^{-8}$ torr. It was charged via a feedthrough by a Solartron 1287 potentiostat. The initial voltage of the as-prepared battery was 1.9 V. It was later charged at 10 microamps to 2.5 V for 10.5 h, followed by a second charging to 3.15 V at 25 microamps for 5 h. At all times the battery remained below the onset voltage of approximately 3.9 V.[54]

Based on later experiments on pellet batteries, it was determined that the battery failed to charge above 3.9 V because the majority of the current passing through the cell was due to electronic conduction through lithium dendrites. In later designs, the lithium anode was replaced with a composite graphite anode which spontaneously alloys with lithium preventing dendrite formation.

X-ray Absorption Measurements NEXAFS spectra were taken at the NIST soft X-ray beamline U7A of the National Synchrotron Light Source at Brookhaven National Laboratory. The incident beam irradiated the sample at 38° from the sample normal. Data were simultaneously collected in 0.2 eV steps from a partial electron yield (PEY) detector, held 35° above the sample normal, and from a fluorescence yield detector positioned perpendicular to the incident beam, or 52° from the sample normal. The PEY detector was biased at -250 V to reject low-energy electrons. The fluorescence yield (FY) data were filtered to include only O K-edge transitions, or only the fluorescence from cobalt in Co L-edge spectra. A clean, high-transmittance gold mesh was used to calibrate the oxygen spectra and to normalize spectral intensity while an FeNiCrCo alloy mesh was used to calibrate cobalt spectra.

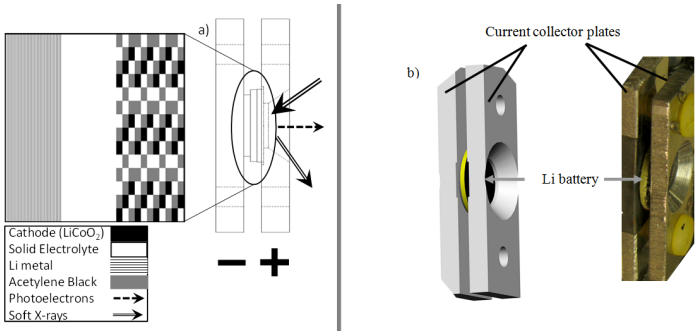

Figure 68: Schematic cross-section, 3D rendering, and photograph of the solid-state battery[136]

NEXAFS Results NEXAFS spectra at the O K-edge in Figure 69a, in both PEY and FY modes, show a sharp resonance at 530 eV and broad pair of resonances around 540 eV with a shoulder feature at ~535 eV. Relative to the PEY spectrum, the FY spectrum contains a more intense 530 eV resonance and a stronger 540eV resonance. The shoulder resonance at 535 eV is lower in energy in the bulk-sensitive FY spectrum than in the PEY spectrum. Later experiments revealed that the muted prepeak is due to the normalization of the O K-edge spectrum. The oxidized sulfide electrolyte absorbs soft X-rays mainly above 532 eV, thereby affecting the post-edge normalization. In Figure 69, both the PEY and FY spectra indicate significant moisture contamination.

Co L-edge spectra in Figure 69b show more dramatic peak height differences between the surface-sensitive PEY data and the bulk-sensitive FY data. In the geometry of our experiment, with the incident beam at magic angle with respect to the sample surface, it is easy to see that FY will be much more bulk sensitive than PEY at the O K and Co L-edge in our sample. Because the incident beam entered the sample at 38° from the sample normal, fluorescence photons were both generated in and were able to escape from the bulk of the sample. Using a density of 5.16 g/cc for $LiCoO_2$[157] and using calculations presented by Henke et al.,[158] the attenuation lengths of 543 eV incident photons and 525 eV exiting fluorescence photons travelling through $LiCoO_2$ are approximately 200 nm and 550 nm, respectively. Using the geometry of the measurements at magic angle, the attenuation length of the incident photons is closer to 125 nm. In comparison, the Auger electrons in PEY have an inelastic mean free path of 2.5 nm in $LiCoO_2$ according to the model of Seah & Dench[124] for similar incident energies. In other words, the information depth of from fluorescence photons should be 50 times higher than that for PEY electrons for our measurement

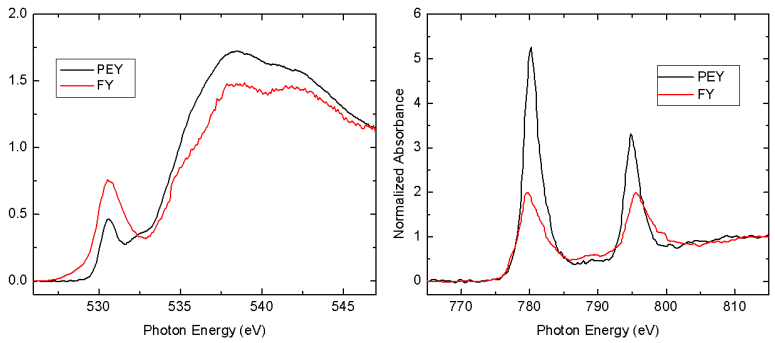

Figure 69: Comparison of normalized fluorescence yield and partial electron yield NEXAFS spectra of $LiCoO_2$ at the a) O K-edge, 3.1V and b) Co L-edge, 2.5V[136]

conditions. The peak area ratios (L_3 vs. L_2) in Figure 69b differ; PEY scans show the 2:1 area ratio, which was expected based on spin considerations,[159] while FY scans indicate a 1.5:1 ratio. However, the normalization of the PEY and FY scans does not match well; furthermore, the inherent broadness of FY NEXAFS makes it difficult to normalize against PEY data in general.

Figure 70 compares the $LiCoO_2$ reference spectrum to the battery at three states of charge. At two of these states of charge, the spectrum was taken while a charging current was flowing. The spectrum of the battery is dramatically different from the reference sample spectrum. While the prepeak energy has not changed (after calibrating the spectra relative to the gold mesh spectra) the remaining features are at lower energies. The prepeak intensity is markedly lower in the battery compared to the reference sample, while the higher-energy features are slightly less intense. As in Figure 69, the oxidized sulfide electrolyte dominates the spectrum, effectively blunting the $LiCoO_2$ spectrum during normalization.

In Figure 70a a small feature between the prepeak and the pair of higher-energy peaks is shown. This feature is seen in the reference sample and at 1.9V, but not at 2.3 V or 3.1 V in which cases current was flowing. Figure 70b compares the PEY spectrum at the Co L-edge of the reference spectrum to that of the battery below the intercalation voltage. No significant changes are seen.

Discussion of NEXAFS results The present design will allow for extensive *in situ* studies at higher voltages and over the course of many cycles. However, the present samples utilized an incompletely amorphized solid electrolyte, leading to a very high internal resistance in the cell. Together with an imperfect electrolyte-lithium-metal interface, the poorly-amorphized solid electrolyte

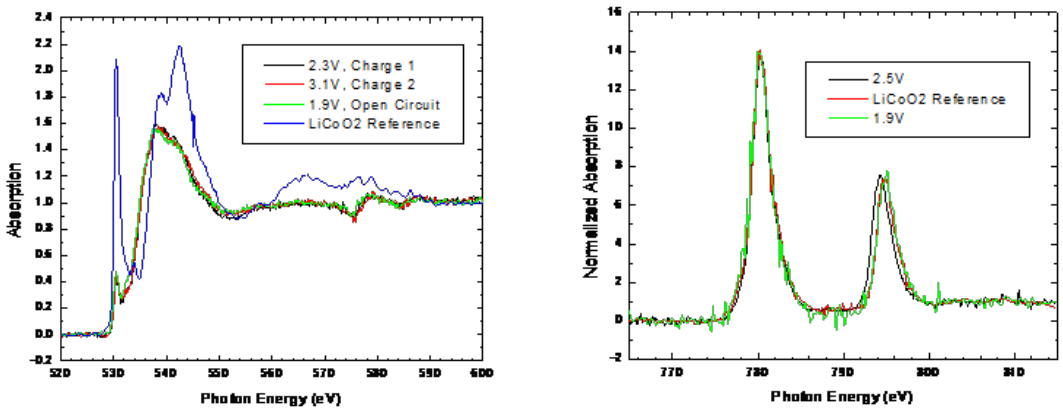

Figure 70: PEY NEXAFS a) at the O K-edge at 1.9V (open circuit), 2.3V (current flowing), and 3.1V (current flowing) as well as of reference $LiCoO_2$ (pressed with 5wt% PVDF binder), and b) at the Co L-edge at 1.9V, at 2.5V and of the same reference $LiCoO_2$ mentioned in (a).[136]

limited the speed of operation of the battery. In the best case, the sulfide electrolyte conductivity has been reported to reach 2.0 10^{-4} S/cm at 75% Li_2S•25%P_2S_5.[61] Polyethylene oxide composites can reach 1.4x10^{-4} S/cm,[160] but only with the addition of lithium salts, 15% ceramic filler as well as 50 wt% aprotic solvents, making them unsuitable for vacuum work. It should be clear, however, that this layered, all-solid-state design for Li and Li-ion batteries will allow soft X-ray studies of any cathode, anode and electrolyte material to be studied under *in situ* conditions.

Historically, soft X-ray studies have used *ex situ* samples and total electron yield (TEY) detection,[13,118,120] in which the drain current resulting from photoemission is measured. This method suffers from background noise and a lack of data from the bulk. In partial electron yield detection, a bias grid reduces the background by rejecting low energy electrons from other elements in the sample. PEY and TEY are surface sensitive due to the low inelastic mean free path of electrons.

The pre edge peak is known to correspond to molecular orbitals formed from O 2p and Co 3d orbitals, while the 540 eV peaks represent transitions from O 1s to molecular orbitals between O 2p and hybridized Co 4sp orbitals.[101] The Co L-edge is split into the L_3 (780 eV) and L_2 (~795 eV) resonances, both of which correspond to transitions from Co 2p states to O 2p-Co 3d molecular orbitals.

In Figure 69a, O K-edge NEXAFS data show that, in the bulk, the O 2p - Co 3d molecular

orbitals are less filled than at the surface. Separately, the O 2p-Co 4sp molecular orbitals are more filled in the bulk than at the surface, leaving fewer unoccupied bound states for X-ray absorption. Fluorescence yield spectra are vulnerable to self-absorption effects in which the photons emitted from the bulk are attenuated. This tends to suppress peaks, fill in gaps between peaks, and broaden peaks. The peaks in the O K-edge fluorescence spectrum shown in Figure 69 may be distorted by self-absorption., suppressing the pair of large peaks. However, the prepeak is in fact more intense in the fluorescence spectrum than in the partial electron yield spectrum; self-absorption cannot explain this difference.

Both FY and PEY O K-edge spectra differ considerably from the above-mentioned *ex situ* results in TEY mode in that the pre edge peak is less intense than the post edge peaks. While the spectra in Figure 69 resolve the peak at 540 eV, the feature at 536 eV appears as only a thin shoulder on the peak. To date, only one bulk sensitive *ex situ* spectrum has shown the O K-edge in Li_xCoO_2 where $x = 0.35$.[55]

Yoon et al.[55] found that in PEY spectra of $Li_{0.4}Mn_2O_4$, the broad peaks near 540 eV were lower in intensity compared to the 530 eV peak. Simultaneously collected FY spectra showed the 530 eV peak to have a comparable intensity to the broad peaks near 540 eV; in this work, the same surface-to-bulk trend is seen in $LiCoO_2$. Yoon et al.[161] found the same trend of a reduced peak height in the bulk of $LiNi_{0.8}Co_{0.15}Al_{0.05}O_2$, yet bulk-sensitive data on $LiCoO_2$ has been missing from the literature until now.

Cobalt L-edge fluorescence yield data is vulnerable to self absorption whereby the photons emitted from the bulk are partly absorbed before they escape the sample. Because absorption is nonlinear, taller peaks such as the L_3 tend to be attenuated more than would the L_2. This may explain the discrepancy in peak area ratios as well as the lower peak intensities in fluorescence yield data. On the other hand, deviations in the expected 2:1 peak area ratios have been observed for several transition metals and their oxides. The ratio is influenced by the 3d band occupancy, and is therefore sensitive to the chemical state of the transition metal ion. ([159]) The observed differences in this ratio between the PEY and FY spectra can point to real differences in the chemical state of the transition metal ion in the surface as compared to the bulk. In future experiments, self-absorption corrections will be made by collecting FY data at multiple angles according to the analytical scheme

proposed by Eisebitt et al.[162]

The partial electron yield Co L-edge spectrum matches the total electron yield results of,[13] but the fluorescence yield data show peak area differences. This may indicate an increased occupancy of Co 3d states in the bulk as compared to the surface. Fluorescent self absorption may also play a role in reducing peak heights.

As in *ex situ* soft X-ray spectroscopy at the oxygen K edge, the present samples are vulnerable to oxygen vacancies near the surface of each cathode particle. However, the vacancy concentration at room temperature will be too low to affect the spectrum.

The soft X-ray NEXAFS spectra in Figure 70 indicate that the O local densities of state in $LiCoO_2$ changes in multiple ways upon charging the battery even before the onset of intercalation. The Co L-edge spectrum, meanwhile, appears not to change at all. The lack of change in cobalt agrees with charge curves[54] showing that intercalation begins at 3.9 V or higher in $LiCoO_2$. This *in situ* measurement of the change in O local densities of state in Li-ion batteries is the first ever of its kind.

Solid state pellet batteries described in the present work are especially useful for *in situ* surface sensitive techniques. While this paper demonstrates the viability of direct soft X-ray spectroscopy on $LiCoO_2$, the novel cell design allows any powdered electrode material to be studied under *in situ* conditions. Also, *in situ* XRD is feasible with some modifications. Thin film solid state batteries also have potential for *in situ* measurements. However, thin film batteries are limited to cathode compositions which can be deposited in thin film form and heat treated while attached to a substrate, and the anode layer may be concealed. Pellet batteries can incorporate any powdered cathode, including sol-gel-derived ceramics, and the cell can be reversed for direct spectroscopic measurements on the anode.

Conclusions An all-solid-state, packaging-free spectroelectrochemical cell has been designed to enable simultaneous, *in situ* surface-sensitive and bulk-sensitive soft X-ray absorption measurements, measurements with electron-beam sources, and mass spectroscopic measurements. The soft X-ray design allows studies complementary to those carried out at hard X-ray energies.

Fluorescence yield data shows, for the first time, that in $LiCoO_2$ oxygen experiences different

electronic environments in the bulk as compared to the surface below the intercalation voltage. Furthermore, oxygen's chemical state changes as a function of lithium ion content. This type of information is key to understanding electrochemical reactions in $LiCoO_2$ and related battery cathode materials.

The present design allows both O K edge and transition metal L-edge NEXAFS spectra to be obtained with a single sample at a soft X-ray synchrotron beamline. While previous *in situ* methods only measured the energy of the transition metal 4p orbitals, the current method measures the transition metal 3d orbitals and the O 2p orbitals, which form molecular orbitals in Li battery cathodes. *In situ* soft X-ray NEXAFS using this battery design can, therefore, detect the occupancies of all the relevant molecular orbitals in transition metal oxide intercalation cathodes.

5.3 In Operando *NEXAFS on Overlithiated* $Li_{1.17}Ni_{0.25}Mn_{0.58}O_2$

In operando X-ray absorption spectroscopy is carried out on both a hard X-ray transmission cell and, for the first time, a soft X-ray-compatible cell, using cathode powder from the same production process. Transmission, near-surface fluorescence, and surface-sensitive Auger electron measurements indicate the oxidation of nickel and of oxygen. Jahn-Teller distortion in Ni EXAFS is deconvoluted, revealing the onsets of Ni^{3+} and Ni^{4+}.

Introduction to soft X-ray *in operando* NEXAFS A variety of cathode materials for lithium-ion batteries has been studied *ex situ* at multiple states of charge using Near-Edge X-ray Absorption Spectroscopy (NEXAFS). More commonly, the same materials are studied *in operando* using a hard X-ray-transparent cell in order to study the delithiation process in greater detail and without needing to disassemble multiple batteries. Here, a single cathode material is studied *in operando* with hard X-rays, and, for the first time, is separately studied *in operando* with a soft X-ray-compatible ceramic battery.

Lithium-ion battery cathode materials generally require a transition metal (TM) ion which can attain multiple oxidation states in order to balance charge as lithium ions enter or exit. The higher-voltage (higher energy density) cathode materials are generally oxides. It is well known that when the TM ion reaches its maximum oxidation state, the oxidation state of oxygen can change, either leading to the loss of dioxygen gas, or at least to spectroscopic changes in NEXAFS at the O K-edge.

It is also well known that NEXAFS techniques are incompatible with coin-cell batteries or pouch-cell batteries. Such cells frequently contain windows of polyimide or aluminum foil which are transparent only to hard X-ray photons. As no window is suitable for soft X-rays, we have developed a cell with no window at all. The electrolyte is comprised of a powdered sulfide glass which contains virtually no oxygen, and the cathode surface is a composite mixture that leaves cathode particles exposed on the surface. The resulting cell can be charged while electrons and photons interact with the cathode particles. Importantly, the entire cell is kept dry at all times, precluding reactions of atmospheric moisture with the cathode particles which would otherwise skew soft X-ray spectroscopy.

Such a device is a true battery, differing from common batteries in that the structure is inverted: the composite cathode material is an outer layer on a solid electrolyte support. A complementary device, the thin film memristor, has recently been used to probe the O K-edge of $LiNbO_2$ while applying a voltage bias across the surface. In that study, the positive (blocking) contact accumulated negative charge while the negative contact accumulated positive oxygen holes.[52] In a true battery, however, delithiation of the positive intercalation electrode is partially compensated by positive oxygen holes.

While soft X-ray techniques are essential in measuring true oxidation states, such techniques do not yield structural information such as the metal-oxygen bond length. Here, soft X-ray *in operando* results are presented for the removal of 30% of the total amount of lithium alongside hard X-ray *in operando* results for the removal of 62% of the lithium in same powdered, overlithiated cathode material. The soft X-ray *in operando* results serve to verify the oxidation of nickel and lack of oxidation of manganese on the surface while revealing the oxidation of oxygen in this material at an early stage of delithiation.

Experimental methods for soft X-ray *in operando* NEXAFS Stoichiometric amounts of lithium acetate, nickel nitrate, and manganese acetate were dissolved in nanopure water and heat-treated as described previously.[136]

Solid state cells were made as described previously[136] using a composite graphite anode (24 wt% graphite) and a composite cathode composed of 74 vol% electrolyte ($70Li_2S{\cdot}30P_2S_5$), 16 vol%

graphite and 10 vol% active material. Three cells were mounted between aluminum plates with 0.4" diameter holes on each side and charged using a Pine WavenowXV potentiostat in galvanostatic mode with un-grounded connections.

At NIST beamline U7A, NEXAFS was carried out using simultaneous PEY and FY detection at the O K-edge, Mn L-edge and Ni L-edge. The analysis chamber was maintained at 3 x 10^{-8} Torr during the experiment. The cell was charged in 1 h increments at rates from 3 uA to 125 nA in order to maintain a cell voltage below 4.8V. The depth of delithiation was calculated according to the theoretical capacity of 361 mAh/g.

The X-ray diffractogram for $Li_{1.17}Ni_{0.25}Mn_{0.58}O_2$ was given in Figure 4.2 in section 4.2.

***In operando* NEXAFS results** In FY detection, Ni NEXAFS (Fig. 72) shows an increase in its unoccupied density of states at the high-energy side of the L_{III} peak together with a reduction at the tip of the peak. This oxidation is first apparent at about 15% delithiation. This trend is in agreement with spectra calculated using CTM4XAS[107] for the transition from Ni^{2+} (d^8) to Ni^{3+} (d^7) (Fig. 71.). CTM4XAS calculates XPS and NEXAFS spectra taking into account the complex symmetry, and charge-transfer properties, of d orbitals. However, the 2p binding energy is derived from literature values; in Figure 71 the energy axis is unlabeled and the spectral alignment is approximate. Although mixed oxidation states are not calculated, the progression from Ni^{2+} to Ni^{3+} clearly shows a rebalancing of spectral weight to the high energy side and away from the low-energy side of the L_{III} edge. The Ni FY results are very consistent with the *ex situ* NEXAFS results of Yoon et al.[55] for $LiNi_{1/3}Mn_{1/3}Co_{1/3}O_2$ at 20% delithiation.

In PEY detection, Mn NEXAFS (Fig. 73) shows virtually no changes its unoccupied density of states at the Mn L_{III} edge. This confirms that although the XANES edge changes, no true oxidation is taking place. This is also in agreement with Yoon et al.[55]

A useful signal-to-noise ratio was obtained for both PEY and FY oxygen NEXAFS (Fig. 74), allowing surface-to-bulk comparisons. The attenuation length was calculated[158] to be 270 nm at the L_{III} edge energy of Mn, indicating that only 1% of the FY signal came from the surface. For PEY electrons, the calculated inelastic mean free path[124] was 2.64 nm, making the PEY detection sensitive only to fully exposed cathode particles. In PEY mode, surface oxidation of the sulfide

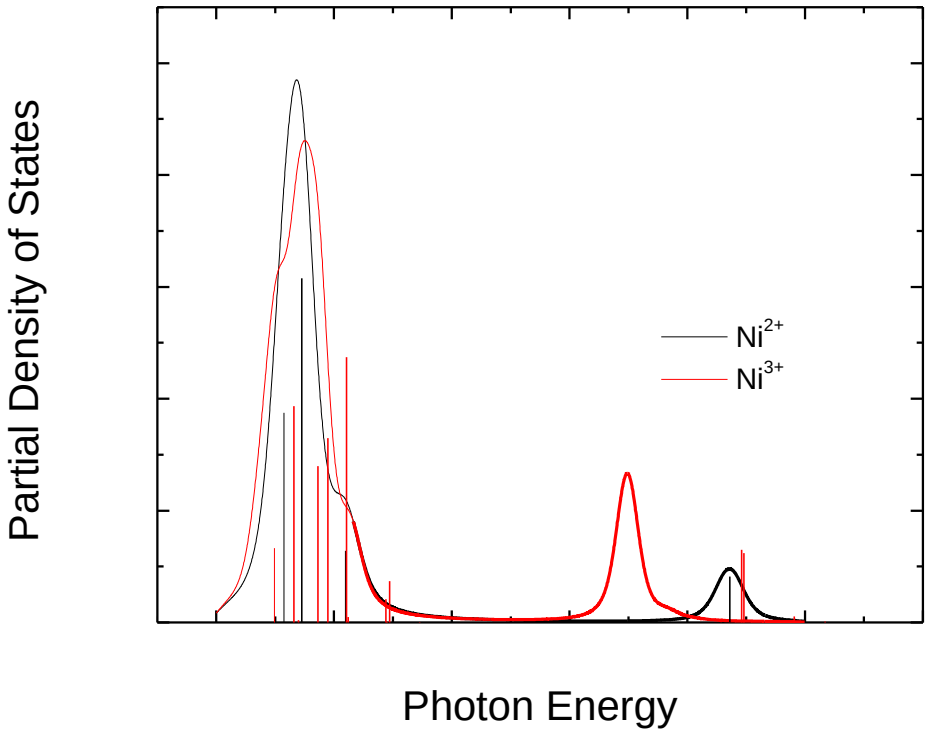

Figure 71: Ni L-edge NEXAFS calculated by CTM4XAS for Ni^{2+} and Ni^{4+}

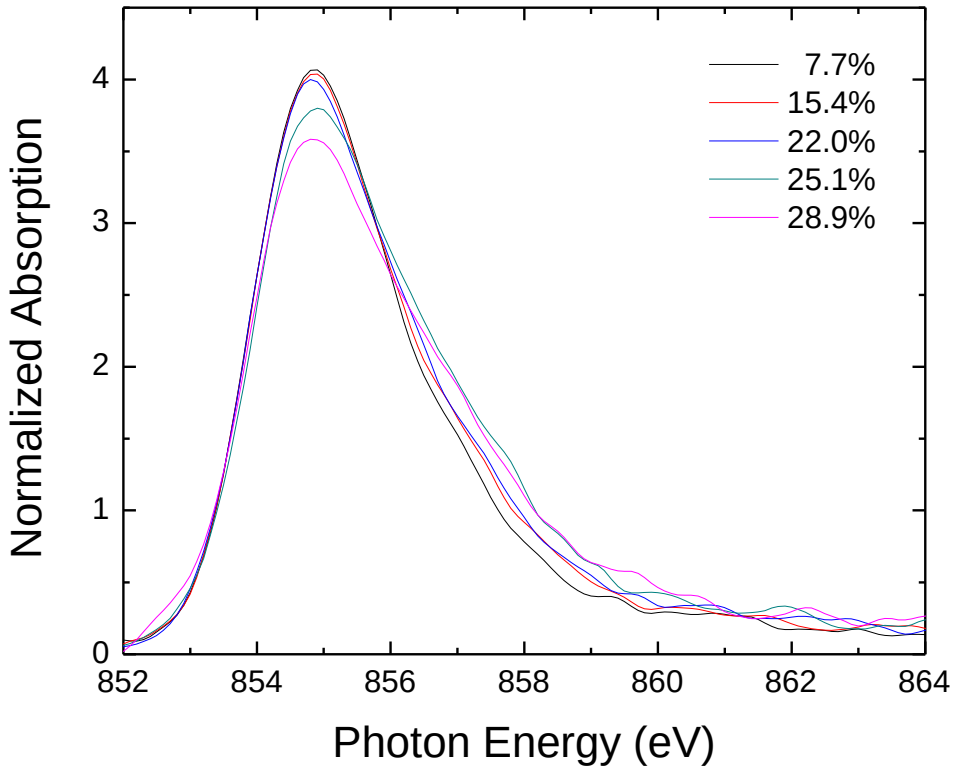

Figure 72: Ni L_{III}-edge NEXAFS for overlithiated compound, FY mode

electrolyte is evidenced above ~531 eV, as seen previously,[136] effectively smoothing the features above the pre-peak. However, the most significant features are lower in energy and indicate the occupation of O 2p orbitals hybridized with Ni 3d and Mn 3d orbitals. In near-bulk-sensitive FY mode, however, the oxygen in the cathode material dominates the signal and shows significant oxidative changes.

In Figure 74, PEY and FY O K-edge NEXAFS are compared at five stages of delithiation. The PEY data consists of single scans which were chosen based on their lack of electrostatic charging effects, which tend to distort the pre-edge for ungrounded samples. The FY data, however, consists of merged scans which were taken in sequence at approximately the same time as the corresponding PEY scan. Dozens of scans were sifted through to ensure that only representative scans, rather than scans with spurious artifacts, were chosen. In Figure 74, the inset shows the full, normalized spectrum. Apart from the resonant absorption features near the Fermi edge, the absorption spectrum is unchanging with delithiation. This is evidence of the high quality of normalization used.

At approximately 527 eV, both types of spectra show a resonant peak indicative of a hybridized O 2p - TM 3d bonding orbital. At 530 eV, however, the second resonant peak is obscured in PEY detection. Both spectra, however, show changes with delithiation. The two resonant peaks are assigned[55] to the Ni e_g and the Mn t_{2g} orbitals at 527.5 eV, which are partly filled, and to the Mn e_g orbital at 529.5 eV, which is empty. Above these features, empty hybridized O 2p - metal 4sp orbitals absorb soft X-rays. Also, the background absorption increases due to the ionization of the O 1s core electron above 546 eV.[95]

Previous soft X-ray studies have studied a finite number of *ex situ* samples;[55] here, far more complex trends can be seen. In PEY detection, part of the spectrum at 530 eV appears to rotate during delithiation, first clockwise and then counter-clockwise. The intensity of the prepeak at 527 eV appears constant. In contrast, FY detection reveals multiple, different trends including an increase in peak area at the Fermi level at ~526 eV as well as growth at 533 eV, above the prepeak region. Contrary to expectations, however, the two resonant prepeaks (and the lower prepeak in PEY mode) show significant losses of intensity which may be related to the changes in M–O bond geometry during delithiation. Similar trends were seen by Sun et al.[163] for their overlithiated material as well as by Yoon et al.[163] for $LiCoO_2$, although no explanation was given.

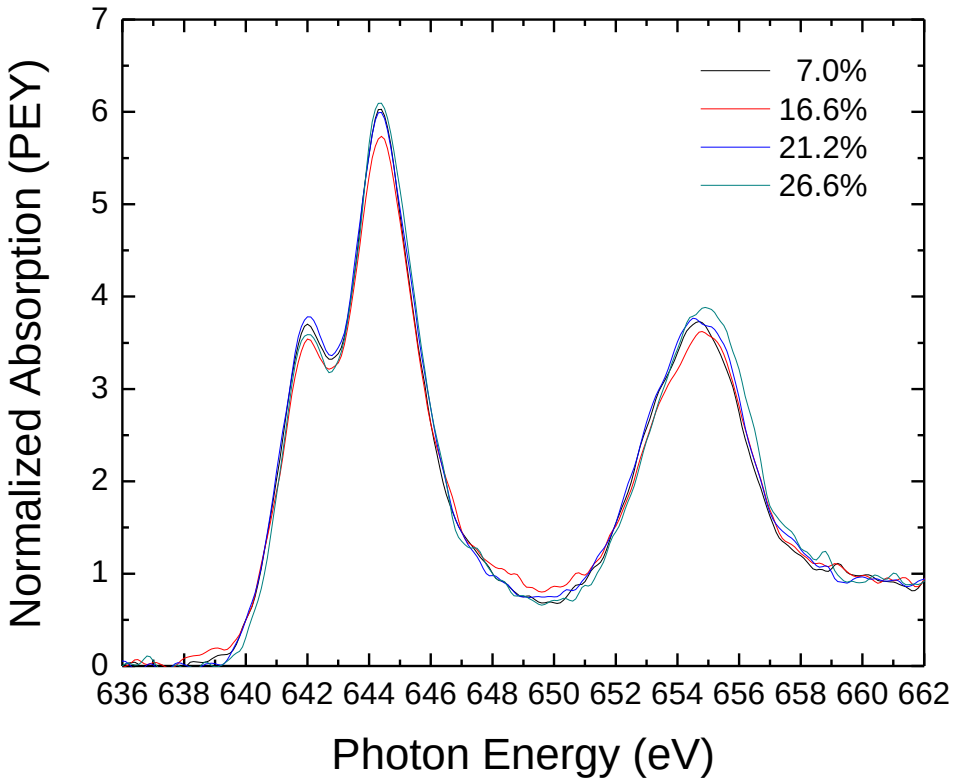

Figure 73: Mn L-edge NEXAFS, overlithiated compound, PEY mode

In spite of the reduction in peak height for the O 2p - metal 3d hybridized orbitals, a monotonic, but small increase in the absorption in FY NEXAFS at 525 eV appears. Unlike the trend in peak heights, this trend is completely monotonic during delithiation.

Discussion Simultaneous PEY and FY detection generally provides surface- and bulk-sensitive spectra for each element. Furthermore, the fluorescence yield for low-Z elements is generally higher than that for higher-Z elements.[46] However, in this case the Mn FY signal was difficult to detect, possibly due to self-absorption by the oxygen in the material. Additionally, the Ni PEY signal was also low in signal-to-noise; this can be attributed to the low percentage of nickel in the material along with the low percentage of active material in the cathode composite.

For the first time, oxidation is seen at the O K-edge, although the observed trends are complex and unexpected. Crucially, oxygen oxidation trends seen in bulk-sensitive FY mode did not manifest in the same manner in PEY mode. Therefore, in this case, the trends seen in FY mode constitute sub-surface oxidation of oxygen ions. In contrast to the hypothesis of peroxide formation on the

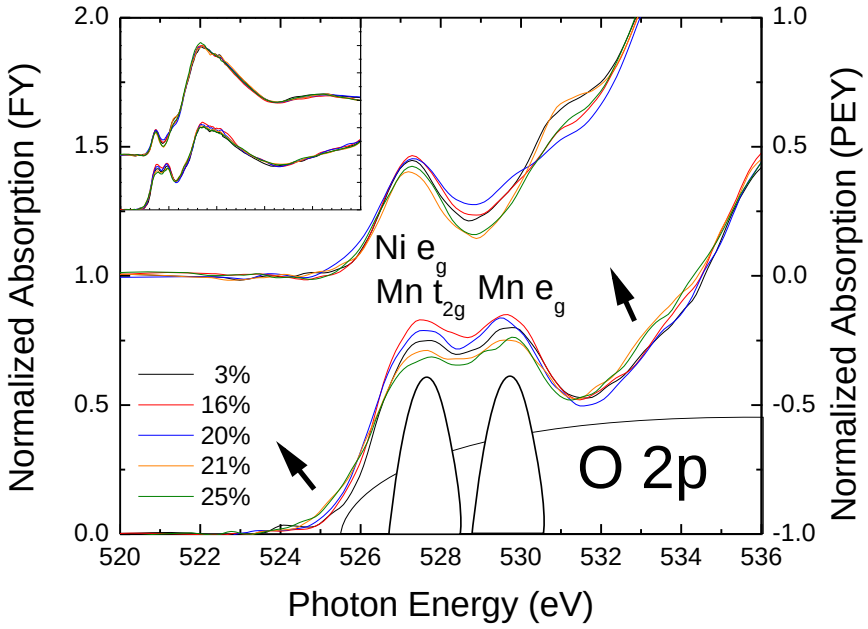

Figure 74: O K-edge NEXAFS, overlithiated compound, PEY mode (righthand axis) and FY mode (lefthand axis) with inset showing full O K-edge spectra

particle surfaces, this suggests an oxidation of oxygen throughout the crystal structure. Such oxidation is unlikely to lead to dioxygen gas evolution and can therefore be reversible, whereas surface peroxides[6] can be expected to react with a liquid electrolyte.

O K-edge PEY signals show that the low percentage of active material left exposed electrolyte regions which were contaminated by trace oxygen exposure; however, the active material was not covered as evidenced by the resonant peak at lower energies. Also, the Mn PEY signal, which is highly surface sensitive, is further evidence that much of the cathode material was completely uncovered. However, due to the oxygen content of the oxidized electrolyte, the normalized PEY absorption showed a muted pre-peak which would otherwise be taller if the cathode material alone was illuminated.

To our knowledge, no previous O K-edge NEXAFS work on this stoichiometry has been performed, although Sun et al.[163] used NEXAFS to study *ex situ* samples of $Li_{1.15}Ni_{0.275}Mn_{0.575}O_2$ and $Li_{1.1}Ni_{0.275}Mg_{0.04}Mn_{0.575}O_2$, although only pristine and fully delithiated samples were studied. Also, the mode of detection was not specified and the spectral normalization was poor. In this

study, care was taken to normalize the O K-edge spectra using a linear pre-edge subtraction which corrected for the slant of the raw spectrum. The post-edge was amplified to unity absorption by a constant factor which added no further slant to the data, making it possible to directly compare consecutive scans.

Conclusions For the first time, soft X-ray *in operando* spectroscopy shows the oxidation of both nickel and oxygen in the cathode layer of a working battery. Because the design of the cell makes use of powdered active material rather than a thin film, the same active material that was used for hard X-ray *in operando* spectroscopy could be studied with soft X-rays. The exposed cathode-vacuum interface was never exposed to any type of electrolyte because lithium was removed through the bulk of the exposed particles. Therefore, an unbiased view of the electronic structure of the cathode material was obtained. Furthermore, because no liquid electrolyte was ever in contact with the cathode interface, the oxidation of oxygen could not be quenched by reaction with the liquid electrolyte. For these reasons, *in operando* NEXAFS on powder-composite batteries does not merely generate a more fine-grained data set as compared to *ex situ* studies, but the data are also a more accurate measure of the electronic structure of the cathode material.

Comparison of *in operando* XANES and NEXAFS shows agreement that nickel oxidizes both in the bulk and at the surface, and that manganese neither reduces nor oxidizes. The inertness of Mn^{4+} has been assumed in many previous studies[55] and confirmed using *ex situ* NEXAFS. *In operando* results confirm the absence of any temporary oxidation or reduction of Mn^{4+}. The increase in absorption at the Fermi level in the O K-edge and its effective shift to lower energies is a clear indication of oxidation in the material. Because the same new feature does not appear in the Ni L-edge or in the static Mn L-edge, it is necessarily an electronic hole localized in an O 2p orbital. Importantly, this feature appeared in the subsurface-sensitive fluorescence yield mode, meaning that oxygen oxidation occurs in the bulk of the material. Due to surface contamination and low signal-to-noise levels, the same monotonic trend was not seen in the PEY dataset. However, oxygen oxidation at the surface will likely be detected by future studies.

5.4 Comparison of Memristor and Battery Experiments

The fine structure in the O K-edge represents the density of electron states which are accessible to the O 1s electron. In XPS, this electron is ejected from the material using photons with much more kinetic energy than would be required to overcome the O 1s binding energy. In NEXAFS, however, photon energies just below the binding energy can be chosen so that the O 1s electron is transferred into bound, yet partially unfilled, states near the Fermi level. This results in absorption features below 546 eV. Ideally, the Dipole Selection Rule would suggest that only the 1s $\rightarrow$ 2p transition would be allowed. In an oxide, however, bonding occurs between O 2p and metal 3d orbitals, leading to orbital overlap and hybridization. To some extent, then, the O 2p orbitals have some d-symmetry character and it is not obvious which features are hybridized and which are not hybridized.

Two methods are necessary in deducing the difference between NEXAFS features of p-symmetry and those of pd-symmetry. First, the metal L-edge absorption which reflects the 2p $\rightarrow$ 3d (or 3p $\rightarrow$ 4d) transition must be compared with the O K-edge. Because oxygen effectively has no 3d orbitals, these spectra can be attributed to the d-symmetry density of states with the caveat that some ligand-to-metal charge transfer can transfer some O 2p electrons into the metal d orbitals.

Second, trends with delithiation and overlithiation can show which orbitals are filled by charge compensating electrons. A decrease in peak height indicates the filling of an orbital, while an increase in peak height indicates the emptying of an orbital. If the O 2p orbitals can be expected to be filled in the pristine material, and the addition of lithium ions causes a certain feature to reduce in height, that feature represents an orbital which was already partially unfilled; therefore the feature represents a hybridized p-d orbital which has received an electron.

In the memristor experiment, it was possible to reduce the lithium concentration at the positive electrode while increasing it at the negative electrode. Because the electrodes were blocking, charge compensation required an increased concentration of electrons at the positive contact and a decreased concentration of electrons at the negative contact. In the O K-edge spectrum, an increase in electron concentration tended to reduce the height of the hybridized Nb 4d orbitals in the pre-edge. Conversely, a decrease in electron concentration led to no increase in the features related

to the Nb 4d orbitals, which are empty for Nb^{3+} (d^0). Instead, the absorption near the Fermi level increased slightly. This suggests some participation due to oxygen holes. Unfortunately, the Nb M-edge spectrum had a low cross-section, and the Nb L-edge was not available at the same beamline. Without trying to detect the same change in the Nb L-edge, it is difficult to conclude that oxygen holes were present. Because niobium is an early transition metal element, it seems likely that its d-electron shell is smaller than for late transition metal elements such as cobalt and nickel.

In the pellet battery experiment, the lithium concentration in the cathode was only decreased. It should be possible to increase the lithium concentration above the stoichiometric level using a lithium metal anode or a titanate anode, but in this case the anode was graphite. Unlike in the memristor experiment, however, two metal L-edges in addition to the O K-edge were available. During delithiation, spectral changes were seen in the O K-edge and the Ni L-edge but not in the Mn L-edge. By comparing changes in the oxygen and nickel spectra, the difference between electron loss from nickel and electron loss from oxygen could be determined. In the Ni L-edge, the low-energy side of the 3d e_g peak decreased in height, indicating that electrons were being transferred into that particular orbital; as CTM4XAS calculations showed, some rebalancing of these Ni 3d electrons is expected. The trend was very different in the O K-edge, however, because the growth of a new feature appeared below the hybridized 3d e_g peak. Because this same feature was not seen in the Ni L-edge, the new feature has exclusively p-symmetry character.

CHAPTER VI

CONCLUSIONS AND FUTURE WORK

6.1 Structural Changes with Delithiation

In spite of the Coulombic attraction which joins positive metal ions to negative oxygen ions, the loosely-bound valence electrons which surround each type of ion will naturally repel each other.[45] If a valence electron is lost from the positive metal ion, but not captured by the negative oxygen ion, the Coulombic repulsion between them will decrease and the metal-oxygen bond distance will, therefore, decrease. Similarly, if a valence electron from oxygen is lost, the result is the same. By monitoring element-specific metal-oxygen bond distances in EXAFS as a function of delithiation, the charge compensation mechanism can be elucidated. In addition, the metal-metal bond distances provide insights into the contraction of the crystal. More importantly, the size and shape of the metal-metal EXAFS peak indicates type of second-nearest-neighbors around each transition metal element.

6.1.1 Manganese EXAFS

For the 333 compound and the overlithiated compound, Mn EXAFS was used to obtain a radial distribution function of neighboring atoms around manganese, including the first nearest neighbor, oxygen, and the second nearest neighbor which includes a planar hexagonal arrangement of transition metal neighbors. For this compound, the second nearest neighbor was expected to be an even distribution of nickel, manganese, and cobalt ions. For the overlithiated material, however, a large preponderance of manganese and a lack of cobalt led to the expectation that manganese neighbors (Mn–Mn) would predominate. For each pristine compound, the Mn–O peaks were similar in shape and size, indicating the same octahedral coordination about manganese. However, for the overlithiated compound the Mn–M peak was distinctly smaller in area and in height. Because manganese is a lower-atomic-number element compared to cobalt or nickel, it is not surprising that this peak would be smaller in the overlithiated compound. Although lithium ions in the lithium planes represent a third nearest neighbor just beyond the second nearest neighbor, a third nearest neighbor peak

was not resolvable from the second nearest neighbor peak. Due to the low scattering cross section of lithium, this was not surprising. It was, therefore, not possible to observe the depopulation of the M–Li shell.

The conclusions of Yoon et al.[44] based on NMR results for a similar overlithiated compound indicated that lithium ions in the overlithated layer tended to group around manganese such that some portion of the manganese ions were surrounded by up to three lithium ions. Furthermore, based on neutron scattering results, it is believed[16] that these lithium ions are irreversibly extracted from the crystal and replaced by transition metal ions diffusing in from the surface of each crystal as a result of oxygen loss and a breakdown of the crystal surface. By following the peak height as a function of delithiation over two cycles, the hypothesis that lithium ions in the transition metal layer are replaced by additional transition metal ions can be tested because the peak height should increase as a result. Conversely, if manganese ions were to diffuse into the lithium-ion layers (which is possible but not expected), the Mn–M peak heights should decrease drastically instead.

From the first charge to the second charge, no increase or decrease in Mn–M peak height was seen, indicating a relatively stable arrangement of neighboring atoms about manganse in the transition metal planes. At the same time, the Mn–O peak appeared to be lower in intensity, possibly revealing oxygen vacancies. It can be concluded that in spite of the loss of oxygen, no influx of transition metal ions into the overlithiated layer could be detected.

As compared to the 333 compound for which the Mn–O (and Co–O) peaks were stable in terms of shape, the Mn–O peak for the overlithiated compound gained significant peak width during delithiation. The peak shape was never resolved into two peaks, indicating that the Mn–O bond became increasingly disordered during the first charge; no Jahn-Teller distortion was evident. The comparison of the pristine compound to the same compound after the first discharge indicates that the peak width of the Mn–O bond had returned almost exactly to its former width in spite of a decrease in peak height.

The first two nearest neighbor shells were fitted using ARTEMIS[99] in order to extract trends in the Mn–O and Mn–M bond distances as a function of delithiation. In both the 333 compound and in the overlithiated compound, a similar trend appeared in which the Mn–M bond lengths decreased rapidly before a slowing of the trend. In each case, this break in the trend occurred long before the

reversible capacity for lithium extraction was reached. This suggests a change in the mechanism of charge compensation which could be consistent with the end of transition metal oxidation and the beginning of reversible oxygen oxidation. Alternately, a more significant loss of oxygen ions from the structure to form dioxygen gas could cause the structure to remain static while lithium is (irreversibly) removed. However, in the 333 compound, although the Mn–O bond distance was largely stabilized, the Co–O bond distance contracted continuously over the entire range. In the overlithiated compound, the Mn–O bond continued to contract over the entire range of delithiation. The trends in metal-oxygen bond distances indicate that the Coulombic attraction between metal and oxygen ions continues to increase during delithiation. This indicates that, in agreement with prior electrochemical results,[17,76] reversible charge compensation in these materials continues beyond the limit that would be expected based on the stoichiometry of the material. In spite of some irreversible capacity loss due to oxygen evolution,[17,76] most of the anomalous capacity of each material is reflected in the metal-oxygen bond distances. In terms of electronic structure, the source of this anomalous capacity is discussed in section 6.2.

6.1.2 Nickel EXAFS

Ni K-edge EXAFS can be expected to be similar to Mn K-edge EXAFS because in each compound, both metals share the same crystalline plane. In the 333 compound, the second nearest neighbors are expected to include an even distribution of Mn, Co, and Ni atoms in equal proportions. In the overlithiated compound, however, NMR results for a similar overlithiated compound suggest[44] that nickel tends to be surrounded by Mn ions inspite of the overlithiation in that layer. Indeed, the Ni–M peaks are more intense in the overlithiated compound as compared to the Mn–M peaks. It is thereby concluded that in the as-synthesized overlithiated compound, Mn is surrounded by lithium ions to a greater degree than is nickel. This conclusion would be difficult to reach using Mn EXAFS alone, but by comparing the two types of simultaneously-obtained data, it is clear that nickel has more transition metal neighbors than does manganese. As was seen in Mn EXAFS, the Ni–M peak in the overlithiated material did not decrease in height with delithiation.

ARTEMIS fitting of the Ni EXAFS for the 333 compound shows a contraction of the Ni–M peak

distance with delithiation which ceases at the same point as does the contraction of the XRD a-axis lattice parameter and the Co-M bond distance. Very similarly, Ni EXAFS for the overlithiated compound shows a contraction of the Ni–M peak distance which ceases along with the contraction of the Mn–M bond distance. However, after this point a subtle trend is seen in which the Mn–M distance increases gradually while the Ni–M distance continues to decrease at a similar gradual rate. This is further evidence that nickel and manganese do not share the same environment in the overlithiated compound and, in fact, are clustered within the overlithiated layer.

Unlike the inert Mn^{4+}, nickel is expected to oxidize from Ni^{2+}, the Jahn-Teller inactive species expected in the pristine compound, to Ni^{3+}, a Jahn-Teller active species, and then to Ni^{4+}, a Jahn-Teller inactive species in order to satisfy charge compensation as lithium is removed. These transformations are seen in the splitting of the Ni–O peak for each material, followed by a coalescence of the two peaks into a single peak again. However, in each case the entire process finished early, meaning that the charge compensation for a significant portion of the known reversible capacity of each material was accomplished without the further oxidation of nickel. It could be expected that after nickel ceases to compensate charge, oxygen could oxidize to form dioxygen gas. However, as was mentioned previously, the continued contraction of the Co–O bond distance (for the 333 compound) and the Mn–O bond distance (for the overlithiated compound) shows that charge compensation continues without the oxidation of nickel. Intead, the anomalous capacity can be explained by the reversible oxidation of oxygen. Intriguingly, the Ni–O bond distance becomes remarkably stable during further delithiation, suggesting that the Coulombic attraction between nickel and oxygen is constant. This could indicate that the bonding orbitals between nickel and oxygen have a fixed electron constant, while the Co–O and Mn–O bonding orbitals do not have a fixed electron content. The charge compensation mechanism is further discussed in section 6.2.

6.2 Electronic Changes with Delithiation

In the previous section, bond distance trends were found using EXAFS. They indicated that although nickel oxidizes to compensate most of the charge lost due to delithiation, some of the charge is compensated by the oxidation of oxygen. A more direct approach to measuring element-specific oxidation trends is XANES, which samples the unoccupied density of states above the Fermi level.

Unfortunately, hard X-ray XANES is virtually insensitive to the electron occupation of transition metal 3d and oxygen 2p orbitals (the valence band) and instead probes the unoccupied metal 4sp orbitals, which are hybridized with unoccupied O 2p orbitals (the conduction band). Still, the loss of 3d electrons reduces the shielding of the core electrons, leading to energy shifts which are correlated with, but not directly proportional to, the occupation of valence band electrons. Although in the literature the XANES position is used to quantify the oxidation state,[111] there is no theoretically sound (or empirically valid) correlation between the XANES position and the 3d orbital occupation, the quantitative XANES positions are not used to assign oxidation states in this work. Instead, by measuring these energy shifts in an element-specific manner, the element or elements responsible for charge compensation can be identified.

By using soft X-ray NEXAFS, however, the symmetry-selected partial density of states of the metal 3d and oxygen 2p orbitals can be probed, allowing the formal oxidation states to be approximated. Although precise quantification of oxidation states is difficult, the type of orbital from which electrons are lost due to charge compensation can be determined.

6.2.1 Mn and Ni XANES

In both the 333 compound and in the overlithiated compound, both in the first and second charge, the Mn XANES spectra showed no rigid shift to higher or lower energies with delithiation. Instead, every Mn XANES spectrum overlapped at fixed points known as isosbestic points. Between these points, the spectra were distorted in the same way in each case: the energy at which 50% of the X-rays were absorbed moved to lower energies while other portions of the spectrum moved to higher energies. In a previous *ex situ* study of the 333 compound, Yoon et al.[55] found that this trend in the Mn K-edge XANES spectrum was not correlated with any change in the Mn L-edge NEXAFS spectrum. This suggests that in spite of the Mn–O bond length contraction seen in EXAFS, electrons are not lost from the Mn 3d orbitals, but from the oxygen 2p orbitals which are not probed by Mn XANES.

Again, Ni EXAFS showed a single Ni–O peak in the starting compound, indicating an Ni^{2+} state. Based on the stoichiometry of the compound, manganese can be expected to be in the Mn^{4+} state to balance charge. The 3d orbital occupation should be an evenly-filled $t_{2g}{}^3$ which leads to

a symmetric oxygen coordination shell, and therefore no Jahn-Teller distortion. Because Jahn-Teller distortion does not appear in Mn EXAFS, combined with the lack of a XANES shift to higher energies, indicates that manganese does not oxidize toward the Mn^{5+} configuration. Although such a high oxidation state is not expected based on the literature, this state would certainly be detectable in XANES as a rigid shift to higher energies. For further insight into the oxidation state of manganese, Mn L-edge and O K-edge NEXAFS are described in section 6.2.2.

Although absolute XANES positions cannot be relied upon to determine absolute oxidation states, the Ni XANES positions for the pristine 333 and overlithiated compounds are consistent with Ni^{2+}.[111] With delithiation of either the 333 or the overlithiated compound, Ni XANES spectra show monotonic shifts to higher energies, but these shifts cease when the Jahn-Teller distortion in Ni EXAFS disappears. It is quite clear that nickel stops oxidizing at the Ni^{4+} state for which the orbital configuration is an evenly-occupied $t_{2g}{}^6$ $e_g{}^0$. It should be noted that while at no point do the XANES reach the energy position expected for Ni^{4+} in $KNiO_6$ in which Ni^{4+} is almost certainly predominant, the XANES is known to be distorted due to bond distances.[110]

Beyond this point, the XANES spectra are stagnant, indicating a constant oxidation state even though reversible charge compensation continues. Again, in principle, a further oxidation of nickel to the unheard-of Ni^{5+} would be apparent in the XANES and a $t_{2g}{}^5$ electron configuration would be lead to Jahn-Teller distortion in Ni EXAFS. Therefore, Ni^{4+} is reached before charge compensation is complete.

In the second charge of the overlithiated compound, a similar trend is seen, starting with a Ni XANES spectrum which is nearly identical to that for the pristine compound. As in the first charge, a point of stagnation is reached where the Ni XANES and EXAFS cease to change. However, in the second cycle the XANES stagnates at a lower energy position. Furthermore, the coalescence of the two Ni–O bonds into a single peak is not completed. It is possible that some Ni^{3+} ions are present in the sample which do not oxidize to Ni^{4+}, possibly due to the formation of an insulating phase. However, the charge compensation *trend* is the same in that the oxidation of nickel ceases before the reversible limit is reached.

The results of the second *in operando* charge cycle are fascinating because the capacity which is available in the second cycle is capacity which was not lost due to irreversible reactions in the

first cycle. Therefore, it is concluded that the charge compensation regime beyond the oxidation of nickel to the quadrivalent state is a valid form of reversible charge compensation. This mysterious form of charge compensation can be *inferred* to involve reversible oxygen oxidation after the full oxidation of nickel. However, without probing the electronic structure of oxygen directly, the exact range over which oxygen oxidizes is not clear. Thus far, it is not clear whether oxygen begins to oxidize before or only after nickel reaches the quadrivalent state.

6.2.2 *In Operando* NEXAFS

To directly probe the O 2p orbitals as well as the metal 3d orbitals soft X-ray NEXAFS techniques are used. A vacuum-compatible *in operando* battery was developed which uses a powder-composite pellet structure to create cathode-vacuum interfaces in addition to cathode-electrolyte interfaces. By charging a single cell at constant current, the lithium concentration can be varied in an *absolutely monotonic* manner which, ideally, is also linear over time. Any contamination of the cathode surfaces will have an identical effect on every soft X-ray scan.

The data resulting from soft X-ray NEXAFS can be relied upon to reveal changes in the symmetry-selected partial density of states in the Mn 3d orbitals, the Ni 3d orbitals, and in the O 2p orbitals. Because all three soft X-ray absorption edges can be accessed in the same *in operando* experiment, and because the experiment was performed very slowly, the three absorption edges are measured virtually simultaneously. Therefore, element-specific trends in oxidation states can be compared from one element to the others to identify active and inactive elements in the charge compensation process. In principle, hard X-ray *in operando* experiments could be dispensed with except that they provide structural information derived from the extended fine structure, which is usually not available at soft X-ray energies due to the close spacing of the absorption edges.

However, the soft X-ray *in operando* battery has not reached its full potential, and methods of improving it are discussed in section 6.4.3. Firstly, the rate capability is low as compared to performance reported in the literature,[164] although these cells utilize low proportions of conductive additive. In this work, a greater quantity of conductive additive was used to obtain high conductivity across the exposed surface of the battery. Unfortunately, the soft X-ray *in operando* battery could only be charged to an estimated 25% delithiation rather than the 60% which was desired.

Secondly, in spite of the high concentration of conductive additive, the spectroscopic changes seen in the Ni L-edge discussed below appear to lag behind the results for the Ni K-edge in terms of oxidation state as a function of lithium content. This suggests that some of the exposed cathode particles are isolated from either the conductive additive network or from the solid electrolyte network. Therefore, changes seen in the spectral features are believed to be overlayed atop unchanging spectral features.

The presence of inactive material makes it difficult to identify absolute oxidation states as a function of lithium concentration, although an improved cell should solve this problem. However, the results of the hard X-ray *in operando* experiment can already be used to discover the limit of transition metal charge compensation. Instead, the information provided by the soft X-ray experiment serves a deeper purpose. In designing lithium-ion battery cathode materials, it is crucial to discover which element is oxidizing and whether or not multiple charge compensation mechanisms can operate simultaneously. In the soft X-ray results described below, it is concluded that in the early stages of delithiation, manganese is absolutely inactive while nickel is certainly oxidizing to a higher oxidation state. Surprisingly, oxygen oxidation, which is not limited to the surface of the crystal, also appears at this early stage in tandem with the oxidation of nickel. Although this result is difficult to quantify in terms of the numerical oxidation state of oxygen and in terms of lithium concentration, it has important implications for liquid-electrolyte batteries because it suggests that the cathode material may be reactive towards the liquid electrolyte even at low potentials.

6.2.2.1 Ex Situ *Scanning Electron Microscopy*

Certainly, the majority of cathode particles were below the surface of the cell and therefore were not available for surface-sensitive spectroscopy due to the nature of the production method. *Ex situ* scanning electron microscopy on the pellet battery used for *in operando* soft X-ray spectroscopy was used to assess the arrangement of particles in the composite cathode and anode layers. In the cathode layers, the conductive additive particles did not appear to form barriers to ionic conduction, although the continuity of the conductive network formed from conductive graphite particles could not be established. The high percentage of electrolyte particles, however suggest that some of the cathode particles could have been isolated from the conductive network while being connected to

the ionic network.

The thickness of the composite cathode layer was approximately 50 microns; attempts to generate thinner layers failed to produce acceptable batteries. Due to the high volume percentage of electrolyte particles, which was estimated at 74%, and because no agglomeration of graphite particles was observed, there is no reason to suspect that bulk particles were delithiated significantly more quickly than surface particles. Instead, it is likely that both surface and bulk cathode particles were delithiated at the same rate, apart from cathode particles which lacked either a connection to the electronic or ionic networks. Therefore, the thickness of the composite cathode layer was not a hindrance to the delithiation of the surface cathode particles, although the thickness is theoretically unnecessary. For future work, it is more important to enhance the conductive network than to create thinner composite cathode layers.

6.2.2.2 Manganese NEXAFS

In operando NEXAFS at the Mn L-edge was performed using both surface-sensitive partial electron yield (PEY) and subsurface-sensitive fluorescence yield (FY) detection modes. The PEY spectrum successfully revealed the d-symmetry density of states, including two separate peaks. The half-filled t_{2g} level appeared approximately 2 eV below the empty e_g level. These results resemble those of Yoon et al.[55] and are consistent with an Mn^{4+} oxidation state. As the cell was delithiated, no significant change in the spectrum was seen. Unfortunately, the signal-to-noise of the FY signal was too low to be analyzed. However, the significant signal-to-noise level of the PEY spectrum is proof that cathode particles are present on the surface and that cathode-vacuum interfaces have been created during the production process.

Although the soft X-ray cell was delithiated only to an estimated 25%, the fact that the Mn L-edge spectrum remained static when the corresponding Mn K-edge spectrum was distorted during delithiation is further evidence that shape changes in the Mn XANES are not indicative of changes in the 3d orbital occupation, but instead are due to changes in the coordination geometry. Furthermore, given the presence of Mn^{4+} in the pristine compound as evidenced by the Mn L-edge spectrum, it is not likely that manganese would oxidize beyond Mn^{4+} at a higher state of charge.

6.2.2.3 Nickel NEXAFS

In operando NEXAFS at the Ni L-edge was also performed using both detection modes, although in this case the signal-to-noise level in the FY mode was superior to that of the PEY mode. This was not surprising given that soft X-ray fluorescence decreases relative to Auger electron yield as a function of atomic number.[46] The lower signal level in the Mn L-edge FY detection mode could be due to the absorption of Mn L-edge fluorescence by oxygen in the sample.

In the pristine sample, a single L-edge peak was found which is consistent[55] with a $t_{2g}^{6}\ e_{g}^{2}$ electron configuration, indicating Ni^{2+}. During the delithiation of the cell, a shoulder grew on the high-energy side of this peak while the tip of the peak decreased in intensity. This change is consistent with both the *ex situ* results of Yoon et al.[55] and calculations performed using CTM4XAS. Because the synchrotron beam was incident on an exposed portion of the composite cathode surface far from the current collectors, this result is evidence that the level of conductive additive was sufficient to transfer charge across the exposed surface of the cell. Thus, a key design goal was achieved.

However, the spectral changes lagged behind the changes that were expected from *ex situ* studies.[55] In other words, a small amount of oxidation was obtained for a large amount of lithium ions removed from the cathode material. Because the conductivity of the sulfide electrolyte is known to be almost entirely due to ionic conductivity as opposed to electronic conductivity,[61] almost all the current passed through the cell can be ascribed to lithium ions being removed from the cathode material. A more likely explanation is that much of the exposed cathode particles on the surface have cathode-vacuum interfaces but lack either cathode-electrolyte interfaces or cathode-conductive-additive interfaces. Cathode particles which are surrounded by electrolyte particles, as well as cathode particles surrounded by conductive additive particles are effectively isolated from the battery charging circuit. Therefore, these particles will not contribute to the spectroscopic changes. However, because these disconnected particles are present in *every* scan, and because the synchrotron beam did not move throughout the experiment, relative spectral changes over time reveal charge compensation trends.

The bonding between nickel and oxygen (as well as between manganese and oxygen) necessarily leads to O 2p - Ni 3d hybridization. In the Ni L-edge NEXAFS spectra, only the d-symmetry e_g^0 orbitals were probed, although the same feature can be expected in the O K-edge NEXAFS spectrum.

6.2.2.4 Oxygen NEXAFS

Both the partial electron yield (PEY) and fluorescence yield (FY) detection modes were highly sensitive to the O K-edge absorption spectrum, making surface-to-subsurface measurements possible. As compared to the PEY mode, the information in the FY spectrum contained information from two orders of magnitude greater depth. Therefore, the amount of information overlap was on the order of one percent, meaning that the FY spectrum provided almost no surface-sensitive information. The PEY spectrum indicated some degree of oxidation of the sulfide electrolyte due to very limited moisture exposure. However, the low energy prepeak feature associated with the Ni e_g^0 feature, which is lower in energy than features corresponding to sulfide electrolyte oxidation, was still visible. However, because the normalization of the spectrum is based on the change in intensity from below the oxygen spectrum to above it, the relative height of this prepeak was reduced relative to its true height. The presence of the prepeak in PEY detection, along with the Mn NEXAFS PEY spectrum, are evidence that the cathode particles were not buried by the oxidized sulfide electrolyte particles.

With delithiation, PEY NEXAFS showed unexpected changes above the prepeak level which appeared to reverse themselves over time. Due to the overlap of differing features, and because no previous O K-edge NEXAFS experiment has ever obtained such a fine-grained data set, it is difficult to make any conclusions on the nature of these features.

The FY NEXAFS spectrum, however, revealed the electronic structure of the material below the surface. In addition to the pre-edge feature associated with the Ni e_g^0 orbitals, an additional absorption feature higher above the Fermi level was assigned to the Mn e_g^0 feature. As a function of delithiation, these two absorption features gradually declined in intensity. Although the decrease of the first feature is correlated with the decline in the peak height seen in Ni L-edge NEXAFS, the decrease in height of the higher-energy feature is not correlated with the peak height seen in Mn

L-edge NEXAFS, which was static. A similar trend can be seen in the *ex situ* data of Yoon et al.,[13] although it was not commented on. It can be speculated that the contraction of the metal-oxygen distances changes the nature of the overlap of p-symmetry and d-symmetry orbitals.

In addition to these changes, however, a new feature is seen to form at the Fermi level below the feature ascribed to Ni e_g^0. This new absorption feature has no analog in the Ni L-edge NEXAFS spectrum, which only shows an increase in absorption above the L_{III} peak. Because the Mn L-edge shows no changes, the feature cannot be associated with the oxidation of manganese. Because the new feature appears in the O K-edge spectrum, which reflects the p-symmetry unoccupied density of states, but not in the metal L-edge spectra, which reflect the d-symmetry density of states, the new absorption represents an unoccupied p-type orbital. There is no indication that this orbital has any d-symmetry character, and therefore, by deduction it represents oxygen holes of an exclusive 2p character. Because the Fermi level effectively moved to lower energies, it is clear that the Fermi level crossed into the O 2p orbitals. Although this result reflects the results for $LiCoO_2$,[13,118,120] it is somewhat nonintuitive for a nickel-based oxide. Charge compensation in this material clearly involves the removal of electrons from both Ni 3d orbitals *and* from O 2p orbitals.

In contrast with all previous *ex situ* NEXAFS studies, these results were obtained from a cathode-vacuum interface. This interface was unaffected by any type of electrolyte, solid or liquid, unlike in *ex situ* experiments. This is significant because electrolyte oxidation is common at the cathode-electrolyte interface. The results of Jiang et al.[109] showed that oxygen gas evolution from overlithiated cathode materials can be intercepted through oxidation of the electrolyte. It is likely that *ex situ* NEXAFS studies such as that of the 333 compound by Yoon et al.[55] could have missed the oxidation of oxygen due to the immediate reaction of some oxygen holes at the surface of the cathode particles.

At the same time, the appearance of subsurface oxygen holes in FY NEXAFS shows that the oxidation of oxygen is a bulk phenomenon which is not limited to the surface where reactions with the electrolyte are possible. Therefore, in bulk-sensitive hard X-ray EXAFS, the indirect effects of oxygen holes are seen in the metal-oxygen bond distances.

6.3 Implications of the Results for Batteries

Although the unexpectedly high reversible capacity of the 333 and overlithiated compounds is ascribed partially to reversible oxidation of oxygen in addition to the irreversible loss of oxygen in the first cycle, this anomalous capacity should not be used for extremely safety-conscious applications such as medical devices or extremely long-term applications such as in spacecraft. Instead, battery charging should be limited to the regime in which nickel oxidizes to compensate for delithiation. Above this regime, long-term capacity fade[17] due to the gradual loss of oxygen gas (in addition to other modes of capacity fade) is possible, although this mode of long-term capacity fade has not yet been demonstrated. It can be recommended that a voltage cutoff be established for each cathode material according to the voltage at which Ni^{4+} forms. Furthermore, battery materials such as $LiMn_{0.5}Ni_{0.5}O_2$ which inherently contain enough nickel to compensate all of the lithium ions in the cell should be used for high-cycle-life and high-safety applications.

However, the discovery of oxygen oxidation in tandem with nickel oxidation reveals that electrolyte oxidation begins long before Ni^{4+} appears suggests that no state of charge, for overlithiated materials, is safe from reactions at the cathode-electrolyte interface. Therefore, the development of coatings for cathode materials including thin lithium-ion conductive carbon layers is an important method of enhancing battery safety and cycle life.

6.4 Implications of the Results for Future Research

The hard X-ray *in operando* experiment in this study utilized pouch cell batteries with conventional electrolytes. Although these techniques are not new, the data reduction techniques discussed in section 3.3 are expected to be useful to future researchers in developing very high-quality EXAFS plots and in fitting them to models using ARTEMIS.

The pellet batteries used in this work were able to sustain current levels of only tens of microamps at room temperature. Although the loading of active material was decreased to make possible an *in operando* study in a limited amount of time, the resulting loading was so low that the signal-to-noise ratio in soft X-ray spectroscopy was low. The active material loading should be increased to 10–15% by volume while simultaneously improving the quality of the interface to enable higher current levels. This would entail a reduction in particle size, heat treatments, and

further optimization of the percentage of conductive additive in the cathode composite. In place of platelike graphite particles, long, narrow forms of carbon such as carbon nanofibers should be used to increase electrical connectivity while leaving more volume for cathode-electrolyte contacts.

***In Situ* and *In Operando* Raman Spectroscopy** Raman spectroscopy utilizes visible incident light and detects visible and infrared light and, therefore, can be performed using a liquid electrolyte with a windowed cell. However, *in operando* Raman spectroscopy using a solid electrolyte is potentially advantageous in cases where the liquid electrolyte resonances may overlap with cathode or anode resonances. Furthermore, in cases where the solid electrolyte interphase SEI forms on the electrodes, especially at the anode, a solid state battery can be used to study the anode material in the absence of SEI.

6.4.1 Experiments with Oxygen Gas

The detection of sub-surface oxygen oxidation early in the delithiation process suggests that oxygen gas could also be released early in the process. Although oxygen evolution was not detected at low states of charge in liquid-electrolyte cells,[16] it is possible that this oxygen is consumed in reactions with the electrolyte.[109] Further experiments on solid electrolyte cells may detect low levels of oxygen gas. Furthermore, oxygen evolution could be enhanced at high temperatures which are known to affect oxide materials even in the absence of a liquid electrolyte, as discussed in section 2.1.1.2. In contrast to liquid electrolyte cells, pellet batteries are ideally suited for very high temperature experiments; the feasibility of experiments at up to 180°C is shown in section A.3.

6.4.2 *In Situ* Magnetometry

A popular tool for measuring the magnetic susceptibility of solid materials is the vibrating sample magnetometer. The machine[165] consists of a vertically vibrating head which suspends a sample on the end of a stiff, insulating, diamagnetic rod. The sample is positioned between two DC electromagnet poles. A copper-wire pickup coil is placed between the sample and one pole of the magnet. In accordance with Faraday's Law, a sample which vibrates in a magnetic field will induce a current in the pickup coil. A lock-in amplifier measures the current in the coil which is in-phase with the vertical vibration which can be 20–40 Hz. To neutralize static charges, a fan blows ionized air across

the sample during the experiment. The DC electromagnet can then apply a range of DC magnetic fields.

Several challenges present themselves in adapting lithium-ion batteries to this technique. Firstly, coin cells are unusable because although they are encased in stainless steel, any residual magnetizeability of the steel will affect the measurements.[166] Secondly, all materials will have some diamagnetic or paramagnetic susceptibility to a magnetic field which will add to or subtract from that of the active material. Thirdly, the vibration of the machine and the turbulence caused by the ionizing fan may cause damage to a battery or, at least, an internal shifting of the active materials. For these reasons, a solid state battery, packaged inside the moisture barrier material used for pouch cells, is ideal due to its rigid construction.

When these challenges have been overcome, an *in situ* experiment would consist of VSM experiments alternating with constant-voltage battery charging steps of 5 hours or more. This will result in a fine-grained dataset in which the magnetic moment of the sample is measured as a function of cell voltage. A drawback of this method is that the VSM cannot be run continuously; this means the experiment will not be *in operando* because battery charging must be interrupted. Because the VSM experiment cannot be automated for safety reasons, data cannot be acquired regularly over 24 hours and the number of data points obtainable depends on the amount of labor available. On the other hand, the magnetic moment of cathode materials will be measureable in fine, monotonic steps of lithium concentration.

6.4.3 *In Operando* X-ray-based Experiments

In light of the *in operando* detection of oxygen holes, more soft X-ray *in operando* NEXAFS investigations should be performed. Not only is there a wide array of possible lithium-ion cathode stoichiometries to investigate, but there are also lithium-air cathode materials which need investigation. Recently, Lu et al.[51] performed *in operando* XPS on a thin film battery while exposing the cell to oxygen gas. The thin film battery, then, acted as both a lithium-ion battery and as a lithium-air battery, effectively increasing its charge capacity by the formation of peroxide ions on the surface. Their experiment, therefore, was the reverse of the oxygen evolution experiment: although they measured O 1s photoemission and did not detect oxygen holes, any oxygen holes in the cathode

material would have been eliminated via oxygen exposure. Although their study was limited to thin film cathode materials, powder-based pellet batteries can incorporate virtually any cathode material.

Determine effects of coatings *in operando* Due to the depth of information available via fluorescence yield detection, cathode materials coated with carbon or AlF_3 could be studied using powder pellet batteries.[167] Furthermore, because *in operando* experiments allow subtle changes to be seen, even oxide-coated cathode materials could be studied using these techniques. It is possible that coated cathode materials could *retain* oxygen during delithiation and therefore contain a higher concentration of oxygen holes.

Determine effects of temperature *in situ* and *in operando* Two experimental possibilities exist for determining the effect of temperature on the O K-edge and metal L-edge spectra. The first is to perform an *in operando* charging experiment at a constant, elevated temperature to determine the degree of ligand-to-metal charge transfer, which should increase with temperature. The experimental time required would depend inversely on the temperature of the experiment. In terms of electrical feedthroughs at NIST beamline U7A, one pair of conductors would be required to provide electrical heating, leaving only one pair available to charge a single battery.

However, a simpler *in situ* experiment is possible which would provide more information. If a series of pellet batteries can be charged at Georgia Institute of Technology to a series of voltages and mounted on a sample bar without individual electrical connections, the entire bar may be heated with one pair of contacts while using the other pair of contacts for a thermocouple on the sample bar. Using this method, the temperature can be increased stepwise and each sample can be scanned in turn. The first advantage of this method is that it generates an array of temperature vs. state of charge data instead of generating a series of spectra at constant temperature. The second advantage is that *low* temperatures may be used in addition to high temperatures. For transition metal oxides there exists a transition temperature known as the Verwey transition temperature below which electronic charges on the O 2p orbitals become periodically ordered. This transition can be seen in the O K-edge spectra as a function of temperature, and it can affect the conductivity of the oxide.[168,169] The disadvantage of this method is that because it is not *in operando*, the state of charge cannot

be varied continuously. However, on a single 8" sample bar it should be possible to mount over a dozen solid state batteries, each at a different state of charge.

Determine effects of rate on charge compensation The soft X-ray *in operando* experiment in this work was, by necessarily, performed very slowly due to the sub-optimal arrangement of cathode and conductive additive particles in the cathode layer. However, in principle the system should allow for faster experiments,[164] especially if high temperatures are used. It remains to be seen whether fast delithiation will generate more or fewer oxygen holes. However, a more practical high-rate experiment would involve charging pouch cell batteries at a quick-EXAFS beamline[170] where the broadband X-ray source can be sampled across the required range of photon energies over a few minutes. This would enable very fast *in operando* experiments in which a battery is charged in only one hour while still obtaining 15 EXAFS scans. At high charging rates, it is possible that nickel oxidation would provide charge compensation over a wider or narrower range of lithium concentration.

6.4.4 Exotic X-ray Spectroscopies

The National Synchrotron Light Source at Brookhaven National Laboratory is scheduled to be shut down and replaced by the NSLS-II in 2013.[138] Much greater photon flux, greater energy resolution, smaller beam sizes, and new, more sophisticated experimental chambers will be available. However, a full complement of beamlines will not be constructed immediately, leaving open many new experimental possibilities. The experiments described here will likely be possible at the new synchrotron light source.

Resonant Photoemission Although X-ray absorption techniques are preferred over standard X-ray photoemission techniques because they provide information regarding the valence band, resonant photoemission (RPES) techniques, in which the photon energy is varied in steps of less than 1 eV between each photoemission scan, can provide detailed information on the nature of O 2p holes and on the nature of p-d bond hybridization.[153] Although there is no reason why a photoemission analyzer cannot be used simultaneously with PEY and FY detection, in practice many beamlines, including U7A and X24A at the NSLS, have these detectors installed on opposite sides of a vacuum

chamber such that both modes may not be used at the same time.[122]

X-ray Raman Spectroscopy (XRS) An X-ray absorption technique which could simultaneously probe light-element orbitals while simultaneously allowing the use of liquid-electrolyte cells would allow for quicker, simpler experiments than those using pellet batteries. Although X-ray Raman Spectroscopy is promising in that it penetrates packaging materials so that low atomic number elements such as oxygen[57] and carbon[171] can be probed, the remaining constituents of lithium batteries still contain these elements in large concentrations. In a typical liquid electrolyte, as discussed in Chapter 2, a polar solvent such as propylene carbonate is used to suspend lithium ions and anions in solution. With a few exceptions, most polar electrolytes rely on oxygen as the negative constituent. Certain nitrogen-based room-temperature ionic liquid (RTIL) systems, and acetonitrile, are oxygen-free solvents that may prove useful.[172]

Enhanced Resolution of Oxidation States One key reason for developing an *in operando* soft X-ray battery was to increase the resolution in energy by minimizing the "core-hole lifetime broadening." This refers to the broadening of spectral features due to the Uncertainty Principle, rather than due to the resolution of the beamline optics. Although the core-hole lifetime broadening is smaller at soft X-ray energies, it is still not small enough to fully resolve the e_g and t_{2g} features of transition metals. Currently, the e_g and t_{2g} can overlap to a large extent, and it should be possible to further resolve them using techniques that are now in development.

The complete resolution of these features could clearly delineate high-spin and low-spin configurations of each transition metal. Although the magnetic moment of an intercalation cathode material is not directly relevant to the performance of a battery, magnetic spectroscopy would help identify the electron configuration of each transition metal. Such information is obtained using X-ray Magnetic Circular Dichroism in which polarized soft X-rays impinge on a sample which is under a high magnetic field. Soft X-ray absorption features, particularly partly occupied electron states at metal L-edges, can change direction as a result, meaning that the absorption can dive below the background level depending on the direction of the polarization.[155] This information is frequently used to measure element-specific magnetic moments in thin film hard drive materials,

which contain multiple ferromagnetic metals. However, at very high magnetic field levels, unpaired spins localized on oxygen orbitals can be detected by XMCD.[84] Such techniques could potentially allow hybridized features in the O K-edge to be differentiated according to empty and partly empty orbitals while identifying the specific metal element hybridized to each feature.

Also, remarkable progress in soft X-ray beamline design has been made at the Swiss Light Source. At the ADDRESS beamline, a novel type of undulator combined with a relatively standard monochromator allows the energy resolution to reach 0.156 eV (156 meV) at the O K-edge using a 4200 line/mm grating. At the Cu L_{III} edge, using an 800 line/mm grating, a resolution of 120 meV was achieved. Such extreme energy resolution in the soft X-ray energy range could help to separate transition metal 3d orbitals and detect very subtle shifts.[173]

APPENDIX A

RELATED EXPERIMENTS

A.1 In Operando *Thin Film Resistivity*

In collaboration with Jordan Greenlee and Prof. Alan Doolittle, it was undertaken to delithiate a thin film of $LiCoO_2$ while simultaneously measuring its electronic resistivity. The results are relevant to battery studies, although the terminology and discussion of the results were tailored for the application of analog memristor applications. Here, the work is reframed in terms of its significance to lithium battery research.

Superficially, this would appear to be simple to achieve by merely submerging a thin film in an electrolyte and passing current through the thin film. Naturally, however, the electrolyte will conduct lithium ions in parallel with the conduction in the solid. In fact, in a thin film the path through the electrolyte is much faster than the path through the solid. It was necessary to only partially submerge the thin film as described below.

This experiment is distinctly different from a related experiment performed by Guan and Prof. Meilin Liu[174] at Georgia Institute of Technology: in that work, the ionic conductivity of a cathode material was measured while preventing electronic conductivity. This was achieved by sandwiching a pellet of cathode material between two electrolyte layers. Through these electrolyte layers, lithium could pass through the cathode but electrons could not. A further difference was that no electrical contact was made to the cathode; therefore, the cathode could not be delithiated while the electronic conductivity was measured.

Background The typical electrode in electrochemistry is a metal alloy which either serves as a substrate where atoms may be deposited, or which is dissolved into the solution. In these cases, the total reaction requires charge transfer at an abrupt interface between the solution and the metal substrate. The rate of the reaction depends on mass transfer in the electrolyte, charge transfer at the surface, and electronic conduction in the metal alloy. The reaction rate can best be increased

by increasing the surface area between the electrolyte and the metal substrate; ultimately, a mesh or sponge of metal can be used to maximize the surface area. Electronic conduction in the metal alloy is seldom low enough to affect the reaction rate.

Intercalation cathode materials benefit from this strategy, but there is a further complication. The solid intercalation cathode material contains lithium ions throughout the bulk, and these must diffuse to the surface before reaching the electrolyte. Furthermore, the positive lithium ions will not be forced to move unless electrons are also extracted from the bulk of the material. The total reaction rate therefore depends on the electrical conductivity and the diffusion coefficient for lithium ions in addition to the previously discussed factors. In an oxide, sulfide, or phosphate intercalation cathode material, the electronic conductivity can easily be rate-limiting, although in some cases doping can overcome this problem.[175]

Experimental Methods A three-electrode jar cell was used to delithiate the thin film through only the lower portion of the film, leaving much of the film exposed. The electrolyte level was controlled using a stainless steel needle and syringe. In this cell, the lower portion of the film together with the lower aluminum metallization constitute the working electrode (WE) while the counterelectrode (CE) and reference electrode (WE) were strips of lithium foil. The cell was charged at fixed voltages for intervals of least 30 minutes, or until the current decreased to less than 20 μA, whichever was longer, using an Arbin BT2000 potentiostat. At higher voltages, the differential capacity was larger, requiring longer intervals. At the same time, voltage was applied across the top two contacts by a Solartron 1287 potentiostat. This voltage was ramped between -1 V and +1 V throughout the delithiation process.

In Figure 75 below, two possible electrode arrangements are given. In the first, the thin film has three metallized contacts (aluminum) where the first is submerged in the electrolyte but the top two are not. The top two electrodes can be used to measure the total conductivity of the thin film. There is a flaw in this design, however, in that stray current between the top contacts can travel to the submerged portion of the thin film and use the electrolyte solution as a parallel path for current. An improved design at right arranges the contacts in-line such that any current between the top two contacts cannot travel to the liquid electrolyte. This ensures that the conductivity measure measures

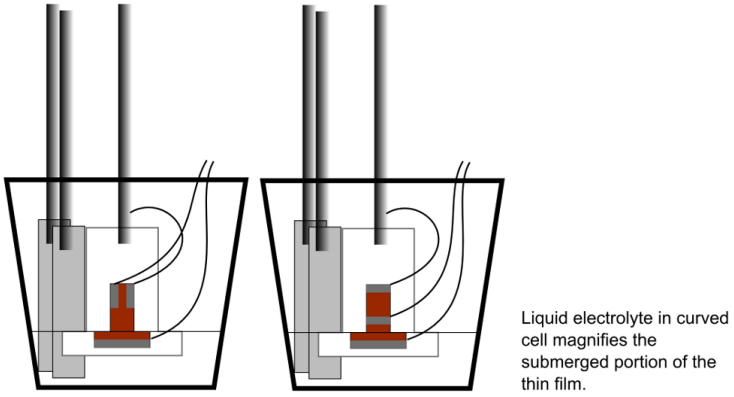

Figure 75: Cross section of jar cell showing three-electrode thin film device with electrolyte meniscus between two contacts

only the thin film itself.

Results The results of the experiment are shown in Figure 76. It was found that as lithium was delithiated from the thin film, the resistivity of the film decreased very rapidly due to the formation of lithium vacancies giving rise to free carriers. The resistance decreased by an order of magnitude, although most of this change came in the first 10% of delithiation as expected from *ex situ* conductivity studies.[78] Unlike in *ex situ* studies, however, extremely small increments of delithiation could be studied in a single experiment.

Ion-gated Transistor Interpretation The interpretation of this experiment as an ion-gated transistor is due to Jordan Greenlee and will be published elsewhere. In this interpretation, the electrolyte is interpreted as a transistor gate, controlling the conductivity of the channel, which is the thin film. The counterelectrode can be seen as the gate metal, while the two top contacts are the source and drain. Unlike in a MOSFET transistor, the source and drain are offset relative to the gate because, in this device, the "gate" can sustain a parallel current of lithium ions. This transistor can be seen as a low-power device because, in lithium battery chemistry, self-discharge is very slow compared to other battery chemistries. This device is complementary to the two-terminal

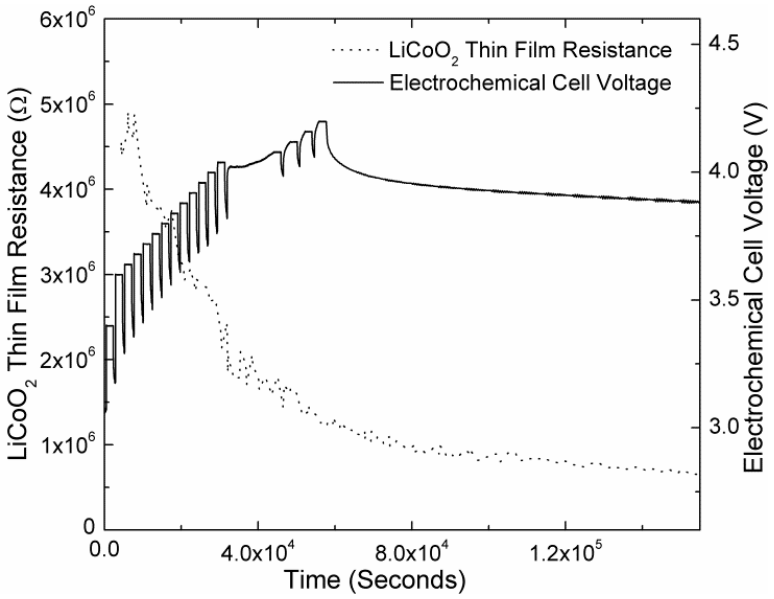

Figure 76: *In Operando* Resistivity vs. Delithiation

memristor[52] (discussed in Section 5.1) as both devices have a smooth analog response which can be exploited in developing brain-like computer circuits.

Intercalation Cathode Interpretation The rate capability of lithium ion batteries depends on the rates of diffusion of lithium ions from the cathode, through the electrolyte, and into the anode. During charge, a positive electrical potential drives lithium ions out of the bulk of the cathode particles to the surface, and this process depends on both conductivity of the material and the diffusion of lithium ions. Unfortunately, during a charging experiment, these two effects are confounded because they can both limit the performance. Sensitive techniques such as Potentiostat Intermittent Titration Technique (PITT) seek to delithiate the cathode (including thin film batteries)[176] very slowly. The experiment of Guan and Liu[174] measured the diffusion of lithium ions through a cathode material while blocking electronic conductivity. The present experiment is complementary to both these techniques in that it combines PITT (slow delithiation at potential steps with rest periods) with an *in operando* measurement of the electronic conductivity of the thin film.

A.2 Ex Situ *and* In Situ *Raman Spectroscopy on Solid Electrolyte*

In situ and *ex situ* Raman spectroscopy on solid electrolyte pellets was attempted with the help of Kevin Blinn in Prof. Meilin Liu's laboratory at Georgia Institute of Technology7. In their work,

solid oxide fuel cells (SOFCs), which resemble pellet batteries, utilize an O^{2-}-conducting solid electrolyte and composite electrodes. At high temperatures, hydrocarbon feedstocks and oxygen gas are used to generate electricity. However, sulfur poisoning from the hydrocarbon feedstock is a primary threat to the longevity of the cell.[177] *In situ* Raman techniques have been developed, in part, by Kevin Blinn for the detection of sulfur poisoning on the surface and published in the Journal of Visualized Experiments.[178]

In Raman spectroscopy, a laser of a fixed wavelength impinges on a sample. Because the laser light is typically red or green, electrons are not ejected from their orbitals as in X-ray absorption. Instead, intermolecular bonds of the proper symmetry absorb this radiation and re-radiate the energy at a longer wavelength. This scattered radiation is detected with the assistance of a monochromator which rotates during a scan to select each wavelength. The resulting data is not element-specific, but instead is bond-specific. For instance, phosphorous-sulfur bonds resonate at a different wavelength from sulfur-sulfur bonds.

Advantageously, both the incident and scattered radiation can pass through a quartz window. To simultaneously heat an electrolyte pellet while performing Raman spectroscopy, an *in situ* reaction cell was used which had been modified by Kevin Blinn.[178] This hermetically sealed, water-cooled cell allowed for gas flow, temperature measurement, as well as heating during an experiment. Because the water cooling channels were separate from the sample compartment, and because the gas ports could be valved off, a sample can be loaded inside a glovebox and then transferred to the Raman spectrometer. In Prof. Liu's laboratory, the effects of flowing hydrogen sulfide on solid oxide fuel cells (SOFC),[179–181] which are ceramic oxide pellets, are studied extensively.

Before loading a sample, the *in situ* cell was detached from the Raman system and the water channels were allowed to dry overnight. The quartz window, which consisted of a 1" diameter quartz disk held against an O-ring using a threaded collar, was removed so that the air inside the cell could be removed during evacuation in the antechamber. The cell was then loaded into the glovebox. A $1/2$" diameter electrolyte pellet was placed onto the heating unit, which resembled a volcano due to its open center and sloped sides. A minor difficulty was that the sample could not be fastened; any clamp on the sample would restrict thermal expansion. Therefore, the cell was kept level at all times.

When the *in situ* cell was removed from the glovebox, a mild sulfur smell was apparent. It was determined that the sealing surfaces and collar threads needed careful scraping. Upon subsequent loadings, the cell was adjusted until it could withstand both vacuum, which pulled the quartz against the O-ring, and positive pressure, which pushed the quartz against the metal ring. It was not found necessary to include second O-ring between the quartz and the threaded collar.

In spite of the sophistication of the *in situ* Raman cell, one limitation remained: the sample was necessarily placed between the heating unit and the quartz window; the resulting thermal gradient increased greatly with temperature because the window never exceeded room temperature significantly. A calibration was performed using a previously developed adaptor consisting a thermocouple probe protruding through a drilled quartz disk. This calibration revealed very large differences between the readings of the internal thermocouple underneath the heating unit, and the protruding thermocouple which nearly touched the sample. In Celsius, the readings above the sample were approximately double the reading the below the sample.

After taking into account the difference in temperature readings, the thermal gradient across the sample remained. As the sample was gradually heated, a translucent film soon formed on the cold quartz window. This film grew thick enough to absorb the scattered radiation coming from the sample itself. The source of this film was the underside of the sample, which was being heated beyond its decomposition temperature. The scattered radiation indicated the presence of sulfur-sulfur bonds in contrast to the combination of phosphorous-sulfur and sulfur-sulfur bonds seen on the sample surface at room temperature. The sulfur-sulfur bonds were not expected as they are not present in Li_2S or P_2S_5.

To investigate the electrolyte heat treatment process without *in situ* heating, a series of *ex situ* samples were fabricated and heat-treated at various temperatures. It was found that samples heated to less than 120°C contained sulfur-sulfur bonds, while those heated to higher temperatures had only phosphorous-sulfur bonds. This temperature is slightly above the melting point of elemental sulfur, 112°C. It was found that the amorphized material lost approximately 1.1 wt% after at least 2 h at all heat treatment temperatures above 120°C. Raman spectroscopy was later used to determine that as-pressed pellets contained a greater extent of sulfur-sulfur bonds as compared to heat-treated pellets. Figure 77 shows a reduction in the S-S stretching-mode peak at 480 cm^{-1} and a reduction in

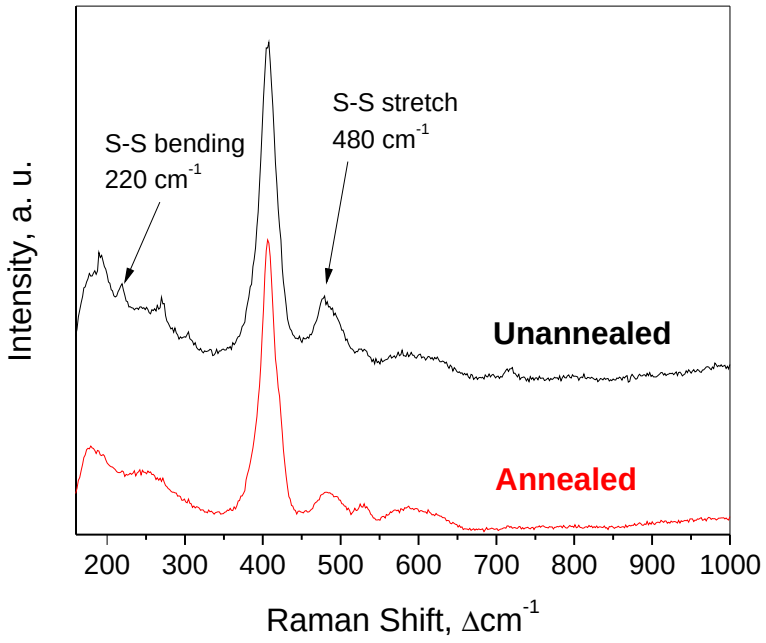

Figure 77: Raman spectra of $70Li_2S{\cdot}30P_2S_5$ Before and After Annealing

the bending-mode peak at 220 cm^{-1}.

The source of the sulfur-sulfur bonding is not known, nor is its effect on the ionic conductivity. Elemental sulfur may be present in the P_2S_5 precursor material, or the S-S bond may be present as a bridging bond in the glassy structure. Further studies should utilize heat-treatment above the melting point of sulfur, and should also limit the thermal gradient across the pellet. *In operando* Raman studies on working batteries will then be enabled, allowing the anodes and cathodes of pellet batteries to be studied in the absence of the Surface Electrolyte Interphase (SEI) which results form the use of liquid electrolyte. Also, oxygen holes, and their relation to metal-oxygen bond hybridization, may be detectable by *in operando* Raman spectroscopy.

A.3 High Temperature EIS on Pellet Batteries

The operation of solid state batteries at high temperatures opens up a wide variety of new possibilities including accelerated experiments and oxygen gas evolution experiments. Furthermore, high temperature *in operando* EIS experiments make it possible to detect the effects of sintering and glass crystallization as a function of temperature and time. The following experiment was presented at the Fall 2012 meeting of the Electrochemical Society.[182]

Unlike a liquid electrolyte, whose composition is homogenous, a sintered solid electrolyte pellet

may have inhomogeneity, a variable degree of crystallinity, and significant porosity. Heat treatment may simultaneously crystallize and sinter the material, frequently at the same temperature, making it difficult to separate the two effects. At the same time, ionic conductivity will naturally vary with the instantaneous temperature. *In operando* heat treatment experiments have been performed to experimentally measure the conductivity as a function of both temperature and time. To separate the reversible effect of temperature on lithium conduction from the irreversible effects of sintering and crystallization, a heat-treatment schedule was devised to repeatedly heat the sample to a high temperature, hold that temperature constant, and then cool the sample to room temperature.

Introduction Commercial lithium-ion batteries are very vulnerable to high temperatures. At the anode, SEI layer growth accelerates with temperature even below rated temperature of 60–80°C.[183] At high temperatures and high states of charge, cathode materials are both resistive and prone to generating oxygen gas, which can ignite the electrolyte. Solid-state thin film batteries[184] are capable of high temperature operation, but are limited to thin film cathode materials. Furthermore, the cathode is typically buried, and exposing the cathode to microscopy or spectroscopy requires heroic efforts.[185] Powder-pellet batteries made using Li2S•P2S5,[61] however, combine powdered electrode materials with powdered sulfide glass to create a free-standing "naked" battery. The percentage of conductive additive has been adjusted to provide conductivity over the exposed surface without covering the active material.[136] The current collectors can include large, open windows through which surface-sensitive microscopy and spectroscopy is performed.

Experimental Methods Half-inch diameter pellets, 1.5 mm thick, were mounted between Al plates using stainless steel disks as blocking electrodes. Stainless steel screws and ceramic "hat" washers held the plates together. A Faraday cage shielded the cell from induction due to the furnace's heating coil.

Furnace Customizations The solid state battery samples were mounted in an MHI, Inc. Robust Radiator furnace which consists of firebrick, silica wool, and a single thick, coiled ceramic heating element.

Insulation and Connections At high temperatures, the sulfide electrolyte will release some amount of hydrogen sulfide. Sulfur-resistant materials (See Appendix C) were used throughout the design, including polyimide foil for electrical insulation of the exposed heating coils, aluminum foil for Faraday shielding, stainless steel wire and overbraid for EIS connections, and PTFE wire sheathing for wire insulation.

Alternating-Current Shielding A difficulty encountered in this experiment was the fact that both the characterization method and the heat source rely on alternating current. While the heat source operates at 60 Hz, EIS spectra clearly show many odd-numbered harmonics above the fundamental frequency. While some of this alternating flux can be shielded using a Faraday cage made from aluminum, a ferromagnetic shield was created from steel pipe. This shield did not entirely eliminate low-frequency induced noise, however.

Sample Mounting The solid state pellet was mounted between two aluminum plates. To prevent corrosion of the aluminum metal (due either to sulfide or lithium-ion reactions) the pellet faces were covered with AISI 321H stainless steel disks which were designed for coin-cell batteries. The thermal expansion (and possible sintering contraction) of the solid state pellet was accommodated using stainless steel wave springs attached under the head of the screws. Electrical isolation was accomplished using alumina ceramic "hat" washers (Thermo Scientific) which accommodate a #2 stainless steel machine screw.

Heat Treatment Schedule Although the room-temperature performance of pellet batteries is important, their performance at temperatures just out of reach for standard batteries, such as 80°C, is crucial for studying oxygen evolution during battery charging. Also, a temperature of 80°C is a more practical choice than room temperature because a furnace will naturally cool itself rapidly before cooling exponentially more slowly to room temperature. Therefore, single-day heating schedules were devised in which the sample is heated at 2°C/min to a lower temperature for one hour, then to an intermediate temperature for one hour, and then to a near-T_g temperature for 3 h or more. After allowing the sample to cool to room temperature overnight, the experiment could be repeated to separate reversible effects of temperature (thermally activated ionic conduction) from irreversible

effects (such as crystallization).

Results In Figure 78, impedance data is plotted in 15 min increments during heating to 180°C at 1°C/min. A symmetrical cell with graphite electrodes was employed. A logarithmic scale for the real part emphasizes the exponential decrease in solution resistance, while a linear scale for the imaginary part illustrates the reduction in interfacial resistance.

During 24 h at 180°C, (Tg =170°C) the electrolyte crystallization and sintering process[186] was monitored by impedance. The evolution of the Nyquist plot is shown in Figure 79. A quick decrease in overall impedance is followed by a gradual increase in low-frequency impedance, suggesting that the optimal heat treatment is far less that 24 h. After cooling, both the bulk and interfacial resistance were reduced by a factor of six.

Cyclic voltammetry at 180°C (Fig. 80) generated large delithiation and relithiation currents. Because the cell was constructed using a graphite anode and was at a low state of charge, the voltage scale is not referenced to V_{Li/Li^+}. Sweep rates of 20 mV/s and 10 mV/s yielded similar results. Although such sweep rates are typical of aqueous electrochemistry experiments, a 0.5 mV/s sweep rate or less is used at room temperature for solid state batteries.

In Figure 81, a full cell using sol-gel synthesized LiNiMnO2 is charged in pulses after equilibrating at 160°C. In Fig. 82, the same experiment is repeated at 180°C. Initial pulses show a polarization resistance of ~350 Ω until depletion sets in at approximately 1 mA. 2 mA pulses were only possible following -2 mA pulses. After cooling, the polarization resistance was lower than it had been before heating began, showing a permanent improvement, rather than destruction, of the cell at 180°C.

Conclusions Monolithic ceramic batteries operate very well above the glass transition temperature of the sulfide electrolyte and are permanently improved by sintering and crystallization at that temperature. In operando thermal, magnetic, mass spectroscopic, microscopic, electron- and photon-spectroscopic techniques are enabled. Pellet batteries continue to operate, unharmed, and at greatly improved performance, near the glass transition temperature of the electrolyte.

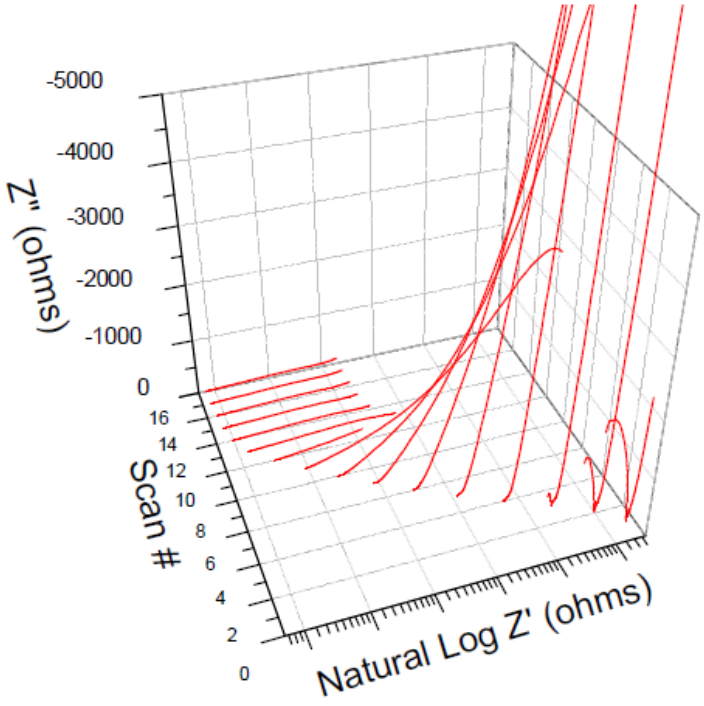

Figure 78: Semilog Nyquist plot during heating

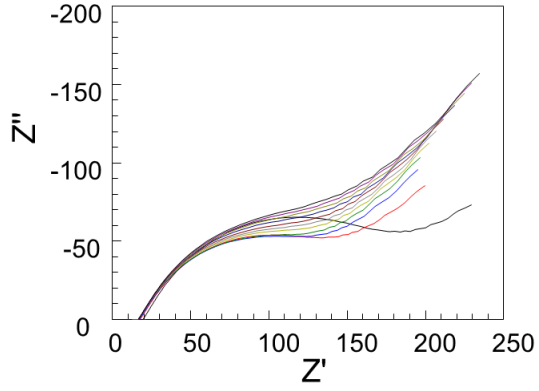

Figure 79: Symmetrical Cell Impedance at 180°C

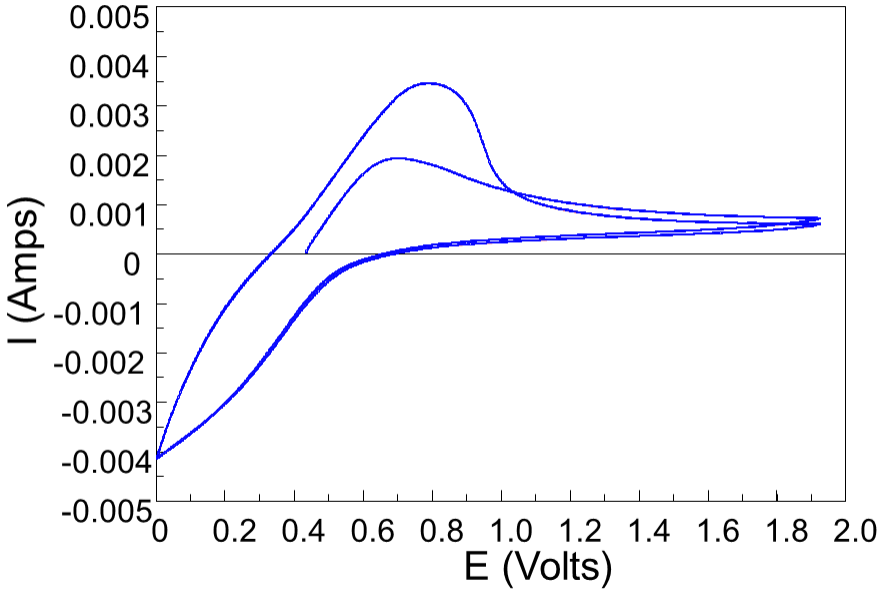

Figure 80: Pulse testing of full cell, LiNiMnO2 cathode

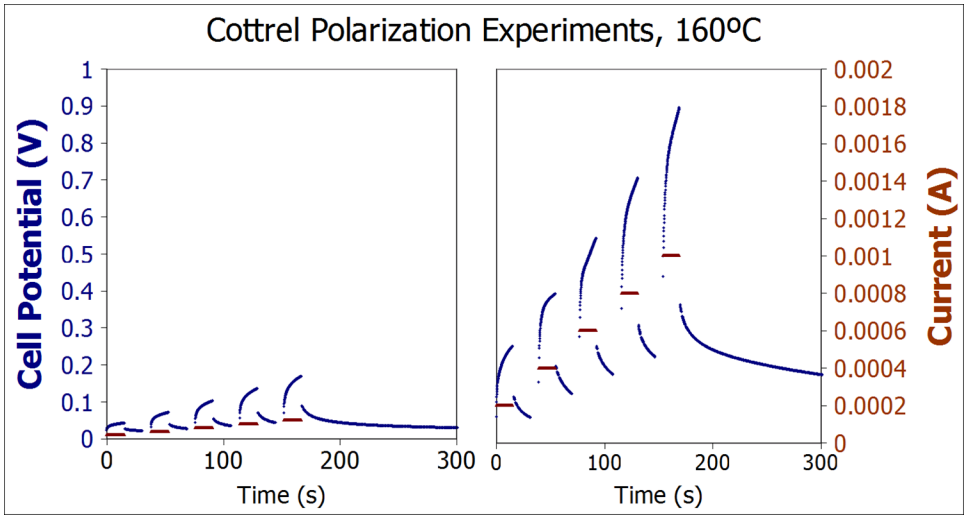

Figure 81: Pulse testing of full cell, LiNiMnO2 cathode

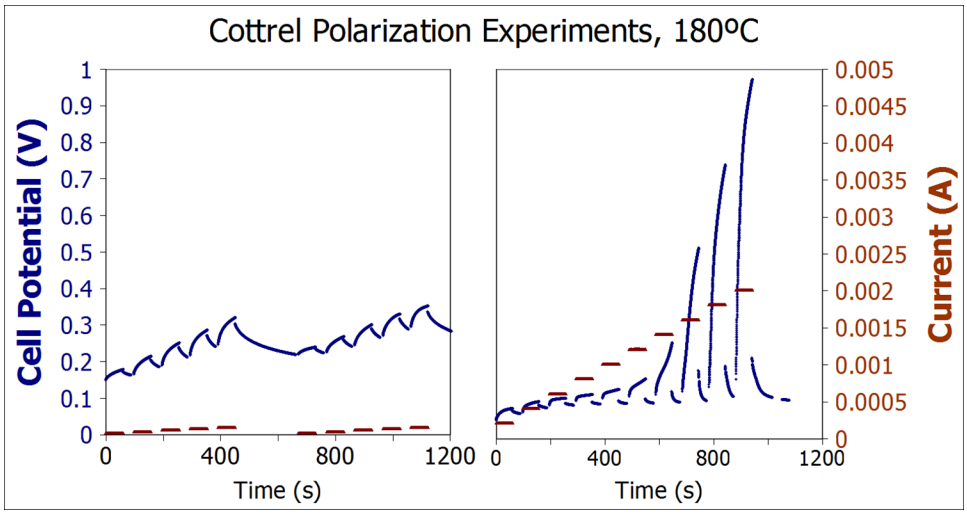

Figure 82: Pulse testing of full cell, LiNiMnO2 cathode

APPENDIX B

EXPERIMENTAL PROCEDURES

B.1 Pouch Cell Assembly

For hard X-ray *in operando* studies, a leak-free pouch cell with no internal shorting, or broken connections, must be constructed. Any internal defects are not repairable at the synchrotron. Therefore, attention must be paid to the quality of the heat-sealing of the moisture barrier material. Figure 83 provides the necessary details of the moisture barrier material.

Pouch Cell Part Preparation

1. Outside glovebox, cut pouch material, aluminum foil, copper foil
2. Outside glovebox, spot-weld active material to aluminum foil
3. Overnight, bake active material in vacuum oven to remove latent moisture
4. Rinse all other materials in ethanol to remove surface moisture
5. Introduce all materials into glovebox
6. Inside glovebox, cut separator material and lithium to size
7. Attach lithium foil to copper foil, add separator material, and heat seal separator onto copper foil

Pouch Cell Assembly Process

1. Fold and Crease Pouch
2. Seal the bottom of the Al strip into the crease to fix it in place
3. Seal the right-hand side of the pouch

4. Align the Cu and Al current collectors at the top of the pouch and fix them in place with paperclips or bulldog clips.
5. Seal the electrode edge with at least 3/8" of sealing surface, then flip the packet and seal the opposite side
6. Seal the remaining side, leaving a small section open for the introduction of electrolyte
7. Mount the cell sideways in order to inject electrolyte
8. Attach electrical leads to read voltage before injecting electrolyte
9. Inject electrolyte while monitoring open circuit voltage
10. Verify voltage is above 2.5 V
11. Seal top surface
12. Trim excess pouch material on the sides
13. Use Kimwipes to remove excess electrolyte
14. Check for leaks along copper electrodes
15. Place cell in jar and seal for removal from glovebox
16. Air out cell in fume hood on a Kimwipe overnight
17. If necessary, add superglue along electrode edges
18. The next day, check for leaks on the Kimwipe

B.2 Air-Free Techniques

Sulfide-based solid electrolytes are inherently vulnerable to attack by moisture, even in low concentrations. Although conventional liquid electrolytes for lithium-ion batteries typically contain fluoride salts in the form of, for instance, $LiPF_6$, must be handled in a glovebox both for the safety of the experimenter and to maintain the performance of the electrolyte, extra care must be taken for sulfide electrolytes. A key difference between liquid electrolytes and sulfide electrolytes is that H_2S

is formed even within the ultra-dry glovebox atmosphere over time, and therefore the smell will escape from the antechamber unless precautions are taken.

Due to the small volumes of sulfide electrolyte employed in creating $1/2$" diameter pellet batteries, large quantities of H_2S gas are not generated. Because compressed H_2S is not used, the concentrations will also be low. However, H_2S is easily detectable at concentrations far below legal limits, which can be found in the Material Safety Data Sheet for hydrogen sulfide.[187] These low levels should not be tolerated, however, but used as an indication of a leak. It is a point of pride in the Alamgir lab that hydrogen sulfide should not be detectable inside the lab on a routine basis. By following the procedures given in this Section, the release of hydrogen sulfide gas can be minimized.

B.2.1 Solid Electrolyte Synthesis

The solid electrolyte powder was generated using a planetary ball mill in a process that combines mechanical alloying with amorphization. Procedures from the literature, specifically those of Prof. Tatsumisago's lab, were used along with advice from Prof. Steve Martin's lab at Iowa State University. However, modifications to the process were necessary to suit the equipment on hand. Where Prof. Tatsumisago's group has a ball mill inside their glovebox, Prof. Martin's group and our group have ball mills outside the glovebox.

The type of material used to construct milling jars is an important parameter in any planetary milling experiment. Where a stainless steel jar can be constructed with a evacuation valve in the lid, this feature would cost thousands of dollars for each ceramic jar. Neither outside group has reported the use of stainless steel milling vials, and we have not experimented with them at Georgia Institute of Technology. Instead, alumina or zirconia jars are used for their extreme abrasion resistance, chemical inertness, and electrically insulating character. With these materials, contamination of the sulfide material is minimized, and any contamination which does occur neither reacts with the sulfide material nor adds electrical conductivity, which is unacceptable in any electrolyte material.

Each group has a different brand of ceramic vials and a different planetary milling machine, each of which is capable of a different maximum rotational speed. Where Prof. Tatsumisago's group can introduce a solvent (hexane) into their milling jar while maintaining an air-free environment, this is

not an option for the other two groups.[188]

Sealing a ceramic vial, which is necessarily constructed without screw threads or bolt holes, can only be accomplished via external mechanical pressure or internal vacuum. In the case of external pressure, an o-ring is compressed between the flat lip of the jar and the flat lid of the jar. The first difficulty with this method is that the clamping mechanism must not get in the way of the clamping mechanism of the planetary mill. The second difficulty is that the sealing cannot be verified. Contaminants such as fibers or powders could negate the effectiveness of the o-ring without any outward sign. With an internal vacuum applied to the jar, a failure to seal is immediately apparent. The combination of the two methods should be avoided. In Prof. Martin's lab[189] adhesive tape is applied to the lid after vacuum sealing; a time-delayed failure of the vacuum seal will not be noticed.

In this work, a vacuum seal was created which tends to last over an hour prior to clamping the jar into the mill; the seal remains strong even after 40 h milling time, and will last for hours after introducing the jar back into the glovebox. In the short term, the vacuum seal is strong enough that the entire jar can be suspended by the lid and shaken. In the long term, a sealed jar in the glovebox will retain at least a weak seal for weeks.

B.2.2 Grinding Method

The goal of grinding lithium sulfide and phosphorous sulfide is to create pellets which conduct lithium ions with ease while not allowing electrons or holes to flow through at all. The resulting powder should press nicely without a binder, should have no XRD peaks between 17° and 60° 2θ, should have a glass transition near 220°C, and should have a crystallization peak in DSC at around 250°C. This document reveals the tricks of the trade.

Required Materials

- 15 x 10 mm alumina balls
- 8 x 6 mm alumina balls
- 10 x 5 mm alumina balls

- Size 140 Viton o-ring

1. Source powders

   (a) Lithium sulfide, phosphorous sulfide, pure, dry.

   (b) Mix 70 mol% Li_2S with 30 mol% P_2S_5 and the mass of P_2S_5 should be greater.

      i. Don't use the molecular weight of P_4S_{10} (444 g/mol)

   (c) Grind these in a mortar & pestle in order to mix them well. Mill vial

2. Mill vial

   (a) Alumina is the "hardest" material available; zirconia and agate are also OK.

   (b) Clean with Alconox, rinse in DI water, bake out at 160°C under vacuum. (setting #4 on the Fischer #280 vacuum oven.)

   (c) Introduce into glovebox while still hot

   (d) When it's cooled off, load balls first, powder second.

   (e) Maximum mass of powder is 3g

   (f) Balls:powder mass ratio is >10:1, typically 12.8:1

   (g) 5 mm balls must be included to grind into the corners

   (h) 10 mm balls cheaper per unit mass!

   (i) This comes to 17 10mm balls (McMaster's are fully dense) and 10 5mm balls from Across International LLC.

3. O-rings

   (a) Circular cross-section Viton o-rings, Dash #140 are to be used.

   (b) Dash #136 is too small- it will cause leaks

Procedure for Vacuum-Sealing Ceramic Milling Vials

1. In the glovebox, clean the o-ring with a dry Kimwipe. Never take the o-rings out of the glovebox or expose them to solvents.

2. Use an alumina rod to burnish the lip of the jar as well as the sealing surface of the lid.

3. Put a Dash #140 rubber o-ring between the vial and the lid.

4. A #136 square-cross-section o-ring can be cut and wrapped around the main o-ring to ensure that it is centered and perfectly circular under the lid.

5. Pump a vacuum, and it's sealed. Pumping slow and refilling fast is preferred, but not necessary.

6. The internal vacuum will be equal to the ultimate pressure you pump to.

7. Seal test #1: Seal the vial in the antechamber and bring it back into the glovebox. Try to lift the whole jar by the lid.

8. Seal test #2: Try to move the lid back and forth. If it's easy to move, the seal is weak.

9. Do not tape, clamp, or rubber-band the jars. If the seal doesn't last long enough for transport to the planetary mill, something was done wrong. No amount of direct air exposure is acceptable.

10. Put each vial in a large, clear plastic jar and remove from the glovebox, but don't apply too much vacuum because the clear plastic jars are weak and will break.

11. In the fume hood, blast the still-sealed clear plastic jars with compressed air to remove the sulfur smell.

12. Before opening the clear plastic jars, observe the alumina jars to see if the lid is on tight. If the alumina lid slides back and forth, the clear plastic jar must be returned to the glovebox so the jar can be re-sealed without ever exposing the alumina jar to atmosphere.

13. Finally, if the jars are still sealed, and at the mill, they can be loaded into the planetary mill and clamped down.

Planetary Mill

1. With a stroboscope we clocked the jars in the Across Technologies mill at 700 rpm, meaning that the main disk is rotating at 350 rpm in the opposite direction. 350 rpm is the number that people report in the literature. 50 Hz is the number that's programmed into the machine.

   (a) Make sure that the mill is well-leveled. There should be a shim making up for the unstable countertop it's sitting on. If the mill is off-balance it will make bad noises and stop turning.

   (b) The total amount of time is 40h. The setting is `cd12 = 40.00`

   (c) 30 hours could be enough for all we know because we haven't tried it.

   (d) After removing the vials from the clamp in the mill, never let it sit. Put the vials into their clear plastic jars and carry them upstairs.

Unloading the powders

1. Before introducing the mill vials into the glovebox, remove them from their clear plastic jars.

2. Put a Corian tile under the vial inside the antechamber to give it stability, and include the large plastic transfer jar so that it's ready for the next run.

3. Pry off the lid of the jar with a scoopula, and let the jar sit for at least 5 minutes. Otherwise the powder will become an aerosol and coat everything in the box.

4. Dump out the loose powder (there won't be much) while noting its color (it should be white.)

5. Scrape out the stuck-on powder with an alumina thermocouple protection tube while watching out for any pockets of yellow (unmilled) powder.

6. Put the balls back in the jar, put the lid on, and shake it by hand in order to remove powder from the balls.

7. Weigh the powder that is recovered. You should get 2.3g (or more) of the 3g that was put in.

8. Grind the resulting powder (which is typically cakey) in a mortar and pestle.

9. Store the powder in a sealed jar, label the jar, and fill out the paper spreadsheet on the window of the glovebox.

10. Wipe out the jar with a Kimwipe, wipe off the o-ring with another Kimwipe, and restart the whole process.

Typical Causes of Error When the vacuum trick fails, it is typically found that powder (either residue from the lid, or powder from the charge) will have appeared on the surface of the o-ring that contacts the lid. When the vacuum trick succeeds, the ceramic lid will frequently slide to one side. Also, placing a small weight on top of the lid seems to increase the odds of success. Taken together, these pieces of information suggest that during vacuuming, the gas within the vial escapes over the top surface of the o-ring, forming a cushion of air which is ideally free from particles. It is hypothesized that the slowest possible vacuuming rate is necessary to ensure a thin, steady flow of gas out of the vial. It is further hypothesized that by converting the powder charge into 2" diameter pellets, the amount of particles would be greatly reduced at the expense of much extra time.

Extra Notes on the Vacuum Trick: The vacuum trick is not magic, but it is somewhat tricky. You put a ceramic vial (not vile; that's the contents) in a vacuum chamber with an o-ring under the lid, you pull a vacuum and then refill with gas, and the lid is stuck on tight. It doesn't matter if you pump fast or slow; it'll seal either way. The vacuum inside the vial is equal to the ultimate vacuum you reach while pumping, as opposed to some intermediate value. But even if you seal at -5 inches of mercury and pump to -30 inches of mercury and refill, the vacuum seal doesn't come undone. It's a one-way process that is not self-limiting. Therefore one may introduce a sealed vial into the glovebox antechamber after milling without breaking the seal.

How can we measure the strength of the seal? By pushing the alumina lid sideways. At -10 inches of mercury it will slide back and forth without breaking the seal. At -30 inches of mercury the lid will be difficult to move.

Why, then, does the vial suddenly come unsealed at all the wrong moments? One problem is using too small an o-ring. Dash number 136 refers to a too-small o-ring which can shift and cause a leak. Dash number 140 refers to a just-right o-ring which can shift all it wants without breaching

on the inside. However, if the #140 o-ring is distorted into an oval shape, a breach on the outside is possible! If you assemble the vial and then wrap a cut-up o-ring around the #140 o-ring, you can tuck it in to enforce circularity. You can leave the cut-up o-ring under the lid during pumping because the opening allows gas to escape. Otherwise, having powder on the o-rings can also cause the seal to fail.

It hardly seems to matter if a square-cross-section $^3/_{32}$" o-ring or a circular cross-section $^3/_{32}$" o-ring is used. They'll both allow the lid to slide back and forth when the vial is sealed at -10 inches of mercury. As long as the o-ring is Viton and Dash number 140, either cross-section is sufficient.

B.2.3 Solid State Battery Construction

In the literature as well as in patent filings, the method of creating powder electrode mixtures and of their application to the electrolyte layer is not given. Therefore, the following methods were developed to create free-standing pellets with pressed-in electrodes.

Barrel Preparation

1. Clean barrel with Kimwipe, doused in propanol, wrapped around a Sharpie.
2. Wipe off the dies
3. Drip stearic acid-in-hexane onto the top lip of the barrel so that it drips down the center. Wait for it to dry to a white layer. Never use stearic acid in propanol.

Electrolyte Preparation

1. Planetary mill the electrolyte to amorphize
2. Heat treat electrolyte to increase its conductivity.
3. Grind by hand with mortar and pestle to deagglomerate.
4. Measure about 150 mg; record precise amount.

For Bare Electrolyte Pellets

1. Insert bottom die
2. Pour in powder while rotating the base (not just the barrel)
3. Slowly insert the ramrod, apply pressure to powder, and rotate a few turns.
4. Reverse direction for a few turns.
5. Reverse direction again while slowly removing ramrod.
6. Add top die, ramrod, and press.

Bottom Electrode (Anode or Cathode) Preparation

1. Insert bottom die
2. Weigh and pour electrode
3. Tamp as described above
4. Add electrolyte powder
5. Tamp electrolyte as described above.

Top Electrode (Anode) Preparation

1. Put anvil on scale and tare.
2. Drip graphite/electrolyte/hexane slurry onto die.
3. Wait until the slurry dries and record the "dry" mass. If you didn't get 10-15 mg, use less hexane in the slurry next time.
4. Use the curved tweezers to bring the dried anvil to the barrel.
5. Use the curved tweezers to carefully invert the top die and insert it into the barrel. Use one finger to push the anvil into the barrel.
6. Add the ramrod and allow it to descend by gravity.

Pressing

1. 1. Add pressure in $1/2$ ton increments, waiting 10 seconds each time.
2. At 5 tons, repeatedly add pressure and wait 10 seconds until 5 tons is held constant.
3. Carefully turn the release valve (use two hands) in order to release pressure smoothly.

Pellet Ejection

1. Invert the barrel while keeping the ramrod in place.
2. Put the barrel in the press with the ramrod on the bottom and the Kimwipe-filled "catcher" on top.
3. Like before, add pressure in 10s increments. Actual pressure should not increase above $1/5$th metric ton.
4. Alternatively, if you hold the "catcher" to prevent it from turning, you can tighten the bolster to eject the pellet quicker.
5. When the pellet is released, observe the pressure. The Kimwipes should maintain some small compressive force on the pellet to prevent cracking. If there isn't enough pressure, keep adding Kimwipes so long as they won't completely prevent ejection.
6. Inspect the pellet. Is the top side flaked and/or cracked? Is more than 50% of the top surface intact?
7. Give the pellet a number in the Excel worksheet and leave the pellet somewhere where it is labeled. Never leave an unlabeled pellet.
8. For bare pellets, record the diameter, thickness, and mass in the Excel worksheet.

Pellet Metrology (Bare electrolyte only)

1. Wipe off caliper jars
2. Grip pellet with metal tweezers with your fingers by the narrowing part of the tweezers.

3. Measure the diameter.

4. Measure several points around the pellet to find the minimum and maximum thickness.

5. Use trigonometry to calculate the angular tilt of the pellet.

6. If the angle is more than 20 minutes of arc, something is amiss.

Pellet Mounting

1. Pair two aluminum or steel plates with plastic bolts and wingnuts.

2. Attach a spade lug to mini-banana adaptor by putting the spade lugs under the bolt heads.

3. Use two coin cell caps, rounded sides inwards, as current collectors.

4. If using Li contacts, put ½" Li foil pieces around the pellet.

5. With tweezers, insert the pellet.

6. Use a black & red plastic clamp to compress the plates, ensuring that the pellet is centered between the two plates and does not hang out.

7. Apply one click of pressure, check for cracking, and tighten the bolts

8. After a few seconds, gradually apply a second click, let the excess pressure off slowly, and tighten the bolts.

9. Tighten each screw alternately (quarter turn each time) until the electrical lugs won't turn.

10. For EIS experiments, leave the clamp in place. Otherwise, remove the clamp.

11. Pick a drawer and insert the banana adaptor in.

12. For electrolyte pellets, the voltage should not read below 0.0001 V; that's a short.

B.2.4 Standard Pellet Recipes

Bare electrolyte pellet

- 200 mg electrolyte which has been both milled in the planetary mill AND ground by hand in a mortar and pestle. • • Unmilled (and/or yellow) powder shall not be used because it serves no purpose. • • 5 metric tons is standard for all types of pellets. Anode half cell
- 10-15 mg graphite or graphite mix on non-dented (top) die. • • 150 mg electrolyte. Cathode half cell (rarely made)
- 10-20 mg cathode mix on dented (bottom) die • • Nothing on top die, especially not stearic acid lubricant • • 150 mg electrolyte as before. Full cell
- 10-20 mg cathode mix on dented (bottom) die • • 150 mg electrolyte as before. • • 10-15 mg graphite or graphite mix on non-dented(top) top die.

Anode half cell

- 10-15 mg graphite or graphite mix on non-dented (top) die.
- 150 mg electrolyte.

Cathode half cell

- 10-20 mg cathode mix on dented (bottom) die
- Nothing on top die, especially not stearic acid lubricant
- 150 mg electrolyte as before.

Full cell

- 10-20 mg cathode mix on dented (bottom) die
- 150 mg electrolyte as before.
- 10-15 mg graphite or graphite mix on non-dented(top) top die.

B.2.5 Powder weighing and batching

1. When pellet pressing use a 1” square plastic disposable weigh boat.
2. Take one from the bottom of the stack and crease it diagonally.
3. For smaller masses, step on the vacuum pedal to reduce pressure and, therefore, buoyancy of the powder.
4. Close the doors on the balance, tare it, and wait ten seconds.
5. If necessary, tare it a second time.
6. Using the shortest scoopula you can find, add powder to the weigh boat until the desired mass (plus about 1 mg extra) is achieved.
7. Step on the vacuum pedal again to make sure the pressure is low.
8. Wait for the balance to stabilize and record the mass inside the glovebox.
9. Carefully lift the weigh boat and fold it along the crease.
10. If powder “pops” out, a quick re-weighing is in order.
11. Pour the powder along the crease into the final container.
12. Weigh the weigh boat to determine the remaining powder.
13. Subtract the remaining mass from the initial mass and record the difference.

Powder Mixture Batching

1. Calculate an 800 mg batch of the desired anode or cathode mixture.
2. Before you start, make sure you won’t run out of any one ingredient.
3. Tare a clean, dry 2 oz glass jar and record the mass on the bottom.
4. Add the exact amount of active material (graphite or LiNiMnO2) into the jar, record the mass.

5. Recalculate the batch ratio to obtain the correct amount of electrolyte powder, and add ~2 mg to account for weighing-dish losses.

6. Tare a glass 60 mm petri dish and weight out electrolyte powder which has been both milled AND ground by hand.

7. Add the electrolyte powder to the slurry jar and re-weigh the petri dish after scraping out any remaining powder.

8. Calculate the true powder mixture ratio from the mass of the graphite plus and the mass of electrolyte powder minus the remaining mass on the petri dish.

9. Calculate the error by subtracting the mass ratio from the ideal mass ratio and dividing by the ideal mass ratio. E.g., (59.6% - 60%)/(60%) = 0.67% error.

10. Close the jar and shake it for at least a minute or until the mixture looks homogeneous.

11. Grind the mixture in a large glass mortar-and-pestle until the powders look smooth and fine. Expect to see chunks of inhomogeneous material appear due to particle fracture.

12. Put the mixture back in the jar and shake it again.

13. Grind the mixture a second time.

14. Label the jar, write down the true mass ratio, error percentage.

15. Add 2 mL of dry hexane to 500 mg of mixture, shake the slurry. This will be fairly thick.

B.2.6 Electrochemical Characterization Workflow

Anode Half-Cell Workflow

1. OCV for 5 min (Any Solartron)

2. Fast CV (600 uV/s), two cycles, between 0.002 V and 10 V. (Any solartron)

3. Charge to 500 mV with -20 uA pulses, 40s on, 10s off. (Solartron with FRA)

4. EIS at 500 mV (Solartron with FRA)

5. Voltage-programmed Tafel curve in 40 mV increments between 400 mV and 4 mV using 40s pulses, 20s rests. (Arbin)

6. If something goes wrong, repeat the Tafel curve but DO NOT apply positive current or the cell will short. Just wait until the OCV rises above 500 mV and re-start from step 5. (Arbin)

7. Charge the half-cell with alternating pulses: 40s x -10 uA, 10s rest, 40s x -20 uA, 10s rest, repeat indefinitely. (Arbin)

8. Perform XRD to check for intercalation.

Cathode Half-Cell Workflow

1. Mount with Li counterelectrode and measure OCV.

2. Perform reverse bias test by linear sweep from the OCV to 0.5V… never go above OCV.

3. At new OCV, perform EIS at 20 mVAC or less

Full Cell Workflow.

1. OCV for 30 min (Any Solartron)

2. Medium CV (400 uV/s), two cycles, between 0.002 V and 5.5 V. (Any solartron)

3. Charge to 2.0 V with +20 uA pulses, 25 min on, 5 min off. (Solartron with FRA)

4. EIS at 2.0 V (Solartron with FRA)

5. Voltage-programmed Tafel curve in 40 mV increments between 3.6 V and 4.2 V using 40s pulses, 20s rests. (Arbin)

6. Charge the half-cell with alternating pulses: 40s x +10 uA, 10s rest, 40s x +20 uA, 10s rest, repeat indefinitely. (Arbin)

7. Perform XRD to check for intercalation.

Bare Electrolyte Pellet Workflow, Blocking Contacts

1. With blocking contacts (coin cell caps).
2. Perform a voltage-programmed stairstep from -120 mV to +120 mV in 20 mV increments, 40s per step.
3. Perform EIS from 1 MHz to 20 mHz at 0VDC (vs. Reference.), 20mVAC, 50 points per decade (distributed logarithmically.) (Solartron with FRA)
4. Carefully dismount the pellet and remount with Li contacts.

Bare Electrolyte Pellet Workflow, Li Contacts

1. With Li contacts (coin cell caps and Li foils ½" diameter)
2. Perform a linear sweep from -20 mV to +20 mV at 100 uV/s. (Solartron with FRA)
3. Perform EIS from 1 MHz to 100 mHz at 0VDC (vs. Reference.), 10mVAC, 50 points per decade (distributed logarithmically.) (Solartron with FRA)

B.2.7 Glovebox Maintenance

B.2.7.1 Glovebox Regeneration Procedure

The following procedure is a supplement to Innovative Technology's instruction manual for their System One gloveboxes. Those instructions should also be read. This document presents the same information in chronological order, as well as some critical information that was missing.

Regenerating the glovebox's purifier column is potentially hazardous because adsorbed gases from the zeolites are being released. Regeneration begins with heating the purifier column; the released gases will pressurize the container and vent off through a valve marked EX and out through a reinforced tygon tube with an ID of 3/8". After three hours of this, regen gas will flow while heating continues for 30 minutes. The heat is then turned off for another 3 hours of purging. The column is then evacuated for four hours, and is then cooled for four more hours. Box atmosphere is then reintroduced into the purification column.

Prerequisites

- The vacuum pump and the regen exhaust line must both be vented.
- The vacuum pump must be on due to the evacuation step.
- 14.5 hours of free time.
- Regen gas: 3-7% Hydrogen in inert gas.
  - Regen gas never enters the box, so it can be N2, etc.
- Valve or flow controller
- Regen pressure: 7-10 psi
- Regen flow: 25-30 scfh (standard cubic feet per hour)
- An assistant to adjust the flowmeter when regeneration begins.

Setup The regen gas cylinder must be secured and connected to a regulator, followed by a valve or flow controller. The output must be connected to the regen gas port on the purifier system. When gas is flowing, a flowmeter on the purifier system itself will register the flow.

1. Check the ventilation lines – the pump and the regen exhaust must be vented - the blue & white plastic vent valve atop the box may also be vented.
2. Open the gas cylinder's main valve and check for leaks.
3. Turn the regulator up to 7-10 psi and check for leaks
4. Open the flow controller – no gas should be flowing.
5. Press BLOWER to turn off the blower.
6. Observe the yellow rods on the column valves – they should be down (closed).
7. Press the REGEN button
8. Start Regen? Hold down the right arrow key and press ENTER to say YES

9. Standard Regen? YES
10. Hand valves open? CLOSED – this refers to the blower valves
11. Is Flow OK? Adjust flow to 25-30 scfh and select YES – company recommends 3 repetitions of this step to purge out the lines.
12. Observe the main screen for HEATING 180.0 – press left and right arrow keys if necessary – if heating does not begin, the flow was not OK; return to step 6.
13. Monitor the room for funky smells escaping from the exhaust lines

Notes:

- At the end of regeneration, box gas is used to repressurize the column
- Working gas can be substituted for forming gas if a "solvent regeneration" is required.
- If regeneration is successful, the REGEN light will go out
- If the regen process is stopped, a message saying POWER FAILURE / REGEN HEATING will appear. The REGEN light should blink, but we know from experience that it might not blink but stay on instead.
- In case of malfunction, pressing the left and right arrow keys simultaneously will reset the controller.
- To Abort, press REGEN and select YES.
- In case of emergency, leave the room and shut off the circuit breakers from outside. This will disable the heating.

B.2.7.2 Glovebox Upkeep

The glovebox is relied upon for the maintenance of an extremely dry workspace. This workspace is used for all lithium battery construction processes as well as some characterization processes; the dry atmosphere is needed for handling lithium metal, lithium compounds, and lithium-based liquid

electrolytes. Organization, cleanliness, and provisions are required in addition to dryness to make efficient work possible. This document provides general principles and a set of steps for periodic cleanup. Knowledge of antechamber operation is assumed.

B.2.7.3 Principles

Dryness Low relative humidity is maintained in part by a steady supply of compressed UHP argon gas which is supplied at less than 1 ppm moisture content. The tank pressure must be maintained above ~100 psi while the line pressure must be around 55-60 psi. At least two argon tanks and one spare should be in place at all times. The prevention of moisture ingress is also needed to maintain this low level of moisture, however. The butyl rubber gloves must not leak and the antechambers must be kept closed, and preferably under vacuum when not in use. Failure scenarios include major unpatched glove leaks, an antechamber with both doors open, loss of line pressure, loss of tank pressure, and the presence of moist material inside the box.

The dry train was provided with a variable-speed blower. Although the recommended speed was 50% of total airflow, it was found through trial and error that a 40% airflow rate seemed to enable lower levels of humidity. A 30% airflow rate, however, was not enough to absorb the moisture which continually diffuses into the glovebox through the gloves.

Organization The organizing principle for the glovebox is that of modular storage. All supplies and tools are categorized and kept in mesh containers; loose supplies and tools tend to fall off of shelves or become disorganized. Starting and finishing a task is easy: a mesh tray corresponding to the work is pulled from the shelf and replaced there after the work is finished. General hand tools go in one tray on a specific shelf while liquid-electrolyte battery supplies go in another tray on a nearby shelf. A notebook with lists of projects, tools, and supplies also contains diagrams of the organization of each side of the box.

Cleanliness Work is typically performed over a fresh sheet of aluminum foil for cleanliness. After work is finished the foil can be crumpled and put in a trash bag. The glovebox floor is covered by sheets of plastic shelf liner known as "bench protector" material. This surface is periodically cleaned with a paper towel wetted by isopropyl alcohol. Isopropyl is preferred over methyl or ethyl

alcohol because of its slower evaporation rate. This reduces the amount of solvents absorbed by the purification column (or "dry train") and hence increases the interval between regenerations. When work is not being performed the workspaces should be clear of equipment and supplies. Aluminum foil should be put in the trash.

Provisions To maintain cleanliness, four things are required at a minimum: disposable gloves, Kimwipes, and aluminum foil. Disposable gloves protect both the glovebox gloves and the materials used in battery construction. Kimwipes are used for cleaning tools or the glovebox. Aluminum foil, like disposable gloves, protects battery materials from the dust on the glovebox floor and vice versa. Four gallon clear plastic trash bags are also needed. Bottles of isopropyl alcohol last many months before running out; these should be checked periodically.

B.2.7.4 Cleanup Procedure

Periodic cleaning of the glovebox involves questioning the necessity of each piece of equipment and all supplies in the box; projects and sub-projects end occasionally. The diagrams in the glovebox notebook (kept in a drawer under the right-hand side of the box) should be consulted to aid in organization. At least 1-2 weeks worth of provisions should be introduced to minimize the use of the antechambers. Trash must also be removed, but this process is more complex than it sounds. To prevent the sulfurous fumes inside the glovebox from escaping, all trash bags must be removed using a large bucket which fits snuggly within the large antechamber. This bucket is introduced with the lid removed so that air can be removed, but after it is filled with trash bags it must be removed from the glovebox with the lid on tight. The danger at this point is of permanently crushing the bucket by vacuuming too hard; only one-half an atmosphere of vacuum is allowable. All material removed from the glovebox is assumed to smell like sulfur and must be kept in the fumehood until it is disposed of, aired out, or cleaned.

1. Put away all tools into their proper places. Check the glovebox notebook for specifics.

2. Remove items that are no longer useful.

3. Clean the workspaces with Kimwipes dampened with isopropanol.

4. Prepare gloves, trash bags, aluminum foil, and Kimwipes for introduction.

5. Introduce the large white bucket (lid open) in the large antechamber together with the provisions from step 4.

6. Put all trash bags in the bucket and put provisions where they belong.

7. Close bucket and remove it from the glovebox without pumping more than 1/2 atm of vacuum. Open the bucket only in the fume hood and remove trash bags.

8. Repeat steps 5-7 until all the trash is removed.

9. Put all 4 gallon trash bags into a larger clear trash bag and tie it shut.

10. Create a "waste pickup sheet" at http://www.chematix.gatech.edu to request waste pickup.

11. Check argon bottles and pressures.

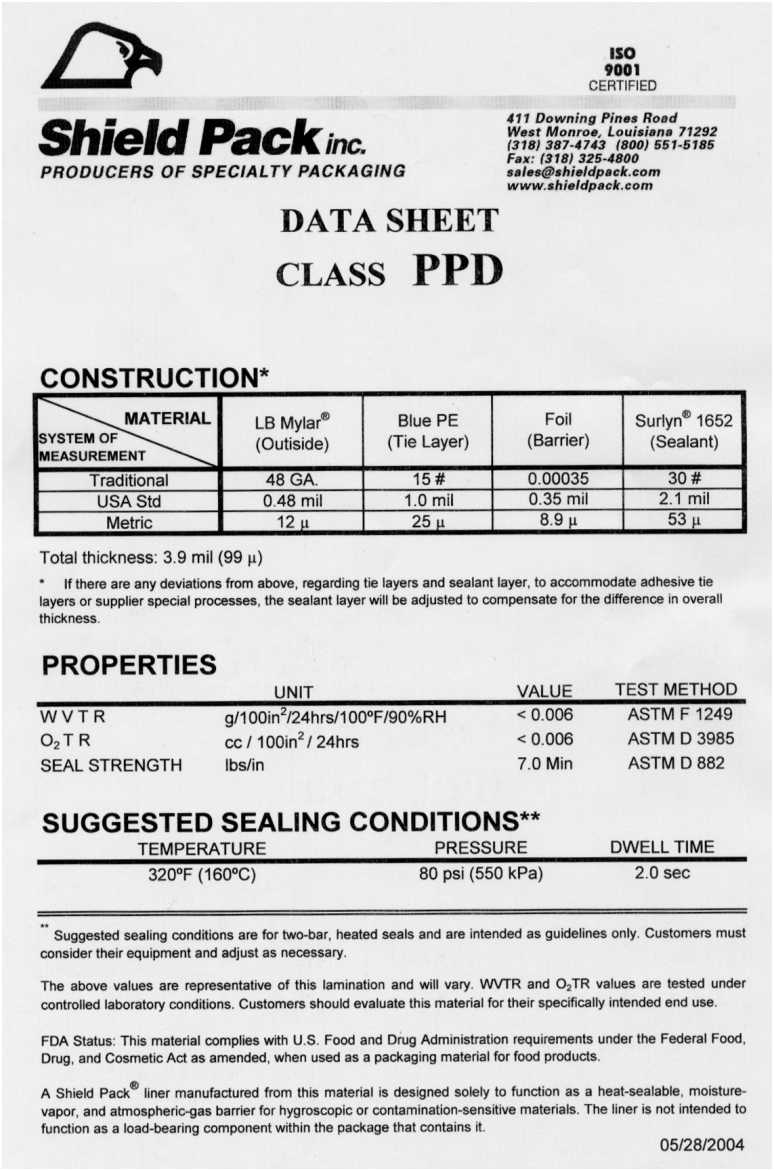

ISO 9001 CERTIFIED

Shield Pack *inc.*
PRODUCERS OF SPECIALTY PACKAGING

411 Downing Pines Road
West Monroe, Louisiana 71292
(318) 387-4743 (800) 551-5185
Fax: (318) 325-4800
sales@shieldpack.com
www.shieldpack.com

DATA SHEET
CLASS PPD

CONSTRUCTION*

MATERIAL / SYSTEM OF MEASUREMENT	LB Mylar® (Outiside)	Blue PE (Tie Layer)	Foil (Barrier)	Surlyn® 1652 (Sealant)
Traditional	48 GA.	15 #	0.00035	30 #
USA Std	0.48 mil	1.0 mil	0.35 mil	2.1 mil
Metric	12 µ	25 µ	8.9 µ	53 µ

Total thickness: 3.9 mil (99 µ)

* If there are any deviations from above, regarding tie layers and sealant layer, to accommodate adhesive tie layers or supplier special processes, the sealant layer will be adjusted to compensate for the difference in overall thickness.

PROPERTIES

	UNIT	VALUE	TEST METHOD
W V T R	g/100in^2/24hrs/100ºF/90%RH	< 0.006	ASTM F 1249
O_2 T R	cc / 100in^2 / 24hrs	< 0.006	ASTM D 3985
SEAL STRENGTH	lbs/in	7.0 Min	ASTM D 882

SUGGESTED SEALING CONDITIONS**

TEMPERATURE	PRESSURE	DWELL TIME
320ºF (160ºC)	80 psi (550 kPa)	2.0 sec

** Suggested sealing conditions are for two-bar, heated seals and are intended as guidelines only. Customers must consider their equipment and adjust as necessary.

The above values are representative of this lamination and will vary. WVTR and O_2TR values are tested under controlled laboratory conditions. Customers should evaluate this material for their specifically intended end use.

FDA Status: This material complies with U.S. Food and Drug Administration requirements under the Federal Food, Drug, and Cosmetic Act as amended, when used as a packaging material for food products.

A Shield Pack® liner manufactured from this material is designed solely to function as a heat-sealable, moisture-vapor, and atmospheric-gas barrier for hygroscopic or contamination-sensitive materials. The liner is not intended to function as a load-bearing component within the package that contains it.

05/28/2004

Figure 83: Datasheet from Shield Pack, Inc. for moisture barrier material including layer thicknesses and sealing parameters[128]

B.2.8 Air-Free Sample Shipping and Transfer

To transfer air sensitive samples to U7A, certain steps must be followed. There are good reasons for each step, and there is usually proof to be had during the process that verifies the reasoning. The table below gives chronological instructions for shipping sample bars to vacuum chambers at the NSLS.

Table 14: Process for vacuum-packaging air-sensitive samples for shipping

Steps	Reasoning
Keep a dry GB atmosphere	Can't start without good samples.
Assemble the sample bar before sealing it in	It's really hard to make a sample bar in a glovebag.
Test sample bar before sealing it in	Self-evident.
Wrap sample bar in a non-hygroscopic stiff plastic.	Electrical insulation and padding is needed; don't prevent vacuuming later.
Add big chunks of indicating Drierite outside the bag	Keeps things dry and acts as proof later.
Seal the bar and bag in Conflat tube	The metal-metal seal is the best available.
Vacuum the tube out through a valve, close the valve, cap the valve.	Upon opening the valve at the beamline, a rush of N_2 will be felt and heard.

Table 15: Process for sample shipping and transfer into a vacuum chamber

Steps	Reasoning
Ship the sealed tube via GT EH&S' shippers	Avoid the $30,000 fine for improper hazardous shipping
Ship to: Brookhaven National Lab Bldg 98 Central Receiving Bldg 725 Experimenter Name U7A Upton, NY 11973	All hazardous material and all FedEx goes through Bldg 98; no hazmat goes through USPS.
Receive the samples in the stockroom the day before beamtime	All packages are rerouted to a beamline based on the recipient name. Packages arrive at ~12:30 PM in the stockroom.
Put sample tube(s) into the glovebag with extra gloves and tools.	Adding tools to the bag adds moisture.
Attach glovebag to the chamber with two super-thick rubber bands and tuck the bag under the flange bolts.	Small leaks allow large amounts of moisture to leak in.
Attach an N_2 tank to a regulator followed by a valve followed by a "hose mender" going into the bag, and attach flowmeter and long exhaust tube.	The first valve regulates flow, the second valve measures flow, and the long exhuast limits backflow.
Use USB humidity gauge from Omega and monitor %RH on a laptop until it hits 0%.	A low %RH must be verified.
Only open sample tube when the bag has been dry for some time.	True relative humidity should be some fraction of one percent, but the gauge won't read that.
Load the sample carefully but quickly and don't do surgery on the bar.	Delicate operations are not to be done in the glovebag.

APPENDIX C

DESIGN OF NOVEL SAMPLE FIXTURES

C.1 Material Selection

In operando electrochemical experiments take place in demanding circumstances which tend to combine the constraints of multiple environments. For instance, charging a solid state lithium battery under high vacuum combines the need for corrosion-resistant materials with the need for vacuum-compatible materials. Charging a liquid electrolyte battery in a magnetic field or while X-rays penetrate the cell are two other challenging combinations. In this work, aluminum was found to be a highly versatile material, frequently exceeding the performance of stainless steel or copper in terms of corrosion resistance, performance in a magnetic field, and transmission of X-rays. Among polymers, polyimide, PTFE, and PEEK gave better performance than nylon and polyethylene. Alumina was successfully used in multiple applications. Table 16 below summarizes the applicability of commonly used materials to the disparate environments used in this work.

C.2 High Vacuum, High Magnetic Field Environments

For electron microscopy and photoelectron spectroscopy, ultra-high vacuum is not required. I.E., high vacuum compatible, but non-bakeable, materials such as PEEK and nylon are allowed. Although nonporous ceramics and UHV-compatible metals are preferred in order to reduce pump-down times, many sample holder designs can be simplified by the use of widely-available nylon fasteners. Stainless steel, but not zinc-plated or plain steel, is allowable. Aluminum, without a porous anodized surface, is also useful. Copper, but not brass which outgasses zinc, is sometimes used. Although alligator clips are available in stainless steel, most are nickel-plated steel and will corrode in battery electrolytes. Similarly, ring terminal connectors are typically tin-plated copper and will fail.

An additional, difficult constraint is found at four beamlines at the NSLS: high magnetic fields. First, the established technique of X-ray Magnetic Circular Dichroism is practiced at U4B using a

Table 16: Applicability of Common Materials to Differing Environments

	High Vacuum	Magnetic Field	Battery Electrolyte, Anode	Battery Electrolyte, Cathode
Aluminum	2XXX, 6XXX (low zinc, non-anodized)	Any	None	1100 or Pure
Stainless Steel	Any	None	(AISI 321H)	(AISI 321)
Ceramics	(nonporous)	Any	(All but silica)	(All but silica)
Copper	(not brass)	Any	Pure	None
Plastics	PTFE, PEEK, polyimide (nylon if degassed)	Any	PTFE, Nylon (No polystyrene, polypropylene)	PTFE, Nylon (No polystyrene, polypropylene)

magnetic field of 0.9 Tesla. Newer detectors being developed by NIST's Dr. Daniel Fischer will utilize magnets of up to 8.5 Tesla. Sample bars used for this purpose must have low magnetic permeability. However, even the smallest quantity of (nominally non-magnetic) stainless steel cannot be trusted in this environment, even at lower magnetic fields. Although 300-series stainless steel should have a non-ferromagnetic FCC austenitic crystal structure, machining the threads of screws and nuts causes a small percentage of BCC ferrite to form, leading to residual magnetism.[166]

The material of choice in this environment is aluminum, especially 6063. Grade 7075 (5-6% Zn) is known for its strength, but its zinc content is a hazard in a vacuum system, especially if the system is to be heated. Grades 2024 and 6061 have 0.25% Zn[190] while 6063 has only 0.1% Zn. Alloy 6063, heat treated to the T5 condition, is the material used for the electron storage ring of the Advanced Photon Source. Alloy 2219, also with 0.1% Zn, is used for flanges.[191] The NSLS-II will also use alloy 6063, but with a T6 heat-treatment.[138]

For even higher temperatures in high vacuum at high magnetic fields, titanium is an excellent candidate for sample bars due to its superior strength, stiffness, higher melting point, and lack of zinc content. However, its cost is typically prohibitive. Aluminum oxide, either sintered or in the form of a sapphire wafer, is a poor choice due its brittleness. Because sample bars are mounted to a manipulator, they occasionally strike the inside of the analysis chamber. The consequences of a shattered sample bar could be disastrous.

C.3 High Temperature, Dry Sulfide Atmosphere

For heat treatment of sulfide materials in a glovebox, a sulfide-resistance material is required; for *in operando* high temperature battery experiments, both conducting, insulating, and mechanically supportive materials are needed. In the literature, lists of suitable and unsuitable materials can be found for wet sulfide environments, possibly in boiling water laced with hydrosulfide (SH^-) ions. In contrast, we are concerned here with materials which react with hot, dry H_2S gas in a low O_2 environment. A number of electron-rich metals on the right-hand side of the periodic table react quickly and destructively with dry sulfide: Ni, Cu, Zn, Sn. In designing high temperature battery holders, this precludes the use of most alligator clips, which are copper or nickel-plated steel, spade terminal connectors, which are only available as tin-plated copper. Zinc-plated steel fasteners are

easily substituted with stainless steel.

In this environment, aluminum remains a good choice for structural parts, but not for wiring or threaded fasteners. Stainless steel was found to take on a yellow patina when first heated in the presence of sulfide, but this patina was not harmful. PTFE was found to be suitable up to 500°F (260°C); it chars just above this temperature. Because aluminum wire is unavailable with insulation of any kind, PTFE tubing was added to bare aluminum wire. However, aluminum was found to be too weak for multiple experimental runs. Stainless steel wire was sheathed in PTFE tubing, although PTFE-insulated and polyimide-insulated stainless wiring is available from specialty suppliers. Because spade terminals (with size #2 bolt holes) are always plated copper, the stainless wire was formed into a hook. A hammer was used to flatten the hook shape in order to make better contact with flat washers; this was done with care to avoid strain-hardening and fracturing the hook.

C.4 O-rings and Gaskets

In both high vacuum and sulfide environments, Viton fluoroelastomer O-rings were found to be satisfactory. In ball-milling experiments, a Viton O-ring was used for up to 40 hours. Although the ball mill apparatus applied a clamping force on the O-ring, the O-ring was relied upon to maintain the seal during transportation of the vial to and from the glovebox. Although silicone O-rings are available and, in theory, should show enhanced resistance to reactions with sulfide, such O-rings were not tested.[192]

For the much longer period of time required for shipping samples to the NSLS and back, an all-metal seal was found to be necessary. For this purpose, copper gaskets and Conflat flanges were used. Such gaskets were largely successful, showing only minimal corrosion within the sealed, inner portion of the gasket. However, high-temperature experiments in which sulfide materials were sealed within a Conflat container as in Figure 84 reveal that the formation of copper sulfides can be destructive. The only alternative in that environment is a soft, annealed aluminum gasket.

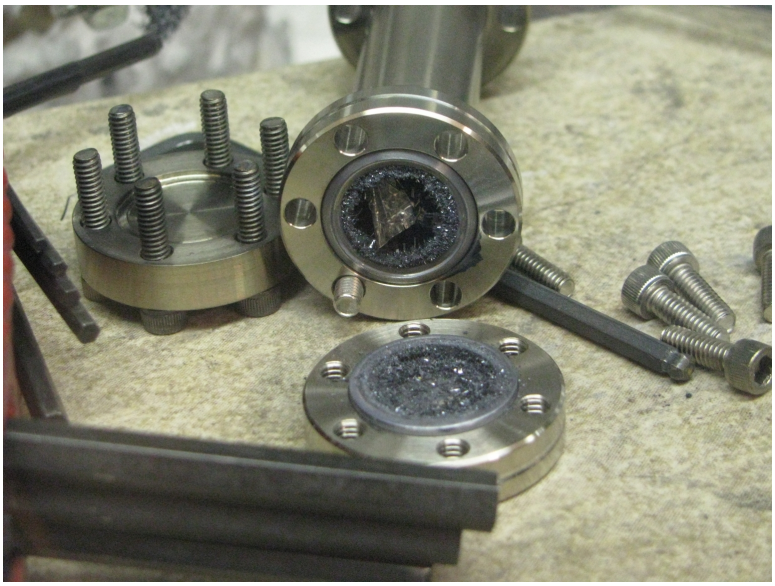

Figure 84: Formation of copper sulfides at high temperatures

C.5 Submersible Thin Film Sample Holder

In this Section a novel sample holder used for the study described Section A.1 is discussed. In that experiment, a thin film with three (aluminum) metallized contacts was submerged in a jar cell. Electrical contacts were maintained using a PTFE bar with a series of threaded and unthreaded holes.

Lithium battery electrolytes create a very harsh environment for many materials. The typical salt, $LiPF_6$, reacts with glass, ceramics, and metals. The typical solvent, dimethyl carbonate, reacts with polymers such as polystyrene and polypropylene. Although aluminum is suitable at high potentials because it passivates to form AlF_3, it is corroded at low potentials, especially at the potential of lithium metal.

Stainless steels are generally acceptable in all parts of the cell, as are PTFE and nylon. A highly transparent polymer is also available for jar-cell batteries: polymethylpentene. This hard-to-obtain plastic does not become cloudy over time due to contact with the electrolyte, as does polypropylene. A jar cell was designed which allows the secure mounting of a thin film electrode at a precise depth in the electrolyte solution.

In Figure 85, the thin film sample holder design is shown. The holder is constructed from a slab of PTFE with size 2-56 holes tapped into the face and a metric M3 tapped hole at the top. The M3 tapped hole accepts a 3 mm aluminum rod which is threaded at the end. The 2-56 holes are spaced to allow the thin film to slide between the shanks of the screws. Electrical contact is ensured by compressing aluminum wires between the screw heads and the aluminum metallizations.

The sample holder and the other electrodes are suspended from the lid of the jar by rubber stoppers with holes. After the cell is fully constructed, it is taped securely to a sturdy platform, and electrolyte is injected last. The depth of the electrolyte is controlled via a 4" stainless steel dispensing needle which is inserted in the lid of the cap.

C.6 Design Criteria for Soft X-ray Sample Holders

For *in operando* studies in vacuum, multiple isolated (floating) electrical connectors must be available in the vacuum chamber. These connections are most useful if they are part of the sample manipulator. At NSLS beamline U12A, the sample manipulator is separate from, and perpendicular

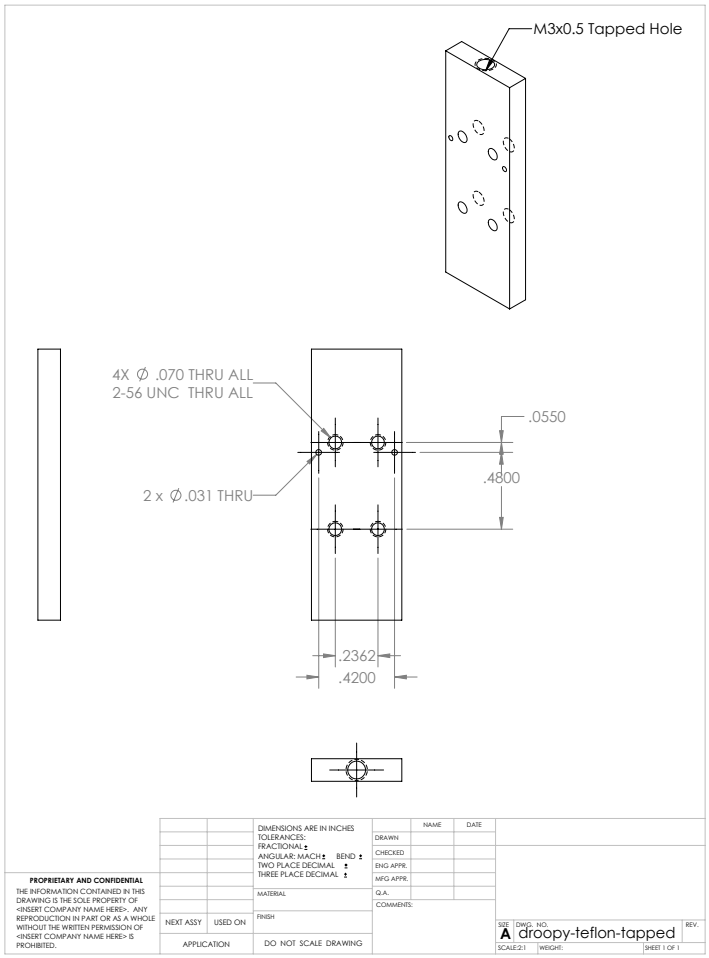

Figure 85: Schematic of submersible sample holder for thin film devices

to, the load lock and the transfer arm. Significant manipulator modifications would be required to create the maximum number of two floating contacts, and sample transfer from the transfer arm is very risky. *In operando* experiments were, therefore, not attempted at U12A and were only used at U7A where the sample manipulatorr and the sample transfer arm are one in the same. A further advantage of the manipulator at U7A is the presence of four floating pins which makes possible experiments on as many as three independent batteries. In this design, the bar itself is connected to three battery cathodes and is grounded while the three additional pins are connected to the three anodes.

C.6.1 U7A Main Chamber

The U7A Main Chamber is large, versatile, and complex. The detectors include a Partial Electron Yield (PEY) detector with a variable grid bias, a fluorescence yield (FY) detector which can detect soft X-rays in spite of ambient light, a very large, moveable XPS analyzer, and a multi-layer mirror detector which amplifies fluroescence from the C K-edge. The PEY and FY detectors are small and are positioned near the incident beam while the multi-layer mirror can be retracted into the bottom of the chamber. The XPS analyzer, in contrast, requires an enormous tube of Mu-Metal which absorbs stray magnetic fields. The Mu-Metal tube has holes to allow a sample bar to pass through; however, these holes are not well-aligned either with the beam or with the sample manipulator axis. It was found that a sample bar must be extremely thin and that the samples must not protrude in front of the manipulator axis. Samples protruding too far will be grounded against the Mu-Metal shield.

C.6.2 U7A Imaging Chamber

The U7A Imaging Chamber is a new type of soft X-ray microscope based around the LARIAT Mk I detector developed by Synchrotron Research, Inc. It is especially interesting because the next-generation LARIAT Mk II design will be used at the NSLS II. The LARIAT Mk I prototype is operated using software which cannot be automated and which cannot cope with beam refills.

More so than the U7A main chamber, the imaging chamber is extremely restrictive in terms of sample placement. Unfortunately, the schematics are proprietary and so the design of sample bars could only proceed by trial and error. The sample must be positioned as close to the magnetic pole

piece as possible, even though this location is at the bottom of a very long and narrow tube. By trial and error, it was found that even a one millimeter gap between the back of the sample bar and the pole piece is detrimental to the data quality. Ideally, the sample bar with touch the pole piece without scratching it.

Although the sample bar must be very long, it must also be very lightweight to avoid falling off of the slip-fit connection to the manipulator. Furthermore, the region around the sample must be devoid of even the least ferromagnetic materials, such as high-grade stainless steel. The slightest amount of ferromagnetism will bend an aluminum sample bar, and possibly detach the sample bar from the manipulator. However, the connections above the sample can utilize plain carbon steel.

C.6.3 Sample Bar Design Criterion

A simple, unambiguous criterion is proposed to simplify sample bar design: a radius about the manipulator axis, within which no collisions are possible, should be specified for each sample chamber and published online. This is necessary firstly for sample bar design, which occurs far away from the NSLS. Secondly, when sample bars are moved within the sample chamber, there is no collision avoidance system. The X,Y, and Z stepper motors are subject to "soft limits" which can be altered arbitrarily. Furthermore, the sample bar cannot be viewed from all angles when inside a sample chamber.

Experimentally, the safe radius can be determined using plastic tubes of differing diameters. Furthermore, the "soft limits" can be programmed according to the range of motion which is safe for each radius of tubing. For the largest diameters, only small movements in X and Y will be possible. This information will save large amounts of valuable beamtime.

C.7 Potentiostat Programmability

In this study, four brands of potentiostats were used. Each potentiostat was designed for a different type of user and therefore had an interface which limited how it could be used. Firstly, the Pine WavenowXV was designed for extreme portability, being very small. The Aftermath software was designed for electrochemical demonstrations and teaching, and to that end, only specific types of fully-formed experiments are available to the user such as Double Step Chronopotentiometry. Primitive experiments such as Square Wave Chronoamperometry (a potential square wave) were available while Square Wave Chonopotentiometry (a current square wave) was not available and had to be constructed from Bulk Electrolysis and Open Circuit steps. To construct a current square wave, these two experiments could be added to the queue individually. Loops were not possible. To charge a battery using ~1 h pulses, hundreds of experiments were sequentially added to a queue (which could not be saved) prior to starting a X-ray Absorption Spectroscopy script with XDAC on the beamline computer. By this method, a solid state battery could be charged using a laptop while a preprogrammed XDAC script was run, and the correspondence between state of charge and a particular scan could be reconstructed later by comparing date stamps on the files. Although the XDAC results files could be numbered ahead of time, the Pine Aftermath files merely incremented without a way to include the sample name.

In contrast, a Biologic potentiostat (which was used only briefly) presented the user with complex flowcharts filled with if-then statements, loops, as well as the bandwidth and stability settings for the op-amps inside the machine. The learning curve was steep, but the adaptability of the machine was very high. Similarly, the Arbin BT2000 battery cycler (with MITS Pro software) allows looping experiments with multiple loop counters and many conditions which can trigger the end of an experimental step. A compromise between programmability and simplicity of use was found in the Solartron 1287 (with Corrware software). Corrware allows for a wide variety of electrochemical experiments to be combined in loops, and impedance experiments can be called via the Zplot program.

APPENDIX D

XAS DATA REDUCTION PROCEDURES

D.1 Hard X-ray Absorption

Data Inspection Many forms of interference can have subtle effects on XAFS data, and this is not always obvious. Frequently, the best method for spotting anomalies is to plot a supposedly flat region, normalized, without including the white line. This will amplify small defects including monochromator glitches as well as EXAFS oscillations from other elements. Plotting the derivative is useful in finding the beginning or end of a region of high data point density; however, monochromator glitches can be skewed by the derivative plot, making many non-glitch points appear to be glitches.

Multiple-Element Data Scans Frequently, to simplify an experiment enough to automate it, it is necessary to measure the X-ray absorption of multiple elements in a single scan. In the case of transition metal K-edges, there is little overlap between subsequent elements. (To check for overlap, the pre-edge region can be plotted by itself so as to auto-scale the absorption axis, thereby revealing weak EXAFS oscillations.) In any case, beamline parameters can typically be held constant across a few edges. An example would be manganese, iron, cobalt, and nickel which are especially common in lithium battery cathodes. In the case of a mixture of K-edges and L-edges, however, overlap is possible and this can be detrimental to pre-edge and post-edge fitting. An example for soft X-rays would be vanadium oxide. For hard X-rays, rare earth element L-edges and transition metal K-edges may overlap; this case will not be considered here. The first step in data reduction is to load the set of scan files once for each absorption edge; ATHENA is not designed to simultaneously treat multiple edges. For each dataset, the E_0 parameter, described in detail in the next section, is set to select the correct edge.

Ideally, the reference chamber will have been loaded with foils of each element. However, this can be difficult to achieve and will increase the absorption to the point where the reference signal

will overload the amplifier at lower energies and drop to zero at higher energies. In some cases it is acceptable to load one element's reference foil and align both datasets to the same edge in the reference scans. In this case it is necessary to set the E_0 parameter of the reference scans for one element, and set the E_0 parameter of the data scans to the element of interest. The accuracy of this method can be checked by comparing monochromator glitches, which are especially common in the Ni K-edge, for correct alignment. The Ni K-edge data can then be aligned according to the Mn K-edge reference foil, provided that the monochromator moves in a repeatable way for each scan.

Energy Scale When an X-ray Absorption experiment is performed, a stepper motor is used to rotate a monochromator. In accordance with Bragg's Law, the rotation of the monochromator crystal controls which wavelength reaches the sample. The translation of stepper motor steps to photon energy in eV is defined by a calibration performed by the beamline scientist. The calibration function is adjusted to be fairly accurate across the range of energies possible at a particular beamline. Therefore, the accuracy of the calibration function will vary from one element to another, and from beamline to beamline. Accordingly, X-ray Absorption data are calibrated to textbook values for each element.[46] The calibration procedure utilizes the reference scan, which is typically the absorption spectrum of the pure element. In ATHENA, the calibration is effected using an Energy Shift.

This Energy Shift moves the energy scale for both the reference scan and for the data scan. The data scan is then plotted with an energy scale defined by a second parameter known as E_0. ATHENA attempts to estimate E_0, but the estimation is poor and changes from scan to scan. Crucially, this E_0 parameter is later re-used for EXAFS background fitting and should not change from scan to scan.

ATHENA hides this problem by plotting all scans according to the E_0 value for the first-selected scan. Unfortunately, when making comparisons not involving the first scan, the alignment of subsequent scans changes depending on the new first-selected scan. Furthermore, when exporting data for plotting, ATHENA offsets each scan according to E_0 in addition to the Energy Shift. When the data are plotted in other programs, the data will appear to lose alignment. For hard X-ray data, E_0 must be fixed before the data are exported. For soft X-ray data, frequent cross comparisons are necessary; therefore E_0 should be held constant in all cases.

Background Subtraction XANES and EXAFS data analysis relies more heavily on data reduction than does X-ray diffraction analysis. In powder diffraction, the peak locations in two-theta can be misaligned, distorted, and can be superimposed over an irregular background function without precluding phase identification and the calculation of lattice parameters. More sophisticated analysis is enabled by accurate diffractogram fitting. XANES, however, must be well-aligned to accurately detect chemical changes. EXAFS analysis requires an accurate background spline function before physically meaningful structural data is obtained. Furthermore, this data reduction is somewhat subjective because an automated procedure would be unable to cope with widely varying types of chemical compounds. Therefore, the analysis programs (such as ATHENA) provide more than a dozen user-adjustable parameters. While these dozen parameters cannot be standardized, the data reduction can be made repeatable by specifying not only the method of choosing each parameter, but also by specifying the order in which these parameters are set in order to avoid path-dependent errors.

The background subtraction procedure described here is designed to be performed only once, without the need for re-tweaking of the parameters. The precise order operations is listed in Section D.4. This greatly simplifies the subsequent data analysis, saving time. A step-by-step procedure, divided into three Phases is given below. The documentation for ATHENA, which describes the basic procedures, should be read and understood before this procedure is applied.

When comparing different compounds containing the same element, the differences between spectra are large. However, in battery studies small changes in composition lead to subtle changes in the chemical environment of the element of interest. Therefore, when analyzing several data files from the same sample it is important to treat them all equally, except for their alignment. This not only ensures a consistent analysis sensitive to small changes, but it also reduces the complexity of the task. The alternative, which is to customize the data reduction parameters for each scan, is time consuming, unreliable, and unnecessary. The key operation in ATHENA is to "Set all marked groups' values to the current" which copies all settings, including the alignment offsets, to each data scan. Frequently, the data scans must then be realigned according to their reference spectra.

A second consideration is the number of times each parameter is adjusted. The most objective and independent parameters should be set first, followed by more subjective and/or dependent

parameters. Interdependent parameters must be varied iteratively after the independent parameters are set. The subjective parameters should be varied to assess the relative merits of each choice. Subjective parameters should be set in such a way that minor changes in those parameters lead to insignificant differences in the final output. In some cases, such as the post-edge fitting points described below, multiple choices can achieve identical results. In these cases, the tie-breaking principle is to utilize the greatest range of data possible.

After alignment and deglitching, the background spline is adjusted. ATHENA will auto-generate settings which may be inconsistent from one scan to the next, or completely wrong. The first setting is the E_0 point, which is the inflection point in the first pre-edge feature. This is found by plotting the first derivative $\mu'(E)$ and choosing the first peak, taking care to exclude noise which is emphasized in a derivative plot. Next, this point can be refined by plotting the second derivative of the data $\mu''(E)$ and finding the nearest zero-crossing. At this point it should be determined whether E_0 changes from scan to scan, such as when the element of interest is oxidizing or reducing. If it does not change, a constant value can be used. If it does change, the final results will be affected in subtle ways which can change the structural conclusions. Unfortunately, the "Set all marked groups' values to the current" operation will set it to a constant value, and these values must be restored manually. Therefore, the E_0 values should be recorded before proceeding. The E_0 point can be allowed to stay constant, and then fine-tuned at the end of the process in order to bring the R-space plot into precise alignment. At this point, the k-spline minimum should be set to approximately 1.5 Å^{-1} such that the spline starts somewhere above the E_0 point. (This is always changed later in the process, but the following steps depend on a good starting spline curve.) Although historically this point was set to 30 eV above E_0 (which transforms to something larger than 1.5 Å^{-1}), modern procedures[98] allow the spline range to extend much closer to the white line without introducing errors. Next, the end of the spline range is chosen to be the highest-energy point in the spectrum unless the absorption of another element is present. If a low-resolution region between two elements is present, the spline range should not extend into the low-resolution region. If EXAFS oscillations are present, the spline range should not end on an oscillation.

Next, the pre-edge starting point, pre-edge endpoint, and the post-edge endpoint are chosen; the correct choices are easily found, although they do depend on E_0 because it defines the energy

scale. The pre-edge region should end somewhere in the high-resolution region just before the first absorption features, and should start as far below those features as possible such that the pre-edge fitting line matches the pre-edge data. The post-edge endpoint is simply the highest-energy point unless the absorption due to a second element is present.

However, when picking the beginning of the post-edge curve, the entire dataset as well as the background spline curve should be taken into account. Although ATHENA performs a quadratic fitting between the post-edge start point and endpoint, a poorly chosen start point can affect the final results. First, the first scan is plotted in energy along with the background spline. A point is chosen where the background spline intersects the data; this point should be as close to the white line as possible without being in the white line. Generally, it can be found between 50 and 200 eV above E_0. Multiple points may satisfy these guidelines, but when all scans are plotted together (normalized $\mu(E)$)), some points will be seen to remain nearly the same for all scans. The ideal candidate is an isosbestic point where all the scans intersect, provided that this isosbestic point is near the background spline. However, a change in the post-edge necessarily changes the normalized plot, so the "Set all marked groups' values to the current" operation, followed by realignment, is performed, and the choice of the post-edge start point is repeated once more.

At this point, the data is well aligned, well normalized, and has a reasonable background spline, although this will be adjusted once more. The data is now plotted as $\chi(k) \cdot k^2$ which represents only the EXAFS oscillations (deviations from the background spline) multiplied by the square of the photoelectron wavevector k, which is defined relative to the E_0 point. If the EXAFS oscillations taper off rapidly, $\chi(k) \cdot k^3$ may be used, although as a side effect, noise at higher k-values will be amplified, affecting the entire range of real space data.

Next these data are Fourier Transformed from k-space into real space using a window function. Although in theory a Fourier Transform operates on an infinite domain, in reality the data is finite in extent. The purpose of a Fourier Window is to soften the edges of the data. Without the window, the abrupt end to the data would represent an infinite derivative which would be Fourier Transformed into an endless series of frequencies extending to infinity. The window function varies from zero to unity with a smoothly-varying functional form at each end of the data. By multiplying the data by the window, the limits of the data reach zero smoothly. (It is not usually necessary to adjust the type

of window.) The domain of the data in k-space is known as the Fourier bandwidth; this bandwidth should be kept constant across all the scans either by using the same window, or using windows of the same width for each scan. By maximizing the Fourier bandwidth, the noise in the real space plot is limited.

The window should begin and end at points near zero-crossings in the data, although to maximize the amount of data used in the transform (by widening the window) points away from the zero-crossings can be used. This can become necessary when plotting all the scans together. Preferably, the window should begin and end at isosbestic points or at points where all the scans are near each other. Certain regions of the k-space data within the window will change greatly from scan to scan; these regions contain the interesting trends.

Finally, the data are Fourier Transformed into real space, starting with the first scan, followed by plotting all the scans. The plot will show Gaussian peaks, which represent atoms neighboring the absorbing atom, along with non-Gaussian "ringing" which is the Fourier Transform of random noise in k-space. Also, at low real space values, there will be some raised background which should not exist; the space between atoms is empty, and the real space plot should reflect that fact. According to Newville et al.,[98] this low-R data is the Fourier Transform of low-frequency noise in k-space which results from an incorrect background spline function. The start of the background spline function, which was previously set to 1.5 Å^{-1}, is then adjusted until the low-R region is very low in amplitude. Increments of 0.2 Å^{-1} are used first, followed by increments of 0.05. Typically, the optimum choice results in low-amplitude "ringing" with almost no background underneath the ringing. In this work, values close to 1.9 Å^{-1} were used for Mn, while 2.5 - 2.6 Å^{-1} were used for Ni. For neutral or metallic elements, however, the background spline function could start at much lower values. The background spline in μ(E) should then intersect as many of the oscillations as possible. At the lower limit, the background curve could curve upwards into the white line, or, if the k-spline minimum is high enough, the background curve could curve downwards into a negative oscillation above the white line.

After the spline range is adjusted, however, the background spline has changed shape and the Fourier Transform window must be adjusted once again. All the data scans should be plotted in k-space to reevaluate the optimum choice. The beginning of the k-spline range can possibly be

tweaked by 0.1 Å^{-1} at this point to ensure the lowest background in the R-space plot. The last step is to check the E_0 values of each scan because it can affect the R-space peak locations. Subtle trends in the R-space data can then be reliably gleaned. A final check of the data quality is to plot all the scans in R-space and determine if the "ringing" is generally similar from scan to scan, or if the ringing in one scan is out of phase with those of the next. If the ringing is different, the data has been treated differently.

D.1.1 EXAFS Parameters

EXAFS Parameter Shifts While a battery is charging, at least one element is oxidizing. This will shift the XANES edge as well as the E_0 position for EXAFS. According to Bruce Ravel, the author of ATHENA and ARTEMIS, there is no way to truly determine E_0 in ATHENA. There are, however, two ways to get a good starting value for E_0; this parameter is later refined in ARTEMIS.[62]

The simplest way to find E_0 is to find the 50% edge jump point, where normalized $\mu x = 0.5$. This point will move with the XANES as the battery charges. A more physically sound method, however, is to find an inflection point in the data near this 50% edge jump. (Inflection points in the pre-edge peaks should not be used.) Unfortunately, these inflection points can disappear while the battery charges. After refinement in ARTEMIS, it may very well be found that E_0 bears no relationship to inflection points and, furthermore, E_0 may not move due to chemical changes because the EXAFS process depends on core electrons rather than on bonding electrons.

In cases where the XANES edge moves while the refined E_0 parameter does not, the spline must be adjusted to avoid major errors in background subtraction. This adjustment should take the form of background spline adjustments, while the Fourier Transform range should be kept constant in order to preserve the Fourier bandwidth and the R-space resolution.

Optimal Parameter Choices In ATHENA, it is quickly found that certain parameters must be co-refined to avoid inconsistencies. The most severe problem is that adjustments of E_0 will shift the pre-edge and post-edge functions, possibly distorting the normalized spectrum. The high-energy limit for the pre-edge line should, therefore, include some margin to prevent it from flattening the pre-edge features. A more insidious problem is adjusting the background curve, especially the low-k limit of the spline. Changes to this curve will change the shape of the k-space data, and the Fourier

Transform window must be adjusted accordingly.

D.2 EXAFS Fitting

The simulation of EXAFS data is performed to verify the accuracy of a structural theory, as well as the accuracy of the data reduction procedure. The entire process is greatly simplified if diffraction experiments have already provided an accurate crystal structure; absorbing atoms in amorphous materials or in solution will not be considered here. A known crystal structure provides the types and distances of neighboring atoms. What remains to be discovered may be Jahn-Teller distortion, which affects the local coordination environment without distorting the long-range structure. Furthermore, delithiation will cause subtle changes in the nearest-neighbor distances as well as changes in disorder. Disorder can include a distribution of bond lengths throughout the sample (static disorder) as well as thermal disorder, which depends on temperature as well as the local environment.

The shapes of EXAFS peaks are generally distorted away from a Gaussian peak shape with the low-R side of the peak distorted by a series of shoulders, and the high-R side of the peak dropping off very rapidly. These peaks also exhibit low-amplitude Fourier ringing with the first high-R ring being resolvable over the noise. To accurately model these peaks, fitting is performed in k-space using at least four parameters. These include ΔE_0, which represents an error in the choice of E_0 in ATHENA. This shift may reveal that the true E_0 point is hidden in the XANES spectrum by overlapping absorption features. The second, S_0^2, is an amplitude factor which represents a percentage loss of photoelectron energy at the absorbing atom. S_0^2should be a constant for the absorbing element and should not depend on any other factors; it should also be between. If E_0 has already been adjusted for the oxidation of the absorbing atom, ΔE_0 should not vary with delithiation, and should never vary from one absorption shell to another. If S_0^2 must be outside the range of 0.5 to 1.0 to fit the data, the atomic coordination number may incorrect. If ΔE_0 is more than ± 8 eV, the data reduction should be repeated in ATHENA using a corrected E_0.

Two additional factors can be varied from shell to shell and from one oxidation state to the next: the XAFS Debye-Waller factor σ^2 which represents disorder, and ΔR which represents an error or change in the interatomic distance. σ^2 is the mean squared displacement of the atom from its average position. It must be positive, but less than 0.01 Å^{-2}. If ΔR must be excessively large to fit

the data, it indicates an error in the crystallographic parameters. Such an error will distort the length of multiple-scattering paths worse than it distorts single-scattering paths. Large errors in ΔR cannot be corrected in ARTEMIS; the proposed crystal structure or cluster in ATOMS must be changed.

Because the ARTEMIS modeling routine is CPU-intensive, and because the auto-save feature renders it storage-intensive as well, the operator must be careful to begin the process with the smallest possible dataset and the smallest possible number of free variables. One should begin by fitting only the first nearest neighbor shell of a single data scan. Clear hypotheses should be formed and tested individually; the least-squares fitting procedure used by ARTEMIS is not robust enough to convert bad guesses into good guesses. A failure to fit the data, resulting in bad fit values, happens frequently.

The first variable to approximate is S_0^2 which represents the percentage of excited electrons which return to the absorbing atom after interacting with neighbor atoms. This can be done by fitting standard EXAFS data[193] against standard crystal structures[194] for the same compound. In cases of complex crystal structures such as manganese, oxides of manganese may be safely substituted. If fitting the reference compound requires a correction to E_0, the process should be iterated. Only the first shell should be fitted, and all four variables should be allowed to vary. After fitting, ΔR and ΔE_0 should be very small, and σ^2 and S_0^2 should be within the ranges stated previously. In fitting experimental data, the S_0^2 value can be taken as a fixed value.

Next, experimental data is fitted using the first nearest-neighbor peak only. With S_0^2 fixed, only three variables are allowed to vary. If ΔR is large, it can temporarily be fixed at zero. Also, constraints can be used in ARTEMIS to limit the range of parameters. However, constraints can severely bias the fitting results and should only be employed to test hypotheses. After fitting the first peak is finished, E_0 must usually be corrected in ATHENA, and the data can be re-fitted in ARTEMIS.

To fit a second-nearest-neighbor shell, more data is selected, and more shells from the simulation are included. Beyond the first nearest neighbor, many subsequent shells overlap. No shells should be skipped without a specific reason. To obtain a close fit to the data, shells beyond the second nearest neighbor should be added, and fitted, until further shells fail to contribute to the fitting. The data range to be modeled should then be adjusted to fit the range of shells which represent data, rather

than noise. In choosing parameters for these further shells, it is likely that the least-squares routine will not be able to differentiate between each shell with any statistical accuracy. The parameters for the second-nearest neighbor shell, then, should be grouped such that ΔR and σ^2 are common to all shells after the first shell. At first, σ^2 should be common to all shells so that the fitting does not fail.

Before introducing a large number of data scans, all the details of parameter groupings, and data ranges, should be decided. The data may be fitted using multiple k-weights simultaneously; a k-weight of 1 is usually a poor choice while a simultaneous fitting of 2 and 3 is typically useful. Finally, a large number of scans are loaded. At this point, ΔE_0 should be held fixed along with S_0^2 and only ΔR and σ^2 should vary from scan to scan. Because parameters are usually not shared among scans, the smallest practical grouping of scans should be used. If ΔE_0 is shared across the data set and allowed to vary, it can improve the choice of E_0 at the expense of much CPU time.

D.2.1 Refinement of E_0

The necessity of refining the choice of E_0 is illustrated in Fig. 86 below which is derived from the Ni K-edge EXAFS data in 4.2. In that study (as in virtually all studies of the Ni K-edge in lithium-ion batteries) the oxidation of nickel with delithiation causes the XANES features to shift to higher energies. In accordance with the default behavior of ATHENA, the E_0 values were obtained from the point at which the normalized absorption reaches 50%. This default behavior is designed to produce an accurate background spline function, which follows the spectrum starting at the E_0 point. In the Figure, black triangles pointing left indicate a large shift of nearly 3 eV as nickel oxidizes from Ni^{2+} to Ni^{3+} to Ni^{4+}. However, k-space fitting in ARTEMIS yielded negative ΔE_0 corrections of more than that magnitude as shown by blue arrows pointing right. Summing the two values, corrected E_0 values were obtained and are shown as red squares.

Instead of using the corrected E_0 values directly, however, the values were averaged and applied in ATHENA. The start of the background spline was then adjusted by up to 3 eV in order to fit the data well. The value of maintaining a constant E_0 is seen in Figure 87. In EXAFS, the shapes of the metal-oxygen and metal-metal curves are very sensitive to the E_0 position because of its quadratic effect on k-space according to Equation 7 in 2.1.3.3. When subtle trends are expected, a constant value for E_0 must be found.

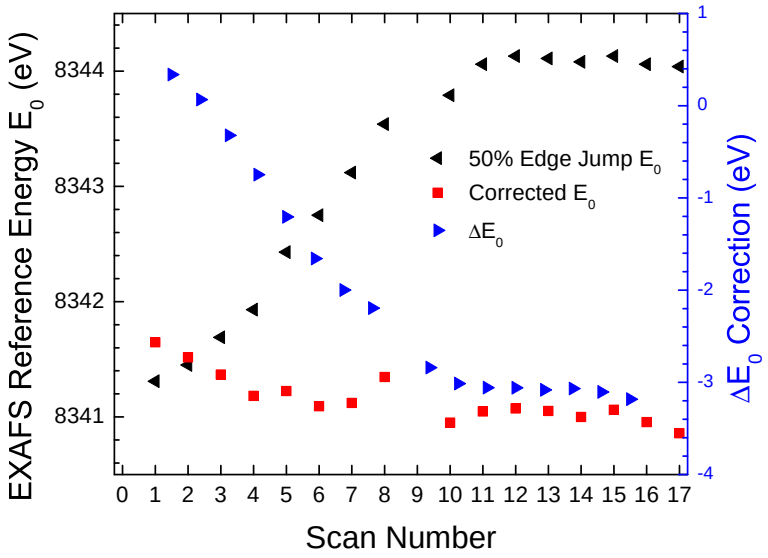

Figure 86: 50% edge jump position for Ni EXAFS from ATHENA, corrections to reference energy ΔE_0 from ARTEMIS, and corrected E_0

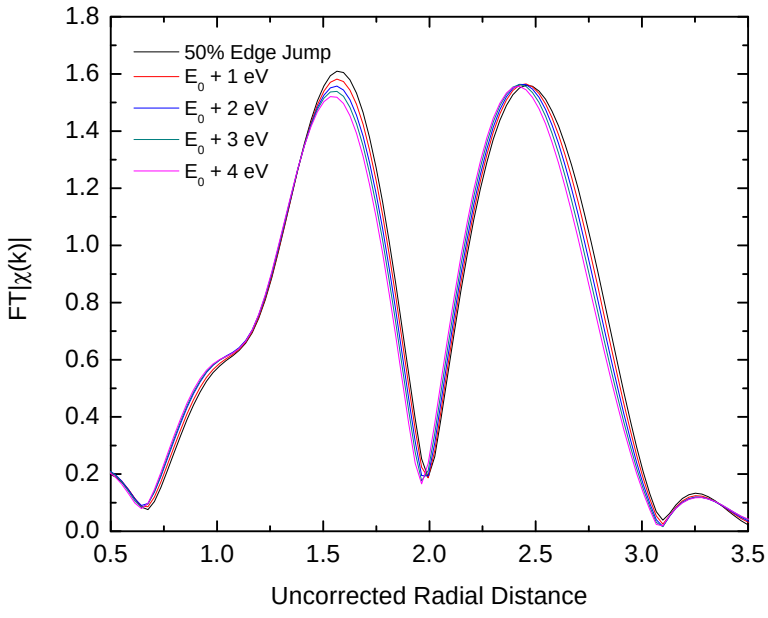

Figure 87: Effect of corrections to reference energy E_0 on EXAFS

D.3 Soft X-ray Absorption

In soft X-ray absorption, the energy resolution is superior (as low as 0.1 eV instead of 0.5 eV), but the signal-to-noise ratio is much lower. Also, the post-edge regions are typically not flat. Worse, the instrumentation is much less reliable: the monochromators can "slip" to the wrong energy, causing horizontal distortion, while the electron yield detectors can be "jumpy", introducing large, spurious spikes or steps into the already noisy data. Furthermore, when the sample is a composite structure, only a fraction of the signal comes from the target material and this further reduces the signal-to-noise ratio. Therefore, different tactics must be employed in data reduction.

Soft X-ray data must be carefully filtered to eliminate bad scans. Due to the frequent beam dumps in the NSLS soft X-ray ring, a large proportion of the scans will be truncated. Also, due to monochromator errors, especially at beamline U7A in the Mn L-edge and Ni L-edge, the L_{III} and L_{II} edges may move to lower energies together, or the L_{II} edge may move to higher energies. If the entire edge moves to lower energies, the absorption features maybe under-sampled because they will occur in the pre-edge (low-point-density) region. (During the experiment, the high point-density region should be extended to account for these errors, thereby taking extra time and increasing the risk of truncating the data due to beam dumps.) If the L_{II} edge moves to higher energies, it will distort the post-edge, making normalization impossible. In such cases, the data can be normalized between the L_{III} and L_{II}.

The E_0 point should be set to the same value for each scan to ensure that fine shifts are detected. Otherwise, the shift induced by the E_0 setting will cause offsets in the plotted data; these shifts mimic chemical shifts and can upset the normalization. (When plotting multiple scans, ATHENA uses the E_0 for the first selected scan, but a change in the first selected scan upsets the analysis.) Each scan should also be aligned manually; auto-alignment is useless for noisy data.

Normalization of soft X-ray data is necessary, but dangerous. Because most soft X-ray absorption features represent resonant transitions from occupied core levels to unoccupied valence bands, the area under the curve represents holes in the valence band; therefore each scan must be normalized in the same way to ensure accurate comparisons. At the NSLS, the beam intensity changes constantly due to infrequent refills, making each scan less intense than the previous scan; the NSLS

II and other synchrotrons utilize top-off injection to prevent this. Also, inevitably, the intensity changes with photon energy, causing raw scans to be sloped. Although normalization is straightforward in hard X-ray data, in soft X-ray data the correct data range for normalization is uncertain and may be found in a sloping, narrow range of energies. The energy range can be cut short due to interfering edges; at U7A chromium in the front-end mirror contaminates the oxygen L-edge, while at U12A nickel in the front-end mirror precludes spectroscopy at the nickel edge. The correct energy range is found by consultation with beamline staff together with trial and error.

Normalization should be deferred until the data are further inspected for trends. This is because normalization distorts the data and can mask (or even reverse) trends in the data. Inspection of the raw scans by eye will reveal true trends. If the signal level is low enough, the pre-edge and post-edge lines will not be parallel, but will cross beneath the main absorption features. This will cause the spectrum to flip when normalized. In Figure 88, the post-edge is lower than the pre-edge, and these lines intersect. When both the pre-edge and post-edge lines are subtracted from the data, the result will be negative. When ATHENA multiplies the data to create an edge step of unity, the absorption features will become negative and will be highly distorted.

A key strategy in these cases is to change the post-edge from a sloping line to a horizontal line by choosing "first order" normalization in ATHENA. The post-edge region will then be averaged rather than fitted to a sloping line, ensuring that none of the data will be subtracted to the left of the cross-over point. This also eliminates any "twisting" effect on the data. A further advantage of this technique is that because the post-edge normalization is merely a vertical scaling, the normalized data can be exported and post-processed in a standard spreadsheet program. To improve the normalization, the data can be scaled vertically by a constant factor.

In many cases it is further necessary to choose slightly different normalization regions from the scan to scan. At the very least, the lowest-energy pre-edge point and the highest-energy post-edge point should remain the same from scan to scan. The two inner points can then be varied over a limited region to ensure that a series of scans are represented fairly, with the pre-edge and post-edge data lining up in spite of noise.

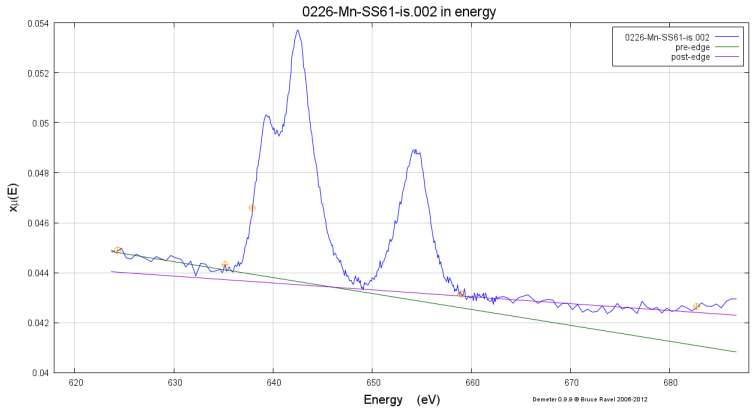

Figure 88: Manganese L-edge spectrum with intersecting pre-edge and post-edge lines

D.4 Data Reduction Steps

The procedure described in Section D.1 is listed in a precise order of operations below. The three Phases are performed in order without going back. However, in Phases Two and Phase Three, repetition is used to refine parameters which are not independent, and to optimize the parameters for multiple scans.

Order of Operations, Phase One 1. Using the reference foil, calibrate element to literature values

2. Align reference scans (by hand if soft x-ray)
3. Deglitch
4. Using each data scan, choose Å^{-1} using the 1st derivative
5. Using each data scan, refine the Å^{-1} using the 2nd derivative
6. Record Å^{-1} points
7. Set k-spline minimum to ~1.5 Å^{-1}.
8. Pick pre-edge points
9. Pick post-edge endpoint

Order of Operations, Phase Two 10. Plot +50 to +300, focussing on +75 to +200

11. Choose a higher-energy point where the background spline and the all the data scans (isosbestic point) intersect

12. “Apply-All” to each data scan

13. Repeat Step 10 to find the lowest-energy point where all the data intersect AND are close to the background spline

14. “Apply-All” to each data scan

15. Invert selection to reference foils and Auto-Align

16. Replot to evaluate the quality of the choice, and repeat Step 13 if necessary

17. Update Å^{-1} points (only if significant redox occurs)

18. At this point, check for isosbestic points in energy space

Order of Operations, Phase Three 19. Plot first scan in k-space

20. Find k-window minimum (nearly zero crossing at the lowest possible k-value) [Do not FT the entire white line, but don’t limit yourself to >30 eV; traditional advice is to stay above $k = 3.0$; my advise is to stay above $k = 2.0$

21. Find k-window maximum (nearly zero crossing at the highest possible k-value)

22. Plot in R-space

23. Adjust k-spline background minimum to reduce the R-space background level to a minimum by adjusting k-spline min in 0.2 Å^{-1} steps between 1.6 and 3.0 Å^{-1}, then fine tune in 0.05 Å^{-1} steps.

24. When real space background is minimized, replot in energy to check for quality of background spline (should follow the data well)

25. Now that the k-spline background is changed, repeat steps 19-24 for the first scan.

26. Apply-All and re-align.

27. Plot ALL scans and repeat steps 19-26.

28. Update Å^{-1} points to ensure good alignment.

REFERENCES

[1] S. T. Anderson, I. W. H. Parry, J. M. Sallee, and C. Fischer, "Automobile Fuel Economy Standards: Impacts, Efficiency, and Alternatives," *Review of Environmental Economics and Policy*, vol. 5, no. 1, pp. 89–108, May 2011. [Online]. Available: http://reep.oxfordjournals.org/cgi/doi/10.1093/reep/req021

[2] B. G. E. Moore, "Cramming more components onto integrated circuits," vol. 38, no. 8, 1975. [Online]. Available: http://www.cs.utexas.edu/users/fussell/courses/cs352h/papers/moore.pdf

[3] A. Carroll and G. Heiser, "An Analysis of Power Consumption in a Smartphone," in *Usenix*, Boston, MA, 2010. [Online]. Available: http://static.usenix.org/events/usenix10/tech/full_papers/Carroll.pdf

[4] J. M. Tarascon and M. Armand, "Issues and challenges facing rechargeable lithium batteries." *Nature*, vol. 414, no. 6861, pp. 359–67, Nov. 2001. [Online]. Available: http://dx.doi.org/10.1038/35104644

[5] M. Armand and J.-M. Tarascon, "Building better batteries." *Nature*, vol. 451, no. 7179, pp. 652–7, Feb. 2008. [Online]. Available: http://www.ncbi.nlm.nih.gov/pubmed/18256660

[6] J. B. Goodenough and Y. Kim, "Challenges for Rechargeable Li Batteries," *Chemistry of Materials*, vol. 22, no. 3, pp. 587–603, Feb. 2010. [Online]. Available: http://pubs.acs.org/doi/abs/10.1021/cm901452z

[7] N. Dimov, S. Kugino, and M. Yoshio, "Carbon-coated silicon as anode material for lithium ion batteries : advantages and limitations," *Electrochimica Acta*, vol. 48, pp. 1579–1587, 2003. [Online]. Available: http://dx.doi.org/10.1016/S0013-4686(03)00030-6

[8] G. Nazri and G. Pistoia, *Lithium Batteries: Science and Technology*. Boston: Kluwer Academic Publishers, 2004.

[9] M. Lundstrom, "Applied physics. Moore's law forever?" *Science (New York, N.Y.)*, vol. 299, no. 5604, pp. 210–1, Jan. 2003. [Online]. Available: http://www.ncbi.nlm.nih.gov/pubmed/12522237

[10] G. Girishkumar, B. McCloskey, A. C. Luntz, S. Swanson, and W. Wilcke, "Lithium-Air Battery: Promise and Challenges," *The Journal of Physical Chemistry Letters*, vol. 1, no. 14, pp. 2193–2203, Jul. 2010. [Online]. Available: http://pubs.acs.org/doi/abs/10.1021/jz1005384

[11] B. Hertzberg, A. Alexeev, and G. Yushin, "Deformations in Si-Li anodes upon electrochemical alloying in nano-confined space." *Journal of the American Chemical Society*, vol. 132, no. 25, pp. 8548–9, Jun. 2010. [Online]. Available: http://www.ncbi.nlm.nih.gov/pubmed/20527882

[12] C. O. Laoire, S. Mukerjee, K. M. Abraham, E. J. Plichta, and M. a. Hendrickson, "Elucidating the Mechanism of Oxygen Reduction for Lithium-Air Battery Applications," *The Journal of Physical Chemistry C*, vol. 113, no. 46, pp. 20 127–20 134, Nov. 2009. [Online]. Available: http://dx.doi.org/10.1021/jp908090s

[13] W.-S. Yoon, K.-B. Kim, M.-G. Kim, M.-K. Lee, H.-J. Shin, J.-M. J.-S. Lee, and C.-H. Yo, "Oxygen Contribution on Li-Ion Intercalation-Deintercalation in LiCoO 2 Investigated by O K-Edge and Co L-Edge X-ray Absorption Spectroscopy," *The Journal of Physical Chemistry B*, vol. 106, no. 10, pp. 2526–2532, Mar. 2002. [Online]. Available: http://pubs.acs.org/doi/abs/10.1021/jp013735e

[14] C. S. Johnson, N. Li, C. Lefief, and M. M. Thackeray, "Anomalous capacity and cycling stability of xLi2MnO3·(1-x)LiMO2 electrodes (M=Mn, Ni, Co) in lithium batteries at 50°C," *Electrochemistry Communications*, vol. 9, no. 4, pp. 787–795, Apr. 2007. [Online]. Available: http://linkinghub.elsevier.com/retrieve/pii/S1388248106005182

[15] Z. Lu and J. R. Dahn, "Understanding the Anomalous Capacity of Li/Li[Ni[sub x]Li[sub (1/3-2x/3)]Mn[sub (2/3-x/3)]]O[sub 2] Cells Using In Situ X-Ray Diffraction and Electrochemical Studies," *Journal of The Electrochemical Society*, vol. 149, no. 7, p. A815, 2002. [Online]. Available: http://jes.ecsdl.org/cgi/doi/10.1149/1.1480014

[16] A. R. Armstrong, M. Holzapfel, P. Novák, C. S. Johnson, S.-h. Kang, M. M. Thackeray, and P. G. Bruce, "Demonstrating oxygen loss and associated structural reorganization in the lithium battery cathode Li[Ni0.2Li0.2Mn0.6]O2." *Journal of the American Chemical Society*, vol. 128, no. 26, pp. 8694–8, Jul. 2006. [Online]. Available: http://www.ncbi.nlm.nih.gov/pubmed/16802836

[17] W. C. West, M. C. Smart, E. Wong, B. V. Ratnakumar, and R. Bugga, "Characterization Studies of Li(Li(1/3-2x/3)Mn(2/3-/3)Nix)O2 Cathodes," in *212th ECS Meeting*, vol. M, no. 3, 2007, pp. Meet. Abstr. MA2007–02 115. [Online]. Available: http://ma.ecsdl.org/content/MA2007-02/3/115.abstract

[18] D. Mills, "Advances in solar thermal electricity technology," *Solar Energy*, vol. 76, no. 1-3, pp. 19–31, Jan. 2004. [Online]. Available: http://linkinghub.elsevier.com/retrieve/pii/S0038092X03001026

[19] B. M. Eberhard, M. Tarpenning, and D. Sadoway, "The 21 st Century Electric Car," Tesla Motors, Tech. Rep., 2006. [Online]. Available: http://www.evworld.com/library/tesla_21centuryev.pdf

[20] J. McDowall, "Conventional battery technologies-present and future," in *2000 Power Engineering Society Summer Meeting (Cat. No.00CH37134)*, vol. 3. IEEE, pp. 1538–1540. [Online]. Available: http://ieeexplore.ieee.org/lpdocs/epic03/wrapper.htm?arnumber=868757

[21] K. Aleklett, M. Höök, K. Jakobsson, M. Lardelli, S. Snowden, and B. Söderbergh, "The Peak of the Oil Age - Analyzing the world oil production Reference Scenario in World Energy Outlook 2008," *Energy Policy*, vol. 38, no. 3, pp. 1398–1414, Mar. 2010. [Online]. Available: http://linkinghub.elsevier.com/retrieve/pii/S0301421509008519

[22] PikeResearch, "Hybrid and Plug-In Electric Vehicles to Surpass 5% of Total U.S. Vehicle Sales by 2017," Pike Research, Tech. Rep., 2011. [Online]. Available: http://www.pikeresearch.com/research/electric-vehicle-market-forecasts

[23] S. Solomon, G.-K. Plattner, R. Knutti, and P. Friedlingstein, "Irreversible climate change due to carbon dioxide emissions." *Proceedings of the National Academy of Sciences of the United States of America*, vol. 106, no. 6, pp. 1704–9, Feb. 2009. [Online]. Available: http://dx.crossref.org/10.1073%2Fpnas.0812721106

[24] S. C. Doney, V. J. Fabry, R. A. Feely, and J. A. Kleypas, "Ocean Acidification: The Other CO 2 Problem," *Annual Review of Marine Science*, vol. 1, no. 1, pp. 169–192, Jan. 2009. [Online]. Available: http://www.annualreviews.org/doi/abs/10.1146/annurev.marine.010908.163834

[25] J. J. Botti and C. E. Miller, "SAE TECHNICAL Powertrains of the Future : Reducing the Impact of Transportation on the Environment," no. 724, 1999.

[26] Federal Highway Administration, "2009 National Household Travel Survey," US DOT, Tech. Rep., 2009. [Online]. Available: http://nhts.ornl.gov/2009/pub/stt.pdf

[27] Clean Air Campaign, "Commuting and Traffic Congestion Fast Facts," Clean Air Campaign, Tech. Rep. [Online]. Available: http://www.cleanaircampaign.org/For-the-Press/Press-Kit/Commuting-and-Traffic-Congestion-Fast-Facts

[28] J. G. Hayes, R. P. R. de Oliveira, S. Vaughan, and M. G. Egan, "Simplified electric vehicle power train models and range estimation," *2011 IEEE Vehicle Power and Propulsion Conference*, pp. 1–5, Sep. 2011. [Online]. Available: http://ieeexplore.ieee.org/lpdocs/epic03/wrapper.htm?arnumber=6043163

[29] S. Edelstein, "Toyota RAV4 EV to go on sale this summer," 2012. [Online]. Available: http://www.digitaltrends.com/cars/toyota-rav4-ev-to-go-on-sale-this-summer/

[30] U. Köhler, J. Kümpers, and M. Ullrich, "High performance nickel-metal hydride and lithium-ion batteries," *Journal of Power Sources*, vol. 105, no. 2, pp. 139–144, Mar. 2002. [Online]. Available: http://linkinghub.elsevier.com/retrieve/pii/S0378775301009326

[31] R. F. Nelson, "Power requirements for batteries in hybrid electric vehicles," *Journal of Power Sources*, vol. 91, no. 1, pp. 2–26, Nov. 2000. [Online]. Available: http://linkinghub.elsevier.com/retrieve/pii/S0378775300004833

[32] B. K. Mahato, E. Y. Weissman, and E. C. Laird, "Some Aspects of Gas Recombination in Lead-Acid Systems," *Journal of The Electrochemical Society*, vol. 121, no. 1, p. 13, 1974. [Online]. Available: http://jes.ecsdl.org/cgi/doi/10.1149/1.2396808

[33] P. Talbott, Ed., *Benjamin Franklin: In Search of a Better World*. London: Yale University, 2005. [Online]. Available: http://www.benfranklin300.org/frankliniana/result.php?id=72&sec=0

[34] S. West and P. Krein, "Equalization of valve-regulated lead-acid batteries: issues and life test results," *INTELEC. Twenty-Second International Telecommunications Energy Conference (Cat. No.00CH37131)*, pp. 439–446, 2000. [Online]. Available: http://ieeexplore.ieee.org/lpdocs/epic03/wrapper.htm?arnumber=884287

[35] R. A. Leising, M. J. Palazzo, E. S. Takeuchi, and K. J. Takeuchi, "Abuse Testing of Lithium-Ion Batteries: Characterization of the Overcharge Reaction of LiCoO2/Graphite Cells," *Journal of The Electrochemical Society*, vol. 148, no. 8, p. A838, 2001. [Online]. Available: http://jes.ecsdl.org/cgi/doi/10.1149/1.1379740

[36] E. Peled, "The Electrochemical Behavior of Alkali and Alkaline Earth Metals in Nonaqueous Battery Systems - The Solid Electrolyte Interphase Model," *Journal of The Electrochemical Society*, vol. 126, no. 12, p. 2047, 1979. [Online]. Available: http://jes.ecsdl.org/cgi/doi/10.1149/1.2128859

[37] T. Ohsaki, T. Kishi, T. Kuboki, N. Takami, N. Shimura, Y. Sato, M. Sekino, and A. Satoh, "Overcharge reaction of lithium-ion batteries," *Journal of Power Sources*, vol. 146, no. 1-2, pp. 97–100, Aug. 2005. [Online]. Available: http://dx.doi.org/10.1016/j.jpowsour.2005.03.105

[38] D. Darlin, "Dell Will Recall Batteries in PCs," New York, NY, Aug. 2006. [Online]. Available: http://www.nytimes.com/2006/08/15/technology/15battery.html?pagewanted=all

[39] Panasonic, "Lithium Ion Batteries: Individual Data Sheet," Panasonic, Inc., Tech. Rep., 2007. [Online]. Available: http://www.panasonic.com/industrial/includes/pdf/Panasonic_LiIon_CGR18650DA.pdf

[40] G. Berdichevsky, K. Kelty, and E. Toomre, "The Tesla Roadster Battery System," pp. 1–5, 2006. [Online]. Available: http://webarchive.teslamotors.com/display_data/TeslaRoadsterBatterySystem.pdf

[41] M. Eberhard, "A Bit About Batteries," p. 1, 2006. [Online]. Available: http://www.teslamotors.com/blog/bit-about-batteries

[42] L. G. Cota, D. Mora, and P. de la Mora, "On the structure of lithium peroxide, Li2O2." *Acta crystallographica. Section B, Structural science*, vol. 61, no. Pt 2, pp. 133–6, Apr. 2005. [Online]. Available: http://www.ncbi.nlm.nih.gov/pubmed/15772444

[43] R. Gummow, D. Liles, and M. Thackeray, "A reinvestigation of the structures of lithium-cobalt-oxides with neutron-diffraction data," *Materials research*, vol. 28, no. 11, pp. 1177–1184, 1993. [Online]. Available: http://www.sciencedirect.com/science/article/pii/002554089390098X http://linkinghub.elsevier.com/retrieve/pii/002554089390098X

[44] W.-S. Yoon, S. Iannopollo, C. P. Grey, D. Carlier, J. Gorman, J. Reed, and G. Ceder, "Local Structure and Cation Ordering in O3 Lithium Nickel Manganese Oxides with Stoichiometry," *Electrochemical and Solid-State Letters*, vol. 7, no. 7, p. A167, 2004. [Online]. Available: http://esl.ecsdl.org/cgi/doi/10.1149/1.1737711

[45] D. F. Shriver and P. W. Atkins, *Inorganic Chemistry*, 4th ed. New York, NY: W. H. Freeman and Company, USA, 2006.

[46] A. Thompson, D. Attwood, E. Gullickson, M. Howells, K.-J. Kim, J. Kirz, and J. Kortright, *X-ray Data Booklet*, lbnl/pub-4 ed. Berkeley, CA: Lawrence Berkeley National Laboratory, 2009. [Online]. Available: http://xdb.lbl.gov

[47] J. Xiao, N. A. Chernova, and M. S. Whittingham, "Layered Mixed Transition Metal Oxide Cathodes with Reduced Cobalt Content for Lithium Ion Batteries," *Chemistry of Materials*, vol. 20, no. 24, pp. 7454–7464, Dec. 2008. [Online]. Available: http://dx.doi.org/10.1021/cm802316d

[48] W. C. West, J. F. Whitacre, V. White, and B. V. Ratnakumar, "Fabrication and testing of all solid-state microscale lithium batteries for microspacecraft applications," *Journal of Micromechanics and Microengineering*, vol. 12, no. 1, pp. 58–62, Jan. 2002. [Online]. Available: http://stacks.iop.org/0960-1317/12/i=1/a=309?key=crossref.a02dcb74d5c653b4715d85c64c7db15a

[49] J. S. Horwitvitz and K. S. Grabowski, "In situ deposition laser deposition thin films by pulsed," *Applied Physics Letters*, vol. 59, no. September, pp. 1565–1567, 1991. [Online]. Available: http://dx.doi.org/10.1063/1.106284

[50] A. Thißen, D. Ensling, M. Liberatore, Q.-H. Wu, F. J. Fernandez Madrigal, M. S. Bhuvaneswari, R. Hunger, and W. Jaegermann, "Experimental routes to in situ characterization of the electronic structure and chemical composition of cathode materials for lithium ion batteries during lithium intercalation and deintercalation using photoelectron spectroscopy and related techniques," *Ionics*, vol. 15, no. 4, pp. 393–403, May 2009. [Online]. Available: http://www.springerlink.com/index/10.1007/s11581-009-0339-z

[51] Y.-C. Lu, E. J. Crumlin, G. M. Veith, J. R. Harding, E. Mutoro, L. Baggetto, N. J. Dudney, Z. Liu, and Y. Shao-Horn, "In Situ Ambient Pressure X-ray Photoelectron Spectroscopy Studies of Lithium-Oxygen Redox Reactions." *Scientific Reports*, vol. 2, p. 715, Jan. 2012. [Online]. Available: http://dx.crossref.org/10.1038%2Fsrep00715

[52] J. D. Greenlee, C. F. Petersburg, W. Laws Calley, C. Jaye, D. A. Fischer, F. M. Alamgir, and A. W. Doolittle, "In-situ oxygen x-ray absorption spectroscopy investigation of the resistance modulation mechanism in LiNbO2 memristors," *Applied Physics Letters*, vol. 100, no. 18, p. 182106, 2012. [Online]. Available: http://dx.doi.org/10.1063/1.4709422

[53] J. D. Greenlee, "Temporal and Spatial Modeling of Analog Memristors," MS Thesis, Georgia Institute of Technology, 2011. [Online]. Available: http://hdl.handle.net/1853/41215

[54] F. M. F. Alamgir, E. Strauss, M. DenBoer, S. Greenbaum, J. F. Whitacre, C.-C. Kao, and S. Neih, "LiCoO2 Thin-Film Batteries," *Journal of The Electrochemical Society*, vol. 152, no. 5, p. A845, 2005. [Online]. Available: http://dx.doi.org/10.1149/1.1872672

[55] W.-S. Yoon, M. Balasubramanian, K. Y. Chung, X.-Q. Yang, J. McBreen, C. P. Grey, and D. A. Fischer, "Investigation of the charge compensation mechanism on the electrochemically Li-ion deintercalated Li1-xCo1/3Ni1/3Mn1/3O2 electrode system by combination of soft and hard X-ray absorption spectroscopy." *Journal of the American Chemical Society*, vol. 127, no. 49, pp. 17 479–87, Dec. 2005. [Online]. Available: http://dx.doi.org/10.1021/ja0530568

[56] S. Oswald, K. Nikolowski, and H. Ehrenberg, "Quasi in situ XPS investigations on intercalation mechanisms in Li-ion battery materials." *Analytical and bioanalytical chemistry*, vol. 393, no. 8, pp. 1871–7, Apr. 2009. [Online]. Available: http://www.ncbi.nlm.nih.gov/pubmed/19066866

[57] N. K. Karan, M. Balasubramanian, T. T. Fister, A. K. Burrell, and P. Du, "Bulk-Sensitive Characterization of the Discharged Products in Li-O 2 Batteries by Nonresonant Inelastic X-ray Scattering," *The Journal of Physical Chemistry C*, vol. 116, no. 34, pp. 18 132–18 138, Aug. 2012. [Online]. Available: http://pubs.acs.org/doi/abs/10.1021/jp306298e

[58] Y.-C. Lu, E. J. Crumlin, G. M. Veith, J. Harding, E. Mutoro, L. Baggetto, and J. Nancy, "Probing Reaction Mechanisms of Li-O 2 batteries via In Situ Ambient Pressure X-ray Photoelectron Spectroscopy," p. 5757, 2012. [Online]. Available: http://ma.ecsdl.org/content/MA2012-02/11/1168.short

[59] J. B. Bates, N. J. Dudney, B. J. Neudecker, F. X. Hart, H. P. Jun, and S. A. Hackney, "Preferred Orientation of Polycrystalline LiCoO2 Films," *Journal of The Electrochemical Society*, vol. 147, no. 1, p. 59, 2000. [Online]. Available: http://jes.ecsdl.org/cgi/doi/10.1149/1.1393157

[60] J. B. Bates, N. J. Dudney, B. Neudecker, A. Ueda, and C. D. Evans, "Thin-film lithium and lithium-ion batteries," *Solid State Ionics*, vol. 135, no. 2000, pp. 33–45, 2000. [Online]. Available: http://dx.doi.org/10.1016/S0167-2738(00)00327-1

[61] A. Hayashi, S. Hama, H. Morimoto, M. Tatsumisago, and T. Minami, "Preparation of Li2S-P2S5 Amorphous Solid Electrolytes by Mechanical Milling," *Journal of the American Ceramic Society*, vol. 84, no. 2, pp. 477–79, Dec. 2001. [Online]. Available: http://doi.wiley.com/10.1111/j.1151-2916.2001.tb00685.x http://dx.doi.org/10.1111/j.1151-2916.2001.tb00685.x

[62] B. Ravel, "Background Removal Using the Autobk Algorithm." [Online]. Available: http://xafs.org/TheoryAnalysis/BackgroundRemovalWithAutobk

[63] D. Linden, *Lithium-ion batteries*, D. Linden, Ed. McGraw Hill, 1995.

[64] D. Aurbach, *Nonaqueous Electrochemistry*. CRC Press, 1999.

[65] H. C. Choi, Y. M. Jung, I. Noda, and S. B. Kim, "A Study of the Mechanism of the Electrochemical Reaction of Lithium with CoO by Two-Dimensional Soft X-ray Absorption Spectroscopy (2D XAS), 2D Raman, and 2D Heterospectral XAS Raman Correlation Analysis," *The Journal of Physical Chemistry B*, vol. 107, no. 24, pp. 5806–5811, Jun. 2003. [Online]. Available: http://dx.doi.org/10.1021/jp030438w

[66] J. Bates, "Electrical properties of amorphous lithium electrolyte thin films," *Solid State Ionics*, vol. 53-56, pp. 647–654, Jul. 1992. [Online]. Available: http://dx.doi.org/10.1016/0167-2738(92)90442-R

[67] N. Dudney, "Sputtering of lithium compounds for preparation of electrolyte thin films," *Solid State Ionics*, vol. 53-56, pp. 655–661, Jul. 1992. [Online]. Available: http://dx.doi.org/10.1016/0167-2738(92)90443-S

[68] J. B. Bates, N. J. Dudney, G. R. Gruzalski, and C. F. Luck, "Thin film battery and method for making same," 1992. [Online]. Available: USPAT5338625

[69] Y. Shao-Horn, L. Croguennec, C. Delmas, E. C. Nelson, and M. a. O'Keefe, "Atomic resolution of lithium ions in LiCoO2." *Nature materials*, vol. 2, no. 7, pp. 464–7, Jul. 2003. [Online]. Available: http://dx.doi.org/10.1038/nmat922

[70] R. Gummow, D. Liles, and M. Thackeray, "Spinel versus layered structures for lithium cobalt oxide synthesised at 400°C," *Materials Research Bulletin*, vol. 28, no. 3, pp. 235–246, Mar. 1993. [Online]. Available: http://dx.doi.org/10.1016/0025-5408(93)90157-9

[71] G. Amatucci, "Cobalt dissolution in LiCoO2-based non-aqueous rechargeable batteries," *Solid State Ionics*, vol. 83, no. 1-2, pp. 167–173, Jan. 1996. [Online]. Available: http://dx.doi.org/10.1016/0167-2738(95)00231-6

[72] G. Vitins, "Lithium Intercalation into Layered LiMnO2," *Journal of The Electrochemical Society*, vol. 144, no. 8, p. 2587, 1997. [Online]. Available: http://dx.doi.org/10.1149/1.1837869

[73] J. Dahn, E. Fuller, M. Obrovac, and U. Vonsacken, "Thermal stability of LixCoO2, LixNiO2 and λ-MnO2 and consequences for the safety of Li-ion cells," *Solid State Ionics*, vol. 69, no. 3-4, pp. 265–270, Aug. 1994. [Online]. Available: http://dx.doi.org/10.1016/0167-2738(94)90415-4 http://linkinghub.elsevier.com/retrieve/pii/0167273894904154

[74] T. Ohzuku and Y. Makimura, "Layered lithium insertion material of LiCo 1/3 Ni 1/3 Mn 1/3 O 2 for lithium-ion batteries," *Chemistry Letters*, pp. 642–643, 2001. [Online]. Available: http://dx.doi.org/10.1246/cl.2001.642

[75] Z. Lu, L. Y. Beaulieu, R. A. Donaberger, C. L. Thomas, and J. R. Dahn, "Synthesis, Structure, and Electrochemical Behavior of Li[Ni[subx]Li[sub1/32x/3]Mn[sub 2/3 x/3]]O[sub 2]," *Journal of The Electrochemical Society*, vol. 149, no. 6, p. A778, 2002. [Online]. Available: http://dx.doi.org/10.1149/1.1471541

[76] Z. Li, N. A. Chernova, M. Roppolo, S. Upreti, C. Petersburg, F. M. Alamgir, and M. S. Whittingham, "Comparative Study of the Capacity and Rate Capability of LiNiyMnyCo1-2yO2 (y = 0.5, 0.45, 0.4, 0.33)," *Journal of The Electrochemical Society*, vol. 158, no. 5, p. A516, 2011. [Online]. Available: http://dx.doi.org/10.1149/1.3562212 http://link.aip.org/link/JESOAN/v158/i5/pA516/s1&Agg=doi

[77] P. Wilkes, *Solid State Theory in Metallurgy*. Cambridge, England: Cambridge University Press, 1973.

[78] J. Molenda, A. Stoklosa, and T. Bak, "Modification in the electronic structure of cobalt bronze LixCoO2 and the resulting electrochemical properties," *Solid State Ionics*, vol. 36, no. 1-2, pp. 53–58, Oct. 1989. [Online]. Available: http://dx.doi.org/10.1016/0167-2738(89)90058-1

[79] J. D. Greiner and H. R. Shanks, "The magnetic susceptibility of rhenium trioxide," *Journal of Solid State Chemistry*, vol. 5, no. 2, pp. 262–265, Sep. 1972. [Online]. Available: http://dx.doi.org/10.1016/0022-4596(72)90038-2

[80] M. G. Stachiotti, F. Cora, C. R. A. Catlow, and C. O. Rodriguez, "First-principles investigation of ReO3sand related oxides," *Physical Review B*, vol. 55, no. 12, pp. 7508–7514, Mar. 1997. [Online]. Available: http://dx.doi.org/10.1103/PhysRevB.55.7508

[81] J. Kuneš, V. Anisimov, S. Skornyakov, A. Lukoyanov, and D. Vollhardt, "NiO: correlated band structure of a charge-transfer insulator," *Physical review letters*, vol. 99, no. 15, p. 156404, 2007. [Online]. Available: http://dx.doi.org/10.1103/PhysRevLett.99.156404

[82] J. Zaanen, G. Sawatzky, and J. Allen, "Band Gaps and Electronic Structure of Transition Metal Compounds," *Physical Review Letters*, vol. 55, no. 4, pp. 418–421, 1985. [Online]. Available: http://dx.doi.org/10.1016/0304-8853(86)90188-5

[83] F. de Groot, G. Vankó, and P. Glatzel, "The 1s x-ray absorption pre-edge structures in transition metal oxides," *Journal of Physics: Condensed Matter*, vol. 40, no. 8, p. 104207, 2009. [Online]. Available: http://dx.doi.org/10.1088/0953-8984/21/10/104207

[84] P. Thakur, J. C. Cezar, N. B. Brookes, R. J. Choudhary, R. Prakash, D. M. Phase, K. H. Chae, and R. Kumar, "Direct observation of oxygen induced room temperature ferromagnetism in MoO[sub 2] thin films by x-ray magnetic circular dichroism characterizations," *Applied Physics Letters*, vol. 94, no. 6, p. 062501, 2009. [Online]. Available: http://dx.doi.org/10.1063/1.3080679

[85] B. Garcia and N. Baffler, "Low-temperature cobalt oxide as rechargeable cathodic material for lithium batteries," vol. 54, pp. 373–377, 1995. [Online]. Available: http://dx.doi.org/10.1016/0378-7753(94)02105-C

[86] A. Hightower, C. C. Ahn, B. Fultz, and P. Rez, "Electron energy-loss spectrometry on lithiated graphite," *Applied Physics Letters*, vol. 77, no. 2, p. 238, 2000. [Online]. Available: http://link.aip.org/link/APPLAB/v77/i2/p238/s1&Agg=doi

[87] D. McNaught and A. Wilkinson, "Faraday constant," 1997. [Online]. Available: http://www.iupac.org/goldbook/F02325.pdf

[88] T. Ohzuku, "Solid-State Redox Reactions of LiCoO[sub 2] (R3m) for 4 Volt Secondary Lithium Cells," *Journal of The Electrochemical Society*, vol. 141, no. 11, p. 2972, 1994. [Online]. Available: http://jes.ecsdl.org/cgi/doi/10.1149/1.2059267

[89] G. Amatucci, J. Tarascon, and L. Klein, *CoO2 The End Member of the LixCoO2 Solid Solution*, 1996, vol. 143, no. 3. [Online]. Available: http://dx.doi.org/10.1007/978-0-387-92675-9

[90] W.-S. Yoon, Y. Paik, X.-Q. Yang, M. Balasubramanian, J. McBreen, and C. P. Grey, "Investigation of the Local Structure of the LiNi[sub 0.5]Mn[sub 0.5]O[sub 2] Cathode Material during Electrochemical Cycling by X-Ray Absorption and NMR Spectroscopy," *Electrochemical and Solid-State Letters*, vol. 5, no. 11, p. A263, 2002. [Online]. Available: http://dx.doi.org/10.1149/1.1513001

[91] D. Templeton and C. H. Dauben, "The Crystal Structure of Sodium Superoxide," *Journal of the American Chemical Society*, vol. 72, no. May, p. 2251, 1950. [Online]. Available: http://pubs.acs.org/doi/abs/10.1021/ja01161a103

[92] C. F. Petersburg, Z. Li, N. A. Chernova, M. S. Whittingham, and F. M. Alamgir, "Oxygen and transition metal involvement in the charge compensation mechanism of LiNi1/3Mn1/3Co1/3O2 cathodes," *Journal of Materials Chemistry*, vol. 22, no. 37, p. 19993, 2012. [Online]. Available: http://dx.doi.org/10.1039/c2jm33392a

[93] M. Newville, "Fundamentals of X-ray Absorption Fine Structure," 2005. [Online]. Available: http://cars9.uchicago.edu/xafs_school/APS_2005/Newville_Intro.pdf

[94] H. Saisho and Y. Gohshi, *Applications of synchrotron radiation to materials analysis*. Amsterdam: Elsevier, 1996. [Online]. Available: http://www.elsevier.com/books/applications-of-synchrotron-radiation-to-materials-analysis/saisho/978-0-444-88857-0

[95] J. Stohr, *Nexafs Spectroscopy*. Berlin: Springer-Verlag, 1996. [Online]. Available: http://www.springer.com/physics/optics+%26+lasers/book/978-3-540-54422-7

[96] E. Gullickson, "X-Ray Interactions With Matter." [Online]. Available: http://henke.lbl.gov/optical_constants/filter2.html

[97] S. Stizza and M. Benfatto, "Vanadium Site Structure in V2O5 Gel by Polarized EXAFS and XANES," *Le Journal de Physique*, 1986. [Online]. Available: http://dx.doi.org/10.1051/jphyscol:19868130

[98] M. Newville, P. Līviņš, Y. Yacoby, J. Rehr, and E. Stern, "Near-edge x-ray-absorption fine structure of Pb: A comparison of theory and experiment," *Physical Review B*, vol. 47, no. 21, pp. 14 126–14 131, Jun. 1993. [Online]. Available: http://dx.doi.org/10.1103/PhysRevB.47.14126

[99] B. Ravel and M. Newville, "ATHENA, ARTEMIS, HEPHAESTUS: data analysis for X-ray absorption spectroscopy using IFEFFIT." *Journal of Synchrotron Radiation*, vol. 12, no. Pt 4, pp. 537–41, Jul. 2005. [Online]. Available: http://dx.doi.org/10.1107/S0909049505012719

[100] J. F. Moulder and J. Chastain, *Handbook of X-Ray Photoelectron Spectroscopy*, J. C. John F. Moulder, Ed. Eden Prairie, MN: Physical Electronics, 1992.

[101] F. De Groot, M. Grioni, J. Fuggle, J. Ghijsen, G. Sawatzky, and H. Petersen, "Oxygen 1s x-ray-absorption edges of transition-metal oxides," *Physical Review B*, vol. 40, no. 8, pp. 5715–5723, 1989. [Online]. Available: http://link.aps.org/doi/10.1103/PhysRevB.40.5715

[102] S. Kurosumi, N. Nagamura, S. Toyoda, K. Horiba, H. Kumigashira, M. Oshima, S. Furutsuki, S.-i. Nishimura, A. Yamada, and N. Mizuno, "Resonant Photoemission Spectroscopy of the Cathode Material Li x FePO 4 for Lithium Ion Battery," *The Journal of Physical Chemistry C*, vol. 115, no. 51, pp. 25 519–25 522, Dec. 2011. [Online]. Available: http://dx.doi.org/10.1021/jp208069m

[103] N. Nucker and J. Fink, "Evidence for holes on oxygen sites in the high-TC, superconductors," *Physical Review B*, vol. 37, no. 10, 1988. [Online]. Available: http://link.aps.org/doi/10.1103/PhysRevB.37.5158

[104] A. A. Lavrentyev, I. Y. Nikiforov, V. A. Dubeiko, B. V. Gabrelian, and J. J. Rehr, "The use of the FEFF8 code to calculate the XANES and electron density of states of some sulfides," *Journal of Synchrotron Radiation*, vol. 8, no. 2, pp. 288–290, Mar. 2001. [Online]. Available: http://dx.doi.org/10.1107/S0909049500018938 http://scripts.iucr.org/cgi-bin/paper?S0909049500018938

[105] N.-E. Sung, Y.-K. Sun, S.-K. Kim, and M.-S. Jang, "In Situ XAFS Study of the Effect of Dopants in Li[sub 1+x]Ni[sub (1-3x)/2]Mn[sub (3+x)/2]O[sub 4] (0<x<1/3), a Li-Ion Battery Cathode Material," *Journal of The Electrochemical Society*, vol. 155, no. 11, p. A845, 2008. [Online]. Available: http://jes.ecsdl.org/cgi/doi/10.1149/1.2976351

[106] F. D. Groot, "Multiplet effects in X-ray spectroscopy," *Coordination Chemistry Reviews*, vol. 249, no. 1-2, pp. 31–63, Jan. 2005. [Online]. Available: http://dx.doi.org/10.1016/j.ccr.2004.03.018

[107] E. Stavitski and F. M. F. de Groot, "The CTM4XAS program for EELS and XAS spectral shape analysis of transition metal L edges." *Micron (Oxford, England : 1993)*, vol. 41, no. 7, pp. 687–94, Oct. 2010. [Online]. Available: http://www.ncbi.nlm.nih.gov/pubmed/20637641 http://dx.doi.org/10.1016/j.micron.2010.06.005

[108] M. M. Thackeray, S.-H. Kang, C. S. Johnson, J. T. Vaughey, R. Benedek, and S. a. Hackney, "Li2MnO3-stabilized LiMO2 (M = Mn, Ni, Co) electrodes for lithium-ion batteries," *Journal of Materials Chemistry*, vol. 17, no. 30, p. 3112, 2007. [Online]. Available: http://dx.doi.org/10.1039/b702425h

[109] M. Jiang, B. Key, Y. S. Meng, and C. P. Grey, "Electrochemical and Structural Study of the Layered, "Li-Excess" Lithium-Ion Battery Electrode Material Li[Li 1/9 Ni 1/3 Mn 5/9]O 2," *Chemistry of Materials*, vol. 21, no. 13, pp. 2733–2745, Jul. 2009. [Online]. Available: http://dx.doi.org/10.1021/cm900279u

[110] G. Bunker, "Interpreting XANES." [Online]. Available: http://gbxafs.iit.edu/training/XANES_intro.pdf

[111] A. N. Mansour and C. A. Melendres, "Analysis of X-ray Absorption Spectra of Some Nickel Oxycompounds Using Theoretical Standards," *The Journal of Physical Chemistry A*, vol. 102, no. 1, pp. 65–81, Jan. 1998. [Online]. Available: http://dx.doi.org/10.1021/jp9619853

[112] A. N. Mansour, L. Croguennec, G. Prado, and C. Delmas, "In situ XAS study of Li x Ni 0.7 Fe 0.15 Co 0.15 O 2 cathode material," *Journal of Synchrotron Radiation*, vol. 8, no. 2, pp. 866–868, Mar. 2001. [Online]. Available: http://scripts.iucr.org/cgi-bin/paper?S0909049501002096

[113] A. Deb, U. Bergmann, S. P. Cramer, and E. J. Cairns, "In Situ X-Ray Absorption Spectroscopic Study of Li[sub 1.05]Ni[sub 0.35]Co[sub 0.25]Mn[sub 0.4]O[sub 2] Cathode Material Coated with LiCoO[sub 2]," *Journal of The Electrochemical Society*, vol. 154, no. 6, p. A534, 2007. [Online]. Available: http://link.aip.org/link/JESOAN/v154/i6/pA534/s1&Agg=doi

[114] A. Ito, Y. Sato, T. Sanada, M. Hatano, H. Horie, Y. Ohsawa, L. Ni, and L. Co, "In situ X-ray absorption spectroscopic study of Li-rich layered cathode material Li[Ni0.17Li0.2Co0.07Mn0.56]O2," *Journal of Power Sources*, vol. 196, no. 16, pp. 6828–6834, Aug. 2011. [Online]. Available: http://dx.doi.org/10.1016/j.jpowsour.2010.09.105 http://linkinghub.elsevier.com/retrieve/pii/S037877531001712X

[115] W. Krzanowski, *Principles of Multivariate Analysis: A User's Perspective*. Oxford University Press, USA, 2000. [Online]. Available: http://www.oup.com/us/catalog/general/subject/Mathematics/?view=usa

[116] U. Bergmann, P. Wernet, P. Glatzel, M. Cavalleri, L. Pettersson, A. Nilsson, and S. Cramer, "X-ray Raman spectroscopy at the oxygen K edge of water and ice: Implications on local structure models," *Physical Review B*, vol. 66, no. 9, pp. 22–25, 2002. [Online]. Available: http://link.aps.org/doi/10.1103/PhysRevB.66.092107

[117] Z. Hussain, L. G. M. Pettersson, A. Nilsson, S. Myneni, Y. Luo, L. A. Näslund, M. Cavalleri, L. Ojamäe, H. Ogasawara, A. Pelmenschikov, P. Wernet, P. Väterlein, and C. Heske, "Spectroscopic probing of local hydrogen-bonding structures in liquid water," *Journal of Physics: Condensed Matter*, vol. 14, no. 8, pp. L213–L219, Mar. 2002. [Online]. Available: http://dx.doi.org/10.1088/0953-8984/14/8/106

[118] L. Montoro, M. Abbate, and R. J.M., "Changes in the Electronic Structure of Chemically Deintercalated LiCoO2," *Electrochemical and Solid-State Letters*, vol. 3, no. 9, p. 410, 1999. [Online]. Available: http://dx.doi.org/10.1149/1.1391162

[119] P. Kuiper, G. Kruizinga, J. Ghijsen, M. Grioni, P. Weijs, F. de Groot, G. Sawatzky, H. Verweij, L. Feiner, and H. Petersen, "X-ray absorption study of the O 2p hole concentration dependence on O stoichiometry in YBa_{2}Cu_{3}O_{x}," *Physical Review B*, vol. 38, no. 10, pp. 6483–6489, Oct. 1988. [Online]. Available: http://link.aps.org/doi/10.1103/PhysRevB.38.6483

[120] Y. Uchimoto, H. Sawada, and T. Yao, "Changes in electronic structure by Li ion deintercalation in LiCoO2 from cobalt L-edge and oxygen K-edge XANES," *Journal of Synchrotron Radiation*, pp. 872–873, 2001. [Online]. Available: http://scripts.iucr.org/cgi-bin/paper?hf5160

[121] BNL, "NSLS Ring Parameters." [Online]. Available: http://www.bnl.gov/ps/nsls/facility/machine/parameters/

[122] Brookhaven National Laboratory, "List of Beamlines by Technique," 2012. [Online]. Available: http://beamlines.ps.bnl.gov/bytechnique.aspx

[123] A. V. Baez and P. Kirkpatrick, "Formation of Optical Images by X-Rays," *Journal of the Optical Society of America*, vol. 6, no. 1895, pp. 766–774, 1946. [Online]. Available: http://dx.doi.org/10.1364/JOSA.38.000766

[124] M. P. Seah and W. A. Dench, "Quantitative electron spectroscopy of surfaces: A standard data base for electron inelastic mean free paths in solids," *Surface and Interface Analysis*, vol. 1, no. 1, pp. 2–11, Feb. 1979. [Online]. Available: http://doi.wiley.com/10.1002/sia.740010103

[125] R. Benoit, Y. Durand, B. Narjoux, G. Quintana, and Y. Georges, "IMFP Grapher." [Online]. Available: http://www.lasurface.com/xps/imfp.php

[126] S. D. Kelly and B. Ravel, "EXAFS Energy Shift and Structural Parameters," *AIP Conference Proceedings*, vol. 882, pp. 132–134, 2007. [Online]. Available: http://dx.doi.org/10.1063/1.2644451

[127] J. O. Thomas, A. S. Andersson, B. Kalska, and L. Haggstrom, "Lithium extraction / insertion in LiFePO 4 : an X-ray diffraction and Mossbauer spectroscopy study," vol. 130, pp. 41–52, 2000. [Online]. Available: http://dx.doi.org/10.1016/S0167-2738(00)00311-8

[128] Shield Pack Inc., "Data Sheet: Class PPD," West Monroe, Louisiana, Tech. Rep., 2004. [Online]. Available: http://www.shieldpack.com

[129] R. Komiya, A. Hayashi, H. Morimoto, and M. Tatsumisago, "Solid state lithium secondary batteries using an amorphous solid obtained by mechanochemical synthesis," pp. 83–87, 2001. [Online]. Available: http://dx.doi.org/10.1016/S0167-2738(01)00711-1

[130] K. Minami, A. Hayashi, and M. Tatsumisago, "Crystallization Process for Superionic Li7P3S11 Glass-Ceramic Electrolytes," *Journal of the American Ceramic Society*, vol. 94, no. 6, pp. 1779–1783, Jun. 2011. [Online]. Available: http://doi.wiley.com/10.1111/j.1551-2916.2010.04335.x

[131] S. Hama, Y. Ueno, and Y. Tsuchida, "Method for Producing All Solid Lithium Battery," *US Patent App. 13/...*, 2008. [Online]. Available: http://www.google.com/patents?hl=en&lr=&vid=USPATAPP13059844

[132] C. Xia and M. Liu, "Low-temperature SOFCs based on Gd0.1Ce0.9O1.95 fabricated by dry pressing," *Solid State Ionics*, vol. 144, no. 3-4, pp. 249–255, Dec. 2001. [Online]. Available: http://linkinghub.elsevier.com/retrieve/pii/S0167273801009808

[133] A. Blyr, C. Cigala, G. Amatucci, D. Guyomard, Y. Chabre, and J. Tarascon, "Self-Discharge of LiMn2O4/C Li-Ion Cells in Their Discharged State," *Journal of The Electrochemical Society*, vol. 145, no. 1, p. 194, 1998. [Online]. Available: http://jes.ecsdl.org/cgi/doi/10.1149/1.1838235

[134] M. Singh, O. Odusanya, G. M. Wilmes, H. B. Eitouni, E. D. Gomez, A. J. Patel, V. L. Chen, M. J. Park, P. Fragouli, H. Iatrou, N. Hadjichristidis, D. Cookson, and N. P. Balsara, "Effect of Molecular Weight on the Mechanical and Electrical Properties of Block Copolymer Electrolytes," *Macromolecules*, vol. 40, no. 13, pp. 4578–4585, Jun. 2007. [Online]. Available: http://pubs.acs.org/doi/abs/10.1021/ma0629541

[135] C. F. Petersburg, E. B. B. Mignucci, and F. Alamgir, "Optimization of Solid State Powder-Compact Lithium-ion Batteries via EIS," in *220th ECS Meeting*, Boston, MA. [Online]. Available: http://ma.ecsdl.org/content/MA2011-02/17/1295.short

[136] C. F. Petersburg, R. C. Daniel, C. Jaye, D. a. Fischer, and F. M. Alamgir, "Soft X-ray characterization technique for Li batteries under operating conditions." *Journal of synchrotron radiation*, vol. 16, no. Pt 5, pp. 610–5, Sep. 2009. [Online]. Available: http://dx.doi.org/10.1107/S0909049509025710

[137] C. J. Patridge, C. Jaye, H. Zhang, A. C. Marschilok, D. a. Fischer, E. S. Takeuchi, and S. Banerjee, "Synthesis, structural characterization, and electronic structure of single-crystalline Cu(x)V2O5 nanowires." *Inorganic chemistry*, vol. 48, no. 7, pp. 3145–52, Apr. 2009. [Online]. Available: http://www.ncbi.nlm.nih.gov/pubmed/19260681

[138] J. Ablett, A. Ackerman, R. Alforque, M. Allaire, D. Arena, A. Baron, B. Deborah, R. Beauman, J. Beebe-Wang, J. Bengtsson, S. Berg, L. Berman, B. Wayne, R. Biscardi, M. Blaskiewicz, A. Blednykh, M. Borland, I. Bozovic, N. Bozovic, and C. Burns, "NSLS-II Conceptual Design Report," Brookhaven National Laboratory, Upton, NY, Tech. Rep., 2006. [Online]. Available: http://www.bnl.gov/nsls2/project/CDR/

[139] D. Zipse, "Earthing-grounding methods: a primer," in *Record of Conference Papers. IEEE incorporated Industry Applications Society. Forty-Eighth Annual Conference. 2001 Petroleum and Chemical Industry Technical Conference (Cat. No.01CH37265)*. IEEE, pp. 11–30. [Online]. Available: http://dx.doi.org/10.1109/PCICON.2001.960503

[140] "USB pinout." [Online]. Available: http://pinouts.ru/Slots/USB_pinout.shtml

[141] F. Ronci, P. Stallworth, F. Alamgir, T. Schiros, J. Van Sluytman, X. Guo, P. Reale, S. Greenbaum, M. DenBoer, and B. Scrosati, "Lithium-7 nuclear magnetic resonance and Ti K-edge X-ray absorption spectroscopic investigation of electrochemical lithium insertion in Li4/3+xTi5/3O4," *Journal of Power Sources*, vol. 119-121, pp. 631–636, Jun. 2003. [Online]. Available: http://dx.doi.org/10.1016/S0378-7753(03)00191-5

[142] N. Leifer, A. Colon, K. Martocci, S. Greenbaum, F. M. Alamgir, T. Reddy, N. Gleason, R. Leising, and E. Takeuchi, "Nuclear Magnetic Resonance and X-Ray Absorption Spectroscopic Studies of Lithium Insertion in Silver Vanadium Oxide Cathodes," *Journal of The Electrochemical Society*, vol. 154, no. 6, p. A500, 2007. [Online]. Available: http://dx.doi.org/10.1149/1.2718402

[143] F. La Mantia, F. Rosciano, N. Tran, and P. Novak, "Quantification of Oxygen Loss from Li[sub 1+x](Ni[sub 1/3]Mn[sub 1/3]Co[sub 1/3])[sub 1-x]O[sub 2] at High Potentials by Differential Electrochemical Mass Spectrometry," *Journal of The Electrochemical Society*, vol. 156, no. 11, p. A823, 2009. [Online]. Available: http://dx.doi.org/10.1149/1.3205495

[144] A. Bianconi, E. Fritsch, G. Calas, and J. Petiau, "X-ray-absorption near-edge structure of 3d transition elements in tetrahedral coordination: The effect of bond-length variation," *Physical Review B*, vol. 32, no. 6, pp. 4292–4295, Sep. 1985. [Online]. Available: http://dx.doi.org/10.1103/PhysRevB.32.4292

[145] B. Ravel and E. Stern, "Local disorder and near edge structure in titanate perovskites," *Physica B: Condensed Matter*, vol. 208-209, pp. 316–318, Mar. 1995. [Online]. Available: http://dx.doi.org/10.1016/0921-4526(94)00686-P

[146] Q. Wang, J. C. Hanson, and A. I. Frenkel, "Solving the structure of reaction intermediates by time-resolved synchrotron x-ray absorption spectroscopy." *The Journal of chemical physics*, vol. 129, no. 23, p. 234502, Dec. 2008. [Online]. Available: http://dx.doi.org/10.1063/1.3040271

[147] M.-K. Song, S. Park, F. M. Alamgir, J. Cho, and M. Liu, "Nanostructured electrodes for lithium-ion and lithium-air batteries: the latest developments, challenges, and perspectives," *Materials Science and Engineering: R: Reports*, vol. 72, no. 11, pp. 203–252, Nov. 2011. [Online]. Available: http://dx.doi.org/10.1016/j.mser.2011.06.001

[148] C. Rumble, T. E. Conry, M. Doeff, E. J. Cairns, J. E. Penner-Hahn, and A. Deb, "Structural and Electrochemical Investigation of Li(Ni[sub 0.4]Co[sub 0.15]Al[sub 0.05]Mn[sub 0.4])O[sub 2] Cathode Material," *Journal of The Electrochemical Society*, vol. 157, no. 12, p. A1317, 2010. [Online]. Available: http://dx.doi.org/10.1149/1.3494211

[149] S.-H. Kang, P. Kempgens, S. Greenbaum, a. J. Kropf, K. Amine, and M. M. Thackeray, "Interpreting the structural and electrochemical complexity of 0.5Li2MnO3?0.5LiMO2 electrodes for lithium batteries (M = Mn0.5?xNi0.5?xCo2x, 0 ?x? 0.5)," *Journal of Materials Chemistry*, vol. 17, no. 20, p. 2069, 2007. [Online]. Available: http://xlink.rsc.org/?DOI=b618715c http://dx.doi.org/10.1039/b618715c

[150] F. M. Alamgir, H. Jain, D. B. Williams, and R. B. Schwarz, "The structure of a metallic glass system using EXELFS and EXAFS as complementary probes." *Micron (Oxford, England : 1993)*, vol. 34, no. 8, pp. 433–9, Jan. 2003. [Online]. Available: http://www.ncbi.nlm.nih.gov/pubmed/14680930

[151] J. J. Hertz, Q. Huang, T. McQueen, T. Klimczuk, J. Bos, L. Viciu, and R. R. Cava, "Magnetism and structure of LixCoO2 and comparison to NaxCoO2," *PHYSICAL REVIEW-SERIES B-*, vol. 77, no. 7, p. 75119, Feb. 2008. [Online]. Available: http://dx.doi.org/10.1103/PhysRevB.77.075119

[152] J. van Elp, J. Wieland, H. Eskes, P. Kuiper, G. Sawatzky, F. de Groot, and T. Turner, "Electronic structure of CoO, Li-doped CoO, and LiCoO2," *Physical Review B*, vol. 44, no. 12, pp. 6090–6103, Sep. 1991. [Online]. Available: http://dx.doi.org/10.1103/PhysRevB.44.6090

[153] Y. Ishida, T. Baba, R. Eguchi, M. Matsunami, M. Taguchi, A. Chainani, Y. Senba, H. Ohashi, Y. Okamoto, H. Takagi, and S. Shin, "Evidence for oxygen holes due to d-p rehybridization in thermoelectric Sr1-xRh2O4," *Physical Review B*, vol. 80, no. 8, p. 081103, Aug. 2009. [Online]. Available: http://dx.doi.org/10.1103/PhysRevB.80.081103

[154] T. Kroll, M. Knupfer, J. Geck, C. Hess, T. Schwieger, G. Krabbes, C. Sekar, D. R. Batchelor, H. Berger, and B. Büchner, "X-ray absorption spectroscopy of NaxCoO2 layered cobaltates," *Physical Review B*, vol. 74, no. 11, pp. 1–6, Sep. 2006. [Online]. Available: http://link.aps.org/doi/10.1103/PhysRevB.74.115123 http://dx.doi.org/10.1103/PhysRevB.74.115123

[155] S. D. Yoon, Y. Chen, A. Yang, T. L. Goodrich, X. Zuo, D. a. Arena, K. Ziemer, C. Vittoria, and V. G. Harris, "Oxygen-defect-induced magnetism to 880 K in semiconducting anatase TiO 2-δ films," *Journal of Physics: Condensed Matter*, vol. 18, no. 27, pp. L355–L361, Jul. 2006. [Online]. Available: http://dx.doi.org/10.1088/0953-8984/18/27/L01 http://stacks.iop.org/0953-8984/18/i=27/a=L01?key=crossref.a5c6eb1d8c853f8582ea4fc6dafa59fb

[156] P. Kuiper, G. Kruizinga, J. Ghijsen, G. Sawatzky, and H. Verweij, "Character of Holes in Li_{x}Ni_{1-x}O and Their Magnetic Behavior," *Physical Review Letters*, vol. 62, no. 2, pp. 221–224, Jan. 1989. [Online]. Available: http://dx.doi.org/10.1103/PhysRevLett.62.221

[157] W. Johnston, R. R. Heikes, and D. Sestrich, "THE PREPARATION , PROPERTIES CRYSTALLOGRAPHY , AND SYSTEM MAGNETIC," *J. Phys. Chem. Solids*, vol. 7, no. 111, pp. 1–13, 1958.

[158] B. Henke, E. Gullikson, and J. Davis, "X-Ray Interactions: Photoabsorption, Scattering, Transmission, and Reflection at E = 50-30,000 eV, Z = 1-92," *Atomic Data and Nuclear Data Tables*, vol. 54, no. 2, pp. 181–342, Jul. 1993. [Online]. Available: http://dx.doi.org/10.1006/adnd.1993.1013

[159] R. Leapman, L. Grunes, and P. Fejes, "Study of the L_ {23} edges in the 3d transition metals and their oxides by electron-energy-loss spectroscopy with comparisons to theory," *Physical Review B*, vol. 26, no. 1, 1982. [Online]. Available: http://prb.aps.org/abstract/PRB/v26/i2/p614_1

[160] H. Pitawala, M. Dissanayake, and V. Seneviratne, "Combined effect of Al2O3 nano-fillers and EC plasticizer on ionic conductivity enhancement in the solid polymer electrolyte (PEO)9LiTf," *Solid State Ionics*, vol. 178, no. 13-14, pp. 885–888, May 2007. [Online]. Available: http://linkinghub.elsevier.com/retrieve/pii/S0167273807001464

[161] W.-S. Yoon, K. Chung, and J. McBreen, "Electronic structural changes of the electrochemically Li-ion deintercalated LiNi0. 8Co0. 15Al0. 05O2 cathode material investigated by X-ray absorption spectroscopy," *Journal of Power . . .* , vol. 174, no. 2, pp. 1015–1020, 2007. [Online]. Available: http://linkinghub.elsevier.com/retrieve/pii/S0378775307013110 http://www.sciencedirect.com/science/article/pii/S0378775307013110

[162] S. Eisebitt, T. Böske, J. Rubensson, and W. Eberhardt, "Determination of absorption coefficients for concentrated samples by fluorescence detection," *Physical Review B*, vol. 47, no. 21, pp. 103–109, 1993. [Online]. Available: http://prb.aps.org/abstract/PRB/v47/i21/p14103_1

[163] Y.-K. Sun, M. G. Kim, S.-H. Kang, and K. Amine, "Electrochemical performance of layered Li[Li0.15Ni0.275xMgxMn0.575]O2 cathode materials for lithium secondary batteries," *Journal of Materials Chemistry*, vol. 13, no. 2, pp. 319–322, Feb. 2003. [Online]. Available: http://xlink.rsc.org/?DOI=b209379k

[164] A. Sakuda, N. Nakamoto, H. Kitaura, A. Hayashi, K. Tadanaga, and M. Tatsumisago, "All-solid-state lithium secondary batteries with metal-sulfide-coated LiCoO2 prepared by thermal decomposition of dithiocarbamato complexes," *Journal of Materials Chemistry*, vol. 22, no. 30, p. 15247, 2012. [Online]. Available: http://xlink.rsc.org/?DOI=c2jm32490c

[165] B. C. Dodrill, "The Performance of the Model 7400 VSM." [Online]. Available: http://www.lakeshore.com

[166] C. T. Corporation, "Magnetic Properties of Stainless Steels." [Online]. Available: http://www.cartech.com/techarticles.aspx?id=1476

[167] K.-S. Lee, S.-T. Myung, D.-W. Kim, and Y.-K. Sun, "AlF3-coated LiCoO2 and Li[Ni1/3Co1/3Mn1/3]O2 blend composite cathode for lithium ion batteries," *Journal of Power Sources*, vol. 196, no. 16, pp. 6974–6977, Aug. 2011. [Online]. Available: http://linkinghub.elsevier.com/retrieve/pii/S0378775310019208

[168] E. J. W. VERWEY, "Electronic Conduction of Magnetite (Fe3O4) and its Transition Point at Low Temperatures," *Nature*, vol. 144, no. 3642, pp. 327–328, Aug. 1939. [Online]. Available: http://www.nature.com/doifinder/10.1038/144327b0

[169] E. Goering, S. Gold, M. Lafkioti, G. Schütz, and V. Brabers, "Oxygen K-edge shift at the Verwey transition of magnetite," *Physical Review B*, vol. 72, no. 3, pp. 1–4, Jul. 2005. [Online]. Available: http://link.aps.org/doi/10.1103/PhysRevB.72.033112

[170] E. Fonda, A. Rochet, M. Ribbens, L. Barthe, S. Belin, and V. Briois, "The SAMBA quick-EXAFS monochromator: XAS with edge jumping." *Journal of synchrotron radiation*, vol. 19, no. Pt 3, pp. 417–24, May 2012. [Online]. Available: http://www.ncbi.nlm.nih.gov/pubmed/22514178

[171] M. Balasubramanian, C. S. Johnson, J. O. Cross, G. T. Seidler, T. T. Fister, E. A. Stern, C. Hamner, and S. O. Mariager, "Fine structure and chemical shifts in nonresonant inelastic x-ray scattering from Li-intercalated graphite," *Applied Physics Letters*, vol. 91, no. 3, p. 031904, 2007. [Online]. Available: http://link.aip.org/link/APPLAB/v91/i3/p031904/s1&Agg=doi

[172] P. C. Howlett, D. R. Macfarlane, and A. F. Hollenkamp, "High Lithium Metal Cycling Efficiency in a Room-Temperature Ionic Liquid," *October*, vol. 14, pp. 97–101, 2004.

[173] V. N. Strocov, T. Schmitt, U. Flechsig, T. Schmidt, A. Imhof, Q. Chen, J. Raabe, R. Betemps, D. Zimoch, J. Krempasky, X. Wang, M. Grioni, A. Piazzalunga, and L. Patthey, "High-resolution soft X-ray beamline ADRESS at the Swiss Light Source for resonant inelastic X-ray scattering and angle-resolved photoelectron spectroscopies." *Journal of synchrotron radiation*, vol. 17, no. 5, pp. 631–43, Sep. 2010. [Online]. Available: dx.doi.org/10.1107/S0909049510019862

[174] J. Guan and M. Liu, "Transport properties of LiMn2O4 electrode materials for lithium-ion batteries," *Solid State Ionics*, vol. 110, no. 1-2, pp. 21–28, Jul. 1998. [Online]. Available: http://linkinghub.elsevier.com/retrieve/pii/S0167273898000964

[175] S.-Y. Chung, J. T. Bloking, and Y.-M. Chiang, "Electronically conductive phospho-olivines as lithium storage electrodes." *Nature materials*, vol. 1, no. 2, pp. 123–8, Oct. 2002. [Online]. Available: http://www.ncbi.nlm.nih.gov/pubmed/12618828

[176] Y.-I. Jang, B. J. Neudecker, and N. J. Dudney, "Lithium Diffusion in LiCoO2 (0.45<x<0.7) Intercalation Cathodes," *Electrochemical and Solid-State Letters*, vol. 4, no. 6, p. A74, 2001. [Online]. Available: http://esl.ecsdl.org/cgi/doi/10.1149/1.1368717

[177] Z. Cheng, J.-H. Wang, Y. Choi, L. Yang, M. C. Lin, and M. Liu, "From Ni-YSZ to sulfur-tolerant anode materials for SOFCs: electrochemical behavior, in situ characterization, modeling, and future perspectives," *Energy & Environmental Science*, vol. 4, no. 11, p. 4380, 2011. [Online]. Available: http://xlink.rsc.org/?DOI=c1ee01758f

[178] K. S. Blinn, X. Li, M. Liu, L. A. Bottomley, and M. Liu, "Probing and mapping electrode surfaces in solid oxide fuel cells." *Journal of visualized experiments : JoVE*, no. 67, pp. 1–9, Jan. 2012. [Online]. Available: http://www.ncbi.nlm.nih.gov/pubmed/23023264

[179] L. Yang, S. Wang, K. Blinn, M. M. Liu, Z. Liu, and Z. Cheng, "Enhanced sulfur and coking tolerance of a mixed ion conductor for SOFCs: BaZr(0.1)Ce(0.7)Y(0.2-x)Yb(x)O(3-delta)." *Science (New York, N.Y.)*, vol. 326, no. 5949, pp. 126–9, Oct. 2009. [Online]. Available: http://www.ncbi.nlm.nih.gov/pubmed/19797657

[180] Z. Cheng and M. Liu, "Characterization of sulfur poisoning of Ni-YSZ anodes for solid oxide fuel cells using in situ Raman microspectroscopy," *Solid State Ionics*, vol. 178, no. 13-14, pp. 925–935, May 2007. [Online]. Available: http://linkinghub.elsevier.com/retrieve/pii/S0167273807001385

[181] L. Yang, Y. Choi, W. Qin, H. Chen, K. Blinn, M. Liu, P. Liu, J. Bai, T. A. Tyson, and M. Liu, "Promotion of water-mediated carbon removal by nanostructured barium oxide/nickel interfaces in solid oxide fuel cells." *Nature communications*, vol. 2, p. 357, Jan. 2011. [Online]. Available: http://dx.doi.org/10.1038/ncomms1359

[182] C. Petersburg, K. Bogaert, and F. Alamgir, "In Operando, Naked, and Hot: High Temperature Batteries Without Packaging," in *Honolulu PRiME 2012*. Honolulu, HI: The Electrochemical Society, 2012. [Online]. Available: http://ma.ecsdl.org/content/MA2012-02/10/794.full.pdf

[183] K. Tikhonov and V. R. Koch, "Li-ion Battery Electrolytes Designed For a Wide Temperature Range," Covalent Associates, Inc., Corvallis, OR, Tech. Rep. 1, 2012. [Online]. Available: http://www.covalentassociates.com/publications.htm

[184] J. Bates, N. Dudney, D. Lubben, G. Gruzalski, B. Kwak, X. Yu, and R. Zuhr, "Thin-film rechargeable lithium batteries," *Journal of Power Sources*, vol. 54, no. 1, pp. 58–62, Mar. 1995. [Online]. Available: http://dx.doi.org.prx.library.gatech.edu/10.1016/0378-7753(94)02040-A

[185] R. Unocic, L. Adamczyk, N. Dudney, D. Alsem, N. Salmon, and K. More, "In-situ TEM Characterization of Electrochemical Processes in Energy Storage Systems," *Microscopy and Microanalysis*, vol. 17, no. S2, pp. 1564–1565, Oct. 2011. [Online]. Available: http://www.journals.cambridge.org/abstract_S1431927611008695

[186] A. Hayashi, T. Ohtomo, F. Mizuno, K. Tadanaga, and M. Tatsumisago, "All-solid-state Li/S batteries with highly conductive glass-ceramic electrolytes," *Electrochemistry Communications*, vol. 5, no. 8, pp. 701–705, 2003. [Online]. Available: http://linkinghub.elsevier.com/retrieve/pii/S138824810300167X

[187] Airgas, "Material Safety Data Sheet: Hydrogen Sulfide," Tech. Rep., 2012. [Online]. Available: http://www.airgas.com/documents/pdf/001029.pdf

[188] S. Hama and M. Hayashi, "Process for Producing Sulfide-Based Solid Electrolyte," 2009.

[189] S. S. Berbano, I. Seo, C. M. Bischoff, K. E. Schuller, and S. W. Martin, "Formation and structure of Na2S+P2S5 amorphous materials prepared by melt-quenching and mechanical milling," *Journal of Non-Crystalline Solids*, vol. 358, no. 1, pp. 93–98, Jan. 2012. [Online]. Available: http://linkinghub.elsevier.com/retrieve/pii/S0022309311005588

[190] Aalco, "Aluminium Alloys - Aluminium 6063/6063A Properties." [Online]. Available: http://www.azom.com/article.aspx?ArticleID=2812

[191] J. Gonczy, R. Ferry, R. Niemann, and B. Roop, "UHV seal studies for the Advanced Photon Source storage ring vacuum system," *Conference Record of the 1991 IEEE Particle Accelerator Conference*, pp. 2304–2306, 1991. [Online]. Available: http://ieeexplore.ieee.org/lpdocs/epic03/wrapper.htm?arnumber=164948

[192] Problem Solving Products Inc., "O-Ring Fluid Compatibility Guide." [Online]. Available: http://www.pspglobal.com/fluid-compatibility/index.html

[193] S. Khalid, "EXAFS Database of Standard Materials." [Online]. Available: http://www.bnl.gov/ps/x18b/data.asp

[194] M. Newville, "The Atoms.inp Archive." [Online]. Available: http://cars9.uchicago.edu/ newville/adb/search.html